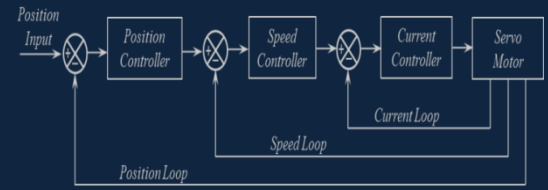




e-ISSN: 2618-575X



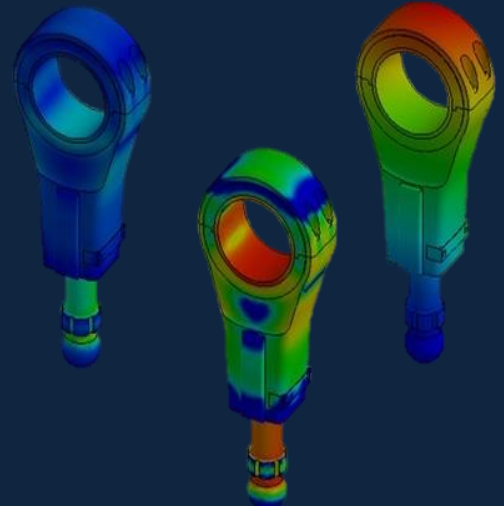
# *International Advanced Researches and Engineering Journal*

Aerospace Engineering,  
Aquaculture and Fisheries Engineering,  
Architecture,  
Bioengineering,  
Cell and Tissue Engineering  
Chemical Engineering,  
Civil Engineering,  
Computer Engineering,  
Electrical and Electronics,  
Energy,  
Environmental Engineering,  
Food Engineering,  
Geomatics Engineering,  
Health in Engineering  
Industrial Engineering,  
Industrial Applications,  
Machine Theory and Dynamics,  
Marine Science and Technology,  
Materials and Nano Science,  
Manufacturing,  
Mechanical Engineering,  
Mechanics,  
Mechatronics,  
Medical,  
Modeling and Simulation,  
Physics Engineering,  
Robotics,  
Sustainable Science Technology,  
Textile Engineering  
Transport Science and Technology

$$F=ma$$

$$E=mc^2$$

$$\int \frac{dy}{dx} dt$$



**Volume: 04 / Issue: 03 / December 2020**



e-ISSN: 2618-575X

Available online at [www.dergipark.org.tr/en](http://www.dergipark.org.tr/en)

INTERNATIONAL ADVANCED RESEARCHES  
and  
ENGINEERING JOURNAL

Journal homepage: [www.dergipark.org.tr/en/pub/iarej](http://www.dergipark.org.tr/en/pub/iarej)

International  
Open Access



Volume 04  
Issue 03

December, 2020

International Advanced Researches and Engineering Journal (IAREJ) is a double-blind peer-reviewed and publicly available online journal that has Editorial Board (<https://dergipark.org.tr/en/pub/iarej/board>). The editor in chief of IAREJ welcomes the submissions that cover theoretical and/or applied researches on **Engineering** and related science with Engineering. The publication language of the Journal is **English**. **Writing Rules** are given in Author Guidelines (<https://dergipark.org.tr/en/pub/iarej/writing-rules>). IAREJ publishes **original papers** that are research papers and technical review papers.

IAREJ publication, which is **open access**, is **free of charge**. There is no article submission and processing charges (APCs).

**IAREJ is indexed & abstracted in:**

Crossref (Doi beginning: 10.35860/iarej.xxxxxx)  
Directory of Open Access Scholarly Researches (ROAD)  
Directory of Research Journals Indexing (DRJI)  
EBSCO  
Google Scholar  
Index Copernicus (ICI Journal Master List)  
J-Gate  
Rootindexing  
Scientific Indexing Services (SIS)  
TUBITAK ULAKBIM TR Dizin (TR index)  
WorldCAT

Authors are responsible from the copyrights of the figures and the contents of the manuscripts, accuracy of the references, quotations and proposed ideas and the Publication Ethics (<https://dergipark.org.tr/en/pub/iarej/page/4240>).

All rights of the issue are reserved by International Advanced Researches and Engineering Journal (IAREJ). IAREJ also allows the author(s) to hold the copyright of own articles.

©

IAREJ

15 December 2020



This is an open access issue under the CC BY-NC license (<http://creativecommons.org/licenses/by-nc/4.0/>).




e-ISSN: 2618-575X

Available online at [www.dergipark.org.tr/en](http://www.dergipark.org.tr/en)

INTERNATIONAL ADVANCED RESEARCHES  
and  
ENGINEERING JOURNAL

Journal homepage: [www.dergipark.org.tr/en/pub/iarej](http://www.dergipark.org.tr/en/pub/iarej)

International  
Open Access 

Volume 04  
Issue 03

December, 2020

## Table of Contents

<b>Review Articles</b>	<b>Pages</b>
<a href="#">Toggling effect on pullout performance of pedicle screws: Review</a> <i>Mehmet Fatih AYCAN and Teyfik DEMİR</i>	161-172
<b>Research Articles</b>	<b>Pages</b>
<a href="#">The comparative study of conventional and ultra-high frequency induction sintering behavior of pure aluminum</a> <i>Burak GÜL, Levent Ulvi GEZİCİ, Mehmet AYVAZ and Uğur ÇAVDAR</i>	173-179
<a href="#">Nonlinear vibration and dynamic response of nano composite conical tube by conveying fluid flow</a> <i>Masoud RAHMANİ and Amin MOSLEMI PETRUDİ</i>	180-190
<a href="#">Effect of spring mid-support condition on the vibrations of the axially moving string</a> <i>Saim KURAL</i>	191-199
<a href="#">Turkish sign language digits classification with CNN using different optimizers</a> <i>Onur SEVLİ and Nazan KEMALOĞLU</i>	200-207
<a href="#">Analysis of parameter changes of a neuronal network model using transfer entropy</a> <i>Sevgi ŞENGÜL AYAN and Deniz GENÇAĞA</i>	208-216
<a href="#">CCII current conveyor and dormand-prince-based chaotic oscillator designs for secure communication applications</a> <i>Murat ALÇIN, Murat TUNA, İhsan PEHLİVAN and İsmail KOYUNCU</i>	217-225
<a href="#">Design of polyrod antenna having isoflux radiation characteristic for satellite communication systems</a> <i>Volkan AKAN</i>	226-232
<a href="#">PAPR reduction using selective mapping scheme in universal filtered multicarrier waveform</a> <i>Şakir ŞİMŞİR and Necmi TAŞPINAR</i>	233-238
<a href="#">Performing reactive power compensation of three-phase induction motor by using parallel active power filter</a> <i>Ömer Ali KARAMAN, Ahmet GÜNDOĞDU and Mehmet CEBECİ</i>	239-248
<a href="#">Liquid level control with different control methods based on Matlab/Simulink and Arduino for the control systems lesson</a> <i>Mehmet YUMURTACI and Özgür VERİM</i>	249-254
<a href="#">Estimation of consistency limits of fine-grained soils via regression analysis: A special case for high and very high plastic clayey soils in Istanbul</a> <i>Zülal AKBAY ARAMA, Muhammed Selahaddin AKIN, Said Enes NURAY and İlknur DALYAN</i>	255-266



## Review Article

## Toggling effect on pullout performance of pedicle screws: Review

Mehmet Fatih Aycan <sup>a,\*</sup>  and Teyfik Demir <sup>b</sup> 

<sup>a</sup>Department of Mechanical Engineering, Gazi University, Ankara, Turkey

<sup>b</sup>Department of Mechanical Engineering, TOBB University of Economics and Technology, Ankara, Turkey

## ARTICLE INFO

## Article history:

Received 17 April 2020

Revised 17 June 2020

Accepted 08 July 2020

## Keywords:

Loosening

Pedicle screws

Pullout strength

Review

Toggling effect

## ABSTRACT

Screw loosening in spine surgery is a clinical complication in patients with poor bone quality. Pedicle screws are subjected to bending moments and axial loads that may cause toggling during daily movements of spine. The purpose of this study was to assess the previous studies related to toggling effect on pullout performance of pedicle screws by surveying the whole literature and to provide some discussion for new studies about pullout performance of pedicle screws after toggling. The search was performed by combining terms of pedicle screw, toggling, screw loosening, fatigue, cyclic loading, and pullout. The retrieved articles dealing with determined terms and also their references were reviewed. Some of these articles were eliminated after review process. Toggling was determined to be crucial for the stabilization performance of pedicle screw because the loosening mechanism of screws was affected directly by cyclic loading. The toggling or cyclic loading affected the holding capacity of pedicle screws negatively, and the possibility of loosening or failure problem for pedicle screws increased with cyclic loading magnitude. Loading conditions, screw properties, test medium, level of spinal region, and cement usage were determined by many researchers as the most important parameters affecting the toggling performance as well as the pullout strength of pedicle screws. The pullout strength of pedicle screws generally decreased with cyclic loading. The parameters of cyclic loading were fairly important for pullout performance of pedicle screws. Screw properties and cement augmentation had critical effects on the stability of screws under cyclic loading, as well.

© 2020, Advanced Researches and Engineering Journal (IAREJ) and the Author(s).

### 1. Introduction

Screw loosening is a prevalent complication for the stabilization of the spine after surgery operations. The complication, proved to be challenging especially in the osteoporotic bones, has negative effects on the performance of pedicle screws [1]. Osteoporosis, namely low bone mineral density (BMD), negatively affects the vertebral body and there is not a possibility of sufficient strength provided by pedicle screws at the screw-bone interface, which results in a loosening or failure problem [2]. Fixation stability and holding capacity of pedicle screws in biomechanical applications are determined by pullout tests performed with axial tension loading [3]. The maximum axial load sustained by the screw is accepted as the pullout strength of screw in ASTM Standard (F543-17) [4-5]. In order to improve the pullout strength of pedicle screw constructs and to perform the stabilization of pedicle

screws on osteoporotic patients, the pullout performance of pedicle screws and loosening mechanisms were studied by many researchers [6-8]. It was determined that many parameters such as screw properties, augmentation conditions, insertion technique, etc. affected the pullout strength of pedicle screws [2, 9-10]. Demir and Başgöl studied the parameters that affected the pullout strength of pedicle screws. They investigated the effect of screw designs, insertion techniques, cement augmentation, screw coating, test conditions, etc. on the pullout strength [11].

Early-stage pullout strength of pedicle screws is crucial for determining the performance of surgery operations [7, 12-13]. On the other hand, there is a necessity of determining long-term pullout strength because it is as important as early-stage performance. In order to determine the long-term pullout performance, the pedicle screws have to be sustained to the cyclic loading which

\* Corresponding author. Tel.: +90-312-5823411; Fax: +90-312-2152004.

E-mail addresses: [mfaycan@gazi.edu.tr](mailto:mfaycan@gazi.edu.tr) (M.F.Aycan), [tdemir@etu.edu.tr](mailto:tdemir@etu.edu.tr) (T.Demir)

ORCID: 0000-0001-9434-5955 (M.F.Aycan), 0000-0001-6352-8302 (T.Demir)

DOI: 10.35860/iarej.722229

simulates the forces that occurred on screws due to movement of the body before pullout testing. When the pedicle screws are subjected to the cyclic loading, the holding capacity is decreased and this decrease enhances the risk of loosening or failure of pedicle screws dramatically [14-17]. In addition to parameters related to the early stage pullout strength, the magnitudes of tensile and compression forces and bending moments are the critical parameters that have to be evaluated for long term pullout performance [1, 16, 18-20].

Reviewing and assessing the articles related to both toggling and pullout is believed to have a valuable contribution to the researchers investigating pedicle screws. Hence, the objective of this article is to review the studies including pullout behaviors of pedicle screws with or without toggling.

## 2. Methods

A comprehensive search was conducted using the keywords of “pedicle screw” and “pullout” combined with the words of “toggling” or “cyclic loading” or “fatigue” or “loosening”. Furthermore, in order to determine the augmentation effect on pullout strength after cyclic loading, the search was repeated with the terms of “bone cement” and “augmentation”.

The effect of pedicle screw properties, the cyclic loading conditions, test medium (human or animal cadaver, polyurethane foam block or synthetic bone model), level of spinal region, and cement usage on pullout performance of pedicle screws were reviewed comprehensively. The search consisted of articles, conference papers, international standards, thesis, books, technical reports, and case reports published in English and Turkish between 1990 and 2019. Articles not including toggling or cyclic loading and not related to pedicle screws were excluded.

## 3. Results

During the literature review conducted with the determined keywords, approximately 180 articles were surveyed. The review included the studies describing the long-term pullout performance of pedicle screws inserted to the human or animal cadaver and polyurethane foam or synthetic models. While studies not related to pedicle screws or cyclic loading were excluded, the studies only providing cyclic loading or fatigue behavior or toggling without pullout tests were included in the search. When the articles were divided into groups according to their relation with toggling and pullout, there were 12 studies investigated only the pullout performance of pedicle screws in the first group; 27 studies including toggling, cyclic loading, fatigue, and pullout testing in the second group; 11 studies related with only toggling, cyclic loading, the fatigue of pedicle screws in the third group; and 6 studies describing the subjects apart from others in

the fourth group. Thus, a total of 56 articles were identified and included in the systematic review. The included articles are given in tables. Table 1, Table 2, Table 3 and Table 4 depict the studies related with only pullout strength, the studies related with pullout performance after toggling/cyclic loading/fatigue, the studies related with just toggling/cyclic loading/fatigue, and the studies related with pullout test and toggling/cyclic loading/fatigue separately, respectively.

## 4. Discussion

To the best of our knowledge, this is the first article that systematically reviews the literature related to toggling effect on the pullout strength of pedicle screws. The effects of cyclic loading conditions (load frequency, screw displacement, load direction, and load level, etc.), screw properties (types, geometry, and material, etc.), test mediums (cadaver, polyurethane foams, and synthetic bone models), the spinal region of cadavers (lumbar, thoracic and cervical) and cement usage on pullout performance with and without toggling were reviewed.

Biomechanical properties of screw fixations are generally determined by using pullout and toggling tests. Pullout testing standardized in ASTM F543 is commonly used to evaluate fixation stability and holding capacity of pedicle screws [5, 21]. The pullout test apparatus and samples are shown in Figure 1. In order to determine the early stage pullout performance of pedicle screws, the pullout test is performed shortly after the insertion process without cyclic loading. In this way, the short term stability of screws is investigated, because the inadequate holding capacity of pedicle screws is a common problem in surgery operations and it has to be determined before causing more catastrophic problems in the future [9]. The early-stage pullout performance of pedicle screws was studied by researchers in different conditions. The pedicle screws inserted to the vertebra are subjected to the loads in time after the operation, also the long-term pullout performance of pedicle screws is important for surgeons. The toggling situation is simulated by cyclic loading in biomechanical applications. Thus, the long term pullout performance is determined by pullout tests after performing cyclic loading. Defining long term pullout performance is as crucial as defining short term performance. In the toggling test, the tensile or compression and bending moments are applied to the pedicle screws until the failure or loosening and any time for pullout testing to determine the decrease in holding capability of pedicle screws.

It was determined that the cyclic loading generally had a negative effect on the pullout performance of pedicle screws. Applying cyclic loading causes tensile and compression forces sinusoidally and bending moment on the head of pedicle screws. The loading components develop a stress region along with the bone-screws

interface and it leads to the loss of the stabilization of fixation in time [15, 20, 22]. The force generated on the screw is transferred through the longitudinal axis of the screw to the bone and the interface is the weakness area in this system [23].

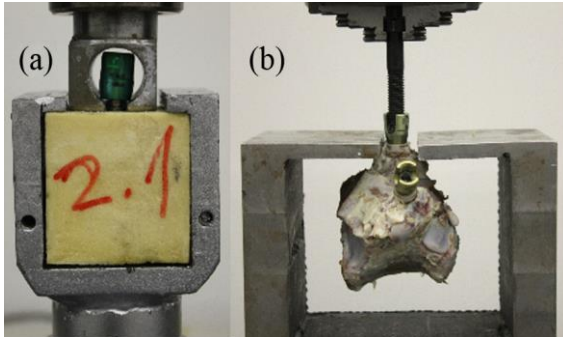


Figure 1. Pullout test apparatus and test samples: (a) PU foam and (b) bovine vertebra [15]

On the other hand, there was another hypothesis that bone tissue which contacted with pedicle screw compressed during the toggling movement, so the compression of bone increased the pullout strength of pedicle screws compared to the initial situation [19]. The bone structure had openings or grooves and these spongy tissues were compressed with compression force in toggling tests. The compressed bone tissue becomes denser and it can withstand the further loads subjected, due to cyclic loading. In some cases, the compression force caused a micro crack in trabeculae bones at higher loading cycles [24]. The magnitude of the force applied to the screw is crucial, and there is a possibility that it may cause damage in the bone adjacent to the screw. The magnitude of forces occurring due to cyclic loading depends on the loading direction and loading conditions, as well. The loads are generally applied to the pedicle screws craniocaudally or mediolaterally or axially in toggling tests [20, 25, 26].

Table 1. The studies related with just pullout strength

No	Authors	Levels	Screw implantation	Cyclic move.	Toggling/Cyclic parameter	Biomechanics	Results	Comments
[2]	Chao KH, et al.	Human Thoracic Lumbar	Cannulated 6x40 mm	-	-	Pullout tests.	Prefilling and cement injection methods has similar fixation strength.	Prefilling and cement injection
[3]	Hashemi A, et al.	PU blocks	Standard 6.5 mm ø	-	-	Pullout tests.	CP augmentation improved the pullout strength in both failed samples and low density PU blocks.	CP bone augmentation
[6]	Choma T, et al.	Human vertebrae	Solid, PFen, Ffen 6.0x45 mm	-	-	Pullout tests.	The fixation strength increased with all augmentation techniques (Pfen, the greatest fixation).	Prefilling and cement injection
[7]	Tolunay T, et al.	PU foam G20, Bovine vertebra	Solid, DLDC cannulated, 7.5x50 mm	-	-	Pullout tests.	The DLDC with PMMA exhibited the highest pullout values. PS without cement has similar strength.	Prefilling and cement injection
[8]	Yaman O, et al.	PU foam G20, Bovine vertebra	Core and threaded types 5.5x45 mm	-	-	Pullout tests.	Transpedicular with helical angles exhibit higher pullout strength compared to the classical screws	Effect of helical angles
[9]	Tolunay T, et al.	PU foam G10 and G40	Solid and cannulated 6.5x45 mm	-	-	Pullout tests. Torsion tests.	The unilateral, sequential, 3-radial hole, drilled, cannulated screw was the ideal alternative.	Effects of hole, gap type, position
[10]	Varghese V, et al.	PU foam G5, G10 and G15	6.5x45 mm	-	-	Pullout tests.	Increasing density and insertion depth (except insertion angle) increased the pullout strength.	Effects of fixation parameters
[12]	Kim YY, et al.	PU foam G5, G15 and G20	Outer and inner diameter shape, threads	-	-	Pullout tests.	The outer cylindrical and inner conical configuration with a V-shaped thread provide max pullout	Cy/Cy-V B S Cy/Co-V B S Co/Co-V B S
[13]	Mehta H, et al.	Human vertebrae	PS with thick crest, thin crest,	-	-	Pullout tests.	The dual lead osteoporotic-specific PS had significantly larger insertion torques, similar pullout properties.	Effect of differential thickness
[38]	Aycan MF, et al.	PU G10, G40, bovine vertebra	7.5x45 mm, 4.5x45 mm core 7.5x60 mm shell	-	-	Pullout tests.	The novel expandable PS with expandable PEEK shells have higher performance than others.	Screw designs (PEEK shell)
[39]	Demir T.	Grade 10, Grade 40	Solid, cannulated 6.0x45 mm	-	-	Pullout tests.	Cannulated screws without cement for the cases (healthy bone) can be a reliable alternative to solid screws.	Artificial fusion (the first)
[40]	Chen L, et al.	PU foam (0.09 g/cm <sup>3</sup> )	Conical, cylind. cannulated, 4.8-6.0x60 mm	-	-	Pullout tests.	For the conically and cylindrically solid shaped screw, prefilling offer improved initial fixation strength.	Prefilling and cement injection

Table 2. The studies related with pullout performed after toggling/cyclic loading/fatigue

No	Authors	Levels	Screw implantation	Cyclic move.	Togglin / Cyclic parameters	Biomechanics	Results	Comments
[1]	Kueny RA, et al.	Human Lumbar	5.5x50 mm, 6.5x50 mm	CC	1 Hz, from 25 N by 25 N every 250 cycles	Pullout tests after toggling.	Injection increased fatigue force, prefilling reduced. Higher diameter increased pullout and fatigue force	Prefilling and screw injection
[15]	Aycaan MF, et al.	PU G10, G40, bovine vertebra	7.5x45 mm, 4.5x45 mm, 7.5x60 mm	CC	±1 mm, 3 Hz, 5000 cycles	Pullout tests after toggling.	Toggling have negative effect on pullout strength, NPS with PMMA was affected by toggling dramatically	Comparing designs (PEEK shell).
[16]	Paik H, et al.	Human vertebra	5x30 mm	CC	0 to -50 N, 1 Hz, 2000 cycles	Pullout tests after toggling.	Hubbing decreases the pullout strength, It causes a fracture in dorsal lamina, pedicle and superior articular facet	Teeter-totter, windshield wiper
[19]	Patel P, et al.	PU foams 0.32 and 0.16 gcm <sup>-3</sup>	4.7x30 mm, 6.7x30 mm	CC	±1 mm at a rate of 0.1 mm.s <sup>-1</sup>	Pullout tests after toggling.	Screw toggling does not affect screw pullout significantly	Effect of toggling on fixation
[20]	Mehmanparast H, et al.	Porcine Lumbar	5x35 mm	CC, ML	±1 mm, 3 Hz, 5000 cycles	Pullout tests after toggling.	CC toggling significantly affects the pullout force and the screw stiffness.	Loosening in CC and ML
[22]	Mehmanparast H, et al.	PU G10, G20, G30	5x35 mm	CC	±1 mm, 3 Hz, 5000 cycles	Pullout tests after toggling.	Toggling is more likely to affect pedicle screw stiffness than pullout force.	Toggled and non-toggled conditions
[25]	Zhu Q, et al.	Human Lumbar	6x45 mm	CC	30 N to 300 N 1000 cycles at 0.5 Hz	Pullout tests after toggling.	There was no significant difference (toggling and pullout performances) between two cements.	PMMA and Sr-HA cement types
[23]	Lill C, et al.	Calf spines	7x55 mm, 6x55 mm	CC	5,000 cycles at ±200 N, 1 Hz.	Pullout tests after cyclic loading.	The pullout strength of pedicle screws reduced after cyclic loading.	Conical and cylindrical screws
[26]	Savage J, et al.	Human cervical	-	Axial	1000 cycles of axial loading	Pullout tests after axial cyclic loading.	C1LM-C2LS has similar stability with a C1LM-C2PS construct after cyclic loading.	Lateral mass translaminar screws.
[29]	Liebsch C, et al.	PU model human vertebra	6.5x45 mm	Cplx. load. tests	5 Hz until 6 mm loosening or 600000 cycles	Cyclic loading.	The loosening characteristics of pedicle screws were similar.	Novel testing model
[33]	Gates TA, et al.	Lumbar vertebral bodies	4.5x25 mm	CC	±200 N at 0.5 Hz for 1000 cycles	Pullout tests after toggling.	A novel anchor for pedicle screws had higher fatigue strength, greater failure force.	PEEK Anchor
[32]	Pishnamaz M, et al.	Human vertebrae	-	CC	3 Hz, 20-200 N, 100,000 cycles	Pullout tests after toggling.	The anchoring stability of high-volume augmented screws is disadvantageous.	The effect of cement volume
[55]	Bostelmann R, et al.	Lumbar (L1-L5)	6.0x45 mm	CC	20-50 N, 0.1 N per cycle and 1 Hz for 5000 cyc.	Pullout tests after toggling.	Augmentation of pedicle screws increased the number of load cycles and failure load.	Load cycles to failure.
[34]	Schmoelz W, et al.	Human Lumbar vertebrae	Cannulated, fenestrated 5.5x35 mm	CC	±50 N by 5 N every 100 cycles until 11,000 cyc.	Pullout tests after toggling.	The novel silicone sustained a higher number of load cycles and load magnitude.	Load cycles to failure
[27]	Mehmanparast H, et al.	Lumbar vertebrae, porcine	-	CC	±1 mm, 3 Hz, 5000 cycles	Pullout tests after toggling.	Toggling method is more likely to affect pedicle screw stiffness than pullout force	Comparing stability of pedicle
[30]	Baluch D, et al.	Human lumbar and thoracic	4.5x40 mm, 6.5x45 mm	CC	±200 N inc. by 25 N every 20 cyc. until 2 mm	Pullout tests after toggling.	Laterally directed cortical pedicle screws have superior resistance to CC toggling.	Laterally, medially directed
[50]	Burval D, et al.	Human lumbar vertebrae	6.25x40 mm	CC	5000 cycles, 3 Hz, ±5 mm	Pullout tests after toggling.	Kyphoplasty technique had significantly greater pullout strength than other techniques.	Transpedicular and kyphoplasty
[46]	Akpolat Y, et al.	Human lumbar vertebrae	6.5x55 mm, 4.5x25 mm	CC	±4 Nm bending, 1 Hz, 100 cycles or until 6° loose.	Pullout tests after axial cyclic loading.	Standard pedicle screw had a better fatigue performance than the CBT screw.	Fatigue behavior of CBT screws
[43]	Lai, D.M., et al.	Human thoracic vertebrae	4.35x35 mm, 5.0x35 mm	CC	10 - 100 N at 1 Hz, 5000 cycles and 10000 cycles	Pullout tests after toggling.	Both sizes of screws exhibited comparable pullout strengths post fatigue loading.	Diameter effect on pullout

The craniocaudal or cephalocaudal were the most used directions for cyclic loading in toggling tests. The general view of the toggling test apparatus commonly used is given in Figure 2.

Although aforementioned studies generally use this cyclic loading, mediolateral, and axial loading methods,

which repeated loading in other directions, cause screw loosening, as well [27]. Mehmanparast et al. [20] investigated the craniocaudal and mediolateral direction effects on the toggling behavior of pedicle screws comparing with non-toggling conditions.

Table 3. The studies related with just toggling/cyclic loading/fatigue

No	Authors	Levels	Screw implantation	Cyclic move.	Toggling/ Cyclic parameters	Biomechanics	Results	Comments
[18]	Benson D, et al.	Human Lumbar vertebra	6x45 mm	CC	20-100 at 2,000 cycles for each load, 10,000 cyc.	Cyclic loading (Fatigue tests)	The kyphoplasty technique has similar resistance to vertical toggle movement	Comparing augmentation techniques
[24]	Sterba W, et al.	Human Lumbar vertebra	6 mm	CC	2 Hz, 2000 cycles, peak load of 50 N (R=0.1)	Cyclic loading.	Straight screw insertion has a better fatigue performance.	Screw insertion technique
[29]	Liebsch C, et al.	PU foam model	6.5x45 mm	CC	5 Hz until 6 mm loosening or 600000 cycles	Cyclic loading.	The loosening characteristics of screws were almost similar.	Novel testing model
[36]	Rodriguez-Olaverri J, et al.	Calf Toracic Lumbar	5.5x30 mm	Lat. bend.	3 Hz with the 100 N, at 10-10,000 cycles	Cyclic loading.	The use of angled screw orientations at the ends of anterior constructs have higher stability after cyclic loading.	End screw angulation on construct stability
[52]	Sven H, et al.	Lumbar vertebra	-	CC	50 cyclic loads, 5-50 N, 5-100 N, 5-200 N	Cyclic loading.	Augmentation increases pedicle screw performances for osteoporotic vertebrae.	Augmentation effect under cyclic loading
[57]	McLachlin S, et al.	Sacral vertebra	Sacral screw	Cyclic tens.- comp.	0.5 Nm for the first 1000 cycles 1 Nm every 1000 cycles, 1 Hz	Cyclic loading.	The PMMA augmentation provided increased resistance to cyclic loading compared	Comparing CTBC with PMMA under cyclic loading.
[27]	Mehmanparast H, et al.	Lumbar vertebra, porcine	-	CC	±1 mm, 3 Hz, 5000 cycles	Pullout tests after toggling.	Toggling method is more likely to affect pedicle screw stiffness than pullout force	Comparing stability under cyclic loading.
[28]	Bianco RJ, et al.	Human lumbar vertebra	5.5x45 mm (single lead and dual lead thread)	CC	0 to 400 N, 4 cycles	Cyclic loading.	Lateral loads induce greater bone deformation and risks of failure than cranial loads.	Comparing resulting forces, displ., and rotations
[35]	Lindtner R, et al.	Human lumbar vertebra	6.5x45 mm	CC	±50 N, incr. 5 N every 100 cycles, 10000 cycles or loosening	Cyclic loading.	Nonmetallic CF/PEEK pedicle screws have a similar resistance with standard titanium screws.	Carbon fiber-reinforced PEEK (CF/PEEK)
[41]	Kiner D, et al.	Human lumbar vertebra	6 mm and 8 mm	CC	2000 cycles, 2 Hz, 50 N (peak load), R=0.1	Fatigue tests.	The larger diameter screws were more resilient than the cement augmented standard diameter screws.	Angled and straight insertion technique
[48]	Lim T, et al.	Lumbar vertebra	6.5x55 mm	CC	± 1 mm, 0.5 Hz, 200 N caudal, 100 N cephalad	Cyclic loading.	Positive correlation between the number of loading cycles to induce screw loosening and bone mineral density	The relation between BMD and number of cycles
[45]	Wang, WT, et al.	Sheep lumbar vertebra	4.5x25 mm	CC	± 200 N, increase 25 N every 20 cyc., until 2 mm	Cyclic loading.	In cyclic loading, maximum displacement was lower in DPTCPS compared to SPPS and SPTCPS.	DPPS, SPPS, DPTCPS or SPTCPS

While the toggling significantly reduced the pullout strength and stiffness of pedicle screws in both methods, craniocaudal toggling affected the pullout force and the screw stiffness significantly. On the other hand, Bianco et al. [28] compared the effect of cyclic loading direction on pedicle screw fixation performance and concluded that the lateral loads (mediolateral loading) caused greater bone deformation and failure risks than cranial loads. The pullout performance of pedicle screws after toggling depended on the direction of cyclic loading because the limits of screw plowing occurred in pedicles was affected by magnitude and direction of loading. The sidewalls of the pedicle restrained the plowing movement during the cyclic loading because the distance between the superior endplate and the inferior endplate was larger than the distance between both sidewalls. Liebsch et al. designed a novel test setup for toggling tests [29]. Complex loading components of combined shear forces, tension forces, and bending moments were generated in a novel toggling test

setup. This testing model eliminated the limitations of uniaxial loading conditions substantially because it was known that the pedicle screws inserted pedicles of vertebra were subjected to complex loading conditions instead of unidirectional loading during movement of the body.

The loading parameters of toggling affected the loosening behavior and holding capacity of pedicle screws directly. Loading level, loading frequency, number of cycles, and displacement limits were the main parameters of toggling affecting the pullout performance.

The toggling parameters were generally determined in order to simulate the physiological conditions of the spine during walking. It was calculated that the pedicle screws inserted to the lumbar vertebra were subjected to the compressive loads between 270 N and 667 N during normal walking for an average patient [30]. Furthermore, some researchers determined that the displacement of 1 mm were produced by forces generated on screws during walking [19, 31].



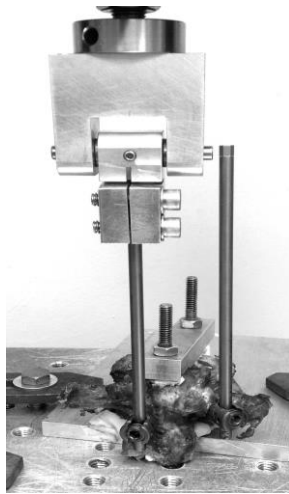


Figure 2. Apparatus for craniocaudal toggle testing [20]

While the number of cycles in toggling tests changed between 200 and 600000 cycles, many researchers used 2000 or 5000 cycles for cyclic loading [15-16, 18, 20]. The preliminary test results showed that the defined number of

cycles was sufficient for loosening the pedicle screws before the pullout test. On the other hand, a higher number of cycles might be used in order to determine the loosening amount of pedicle screws under cyclic loading without pullout testing. In this toggling method, the effect of the number of cycles on the loosening behavior of pedicle screws was investigated.

The toggling tests were performed with two protocols: displacement-controlled and load-controlled. In the displacement-controlled tests, the maximum displacement of the pedicle screw head in one axis was controlled in determining limit values which were defined in several studies as  $\pm 1$  mm, but there was a use of 6 mm displacement value in literature [15, 19, 20, 22, 29]. The applied load to the screw reached the highest level at the beginning of the test and also the peak load was provided at this time. The load level decreased in time until the end of the test or failure of the pedicle screw. The load applied to the screw in response to the displacement had exponential decay during the toggling test.

Table 4. The studies related with pullout test and toggling/cyclic loading/fatigue separately

No	Authors	Levels	Screw implantation	Cyclic move.	Toggling/ Cyclic parameters	Biomechanics	Results	Comments
[14]	Demir T.	PU foam G20 and calf vertebrae	7.5x45 mm expandable, 4.0x40 mm cannulated	-	100 N, 10 Hz, 1000000 cycles	Pullout tests. Flexion/ Extension tests. Axial gripping capacity tests. Torsional gripping tests. Toggling tests.	The pullout and fatigue values for expandable PEEK shell were higher than classical pedicle screw.	Novel PEEK expandable shell and classical pedicle screws
[17]	Brasiliense L, et al.	Lumbar vertebra and PU foam	6.5x40 mm Dual threaded and single thread	CC	2,500 cycles, 2.5 Hz, 75 N (peak load)	Fatigue tests. Pullout tests.	Dual-threaded screws failed at a higher load and endured a higher cycles of loading	Flank overlap area
[42]	Wittenberg R, et al.	Human lumbar, sacra vertebrae	6.25 mm, 5 mm, 6 mm,	CC	$\pm 2$ mm, 200 N, 5000 cycles	Pullout tests. Cyclic transverse bending.	PMMA and a biodegradable CBC both increased the axial pullout force and the transverse bending stiffness.	Diameter effect on pullout strength
[31]	Lotz J, et al.	Human lumbar vertebrae	6.5x45 mm	Superior - interior direction	$\pm 1$ mm, 3 Hz, 5000 cycles	Pullout tests. Cyclic transverse loading.	Augmentation has positive effect on pullout strength, stiffness and absorbed energy under cyclic loading.	Carbonated apatite cancellous bone cement
[37]	Inceoglu S, et al.	Bovine lumbar vertebrae, PU foam	6.5x40 mm	Axial	0.1, 1, 5 and 50 mm/min rates, during 15 min	Pullout tests. Cyclic loading.	The results showed that the loading rate significantly affected the strength and stiffness of the interface.	Effects of loading rate on the stiffness and strength
[44]	Hirano T, et al.	Human lumbar vertebrae	6.25x40 mm	CC	3 mm/min, 29,4N, 5 cyc 2 mm/min, 19,6N, 5 cyc.	Cyclic loading. Pullout tests.	Approximately 80% of the CC stiffness and 60% of the pullout strength of the pedicle screw depended on the pedicle.	Pedicle and pedicle+ vertebra body
[47]	Wray S, et al.	Human Lumbar	5.5x30 mm 6.5x40 mm	CC	5 kN, 10 mm/min	Pullout tests. Toggling tests.	The shorter cortical screws and traditional pedicle screws has similar pullout and toggling performances.	Pedicle trajectory, cortical trajectory
[49]	Yamagata M, et al.	Lumbar vertebrae	4.5 mm, 5.0 mm, 6.0 mm, 6.5 mm	Four point bending (fatigue)	1000 cycles per min, until 5000000 cyc	Fatigue, compression, torsion and pullout tests.	Linear positive correlation between the BMD of the vertebral body and the pullout strength of the pedicle screw.	
[51]	Zdeblick T, et al.	Human lumbar vertebrae	6.5x45 mm	CC	0.5 Hz, 300 N	Toggling and pullout tests.	Probing or drilling does not affect the insertional torque and pullout strength.	Probing and drilling effect

Furthermore, the loading values were maintained at defined loading limits in load controlled tests. The peak load with loading ratio (R) in a sinusoidal pattern of compression or peak loads in the sinusoidal pattern of compression and tension forces was used in load controlled tests. For unilateral loading, while the peak load changed from 50 N to 300 N, the loading ratio was defined as 0.1 in most of the studies [24, 25, 32]. Besides, the peak loads between  $\pm 50$  N and  $\pm 200$  N were used by many researchers [33-35]. The load controlled protocol was generally used in order to determine the number of cycles at which the bone-screw interface failed or loosening the amount of pedicle screws for a defined number of cycles. For sinusoidal loading, another crucial parameter was loading frequency. Although, different frequency values which showed the interval of loading in one second were defined as a value of between 0.5 Hz and 5 Hz in many studies, 2 Hz or 3 Hz was the most preferable frequency values for cyclic loading [15, 20, 24, 29, 33, 36]. To the best of our knowledge, there are no studies investigated the effect of loading frequency on toggling behavior. However, Inceoglu et al. [37] investigated the effects of loading rate on the pullout behavior of pedicle screws inserted to the polyurethane foams and bovine bone. Thus, the results suggested that the mechanics of the bone-screw interface changed depending on the loading frequency as the loading rate. The bone-screw interfaces in different test mediums and screw designs have a different mechanic and viscoelastic behaviors, as well. Also, it is estimated that the loading frequency affects the toggling behavior, but there is no exact relation between loading frequency and toggling behavior. These speculations have to be verified with further and more detailed analyses for different test mediums and screw designs.

The pedicle screw type was the most important parameter affecting the pullout performance with or without toggling [7, 14, 15, 19, 35]. The screw types (conventional, cannulated, expandable, dual lead dual cored, cancellous, cortical, etc.), which had a significant effect on early-stage pullout performance of pedicle screws, were compared by many researchers in different biomechanical test conditions [7, 14, 19, 38, 39]. The long term pullout performances of new designs were compared with the conventional pedicle screw and early-stage pullout strengths of the same designs. The early stage and long-term pullout performances of a novel expandable pedicle screw consisted of a polyether ether ketone (PEEK) shell and a titanium core screw, and cannulated and conventional pedicle screws were compared in several test mediums [15, 38]. The novel expandable pedicle screw had higher early-stage pullout strength than others and had a lower decrease in pullout strength after toggling tests. The samples of pedicle screws are given in Figure 3. The PEEK shell prevented the load transfer from screw to



Figure 3. Pedicle screws used by Aycan et al.: a) novel expandable (PEEK shell), b) cannulated, c) standard [15]

test medium by creating a new interface between the screw and test medium. It absorbed the part of the load generated on screw due to its good damping property, and the loosening values in novel expandable screws were lower than others. Similarly, the pedicle screws with PEEK anchor had higher pullout performance after toggling. Reducing the translation amount during cyclic loading, the anchor resulted in a significant reduction in axial motion at a defined number of cycles [33]. Moreover, the loosening behavior of carbon fiber reinforced PEEK pedicle screw was compared to the conventional titanium pedicle screw by using pullout tests after toggling and it was concluded that the novel PEEK pedicle screws, which had lower elastic modulus, were not successful in withstanding to the loosening [35].

The geometry or design parameters of pedicle screws have a notable influence on early-stage and long-term pullout performances. Outer geometry, thread types, cannula or hole orientation, etc. in pedicle screws affected the pullout performance drastically. The pedicle screws which had conical or cylindrical geometries showed different pullout behaviors in different test mediums. While the conical pedicle screws had lower pullout strength than the cylindrical pedicle screws in the case of without cyclic loading, there was no significant difference between the pullout performance of both screw types [23].

The early-stage pullout performance of conical and cylindrical pedicle screws with and without cement augmentation in severe osteoporosis cases were investigated and the results showed that conical and cylindrical screws had almost similar strength values [19], [40]. Using larger diameter provided sufficient improvement for both early-stage pullout strength and fatigue strength [1, 41], it was concluded that the outer geometry of pedicle screws had no significant effect on pullout performance after toggling. Furthermore, Wittenberg et al. [42] compared the axial pullout strength and transverse bending stiffness of pedicle screws which had different diameters, and it was found that the bending stiffness of pedicle screws had not been affected by increasing diameter (1 mm) of the screw. Patel et al. [19]

investigated the pullout behavior of cortical (4.7 mm major diameter) and cancellous (6.7 mm major diameter) pedicle screws after cyclic loading. It was determined that there was no significant difference between the pullout strengths with and without cyclic loading. Although increasing of diameter provided higher pullout strength immediately after fixation, there is no significant effect of outer diameter size on fixation strength after 5000 and 10000 cycles fatigue loading [43]. On the other hand, even if the results showed that the larger diameter, the higher pullout strength for pedicle screws, the outer diameter of the pedicle screw would be limited by the anatomical structure of the pedicle canal. The vertebra consisted of trabecular and cortical bones from the inside to outside and the load-carrying capacity depended on the bone structures along the cross-section, as well. It was determined that more than 80% of the craniocaudal stiffness and almost 60% of the pullout strength of pedicle screws were provided by the cortical bone in pedicles [17, 44]. Therefore, the smaller diameter screws have a reduced risk of surgical complications in surgery [43]. Dual-threaded pedicle screws were improved instead of single thread screws in order to enhance the pullout performance.

While dual-threaded screws had a trend for better pullout strength than single-threaded ones, there was no significant difference between both screws which had the same geometrical properties. Moreover, screws had similar failure loads and the number of cycles to failure after toggling [17]. The dual-threaded pedicle screws pattern in the cortical zone of pedicle provided greater bone purchase in loading for samples with high BMD and the advantage of dual-threaded pedicle screws were generally lost in high porosity foam or osteoporotic bone samples due to lack of sufficient bone-screw interface, unlike compacting solid foam or healthy bone samples. The biomechanical properties of dual threaded pedicle screws (standard pitch, dual pitch, standard pitch titanium coated, dual pitch titanium coated) were compared for different conditions (at 0 time and postoperative 6 months). The screws were coated with titanium which has good histocompatibility and adhesion properties by a plasma-spray titanium coating method. The dual pitch titanium-coated pedicle screws had significantly higher pullout strength and fatigue performance than standard pedicle screws for early time and post-operative conditions [45]. In addition to this, the long-term pullout performance of cortical bone trajectory pedicle screws and traditional pedicle screws were compared under cyclically sagittal bending conditions [46]. The cortical bone trajectory pedicle screws had better fatigue performance than the traditional pedicle screws since there was no sufficient cortical purchase to withstand the small diameter and length of cortical bone trajectory pedicle screws in maintaining stability under cyclic loading in vertebrae

with low BMD. Wray et al. [47] determined that the cortical trajectory provided higher bone density for screw stability by comparing with a traditional trajectory in both high bone density and poor bone density. The cortical trajectory had an advantage in osteoporotic patients due to having inherently greater bone density along its path.

Human or animal cadaver, polyurethane foam block, and synthetic bone models were used as a test medium for biomechanical tests. There was a strong correlation between the biomechanical properties of pedicle screws and BMD values of bone [48]. It was concluded that the higher BMD, the higher holding performance for pedicle screws. BMD, which was an indication of the ability to resist shear loading, may be a critical value for loosening of screws inserted to the anterior of vertebral bodies and the number of loading cycles to failure increased by increasing of BMD value of vertebral bodies [48, 49]. While the cyclic loading caused a 20% decrease in pullout strength in healthy bone, it caused a 33% decrease in osteoporotic bone [50]. Pullout performance of pedicle screws was affected by the BMD value of pedicles and there was a significant relationship between pullout performance and BMD regardless of the application type of toggling [20]. Furthermore, the pedicle size of the vertebral body was as effective as BMD on pullout performance. It was concluded that smaller pedicles obtained a greater number of cycles to failure for pedicle screws and the pedicle screws inserted to the smaller pedicles had higher pullout and fatigue strength in case of osteoporosis [51]. The pedicle size depended on the spinal region of the spine as well so that the spinal region of the cadaver affected the pullout performance of pedicle screws with or without cyclic loading [16, 20, 24]. Mehmanparast et al. determined that the pullout strength of the pedicle screws decreased from L1 to L3 of the porcine lumbar region. This decrease was explained in part by changing the pedicle cross-sectional area for each level [20]. Furthermore, the polyurethane foams standardized with related ASTM standards are used in the biomechanical applications for testing pedicle screws. The density of foams determines the severity of the disease: Grade 10 mimics osteoporotic bone and Grade 40 mimics healthy bone. The decrease of density for polyurethane foams caused a decrease in the pullout strength of pedicle screws after toggling, as expected [15, 19, 22]. Aycan et al. [15] determined that the pedicle screws implanted to the Grade 10 had lower pullout strength than those implanted to Grade 40, and pedicle screws in both foams acted almost similarly. While polyurethane foams produced in different densities were used as a test medium, they did not replicate the viscoelastic properties of bone. The differences in densities of polyurethane foams helped the understanding of the pullout mechanism of pedicle screws, but it was suggested that the tests had to be performed in vivo [19].

Cement augmentation is one of the techniques used for increasing holding capacity of pedicle screws in spinal surgery operations. The pullout performance of pedicle screws increased significantly with cement usage. Cement augmentation has a positive effect on both early-stage and long term pullout strength of pedicle screws comparing to non-cemented pedicle screws. While the cement augmentation increased the screw anchorage performance significantly in bones with poor BMD, there was no significant effect on screw stability for healthy bones [52]. Burval et al. [50] investigated the pullout failure of cemented pedicle screws on either primarily or after 5000 cycles tangential fatigue and it was concluded that cement augmentation improved the early stage fixation and fatigue strength of pedicle screws. Aycan et al. [15, 38] compared the early stage and long term pullout strengths of cemented cannulated pedicle screws, cemented conventional pedicle screws, and non-cemented conventional pedicle screws. The results showed that the cemented conventional pedicle screws had the highest pullout strength values for all test conditions with or without toggling. Augmentation of conventional screws was performed with the prefilling method and there was a large and sufficient interface between bone and screw. For instance, according to the study of Aycan et al., the pullout strength of conventional pedicle screws increased to 57% in Grade 10 foam, 51% in Grade 40 foam, and 110% in a bovine vertebra with cement usage. However, the highest pullout decrease after cyclic loading belonged to the cemented conventional pedicle screws. The cement augmentation created a large bone-screw interface and it took an active role in transferring loads from screw to the bone as a mechanical locking mechanism [53, 54]. The brittle behavior of the cement interface significantly increased due to material properties of the cement when compared to the connective tissue after the syndesmosis process in bone structure [15]. Furthermore, this brittle structure did not withstand the sinusoidal loading generated so much and the damage of interface decreased the load transfer capability dramatically. The cement augmentation method is crucial for creating a sufficient interface that enables to successful load transfer. While the conventional pedicle screws cemented with the prefilling method, the injection method is used for cannulated pedicle screws in biomechanical applications. The simulation of cement augmentation methods is shown in Figure 4. The prefilling method created a large cement interface between test material and pedicle screws as mentioned before and it provided that conventional pedicle screws had higher pullout strength than cannulated pedicle screws in all test conditions. On the other hand, the injection method did not succeed in providing enough cement interface, unlike the prefilling method. The penetration of cement from screw to bone (or test medium) was not sufficient to create a large interface

due to using hand pressure in the injection of cement and obstruction of the radial hole during the insertion process [7]. On the other hand, Kueny et al. investigated the effect of augmentation method on pullout performance of pedicle screws after toggling and they concluded that the pedicle screw cemented with screw injection had a higher pullout and fatigue strength than the pedicle screw cemented with prefilling method [1]. It was determined that the cement in contact with cortical shell had a significant effect on the fixation strength of bone screws and they hypothesized that in injection method, there was a wider cement distribution which was closer to the pedicle and had a greater contact to the posterior vertebral wall leading to the higher fixation strength. Furthermore, the effect of fenestrated tap, direct injection, and kyphoplasty methods on toggling behavior of cannulated pedicle screws were investigated and it was concluded that the pedicle screw cemented with direct injection method had superior resistance to vertical toggle, and the fenestrated tap method had lower resistance to motion than other methods [18]. Besides, the kyphoplasty method had almost similar resistance to cyclic loading with a decreased risk of cement leakage in comparison with the direct injection method. Moreover, Bostelmann et al. suggested that the pullout performance of pedicle screws increased with augmentation process (cement first, in situ augmented, percutaneously application) compared with non-cemented pedicle screws, but the augmentation methods had no effect on loosening or failure of pedicle screws [55]. The kyphoplasty and traditional transpedicular augmentation methods were compared in osteoporotic vertebrae. Although both methods increased the pullout and fatigue strengths, the kyphoplasty method provided higher pullout strength compared to the traditional transpedicular augmentation method [50]. The kyphoplasty method created a larger contact surface area with trabecular bone tissue than transpedicular augmentation. The reason for providing higher biomechanical properties for the kyphoplasty method was not only the application technique but also the cement amount in the study of Burval et al. [50]. While the amount of 4 cc PMMA was used in the kyphoplasty method due to creating a balloon in bone tissue, the transpedicular augmentation process was performed with 2.5 cc cement. It was hypothesized that the higher amount of cement, the higher cement interface between screw and bone. Unfortunately, Pishnamaz et al. determined that increasing cement amount in augmentation methods had a negative effect on holding the capability of pedicle screws [32].

The forces generated due to the cyclic loading on the head of the screw sometimes caused the rotation of the screw with a fulcrum in the pedicle, and a large amount of cement limited the rotation movement of the screw in the fulcrum of the pedicle. The limitation of the rotation led to

an increase in higher forces on pedicle during the cyclic loading and finally these forces caused the loss of the stability of fixation and cut out of the screw through the superior endplate as a result of cyclic loading [32, 55]. Schmoelz et al. compared the pullout performance after cycling loading of pedicle screws which augmented with medical silicone using the kyphoplasty method and in situ augmented with PMMA [34]. A balloon cavity was created and filled with 3 ml of self-curing elastomer before the insertion of the screw in the novel augmentation method. After the implantation of cannulated pedicle screws, they were augmented in situ with 2 ml PMMA. The novel augmentation method had higher pedicle screw anchorage under cyclic loading in comparison with conventional PMMA augmentation. Although the cement type and amount of cement were different in comparison to kyphoplasty and in situ augmentation methods, the results showed that self-curing elastomeric silicone might be a good alternative to the PMMA. The material properties of cements were determinant on the anchorage performance of pedicle screws. The PMMA, which had higher stiffness than bone, interdigitated with trabecular bone tissue and provided reinforcement and interlocking mechanism with trabecular bone [56]. On the other hand, the stiffness of elastomer silicone was almost similar with the bulk stiffness value of trabecular bone instead of the stiffness of single trabecula, and this resemblance between silicone and trabecular bone enabled silicone to have higher anchorage performance due to creating a cavity and filling it with silicone [34]. Both the novel bioactive bone cement (Sr-HA) and PMMA were filled to the pedicle holes by the prefilling method within about 3 minutes before the insertion of the screw. While the PMMA cemented pedicle screws had higher pullout and toggling performance than Sr-Ha cemented ones, it was hypothesized that Sr-HA and PMMA cements provided an almost similar fixation performance for pedicle screws.

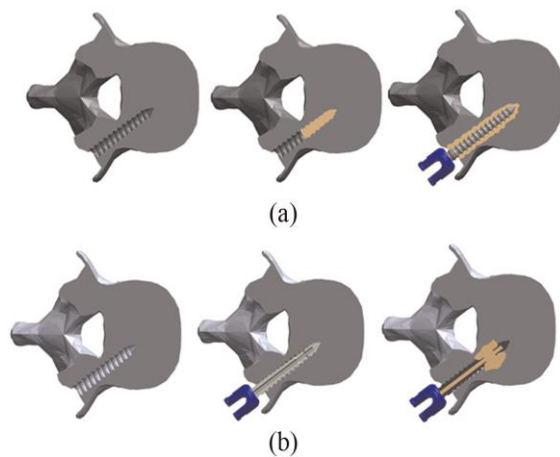


Figure 4. Cement application techniques; (a) prefilling, (b) injection [7]

Despite having lower mechanical strength, Sr-HA cement provided a larger bone-screw interface and it also covered most of the length of the screw after insertion due to having longer handling time than PMMA [25]. Moreover, the modulus of elasticity of PMMA was drastically higher than bone, which was almost similar to calcium triglyceride bone cement (CTBC). While this similarity provided some advantages to the CTBC compared to PMMA for in vivo usage, more cycles and bending moments applied higher were required in order to reach the same screw loosening for PMMA due to lower mechanical properties of CTBC [57].

## 5. Conclusions

The toggling test, which simulates the movement of the body in time, is performed in order to determine the long-term pullout performance of pedicle screws. It was concluded that the pullout strength of pedicle screws generally decreased with toggling. The parameters of cyclic loading determined by observing the movement of the spine were fairly crucial for the pullout performance of pedicle screws because they had an important impact on the stability of screws. The cement augmentation, design parameters of screws, and properties of test medium had important roles in determining the holding capacity of pedicle screws under cyclic loading, as well. Although the cement augmentation increases the pullout strength without cyclic loading indisputably, there are various studies providing different results about the effect of cement augmentation on pullout performance after toggling. In these studies, the types or design parameters of pedicle screws affected the pullout performance directly as expected. The screw types as normal, cannulated or expandable screws, conical or cylindrical, cortical or trabecular, and the design parameters as outer diameter, core diameter, length, lead, and core geometries were compared in different studies. Furthermore, the pullout performance of screws changes with insertion techniques, test medium, and spinal level; however, there is not a certain discussion whether these parameters have a significant effect on long term pullout behavior or not.

## Declaration

The author(s) declared no potential conflicts of interest with respect to the research, authorship, and/or publication of this article. The author(s) also declared that this article is original, was prepared in accordance with international publication and research ethics, and ethical committee permission or any special permission is not required.

## Nomenclature

<i>BMD</i>	: Bone mineral density
<i>ASTM</i>	: American Society for Testing and Materials
<i>CC</i>	: Craniocaudal
<i>PEEK</i>	: Polyether ether ketone

PMMA : Poly (methyl methacrylate)  
 Sr-HA : Strontium-containing Hydroxyapatite  
 CTBC : Calcium triglyceride bone cement

## References

- Kueny, R.A., Kolb, J., Lehmann, W., Püschel, K., Morlock, M.M. and Huber, G., *Influence of the screw augmentation technique and a diameter increase on pedicle screw fixation in the osteoporotic spine: pullout versus fatigue testing*. Eur Spine J, 2014. **23**(10): p. 2196-2202.
- Chao, K.H., Lai, Y.S., Chen, W.C., Chang, C.M., McClean, C.J., Fan, C.Y. et al. *Biomechanical analysis of different types of pedicle screw augmentation: A cadaveric and synthetic bone sample study of instrumented vertebral specimens*. Med Eng Phys, 2013. **35**(10): p. 1506-1512.
- Hashemi, A., Bednar, D. and Ziada, S., *Pullout strength of pedicle screws augmented with particulate calcium phosphate: An experimental study*. Spine J, 2009. **9**(5): p. 404-410.
- Melkerson M, Kirkpatrick J, and Griffith S., *Spinal implants: Are we evaluating them appropriately?* (STP1431 ed). 2003, Dallas: ASTM International.
- ASTM International. F543-17 Standard Specification and Test Methods for Metallic Medical Bone Screws. West Conshohocken, PA; ASTM International, 2017.
- Choma, T., Pfeiffer, F., Swope, R. and Hirner, J.P., *Pedicle screw design and cement augmentation in osteoporotic vertebrae*. Spine, 2012. **37**(26): p. 1628-1632.
- Tolunay, T., Başgül, C., Demir, T., Yaman, M.E. and Arslan, K.A., *Pullout performance comparison of pedicle screws based on cement application and design parameters*. Proc Inst Mech Eng H, 2015. **229**(11): p. 786-793.
- Yaman, O., Demir, T., Arslan, A.K., Iyidiker, M.A., Tolunay, T., Camuscu, N., et al. *The comparison of pullout strengths of various pedicle screw designs on synthetic foams and ovine vertebrae*. Turk Neurosurg, 2015. **25**(4): p. 532-538.
- Tolunay, T., Arslan, A.K., Yaman, O., Dalbayrak, S. and Demir, T., *Biomechanical performance of various cement-augmented cannulated pedicle screw designs for osteoporotic bones*. Spine Deform, 2015. **3**(3): p. 205-210.
- Varghese, V., Kumar, G.S. and Krishnan, V., *Effect of various factors on pull out strength of pedicle screw in normal and osteoporotic cancellous bone models*. Med Eng Phys, 2017. **40**: p. 28-38.
- Demir, T. and Başgül, C., *The pullout performance of pedicle screws*. 2015, London: Springer International Publishing.
- Kim, Y.Y., Choi, W.S. and Rhyu, K.W., *Assessment of pedicle screw pullout strength based on various screw designs and bone densities-an ex vivo biomechanical study*. Spine J, 2012. **12**(2): p. 164-168.
- Mehta, H., Santos, E., Ledonio, C., Sembrano, J., Ellingson, A., Pare, P., et al. *Biomechanical analysis of pedicle screw thread differential design in an osteoporotic cadaver model*. Clin Biomech, 2012. **27**(3): p. 234-240.
- Demir T., *A new alternative to expandable pedicle screws: Expandable poly-ether-ether-ketone shell*. Proc Inst Mech Eng H, 2015. **229**(5): p. 386-394.
- Aycan, M.F., Yaman, M.E., Usta, Y., Demir, T. and Tolunay, T., *Investigation of toggling effect on pullout performance of pedicle screws*. Proc Inst Mech Eng H, 2018. **232**(4): p. 395-402.
- Paik, H., Dmitriev, A., Lehman, R., Gaume, R.E., Ambati, D.V., Kang, D.G., et al. *The biomechanical effect of pedicle screw hubbing on pullout resistance in the thoracic spine*. Spine J, 2012. **12**(5): p. 417-424.
- Brasiliense, L., Lazaro, B., Reyes, P., Newcomb, A.G., Turner, J.L., Crandall, D.G., et al. *Characteristics of immediate and fatigue strength of a dual-threaded pedicle screw in cadaveric spines*. Spine J, 2013. **13**(8): p. 947-956.
- Benson, D., Lansford, T., Cotton, J., Burton, D., Jackson, R.S. and McIff, T., *Biomechanical analysis of cement augmentation techniques on pedicle screw fixation in osteopenic bone: a cadaveric study*. Spine Deform, 2014. **2**(1): p. 28-33.
- Patel, P., Hukins, D. and Shepherd, D., *The effect of "toggling" on the pullout strength of bone screws in normal and osteoporotic bone models*. Open Mech Eng J, 2013. **7**: p. 35-39.
- Mehmanparast, H., Petit, Y. and Mac-Thiong, J.M., *Comparison of pedicle screw loosening mechanisms and the effect on fixation strength*. J Biomech Eng, 2015. **137**(12): p. 121003-1/7.
- Elder, B., Lo, S.F., Holme, S.C., Goodwin, C.R., Kosztowski, T.A., Lina, I.A., et al. *The biomechanics of pedicle screw augmentation with cement*. Spine J, 2015. **15**(6): p. 1432-1445.
- Mehmanparast, H., Mac-Thiong, J. and Petit, Y., *Biomechanical evaluation of pedicle screw loosening mechanism using synthetic bone surrogate of various densities*. Conf Proc IEEE Eng Med Biol Soc, 2014. **2014**: p. 4346-4349.
- Lill, C., Schlegel, U., Wahl, D. and Schneider, E., *Comparison of the in vitro holding strengths of conical and cylindrical pedicle screws in a fully inserted setting and backed out 180°*. J Spinal Disord, 2000. **13**(3): p. 259-266.
- Sterba, W., Kim, D.G., Fyhrie, D., Yeni, Y.N. and Vaidya, R., *Biomechanical analysis of differing pedicle screw insertion angles*. Clin Biomech, 2007. **22**(4): p. 385-391.
- Zhu, Q., Kingwell, S., Li, Z., Pan, H., Lu, W.W. and Oxland, T.R., *Enhancing pedicle screw fixation in the aging spine with a novel bioactive bone cement*. Spine, 2012. **37**(17): p. 1030-1037.
- Savage, J., Limthongkul, W., Park, H.S., Zhang, L.Q. and Karaikevic, E.E., *A comparison of biomechanical stability and pullout strength of two C1-C2 fixation constructs*. Spine J, 2011. **11**(7): p. 654-658.
- Mehmanparast, H., Mac-Thiong, J. and Petit, Y., *In vitro evaluation of pedicle screw loosening mechanism: a preliminary study on animal model*. Scoliosis, 2015. **10**(Suppl 1): O25.
- Bianco, R.J., Aubin, C.E., Mac-Thiong, J.M., Wagnac, E. and Arnoux, P.J., *Pedicle screw fixation under nonaxial loads: a cadaveric study*. Spine, 2016. **41**(3): p. 124-130.
- Liebsch, C., Zimmermann, J., Graf, N., Schilling, C., Wilke, H.J. and Kienle, A., *In vitro validation of a novel mechanical model for testing the anchorage capacity of pedicle screws using physiological load application*. J Mech Behav Biomed Mater, 2018. **77**: p. 578-585.
- Baluch, D., Patel, A., Lullo, B., Havey, R.M., Voronov, L.I., Nguyen, N.L., et al. *Effect of physiological loads on cortical and traditional pedicle screw fixation*. Spine, 2014. **39**(22): p. 1297-1302.
- Lotz, J., Hu, S., Chiu, D., Yu, M., Colliou, O. and Poser, R.D., *Carbonated apatite cement augmentation of pedicle screw fixation in the lumbar spine*. Spine, 1997. **22**(23): p. 2716-2723.

32. Pishnamaz, M., Lange, H., Herren, C., Na, H.S., Lichte, P., Hildebrand, F., et al. *The quantity of bone cement influences the anchorage of augmented pedicle screws in the osteoporotic spine: A biomechanical human cadaveric study.* Clin Biomech, 2018. **52**: p. 14-19.
33. Gates, T.A., Moldavsky, M., Salloum, K., Dunbar, G.L., Park, J. and Bucklen, B., *Biomechanical analysis of a novel pedicle screw anchor designed for the osteoporotic population.* World Neurosurg, 2015. **83**(6): p. 965-969.
34. Schmoelz, W., Keiler, A., Kenschake, M., Lindtner, R.A. and Gasbarrini, A., *Effect of pedicle screw augmentation with a self-curing elastomeric material under cranio-caudal cyclic loading - A cadaveric biomechanical study.* J Orthop Surg Res, 2018. **13**(1): p. 251-258.
35. Lindtner, R., Schmid, R., Nydegger, T., Kenschake, M. and Schmoelz, W., *Pedicle screw anchorage of carbon fiber-reinforced PEEK screws under cyclic loading.* Eur Spine J, 2018. **27**(8): p. 1775-1784.
36. Rodriguez-Olaverri, J., Hasharoni, A., DeWal, H., Nuzzo, R.M., Kummer, F.J. and Errico, T.J., *The effect of end screw orientation on the stability of anterior instrumentation in cyclic lateral bending.* Spine J, 2005. **5**(5): p. 554-557.
37. Inceoglu, S., Ehlert, M., Akbay, A. and McLain, R.F., *Axial cyclic behavior of the bone-screw interface.* Med Eng Phys, 2006. **28**(9): p. 888-893.
38. Aycaan, M.F., Tolunay, T., Demir, T., Yaman, M.E. and Usta, Y., *Pullout performance comparison of novel expandable pedicle screw with expandable poly-ether-ether-ketone shells and cement-augmented pedicle screws.* Proc Inst Mech Eng H, 2017. **231**(2): p. 169-175.
39. Demir, T., *Possible usage of cannulated pedicle screws without cement augmentation.* Applied Bionics and Biomechanics, 2014. **11**(3): p. 149-155.
40. Chen, L., Tai, C., Lee, D., Lai, P.L., Lee, Y.C., Niu, C.C., et al. *Pullout strength of pedicle screws with cement augmentation in severe osteoporosis: a comparative study between cannulated screws with cement injection and solid screws with cement pre-filling.* BMC Musculoskelet Disord, 2011. **12**: p. 12-33.
41. Kiner, D., Wybo, C., Sterba, W., Yeni, Y.N., Bartol, S.W. and Vaidya, R., *Biomechanical analysis of different techniques in revision spinal instrumentation: larger diameter screws versus cement augmentation.* Spine, 2008. **33**(24): p. 2618-2622.
42. Wittenberg, R., Lee, K., Shea, M., White, A.A. and Hayes, W.C., *Effect of screw diameter, insertion technique, and bone cement augmentation of pedicular screw fixation strength.* Clin Orthop Relat Res, 1993. (296): p. 278-287.
43. Lai, D.M., Shih, Y.T., Chen, Y.H., Chien, A. and Wang, J.L., *Effect of pedicle screw diameter on screw fixation efficacy in human osteoporotic thoracic vertebrae.* Journal of Biomechanics, 2018. **70**: p.196-203.
44. Hirano, T., Hasegawa, K., Takahashi, H., Uchiyama, S., Hara, T., Washio, T., et al. *Structural characteristics of the pedicle and its role in screw stability.* Spine, 1997. **22**(21): p. 2504-2509.
45. Wang, W.T., Guo, C.H., Duan, K., Ma, M.J., Jiang, Y., Liu, T.J., et al. *Dual pitch titanium-coated pedicle screws improve initial and early fixation in a polyetheretherketone rod semi-rigid fixation system in sheep.* Chinese Medical Journal, 2019. **132**(21): p. 2594-2600.
46. Akpolat, Y., İnceoğlu, S., Kinne, N., Hunt, D. and Cheng, W.K., *Fatigue performance of cortical bone trajectory screw compared with standard trajectory pedicle screw.* Spine, 2016. **41**(6): p. 335-341.
47. Wray, S., Mimran, R., Vadapalli, S., Shetye, S.S., McGilvray, K.C. and Puttlitz, C.M., *Pedicle screw placement in the lumbar spine: effect of trajectory and screw design on acute biomechanical purchase.* J Neurosurg Spine, 2015. **22**(5): p. 503-510.
48. Lim, T., An, H., Hasegawa, T., McGrady, L., Hasanoglu, K.Y. and Wilson, C.R., *Prediction of fatigue screw loosening in anterior spinal fixation using dual energy X-ray absorptiometry.* Spine, 1995. **20**(23): p. 2565-2568.
49. Yamagata, M., Kitahara, H., Minami, S., Takahashi, K., Isobe, K., Moriya, H., et al. *Mechanical stability of the pedicle screw fixation systems for the lumbar spine.* Spine, 1992;. **17**(3 Suppl): p. 51-54.
50. Burval, D., McLain, R., Milks, R. and Inceoglu, S., *Primary pedicle screw augmentation in osteoporotic lumbar vertebrae.* Spine, 2007. **32**(10): p. 1077-1083.
51. Zdeblick, T., Kunz, D., Cooke, M. and McCabe, R., *Pedicle screw pullout strength. Correlation with insertional torque.* Spine, 1993. **18**(12): p. 1673-1676.
52. Sven, H., Yannick, L., Daniel, B., Heini, P. and Benneker, L., *Influence of screw augmentation in posterior dynamic and rigid stabilization systems in osteoporotic lumbar vertebrae: A biomechanical cadaveric study.* Spine, 2014. **39**(6): p. 384-389.
53. Huiskes, R. and Nunamaker, D., *Local stresses and bone adaption around orthopedic implants.* Calcif Tissue Int, 1984. **36**(Suppl 1): p. 110-117.
54. Funk, M. and Litsky, A., *Effect of cement modulus on the shear properties of the bone-cement interface.* Biomaterials, 1998. **19**(17): p. 1561-1567.
55. Bostelmann, R., Keiler, A., Steiger, H., Scholz, A., Cornelius, J.F. and Schmoelz, W., *Effect of augmentation techniques on the failure of pedicle screws under cranio-caudal cyclic loading.* Eur Spine J, 2017. **26**(1): p. 181-188.
56. Windolf, M., *Biomechanics of implant augmentation.* Unfallchirurg, 2015. **118**(9): p. 765-771.
57. McLachlin, S., Al Saleh, K., Gurr, K., Bailey, S.I., Bailey, C.S. and Dunning, C.E., *Comparative assessment of sacral screw loosening augmented with pmma versus a calcium triglyceride bone cement.* Spine, 2011. **36**(11): p. 699-704.



## Research Article

# The comparative study of conventional and ultra-high frequency induction sintering behavior of pure aluminum

**Burak Gül<sup>a</sup>** , **Levent Ulvi Gezici<sup>a</sup>** , **Mehmet Ayvaz<sup>b,\*</sup>**  and **Uğur Çavdar<sup>c</sup>** 

<sup>a</sup>Celal Bayar University, Engineering Faculty, Department of Mechanical Engineering, 45140 Manisa, Turkey

<sup>b</sup>Vocational School Of Manisa Technical Sciences, Manisa Celal Bayar University, Manisa 45140, Türkiye

<sup>c</sup>Izmir Democracy University, Engineering Faculty, Mechanical Engineering Department, İDU Campus, 35140, İzmir/Turkey

## ARTICLE INFO

### Article history:

Received 29 April 2020

Revised 22 May 2020

Accepted 27 May 2020

### Keywords:

Aluminum

Induction sintering

Powder metallurgy

Rapid Sintering

## ABSTRACT

In this study, compressibility, and conventional and ultra-high frequency induction sintering behaviors of 99.8% purity and 50-70 µm size range aluminum powders were investigated. In the compressibility studies, uniaxial-cold pressing method was used. Green samples were produced in the range of 50-275 MPa using different pressures. By measuring the apparent densities of the produced samples, the optimum compressibility pressure was determined as 200 MPa. Pure aluminum powder metal samples produced with this ideal pressing pressure were sintered in both classical and ultra-high frequency induction methods in the range of 500-600 °C. Sintering was performed as 40 min in the traditional method and 5 min in the ultra-high frequency induction sintering method. As a result of the tests carried out in this study, it was determined that pure aluminum samples were successfully sintered with a high frequency induction system in a shorter time than traditional sintering method.

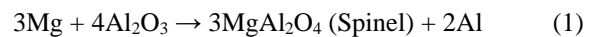
© 2020, Advanced Researches and Engineering Journal (IAREJ) and the Author(s).

## 1. Introduction

Because of their superior strength to weight ratio, easy machining and excellent corrosion resistance, aluminum alloys and aluminum matrix composites (AMCs) have been applications in the automobile industry such as cylinder blocks, pistons and piston insert rings [1]. In addition to this, the aluminum alloys and AMCs are widely utilized in marine, aerospace and defence industries [2-5]. One of the manufacturing process of the AMCs is powder metallurgy (PM). When compared to other manufacturing processes likely conventional casting method, energy conservation can be increased up to 50% by using PM. Additionally, due to having final products via PM, there are nearly no raw materials [6]. Therefore, many researchers have focused their efforts on the study of the sintered AMCs.

Sintering of AMCs has some challenges. One of them is oxide layers. Aluminum powder have always oxide layers and these oxide layers prevent sintering. Eliminating these oxide layers is not possible with low temperature which is carried out for sintering AMCs. There are two processes

most commonly used to decrease negative effect of the oxide layers on the sintering behavior and mechanical properties of the AMCs. First process is to increase contact areas among powders. For this purpose, higher compaction pressure is carried out to destroy oxide layers or some elements are added to create a liquid phase during sintering such as Cu [7-9]. In this way liquid phase can diffuse interfaces of powders. Hence interfacial bonding between powders is improved. Second process is to add elements which can help to decomposition aluminum oxide or reduce oxide [9-12]. Magnesium is very reactive and so it is used as a solid reducing agent. A possible reaction is



Gokce and Fındık, in their study, investigated mechanical and physical properties of the Al-1%Mg sintered parts. This study shows that while the sintering of the wax added Al-1%Mg composite samples for dewaxing, large porosities were being formed and so volume increased, and density decreased. Consequently,

\* Corresponding author. Tel.: +90 232 260 1001; Fax: +90 232 260 1004

E-mail addresses: [burak.gul1963@gmail.com](mailto:burak.gul1963@gmail.com) (B. Gül), [levent.gezici@gmail.com](mailto:levent.gezici@gmail.com) (L.U. Gezici), [m.ayvaz@cbu.edu.tr](mailto:m.ayvaz@cbu.edu.tr) (M. Ayvaz),

[ugur.cavdar@idu.edu.tr](mailto:ugur.cavdar@idu.edu.tr) (U. Çavdar)

ORCID: 0000-0002-4446-4259 (B. Gül), 0000-0002-0353-3270 (L.U. Gezici), 0000-0002-9671-8679 (M. Ayvaz), 0000-0002-3434-6670 (U. Çavdar)

DOI: 10.35860/iarej.729395



TRS of the wax added Al-1% Mg composite samples the increased as nearly 10 times in wax free samples [13].

Oh and Anh investigated effects of the Mg addition and compaction pressure on mechanical and microstructure properties of Al-3Cu composites. For this purpose, the compaction pressures of 100, 250, 500 MPa were carried out and Mg was added in three different compositions, 0.5, 1.5, and 2.5 wt.%. The study shows that because of the limited wettability of Mg element compared with Cu, the sintered density decreases with the increase of Mg addition. They reported that with the addition of small amount of Mg, the oxide layer is broken and also  $MgAl_2O_4$  spinel structures are formed, so contact area between Al and Cu increases. As a result, small amount of Mg addition improves the mechanical behavior of Al-Cu composites [9].

Gokce et al. investigated effects of Mg content on mechanical properties and aging behavior of Al4CuXMg composites. For this purpose, four different premixed powder compositions, Al4Cu, Al4Cu0.5Mg, Al4Cu1Mg, Al4Cu2Mg, were used. Premixed powders were pressed at 400 MPa. Green compacts were sintered at 615 °C for 1.5 h. After sintering, specimens were aged at 180 °C. Aging time was varied between 6 h and 48 h. AS a result, highest hardness value was measured from 24 h aged Al4Cu2Mg alloy [14].

Boland et al. studied to improve the mechanical properties of P/M Al-Cu-Mg composites by using different Mg and Cu addition. In this study, 3.4, 4.4 and 5.4 wt.% Cu and 0.5, 1.5 and 2.5 wt.% Mg was added. Also, composites were compacted at pressures from 100 to 500 MPa and then sintered at various temperatures between 560 and 630 °C and times between 1 and 100 min. It was reported that the optimum manufacture process for P/M 2324 (Al-4.4Cu-1.5Mg) included a compaction pressure 400 MPa followed by sintering at 600 °C for 20 min [15].

Gokce et al. investigated mechanical properties of P/M pure Al, Al5Cu and Al5Cu0.5Mg parts. Pure Al and premixed powders were pressed in uniaxially at 400 MPa. Pure Al compacts were sintered at 600 °C for 2 h. Al5Cu and Al5Cu0.5Mg composites were sintered at 590 °C for 90 min. The tests show that although the Al5Cu0.5Mg composites have the lowest density, they have the highest TRS and hardness [16].

Reducing the temperature and application time will also reduce the formation and thickness of the oxide layer [17]. Microwave, spark plasma and induction sintering are common sintering methods that reduce sintering temperature and time. Sintering of aluminum alloys and composites by microwave and spark plasma method has been studied in many aspects [18-22]. In their study, Zadra et al. Sintered pure aluminum with spark plasma sintering (SPS) method at 470-525 °C temperatures. They reported that sintered samples had a hardness of 27 HV0.1 [23]. Zeng et al.

produced the pure Al P/M using SPS method. The sintering temperature range was chosen as 450-600 °C. The highest hardness was determined as 37.7 HV in the samples sintered at 550 °C [24]. Kwon et al. manufactured the P/M pure Al parts using SPS process at 280-560 °C and reported that the relative density increased as the sintering temperature increased. [25]. Induction sintering method, another rapid sintering method, was widely studied on sintering of carbide and oxide ceramics such as WC, TiC,  $B_4C$ ,  $Al_2O_3$  and iron-based metallic parts. However, the sintering of aluminum-based parts has not become widespread [26-30]. Induction heating technology is used in production methods and stages such as heating, melting, welding and sintering [31]. In this technology, the heating parameters depend on the electromagnetic properties of the material to be heated. In induction sintering, ohmic heating takes place with the electromagnetic field changing with eddy currents. Skin Effect is the mechanism that concentrates the current density on the surface [32-34]. The relationship between electrical conductivity ( $\sigma$ ), current frequency ( $f$ ), magnetic permeability ( $\mu$ ) and skin depth ( $\delta$ ) is expressed in Eq. 2:

$$\delta = \frac{1}{\sqrt{\sigma\pi f\mu}} \quad (2)$$

Induction sintering is a widely used method for the rapid sintering of iron-based P/M parts due to its electromagnetic properties. With this study, it was aimed to reveal the sinterability of aluminum based powder metal parts by induction fast sintering. For this purpose, the P/M pure aluminum green samples were manufactured by cold pressing method, by applying 200 MPa and sintered by using 40 minutes conventional and 5 minutes ultra-high frequency induction method with 11 different temperatures between 500-600 °C temperatures. When comparing the test and analysis results of the samples sintered with the conventional and ultra-high frequency induction sintering (UHFIS) method, it was found that aluminum alloys were successfully sintered in a much shorter time with the ultra-high frequency induction sintering method.

## 2. Materials and Method

In this study, pure aluminum powders with 99.8% purity and 50-70  $\mu m$  powder size range were used. The compressibility of aluminum powders was first investigated. For this purpose, aluminum powders prepared by weighing on a scale with a sensitivity of 0.0001 gr were uniaxial cold pressed via hydraulic press. In the compressibility analysis, pressing was performed in the pressure range of 50-275 MPa with 25 MPa intervals. After pressing, the density of the samples was calculated in accordance with the Archimedes principle [32].

The 11 green samples pressed at 200 MPa compaction pressure determined as a result of compressibility tests have

traditionally been sintered in the ash furnace. In the other 11 green samples, ultra-high frequency induction sintering was applied using 8 kW power and 900 kHz high frequency induction heating machine. In the induction and conventional sintering methods, 500-600 °C was chosen as the sintering temperature range with 10°C intervals. In sintering of the green samples, the application time was 40 minutes in the traditional method. In ultra-high frequency sintering, the sintering time was 5 minutes. The image of the samples after sintering can be seen in Figure 1.

Sintered densities of the samples were measured by the Archimedes principle. The sintered density is defined in Eq. 3:

$$\rho = \frac{m_a}{m_c - m_w} \times \rho_{water} \quad (3)$$

Where:

$m_a$  is weight of sintered part in air,  $m_c$  is weight of sintered part in air after submerged from water,  $m_w$  is weight of sintered part in water.

The samples were sanded with 180-1200 grid sandpaper respectively, polished with 3 and 1 micron diamond solutions via Metkon Farcipol 1V polishing machine. The polished samples were etched with Keller solution (2.5 ml HNO<sub>3</sub>, 1.5 ml HCl, 1 ml HF, 95 ml water). The metallographic examinations were carried out via Nikon Eclipse LV150N optic microscope. The Bulut Makine BMS 200 RB hardness tester was used for the Brinell hardness measurements of the samples. Hardness measurements were carried out in accordance with ASTM E10-15a standards [35]. In the Brinell hardness tests, 62.5 kg load was applied, and 2.5 mm diameter steel ball indenter was used. Measurements were repeated 5 times for each sample and these 5 measurements were averaged.

### 3. Results and Discussions

To determine the compressibility of 2.5 and 5 g pure aluminum powders, the powders were pressed using the uniaxial cold pressing method in the pressure range of 50-275 MPa. Compressibility graphs of pressed samples obtained by density measurements performed with the Archimedes principle are shown in Figure 2. As is well known, aluminum powders have higher compressibility than iron alloy powders [36]. Therefore, it is possible to achieve high green density in P/M aluminum parts with lower compacting pressures. [37]. In the 50-175 MPa compaction pressure range, the density was found to be about 2.40 to 2.5 g/cm<sup>3</sup>. The substantial increase in density occurred when the compaction pressure increased from 175 MPa to 200 MPa. Even after the compaction pressure was increased up to 275 MPa after 200 MPa, there was no significant increase in density values. This result showed that the ideal compressibility for the aluminum powders used was at a compaction pressure of 200 MPa.

Figure 3 shows the weight changes depending on the sintering temperature in the samples pressed with 200 MPa compaction pressure and then sintered with traditional and UHFIS methods. There were two main reasons for weight change in aluminum powder metal samples. The first was the weight increase observed as a result of oxidation. Another was the weight reductions that occurred as a result of evaporation of paraffin-based mold lubricants or lubricants added to the powder mixture that penetrated the powder metal sample surface during evaporation. In this study, no lubricant or binder was added to the powder mixture. However, solid paraffin lubricants have been used to prevent aluminum powders from plastering on the mold walls, which is a common problem in cold pressing of aluminum powders. These lubricants were determined to penetrate the unsintered sample surfaces after pressing. Compared to the UHFIS method of the traditional method, the lubricant gave more successful results in flying. The main reason for this was that the traditional sintering time was much longer than UHFIS. Another reason for this was that the electromagnetic properties required for induction heating were not found in the solid paraffin lubricant.

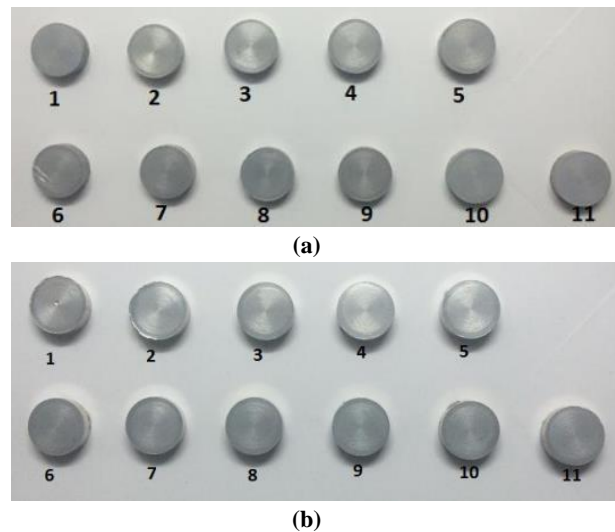


Figure 1. Sintered Samples with Traditional (a) and UHFIS (b) Methods

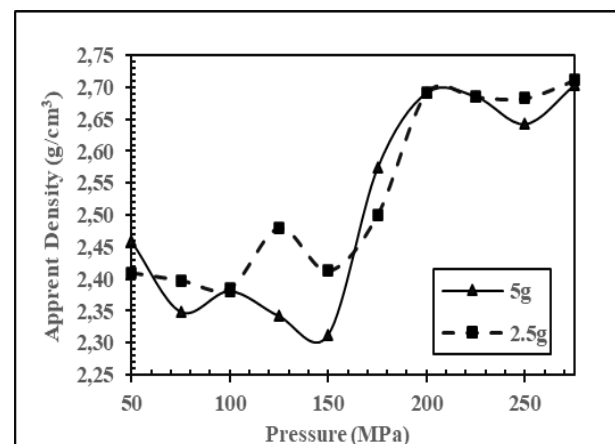


Figure 2. Graph of density as a function of compacting pressure

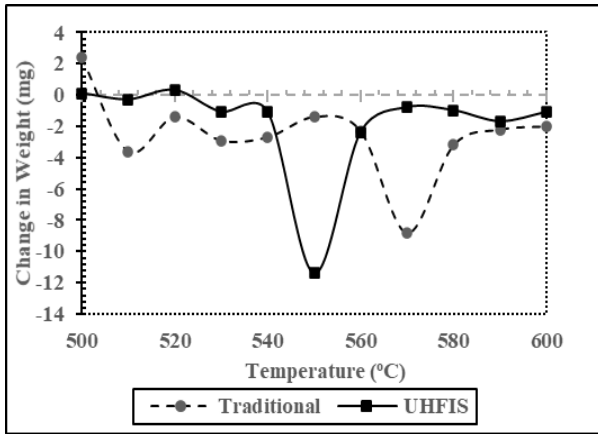


Figure 3. Change in weight as a function of sintering temperature

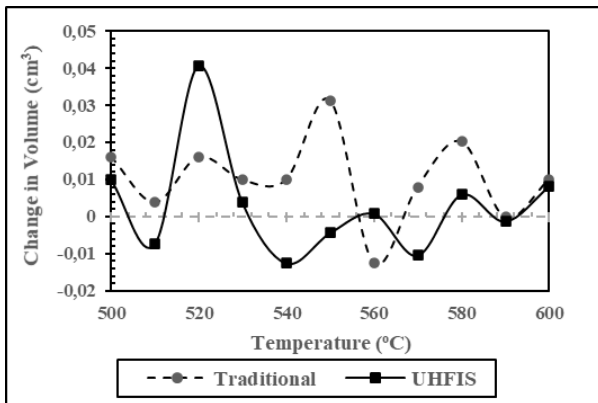


Figure 4. Change in volume as a function of sintering temperature

The volume changes depending on the sintering temperature in the samples sintered with traditional and UHFIS methods are shown in Figure 4. In powder metal samples, volume increase may occur due to grain growth, flying lubricant and binder, swelling caused by phase transformations. The main mechanism for the decrease in volume is that the pores are closed by sintering after pressing. The lowest volume change was observed in UHFIS at 540 °C, while the traditional method generally showed an increase in volume. However, a decrease in volume was determined in the sintering process performed at 560 °C.

The density changes depending on the sintering temperature in the samples sintered with traditional and UHFIS methods are given in Figure 5. The samples with the highest density obtained in samples sintered by UHFIS method were samples sintered at 540 °C. The lowest density values were measured in the samples sintered at 560 °C. In the sintering carried out in the traditional method in the 520-580 °C temperature range, the density values were measured close to each other, in the range of approximately 2.65-2.66 gr/cm<sup>3</sup>. In the traditional method, the lowest density was determined in the sample sintered at 500 °C. In general, in the UHFIS method, the apparent density was obtained higher than the traditional method. This result shows that the UHFIS method, where heating with the electromagnetic mechanism takes place, is effective in closing the pores even in a shorter time compared to conventional sintering. Thus, it can be said

that the UHFIS method has a positive effect on the sinterability of aluminum.

The hardness changes of the samples sintered by traditional and UHFIS methods depending on the sintering temperature are given in Figure 6. Higher hardness values were obtained in samples sintered by the UHFIS method compared to the traditional method. When the density changes depending on the sintering temperature (Fig. 5) and the hardness changes (Fig. 6) are examined together, it is understood that for the traditional method, the samples are insufficiently sintered at 500 °C sintering temperature. In these samples sintered by the traditional method, while the hardness increased up to 550 °C, as a result of the grain size, it decreased again by about 14% after 550 °C. Although the highest hardness value was measured at 500 °C in samples sintered by UHFIS method, when the density and hardness values of 540 °C sintered samples are examined together, it can be said that this temperature is the ideal sintering temperature of aluminum samples for the UHFIS method.

Figure 7 shows the microstructures of sintered samples at 520, 540, 560, 580 and 600 °C by UHFIS method, respectively. Microstructure images were obtained with an optical microscope at 500x magnification.

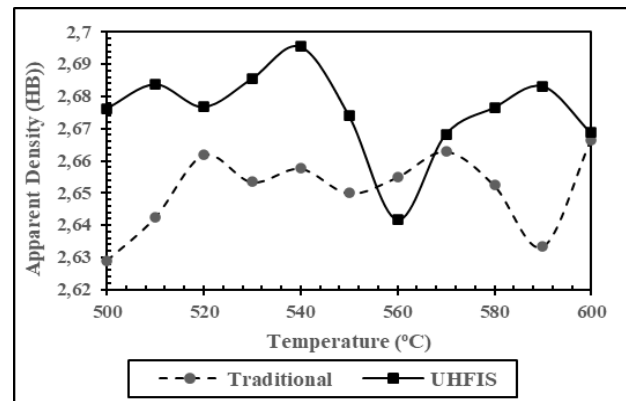


Figure 5. Apparent density of sintered samples as a function of sintering temperature

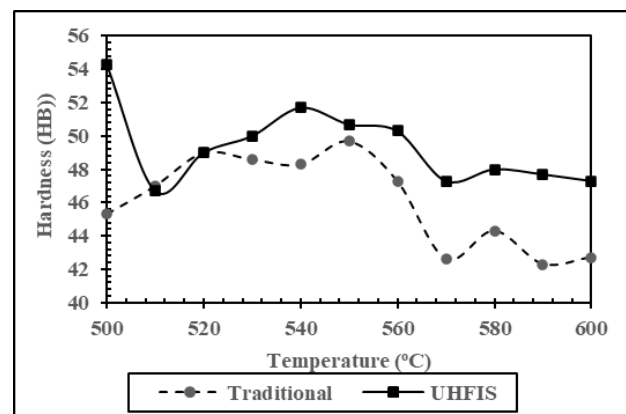


Figure 6. Hardness of the sintered samples as a function of sintering temperature

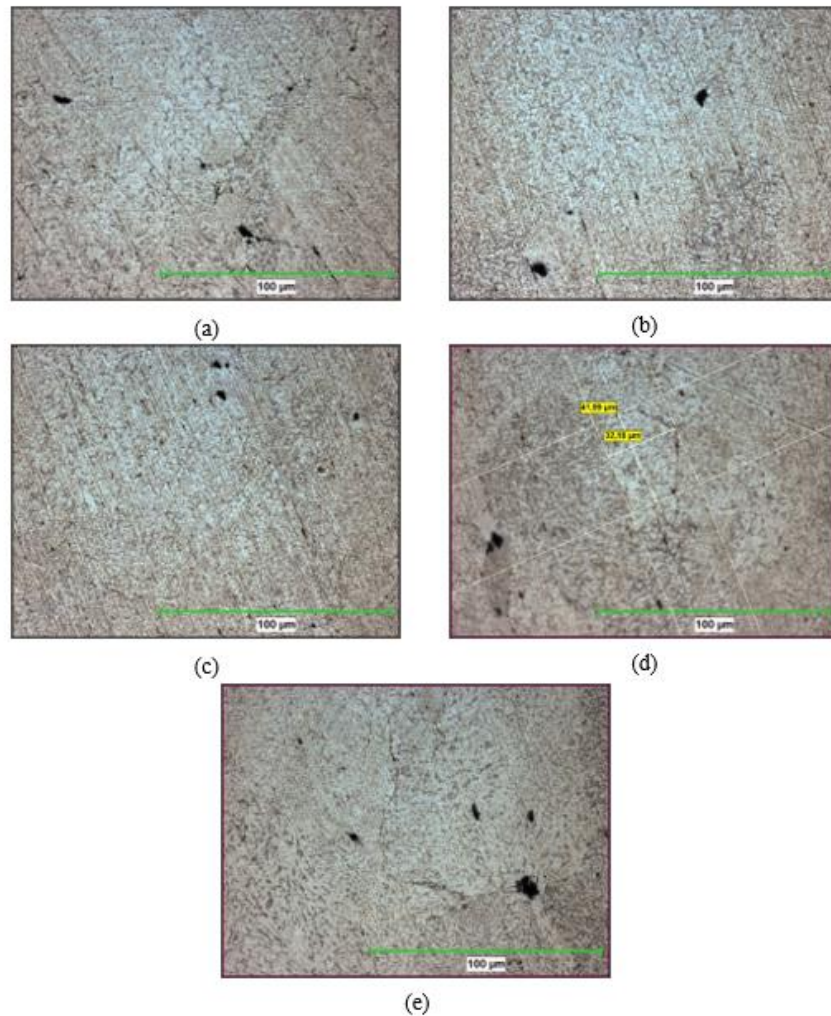


Figure 7. Microstructures of sintered samples at various temperatures by UHFIS Method: a) 520 °C, b) 540 °C, c) 560 °C, d) 580 °C and e) 600 °C.

When the microstructure images were examined, it was seen that after the sintering, the number of pores between the particles was considerably decreased and the existing pores were small in size. Besides, the effect of eddy currents in the microstructure of the sample sintered at 600 °C was determined.

In Figure 8, microstructure images of the samples sintered by traditional and UHFIS methods are given at 600 °C, respectively. Images were taken under an optical microscope at 200x magnification. These microstructure images show differences in the size and distribution of the pores of these two samples with similar density. In the traditional method, the pores after sintering were much larger than the pores in the samples sintered by the UHFIS method. In addition, it was determined that these pores showed a more homogeneous distribution in the samples sintered by the UHFIS method. This indicates the sintering behavior and success of P / M pure aluminum with the UHFIS method.

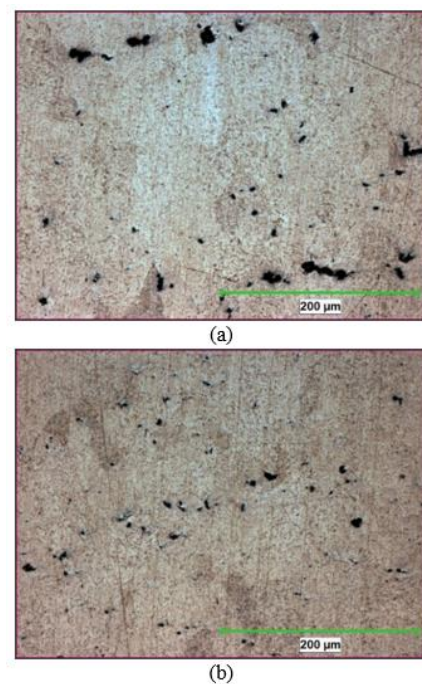


Figure 8. Microstructures of sintered samples with (a) traditional and (b) UHFIS Methods at 600 °C

#### 4. Conclusions

In this study, compressibility of uniaxial cold pressing with pure aluminum powders having 99.8% purity and 50-70  $\mu\text{m}$  size was investigated. Traditional and ultra-high frequency induction sintering behaviors of samples pressed with optimum compaction pressure determined by compressibility tests were compared. Sintering processes were carried out with both methods at 10 °C intervals in the range of 500-600 °C. In the traditional method, sintering was performed as 40 minutes. In the UHFIS method, sintering was applied for 5 minutes. The results are as follows:

- The optimum compaction pressure of pure aluminum powders with 99.8% purity and 50-70  $\mu\text{m}$  size is 200 MPa.
- Traditional method is more successful in evaporating lubricant than UHFIS method.
- Density values of samples sintered by UHFIS method are higher than density values of samples sintered by traditional method.
- The hardness values of the samples sintered by UHFIS method are higher than the hardness values of the samples sintered by the traditional method.
- The UHFIS method decreases the pore size more effectively and the distribution of the pores in the internal structure becomes more homogeneous.
- Pure aluminum powders, 5 min the optimum sintering temperature is 540 °C during sintering with UHFIS method.
- Thanks to the work done, it was shown that it was successfully sintered to pure aluminum powder metal samples in less than 8 times less time by using induction.

#### Declaration

The author(s) declared no potential conflicts of interest with respect to the research, authorship, and/or publication of this article. The author(s) also declared that this article is original, was prepared in accordance with international publication and research ethics, and ethical committee permission or any special permission is not required.

#### References

1. Deuis, R. L., Subramanian, C., Yellup, J. M., Dry Sliding Wear of Aluminium Composite-A Review. *Composites Science and Technology*, 1997. 57: p. 415-435.
2. Surappa, M. K., *Aluminium Matrix Composites: Challenges and Opportunities*. Sadhana, 2003. 28: p. 319-334.
3. Singla, M., Dwivedi, D. D., Singh, L., Chawla, V., *Development of Aluminum Based Silicon Carbide Particulate Metal Matrix Composite*. *Journal of Minerals Materials Characterization & Engineering*, 2009. 8(6): p. 455-467.
4. Şimşek, İ, Şimşek, D., Özyürek, D. *The effect of different sliding speeds on wear behavior of ZrO<sub>2</sub> reinforcement aluminum matrix composite materials*. *International Advanced Researches and Engineering Journal*, 2020. 4(1):p. 1-7.
5. Cetinel, H., Ayvaz, M., *The Effect of Aging Parameters and Roughness on the Wear Properties of Aluminum Alloy 6082*. *Materials Testing*, 2014. 56: p. 988-993.
6. Narayan, S., Rajeshkannan, An., *Workability Behavior of Powder Metallurgy Carbide Reinforced Aluminum Composites During Hot Forging*. *Materials and Manufacturing Processes*, 2015. 30: p. 1196-1201.
7. German, R. M., Suri, P., Park, S. J., *Review: Liquid Phase Sintering*. *Journal of Materials Science*, 2009. 44(1): p. 1-39.
8. Kehl, W., Fischmeister, H. F., *Liquid Phase Sintering of Al-Cu Compacts*. *Powder Metall*, 1980. 23(3): p. 113-119.
9. Oh, M. C., Ahn, B., *Effect of Mg Composition on Sintering Behaviours and Mechanical Properties of Al-Cu-Mg Alloy*. *Transactions of Nonferrous Metals Society of China*, 2014. 24: p.53-58.
10. Schaffer, G. B., Yao, J.-Y., Bonner, S. J., Crossin, E., Pas., S. J., Hill, A. J., *The Effect of Tin and Nitrogen on Liquid Phase Sintering of Al-Cu-Mg-Si Alloys*. *Acta Materialia*, 2008. 56: p. 2651-2624.
11. Rudianto, H., Jang, G. J., Yang, S. S., Kim, Y. J., Dlouhy, I., *Evaluation of Sintering Behavior of Premix Al-Zn-Mg-Cu Alloy Powder*. *Advances in Materials Science and Engineering*, 2015. 2015: p. 1-8.
12. Schaffer, G. B., Sercombe, T. B., Lumley, R. N., *Liquid Phase Sintering of Aluminium Alloys*. *Materials Chemistry and Physics*, 2001. 67: p. 85-91.
13. Gokce, A., Findik, F., *Mechanical and Physical Properties of Sintering Aluminum Powders*. *Journal of Achievements in Materials and Manufacturing Engineering*, 2008. 30(2): p. 157-164.
14. Gokce, A., Findik, F., Kurt, A. O., *Effects of Mg content on Aging Behavior of Al<sub>4</sub>Cu<sub>x</sub>Mg PM Alloy*. *Materials and Design*, 2013. 46: p. 524-531.
15. Boland, C. D., Hexemer Jr, R. L., Donaldson, I. W., Bishop, D. P., *Industrial Processing of a Novel Al-Cu-Mg Powder Metallurgy Alloy*. *Materials Science & Engineering A*, 2013. 559: p. 902-908.
16. Gokce, A., Findik, F., Kurt, A. O., *Microstructural Examination and Properties of Premixed Al-Cu-Mg Powder Metallurgy Alloy*. *Materials Characterization*, 2011. 62: p. 730-735.
17. Daran, J. D., Grönbeck, H., Hellman, A., *Mechanism for Limiting Thickness of Thin Oxide Films on Aluminum*. *Physical Review Letters*, 2014. 112: p. 146103/1-5.
18. Mamedov, V., *Spark Plasma Sintering as Advanced PM Sintering Method*. *Powder Metallurgy*, 2002. 45(49): p. 322-328.
19. Matli, P. R., Shakoore, R. A., Mohammed, A. M. A., Gupta, M., *Microwave Rapid Sintering of Al-Metal Matrix Composites: A Review on the Effect of Reinforcements, Microstructure and Mechanical Properties*. *Metals*, 2016. 6: p. 1-19.
20. Ghasali, E., Yazdani-rad, R., Asadian, K., Ebadzadeg, T., *Production of Al-SiC-TiC Hybrid Composites Using Pure and 1056 Aluminum Powders Prepared Through Microwave and Conventional Heating Methods*. *Journal of Alloy and Compounds*, 2017. 690: p. 521-518.
21. Ghasali, E., Pakseresht, A. H., Alizadeh, M., Shirvanimoghaddam, K., Ebadzadeh, T., *Vanadium Carbide Reinforced Aluminum Matrix Composite Prepared by Conventional, Microwave and Spark Plasma Sintering*. *Journal of Alloys and Compounds*, 2016. 688: p. 527-533.
22. Guo, B., Ni, S., Yi, J., Shen, R., Tang, Z., Du, Y., Song, M., *Microstructures and Mechanical Properties of Carbon*

- Nanotubes Reinforced Pure Aluminum Composites Synthesized by Spark Plasma Sintering and Hot Rolling.* Materials Science & Engineering A, 2017. 698: p. 282-288.
23. Zadra, M., Casari, F., Girardini, L., Molinari, A., *Spark Plasma Sintering of Pure Aluminium powder: mechanical properties and fracture analysis.* Powder Metallurgy 2007. 50(1): p. 40-45.
  24. Zeng, W., Qin, W., Gu, C., Sun, H., Ma, Y., Cao, X., *Microstructure and Properties of Pure Aluminum Prepared by Spark Plasma Sintering.* Metallurgical Research and Technology, 2019. 166: p. 1-6.
  25. Kwon, H., Park, D. H., Park, Y., Silvian, J. F., Kawasaki, A., Park, Y., *Spark Plasma Sintering Behavior of pure Aluminum Depending on Various Sintering Temperatures.* Met. Mater. Int., 2010. 16(1): p. 71-75.
  26. Nakamura, M., Chida, N., Ohba, T., Sugaya, Y., *Development of Rapid Sintering Technique on Carbon Steels by the Induction Heating Method.* Journal of the Japan Society of Powder and Powder Metallurgy, 1999. 46(5): p. 538-543.
  27. Çavdar, U., Atik, E., *Investigation of Conventional- and Induction- Sintered Iron and Iron-Based Powder Metal Compacts.* The Journal of the Minerals, Metals & Materials Society, 2014. 66(6): p. 1027-1034.
  28. Oh, S.-J., Kim, B.-S., Shon, I.-J., *Mechanical Properties and Rapid Consolidation of Nanostructured WC and WC-Al<sub>2</sub>O<sub>3</sub> Composites by High-Frequency Induction-Heated Sintering.* Int. Journal of Refractory Metals and Hard Metals, 2016. 58: p. 189-195.
  29. Kim, H.-C., Kim, D.-K., Woo, K.-D., Ko, I.-Y., Shon, I.-J., *Consolidation of Bindersless WC-TiC by High Frequency Induction Heating Sintering.* Int. Journal of Refractory Metals and Hard Metals, 2008. 26: p. 48-54.
  30. Shon, I.-J., *High-Frequency Induction Sintering of B<sub>4</sub>C Ceramics and Its Mechanical Properties.* Ceramics International, 2016. 42: p. 19406-19412.
  31. Bayerl, T., Schledjewski, R., Mitschang, P., *Induction Heating of Thermoplastic Materials by Particulate Heating Promoters.* Polymers & Polymer Composites, 2012. 20(4): p. 333-342.
  32. Takajo, S., Endo, I., Kajinaga, Y., Itoh, S., *Complex Magnetic Permeability of Packed Metal Powders.* Trans. JIM, 1979. 20: p. 617-626.
  33. Crocoran, J., Nagy, P.B., *Compensation of the Skin Effect in Low-Frequency Potential Drop Measurements.* Journal of Nondestructive Evaluation, 2016. 35:p. 35-58.
  34. Hermal, W., Leitner, G., Krumpold, R., *Review of Induction Sintering: Fundamentals and Applications.* Powder Metal, 1980. 3: p. 130-135.
  35. ASTM E10-15a, *Standard Test Method for Brinell Hardness of Metallic Materials*, ASTM International, West Conshohocken, PA, 2015, www.astm.org.
  36. Bol'shechenko, A. G., Gaiduchenko, A. K., Radomysel'skii I. D., Zhukovskaya, L. A., Kostyuk, V. A., *Effect of Some Factors on the Compressibility of Iron Powders.* Soviet Powder Metallurgy and Metal Ceramics, 1972. 11: p.952-955.
  37. German, R. M., *Powder Metallurgy Science.* 1984, U.S.A. Metal Powder Industries Federation.

**Research Article**

## Nonlinear vibration and dynamic response of nano composite conical tube by conveying fluid flow

Masoud Rahmani <sup>a,\*</sup>  and Amin Moslemi Petrucci <sup>a</sup> 

<sup>a</sup>Department of Mechanical Engineering, Tehran University, Tehran, Iran

## ARTICLE INFO

*Article history:*

Received 09 June 2020

Revised 18 July 2020

Accepted 29 July 2020

*Keywords:*

Conical tube

Fluid flow

Galerkin method

Vibrations

## ABSTRACT

Modeling of tubes containing fluid flow is widely used in the study of heat exchangers, nuclear reactors, micro and nano tools, etc. This system is structurally simple but very complex in terms of dynamic behavior and vibrations. In this paper, an analytical relationship for nonlinear vibrations of self-excitation of a nanocomposite conical tube containing fluid flow is extracted, one end of which is free and the other side is fixed and is under gravitational force. The base material is assumed to be 1200 series aluminum, which is reinforced with carbon nanotubes. The Hamiltonian equations are obtained, assuming the Euler–Bernoulli beam theory and the use of the Galerkin method, dissected the partial derivative equations into Ordinary Differential Equations (ODE), then solved by MATLAB coding and investigated the effect of various parameters on system behavior. As the fluid velocity increases, the amplitude of the vibration increases and the nonlinear effects of the system increase, so more modes are needed to converge the responses. In a conical tube, the  $\beta_T$  coefficient increases with increasing inner diameter along the tube and the system becomes more stable. Increasing the length of the pipe makes the opening conical pipe more stable and the closing conical pipe more unstable. The change in length has no effect on the stability of the cylindrical tube.

© 2020, Advanced Researches and Engineering Journal (IAREJ) and the Author(s).

### 1. Introduction

The issue of fluid flow pipes has been seriously studied since about 1950 to analyze the vibrations of oil pipelines. Although this system is structurally simple, it is very complex in terms of dynamic behavior. Various nonlinear phenomena are more pronounced in the dynamic behavior of these systems, especially in tubes with free ends. Modeling of such systems is used in heat exchangers, nuclear reactors, micro and nano tools, robots and underwater equipment, etc. One of the main features of these systems is that if the velocity of the material being transferred is high enough, the structure may suffer from deflection or oscillation instability in bending modes. For these structures, the rate of acceleration that leads to the onset of instability is called the critical mass transfer rate. In analyzing such systems, it is usually to determine two cases. The first is the critical velocity of the mass being transferred and the second is the relation between the

characteristic frequencies (specific values) and the velocity of the transfer mass. The first is the main goal of sustainability analysis, and the second is important if the characteristics of the free frequency and the response to a set of specific excitation are considered. Extensive research has been done on various types of tubes containing fluid flow, but most of this research has been limited to linear models and a small number of variable cross-sections. Probing biomechanical properties with a centrifugal force quartz crystal microbalance [1]. This study examines flexible tubes containing flow. Lu et al. [2] investigated internal resonance and stress distribution of pipes conveying fluid in supercritical regime. Xinbo [3] showed in experimental device for the study of liquid–solid coupled flutter instability of salt cavern leaching tubing. Amabili et al. [4] studied the effects of geometric defects on the nonlinear stability of a cylindrical shell containing fluid flow and the effect of Van der Waals force. Liang et al. [5] analyzing the vibrations caused by

\* Corresponding author. Tel.: +9801142565736; Fax: +9801142565736.

E-mail addresses: [mrahmani@ihu.ac.ir](mailto:mrahmani@ihu.ac.ir) (M. Rahmani), [amin.tehran2020@gmail.com](mailto:amin.tehran2020@gmail.com) (A. Moslemi Petrucci)

ORCID: 0000-0002-0519-0670 (M. Rahmani), 0000-0002-5928-0479 (A. Moslemi Petrucci)

DOI: 10.35860/iarej.750166

the flow and stability of double-walled carbon nanotubes based on the theory of coupling stress, investigated the side and fixed effect of Winkler elastic constant (spring stiffness). Sadeghi et al. [6] investigated the effect of mass at the end of the tube for three-dimensional mode. Ghayesh et al. [7] studied the motion of a tube integrated containing the flow, taking into account the flexibility of the tube in two dimensions. One of the areas that has received the most attention recently is the nanoscale and the use of nanocomposites. Farajpour et al. [8] investigated the nonlinear mechanics of nanotubes containing fluid flow. Liang et al. [9] investigated the free vibrations and dynamics of the rotating tube containing the fluid flow. Their study found that rotational motion reinforces tube strength and eliminates the buckling instability. Lu et al. [10] investigated the effects of nonlinear vibrations on the fatigue life of fluid transfer tubes made of Functionally Graded Material (FGM) materials. The results of fatigue analysis show that internal resonance shortens the life of fatigue and reduces the distribution coefficient of FGM tube, reduces resonance response and maximum tube tension. Mohammadi et al. [11] investigated an efficient solver for fully coupled solution of interaction between incompressible fluid flow and nanocomposite truncated conical shells. The dynamic instabilities of nanocomposite truncated conical shells containing a quiescent or a flowing inviscid fluid are scrutinized. Nonlinear dynamic equations are established according to the Novozhilov's nonlinear shell theory along with Green's strains and Hamilton principle. Dinh et al. [12] investigated for electro-thermo-mechanical vibration of nanocomposite cylindrical shells with an internal fluid flow. Khudayarov et al. [13] investigated numerical simulation of vibration of composite pipelines conveying fluids with account for lumped masses. Sedighi [14] investigated divergence and flutter instability of magneto-thermo-elastic Cubic boron nitride (C-BN) hetero-nanotubes conveying fluid. On the basis of finite element analysis, an eigenvalue problem is performed to examine the vibrational characteristics of a hetero-nanotube made of C-BN nanotubes in magnetic and thermal environment. Bahaadini et al. [15] investigated dynamic stability of viscoelastic nanotubes conveying pulsating magnetic Nano flow under magnetic field. Dynamic stability analysis of viscoelastic carbon nanotubes (CNTs) conveying pulsating magnetic Nano flow subjected to a longitudinal magnetic field. Li et al. [16] analytically investigated Vibration of a Fluid-Conveying Pipe Flexibly Restrained at the Ends. In their studies the effects of different spring stiffness coefficients on the parametric resonance responses are presented. According to a review of similar research, the nonlinear vibrations of the tube with the variable cross-section have not been analyzed analytically. In this study, a nonlinear analytical relation is obtained for the self-excitation

vibrations of the nanocomposite conical tube with a free end that contains a fluid flow and is under gravity.

## 2. Problem Statement

Figure 1 shows the geometric parameters of the tube. In this study, it is assumed that the fluid is incompressible, so the volumetric flow rate is constant along the tube and the velocity obtained by dividing the flow rate by the fluid cross section. The total cross-sectional area at each point is determined by  $A_e(s)$ , the area of the section containing the  $A_f(s)$  fluid, and the cross-sectional area of the tube with  $A_p(s)$ . The tube is assumed to be a fixed head. The flow entry's the tube from the top and is under gravity and exits from the bottom of the tube.

The equations of motion in the form of a partial differential equation derivative are a function of  $x$  and  $t$ , which must be written to the matrix form of the finite element to solve the equations. The matrix form can be solved in a variety of ways, including the Runge-Kutta method. The steps for converting equations to the matrix form of finite element components are as follows, that is, first, using the Galerkin method, write the equations of the Partial Differential Equations as a weak form, and then the common matrix that you see these steps in Figure 2.

The Galerkin method is a special case of the residual weight method, which is a function of weight equal to the approximation function.

### 2.1 Fourth Order Runge-Kutta Method

This method has several levels that in this article, the fourth order mode is used. Fourth Order Runge-Kutta Method is a numerical technique used to solve ordinary differential equation of the form.

$$\frac{dy}{dx} = f(x, y), y(0) = y_0 \quad (1)$$

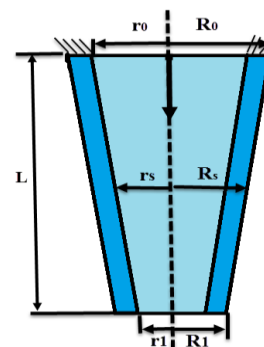


Figure 1. Geometry of the problem



Figure 2. Steps to convert partial derivative equations into a matrix form



$K_1, K_2, K_3,$  and  $K_4$  are the values of the Runge-Kutta method, which should be weighted average of these values with the values of displacement and velocity in the previous step in order to calculate the velocity and displacement in each step [17].

$$\begin{aligned}
 k_1 &= hf(x_i, y_i), k_2 = hf(x_i + \frac{h}{2}, y_i + \frac{k_1}{2}), \\
 k_3 &= hf(x_i + \frac{h}{2}, y_i + \frac{k_2}{2}), \\
 k_4 &= hf(x_i + h, y_i + k_3) \\
 &= y_i + \frac{1}{6}(k_1 + 2k_2 + 2k_3 + k_4)
 \end{aligned}
 \tag{2}$$

in which  $h$  is time step of solving. Classical elasticity theories deal with issues in which the displacements are small, but in the case under consideration it is possible to make large displacements, which makes the importance of nonlinear terms important. In elasticity  $(x, y, z)$  it indicates the position of the material point in the elastic body and  $(u, v, w)$  corresponds to the displacements of the same material point. Properties of composite material reinforced by carbon nanotube are obtained using the following relations [18]:

$$E_{11c} = \eta_1 V_{CNT} E_{11}^{CNT} + V_m E^m \tag{3}$$

$$\frac{\eta_2}{E_{22c}} = \frac{V_{CNT}}{E_{22}^{CNT}} + \frac{V_m}{E^m} \tag{4}$$

$$\frac{\eta_3}{G_{12c}} = \frac{V_{CNT}}{G_{12}^{CNT}} + \frac{V_m}{G^m} \tag{5}$$

$$v_{12c} = V_{CNT} v_{12}^{CNT} + V_m v^m \tag{6}$$

$$\rho_{0c} = V_{CNT} \rho_0^{CNT} + V_m \rho_0^m \tag{7}$$

$$a_{11c} = V_{CNT} a_{11}^{CNT} + V_m a^m \tag{8}$$

$$a_{22c} = (1 + v_{12}^{CNT}) V_{CNT} a_{22}^{CNT} + (1 + v^m) V_m a^m - v_{12} a_{11c} \tag{9}$$

In this relation  $E_{11}^{CNT}$  and  $E_{22}^{CNT}$  are elastic modulus and  $G_{12}^{CNT}$  shear modulus of single-walled carbon nanotubes.  $\eta_1, \eta_2$  and  $\eta_3$  are the carbon nanotube performance parameters.  $V_{CNT}$  and  $V_m$ , respectively, are the volume fraction of carbon nanotubes and matrices that apply to the  $V_{CNT} + V_m = 1$  relation.  $v_{12}^{CNT}$  and  $\rho_0^{CNT}$  are Poisson's ratio and density of carbon nanotubes  $v^m$  and  $\rho_0^m$  are Poisson's ratio and density of matrix. In these relations,  $\alpha_{11}^{CNT}$ ,  $\alpha_{22}^{CNT}$  and  $\alpha^m$  are the thermal expansion coefficients of the carbon nanotube and the matrix. The properties of carbon nanotubes are presented in Table 1 and the values of carbon nanotube performance parameters are presented in Table 2.

The base material is assumed to be 1200 series aluminum, which is reinforced with carbon nanotubes. The

fluid passing through the pipe is also assumed to be water. The main mechanical properties of aluminum are listed in Table 3.

The assumption of the problem is that the fluid is incompressible and turbulent that the diameter of the tube is small compared to the length. Assuming the Euler–Bernoulli beam theory was used for the problem, rotational inertia and shear deformation were ignored, assuming that the central axis of the tube did not change in length (the condition of non-expansion). The energy method is based on Hamilton's principle and is as follows:

$$\delta \int_{t_1}^{t_2} L dt + \int_{t_1}^{t_2} \delta W dt = 0 \tag{10}$$

In this relation,  $L$  is the Lagrangian system ( $L = T_P + T_F - V_P - V_F$ ) where  $T_P$  and  $V_P$  are kinetic energy and tube potential and  $T_F$  and  $V_F$  are kinetic energy and fluid potential, respectively.  $\delta W$  virtual work is a force that is not included in Lagrangian. But Hamilton's original form is established for closed systems, that is, in a system where there is no mass flow in or out, the Hamilton principle should be used to investigate the problem, that the system is assumed to be independent of the lost forces  $\delta W = 0$ :

$$\delta \int_{t_1}^{t_2} L dt = \int_{t_1}^{t_2} \left[ MU \left( \frac{\partial \vec{R}}{\partial t} + U \vec{\tau} \right) \cdot \delta \vec{R} \right] dt \tag{11}$$

$\vec{T}$  and  $\vec{R}$  are the position vectors and the vector unit tangent to the tube, respectively. The relation was established in 1961 by Benjamin [21] about flow tube that was modeled with the Euler–Bernoulli beam. The  $MU$  term coefficient is the amount of energy that is added to or reduced from the system by the end of the tube, the right side of the relation was considered as the transfer virtual momentum through the free surface of the end of the tube. This term is directly related to the instability mechanism. The energy finding by the tube is as follows:

$$\Delta W = - \int_0^{t_1} MU (\dot{R}^2 + U \vec{\tau} \cdot \vec{R}) dt \tag{12}$$

Table 1. Material properties of single-walled carbon nanotube (10,10) ( $v_{12}^{CNT} = 0.175$ ) [19]

Temperature (K)	700	500	300
$E_{11}^{CNT}$ (TPa)	5.4744	5.5308	5.6466
$E_{22}^{CNT}$ (TPa)	6.8641	6.9348	7.0800
$G_{12}^{CNT}$ (TPa)	1.9644	1.9643	1.9445
$\alpha_{11}^{CNT}$ (10 <sup>-6</sup> /K)	4.6677	4.5361	3.4584
$\alpha_2^{CNT}$ (10 <sup>-6</sup> /K)	4.8943	8.0189	5.1682

Table 2. Efficiency parameters for different values of  $V_{CNT}$  [19]

$\eta_3$	$\eta_2$	$\eta_1$	$V_{CNT}$
0.934	0.934	0.149	0.11
0.941	0.941	0.150	0.14
1.381	1.381	0.149	0.17

Table 3. Mechanical properties of 1200 series aluminum [20]

properties	E(Gpa)	G(Gpa)	ρ(g/cm <sup>3</sup> )	ν
value	70	28	2.7	0.29

If the two ends of the tube are fixed  $\Delta W = 0$  and the system is conservative. For small input velocity's, the fluid is  $\Delta W < 0$  and the system is stable, but for large enough velocity's, the value of  $\Delta W$  is positive and the system is unstable. Defining an exact relation for kinetic energy is very important in large deformations. Stoker [22] introduces the following relation for this purpose:

$$V = \frac{E}{2} \int_0^L [A\varepsilon^2 + 1(1+\varepsilon)^2 k^2] dx \tag{13}$$

X the Lagrangian coordinates, A cross-sectional area, I moment of inertia, and  $\varepsilon$  strain. The tube with the assumption of non-expandability  $\varepsilon = 0$ , the relation is as follows:

$$V = \frac{EI}{2} \int_0^L k^2 dx = \frac{EI}{2} \int_0^L k^2 ds \tag{14}$$

Gravitational energy is dependent on mass and is in a uniform field as follows:

$$G = \int \rho gx dV \tag{15}$$

The gravitational energy in the present case is written as follows:

$$G = -(m+M)g \int_0^L (X+u) ds \tag{16}$$

The kinetic energy of the whole system is the sum of the kinetic energy of the tube,  $T_p$ , and the kinetic energy of the  $T_F$  fluid, which is defined as follows:

$$T_p = \frac{m}{2} \int_0^L V_p^2 ds \quad , \quad T_F = \frac{m}{2} \int_0^L V_F^2 ds \tag{17}$$

Using the Hamilton principle, after performing the necessary calculations, the equation of motion is obtained as follows (for a fixed cross-sectional area):

$$\begin{aligned} &(m+M)\ddot{y} + 2MU\dot{y}'(1+y^2) + \\ &(m+M)gy'(1+\frac{1}{2}y^2) + y''(MU^2(1+y^2) \\ &+(M\dot{U} - (m+M)g(L-s)(1+\frac{3}{2}y^2)) \\ &+EI(y'''(1+y^2) + 4y'y''y''' + y''^3) \\ &-y''(\int_s^L \int_0^s (m+M)(\dot{y}^2 + y'\dot{y}') ds ds \\ &+ \int_s^L (\frac{M\dot{U}}{2}y^2 + 2MUy'\dot{y}') \\ &+ MU^2y'y'' ds) + y' \int_0^s (m+M)(\dot{y}^2 + y'\dot{y}') ds = 0 \end{aligned} \tag{18}$$

Assuming the steady flow is the dimensionless linear equation as follows:

Table 4. Physical concepts in the equation of motion.

Phrase	Physical concept
$(m+M)\frac{\partial^2 y}{\partial t^2}$	Inertial force
$2MU\frac{\partial^2 y}{\partial x \partial t}$	Coriolis force
$MU^2\frac{\partial^2 y}{\partial x^2}$	Center side force
$-(m+M)g((L-x)y)'$	The force of gravity
$EI\frac{\partial^4 y}{\partial x^4}$	Durable bending force
$M\frac{dU}{dt}$	The force of the unstable flow

$$\eta'''' + \ddot{\eta} + 2u\sqrt{\beta}\dot{\eta}' + \eta''(u^2 - \gamma(1-\xi)) + \gamma\eta' = 0 \tag{19}$$

Which are its dimensionless parameters:

$$\begin{aligned} \xi &= \frac{x}{L} \\ \eta &= \frac{y}{L} \\ \tau &= \left(\frac{EI}{m+M}\right)^{1/2} \frac{t}{L^2} \\ \gamma &= \frac{m+M}{EI} L^3 g \\ \beta &= \frac{M}{m+M} \end{aligned} \tag{20}$$

Using these dimensionless parameters, Equation 18 becomes the following form:

$$\begin{aligned} &\eta'''' + \ddot{\eta} + 2u\sqrt{\beta}\dot{\eta}'(1+\eta^2) + \eta''(u^2(1+\eta^2) \\ &+(u\sqrt{\beta}-\gamma)(1-\xi)(1+\frac{3}{2}\eta^2)) + \gamma\dot{\eta}(1+\frac{1}{2}\eta^2) \\ &+\eta''''\eta^2 + 4\eta'\eta''\eta'''' + \eta^3 - \eta''(\int_\xi^1 \int_0^\xi (\dot{\eta}^2 + \eta'\dot{\eta}') d\xi d\xi \\ &+ \int_\xi^1 (\frac{\dot{u}\sqrt{\beta}}{2}\eta^2 + 2u\sqrt{\beta}\eta'\dot{\eta}' + u^2\eta'\eta'') d\xi) \\ &+\eta' \int_0^\xi (\dot{\eta}^2 + \eta\eta) d\xi d\xi = 0 \end{aligned} \tag{21}$$

Physically, u is the dimensionless velocity of fluid,  $\gamma$  is the ratio of gravitational force to bending strength, and  $\beta$  is the ratio of fluid mass to total mass per unit length of pipe. Positive values of  $\gamma$  mean that the tube is hanging, ie the upper end of the tube is fixed and the lower end of the tube is free. Negative  $\gamma$  values mean that the lower end of the tube is fixed and the upper end of the tube is free. Considering the change in cross section, the equation of motion is as follows:

$$\begin{aligned}
 &(m_s + M_s) \ddot{y} + 2M_s U_s \dot{y}'(1 + y^2) + \\
 &(m_s + M_s) g y'(1 + \frac{1}{2} y^2) + y''(M_L U_L^2 (1 + y^2)) \\
 &- g (1 + \frac{3}{2} y^2) \int_s^L (m_s + M_s) ds \\
 &+ EI_s (y'''' + 4y'y''y'''' + y^3 + y''y''y''y'') \\
 &+ EI_s (2y'' + 2y''y''y'' + 3y^2 y') + EI_s'' (y'' + y''y''y'') \quad (22) \\
 &- y'' (\int_s^L (m_s + M_s) \int_0^s (\dot{y}^2 + y'\dot{y}') ds ds) \\
 &+ \int_s^L (2M_s U_s y' \dot{y}' + M_L U_L^2 y' y'') ds) \\
 &+ y'(m + M) \int_0^s (\dot{y}^2 + y'\dot{y}') ds = 0
 \end{aligned}$$

The geometric characteristics of the tube is shown in Figure 1. Geometric dimensionless parameters are written based on the geometric characteristics of the tube. The moment of inertia and mass, the cross-sectional area and density are dimensionless and the relations related to the radius and dimensionless dimension are obtained as:

$$\begin{aligned}
 r_s &= r + \frac{r - r_1}{L} s, \\
 R_s &= R + \frac{R - R_1}{L} s \quad (23) \\
 A_e(s) &= \pi R_s^2, A_f(s) = \pi r_s^2, \\
 A_p(s) &= A_e(s) - A_f(s) = \pi(R_s^2 - r_s^2)
 \end{aligned}$$

By dividing the area and moment of inertia by their values at the beginning of their tube, it becomes dimensionless:

$$\begin{aligned}
 A_e^* &= \frac{A_e(s)}{A_e(0)} = \frac{R_s^2}{R_0^2}, A_f^* = \frac{A_f(s)}{A_f(0)} = \frac{r_s^2}{R_0^2}, \\
 A_p^* &= \frac{A_p(s)}{A_e(0)} = \frac{R_s^2 - r_s^2}{R_0^2} \\
 I^* &= \frac{I(s)}{I(0)} = \frac{R_s^4 - r_s^4}{R_0^4 - r_1^4} \quad (24) \\
 x &= \frac{L}{R}, \lambda = \frac{r}{R}, a_i = \frac{r - r_1}{L}, \\
 a_e &= \frac{R - R_1}{L}, \xi = \frac{s}{L}, \eta = \frac{y}{L}
 \end{aligned}$$

Therefore, the area and time of the dimensionless moment of inertia are as follows:

$$\begin{aligned}
 A_f^*(\xi) &= a_i^2 x^2 \xi^2 - 2a_i \lambda x \xi + \lambda^2 \\
 A_e^*(\xi) &= a_e^2 x^2 \xi^2 - 2a_e \lambda x \xi + 1 \\
 A_p^*(\xi) &= x^2 (a_e^2 - a_i^2) \xi^2 \\
 &+ 2x(a_i \lambda - a_e) \xi + 1 - \lambda^2 \quad (25) \\
 I^*(\xi) &= \frac{x^4 (a_e^4 - a_i^4)}{1 - \lambda^4} \lambda^4 + \frac{4x^3 (a_i^3 - a_e^3)}{1 - \lambda^4} \xi^3 \\
 &+ \frac{6x^2 (a_e^2 - a_i^2 \lambda^2)}{1 - \lambda^4} \xi^2 + \frac{4x(a_i \lambda^3 - a_e)}{1 - \lambda^4} \xi + 1
 \end{aligned}$$

Other dimensionless parameters are defined as follows:

$$\begin{aligned}
 p^* &= \frac{\rho_p}{\rho_f}, u = \left(\frac{\rho_f A_f}{EI}\right)^{\frac{1}{2}}_{\xi=0} U.L, \\
 \tau &= \left(\frac{EI}{\rho_p A_p + \rho_f A_f}\right)^{\frac{1}{2}}_{\xi=0} \frac{t}{L}, \quad (26) \\
 \gamma &= \left(\frac{\rho_p A_p + \rho_f A_f}{EI}\right)^{\frac{1}{2}}_{\xi=0} L^3 g
 \end{aligned}$$

To shorten the equations, the following parameter is defined:

$$\Lambda = \frac{\lambda^2}{\lambda^2(1 - p^*) + p^*} \quad (27)$$

Finally, dimensional equation in the form below:

$$\begin{aligned}
 \frac{\Lambda}{\lambda^2} &= (A_f^* + \rho^* A_p^*) \ddot{\eta} + 2u\sqrt{\Lambda} \dot{\eta}'(1 + \eta^2) + \\
 \eta'' &\left(\frac{u^2 \lambda^2}{A_f^*(1)}(1 + \eta^2) - \right. \\
 \frac{\Lambda}{\lambda^2} &\gamma (1 + \frac{3}{2} \eta^2) \int_{\xi}^1 (A_f^* + \rho^* A_p^*) d\xi) \\
 &+ \frac{\Lambda}{\lambda^2} \gamma (A_f^* + \rho^* A_p^*) \eta'(1 + \frac{1}{2} \eta^2) + \\
 I^* &(\eta'''' \eta^2 + 4\eta' \eta'' \eta'''' + \eta^3 + \eta''''y'') + \quad (28) \\
 I^{*'} &(2\eta''''(1 + \eta^2) + 3\eta^2 \eta') + I^{*''} \eta''(1 + \eta^2) \\
 -\eta'' &\left(\frac{\Lambda}{\lambda^2} \int_{\xi}^1 (A_f^* + \rho^* A_p^*) \int_0^{\xi} (\dot{\eta}^2 + \eta' \dot{\eta}') d\xi d\xi \right. \\
 &+ \int_{\xi}^1 (2u\sqrt{\Lambda} \eta' \dot{\eta}' + \frac{u^2 \lambda^2}{A_f^*(1)} \eta' \eta''') d\xi) + \\
 \frac{\Lambda}{\lambda^2} &(A_f^* + \rho^* A_p^*) \eta' \int_0^{\xi} (\dot{\eta}^2 + \eta' \dot{\eta}') d\xi d\xi = 0
 \end{aligned}$$

After obtaining the equations of motion, it is necessary to use the Galerkin method mentioned earlier to make the equations discrete and matrix.

$$\begin{aligned}
 & m_{ij} \ddot{q}_j + c_{ij} \dot{q}_j + k_{ij} q_j + B_{ijkl} q_j q_k q_l + \\
 & D_{ijkl} q_j q_k \dot{q}_l + E_{ijkl} q_j \dot{q}_k \dot{q}_l + F_{ijkl} q_j q_k \ddot{q}_l = 0, \\
 & m_{ij} = \frac{\Lambda}{\lambda^2} \int_0^1 (A_f^* + \rho^* A_p^*) \varphi_i \varphi_j d\xi \\
 & c_{ij} = 2u\sqrt{\Lambda} \int_0^1 \varphi_i \varphi_j' d\xi, \\
 & k_{ij} = \int_0^1 I^* \varphi_i \varphi_j'' d\xi + 2 \int_0^1 I^{**} \varphi_i \varphi_j'' d\xi + \int_0^1 I^{***} \varphi_i \varphi_j'' d\xi + \\
 & \frac{u^2 \lambda^2}{A_f^*(1)} \int_0^1 \varphi_i \varphi_j'' d\xi + \frac{\Lambda}{\lambda^2} \gamma \int_0^1 (A_f^* + \rho^* A_p^*) \varphi_i \varphi_j' d\xi \\
 & - \int_0^1 \varphi_i \varphi_j'' \int_{\xi}^1 (A_f^* + \rho^* A_p^*) d\xi, \\
 & B_{ijkl} = \frac{u^2 \lambda^2}{A_f^*(1)} \int_0^1 \varphi_i (\varphi_j' \varphi_k' \varphi_l'') \int_{\xi}^1 \varphi_k' \varphi_l'' d\xi \\
 & + \frac{\Lambda}{\lambda^2} \gamma \left( \frac{1}{2} \int_0^1 (A_f^* + \rho^* A_p^*) \varphi_i' \varphi_j' \varphi_k' \varphi_l' d\xi \right. \\
 & \left. - \frac{3}{2} \int_0^1 \varphi_i \varphi_j' \varphi_k' \varphi_l'' \int_{\xi}^1 (A_f^* + \rho^* A_p^*) d\xi \right. \\
 & \left. + \int_0^1 I^{**} \varphi_i (2\varphi_j' \varphi_k' \varphi_l'' + 3\varphi_i \varphi_j' \varphi_k'' \varphi_l'') d\xi \right. \\
 & \left. + \int_0^1 I^{***} \varphi_i \varphi_j' \varphi_k' \varphi_l'' d\xi \right) \\
 & D_{ijkl} = 2u\sqrt{\Lambda} \int_0^1 \varphi_i (\varphi_j' \varphi_k' \varphi_l' - \\
 & \varphi_l'' \int_{\xi}^1 \varphi_k' \varphi_l') d\xi, E_{ijkl} = F_{ijkl} = \\
 & \frac{\Lambda}{\lambda^2} \gamma \left( \int_0^1 (A_f^* + \rho^* A_p^*) \varphi_i \varphi_j' \int_0^{\xi} \varphi_k' \varphi_l' d\xi \right. \\
 & \left. - \int_0^1 \varphi_i \varphi_j'' \int_{\xi}^1 (A_f^* + \rho^* A_p^*) \int_0^{\xi} \varphi_k' \varphi_l' d\xi \right)
 \end{aligned} \tag{29}$$

$$\begin{aligned}
 & [m_{ij}]_{N \times N} \begin{Bmatrix} \ddot{q}_1 \\ \ddot{q}_2 \\ \dots \\ \ddot{q}_N \end{Bmatrix}_{N \times 1} + [c_{ij}]_{N \times N} \begin{Bmatrix} \dot{q}_1 \\ \dot{q}_2 \\ \dots \\ \dot{q}_N \end{Bmatrix}_{N \times 1} \\
 & + [k_{ij}]_{N \times N} \begin{Bmatrix} q_1 \\ q_2 \\ \dots \\ q_N \end{Bmatrix}_{N \times 1} + [B_{ijkl}]_{N \times N^3} \begin{Bmatrix} q_1 q_1 q_1 \\ q_1 q_1 q_2 \\ \dots \\ q_N q_N q_N \end{Bmatrix}_{N^3 \times 1} \\
 & + [D_{ijkl}]_{N \times N^3} \begin{Bmatrix} q_1 q_1 \dot{q}_1 \\ q_1 q_1 \dot{q}_2 \\ \dots \\ q_N q_N \dot{q}_N \end{Bmatrix}_{N^3 \times 1} \\
 & + [E_{ijkl}]_{N \times N^3} \begin{Bmatrix} q_1 \dot{q}_1 q_1 \\ q_1 \dot{q}_1 q_2 \\ \dots \\ q_N \dot{q}_N q_N \end{Bmatrix}_{N^3 \times 1} \\
 & + [F_{ijkl}]_{N \times N^3} \begin{Bmatrix} q_1 q_1 \ddot{q}_1 \\ q_1 q_1 \ddot{q}_2 \\ \dots \\ q_N q_N \ddot{q}_N \end{Bmatrix}_{N^3 \times 1} = \begin{Bmatrix} 0 \\ 0 \\ \dots \\ 0 \end{Bmatrix}_{N \times 1}
 \end{aligned} \tag{30}$$

**3. Results and Discussion**

Numerical methods must be used to solve the equations obtained in the relation. In this study, MATLAB software and Simulink part have been used to solve these equations. The equations in Simulink are solved by Runge-Kutta method. The time step and tolerance are also considered one thousandth. The values of entry of a matrix the coefficients are calculated by the codes written in MATLAB. The figure shows the Simulink model used.

First, it is necessary to evaluate the results with the work of other researchers, and for this purpose, two diagrams of the figures are presented is shown in Figure 4. The diagram of critical velocity changes in terms of coefficient using different modes for solution.

The final matrix form of motion equations will be as follows:

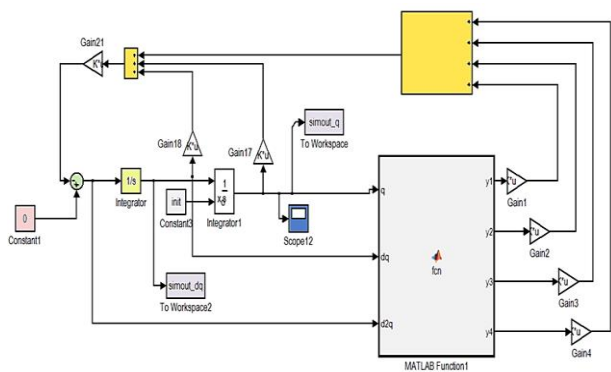


Figure 3. Simulink model of nonlinear differential equation solution

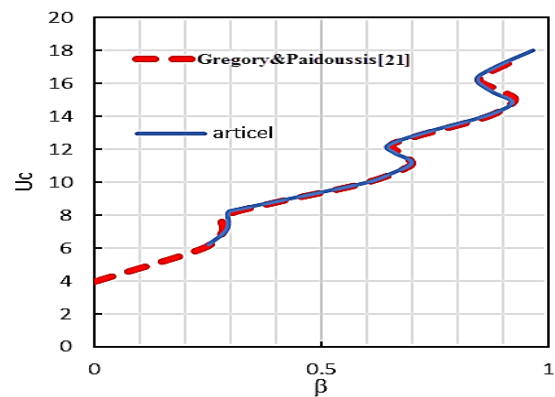


Figure 4. Evaluate results with other research work in ref [23]

According to Figure 5, as the number of modes used in the Galerkin method for solving increases, the jumps that appear in the diagram increase, and the location of the jumps displacement to the left of the diagram. Figures 6 are shown to investigate the effect of gravity and the length of the tube on the critical velocity of the diagrams. As mentioned, to solve the nonlinear equations, the Simulink model is created according to the figure, which solves the differential equations discretized by the Galerkin method by the Rang-Kota numerical method. To ensure the correctness of the nonlinear equations, as well as the correctness of the written program for integral calculations and the Simulink model, since the results have not been worked on the cone tube so far, the results for the cylindrical tube state are compared with the research of Wang et al [24]. The comparison is shown in Figure 5. (Dimensional parameters used for evaluation:  $\beta=0.213$ ,  $\gamma=26.75$ ).

It can be seen that the results are in good agreement with each other. In both graphs the critical velocity is about 8.5.

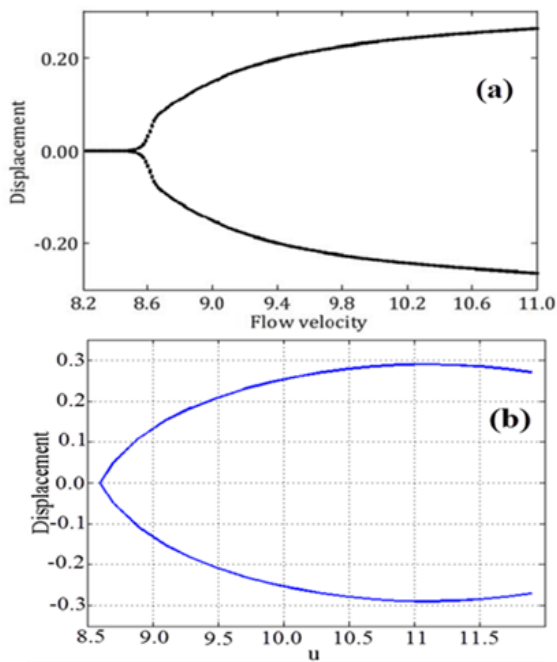


Figure 5. Diagram of the range of motion of a cylindrical tube after the occurrence of instability with a change in velocity (a) Wang et al [24] (b) current article.

Table 5. Default values of dimensionless parameters.

Parameter	Value
X	40
$\gamma$	0
$\rho^*$	2
$\lambda$	0.5
$I^*$	2
$A_p^*$	0.14
$A_f^*$	0.11

The values of the  $\beta_T$  and  $\alpha_i$  parameters are also indicated in each figure. Due to the fact that with increasing  $\beta$  coefficient, the modes that lead to system instability change, and considering that according to the observations of this change, the modes move towards higher modes, to see the jumps in the diagram, the modes used for solving must be increased. Otherwise jumps that occur at higher  $\beta$  coefficients will not appear in the graph.

According to Figure 6, as the number of modes used in the Galerkin method to solve increases, the number of jumps that appear in the graph increases and the location of the jumps shifts to the left of the graph. To investigate the effect of the direction of gravity and the length of the tube on the critical velocity is shown in Figures 7 and 8. ( $\alpha_e=0$ ,  $\beta=0.5$ ,  $\gamma_{(H)}=0.00251 \times (X/2)^3$ )

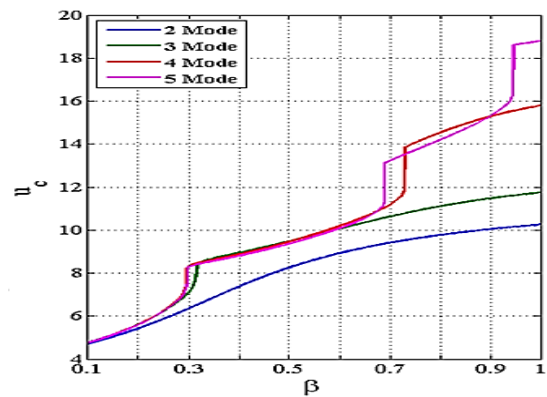


Figure 6. Critical velocity changes in different modes.

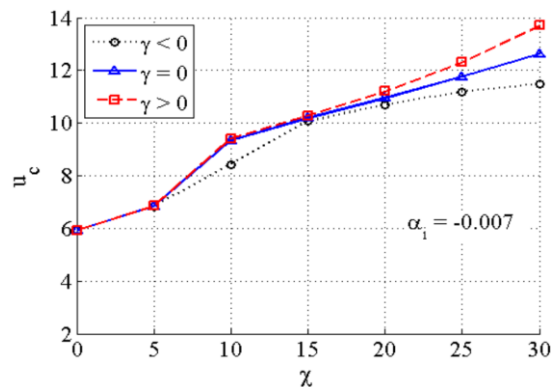


Figure 7. The Effect of gravity and the length of the tube.

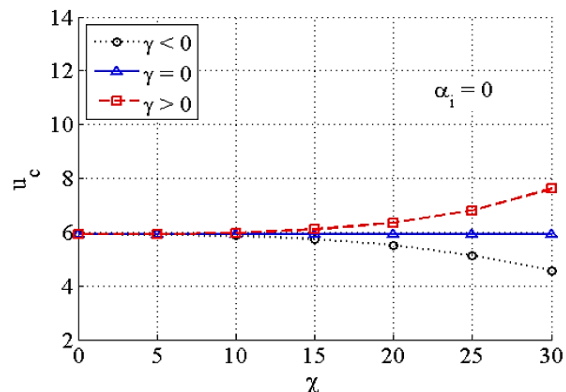


Figure 8. The Effect of gravity and the length of the tube.

As can be seen in Figures 7 and 8, the negative  $\gamma$  makes the system more unstable because the critical speed of the fluid is reduced. As  $\gamma$  increases, the critical speed of the fluid increases and the system becomes more stable. This effect is the same for conical and cylindrical pipes. It should be noted that  $\alpha_i$  and  $\alpha_e$  indicate the slope of the inner and outer wall of the pipe. Since  $\gamma$  is negative, it means that the free end of the tube is above the fixed end and the fluid flow is upwards. Therefore, the weight of the pipe and the fluid increases the tendency to deflection and instability in the pipe, thus becoming unstable at a lower speed. Fluid velocity is one of the main parameters of the problem. In the figure, the effect of velocity on changes in the amplitude of displacement after instability is shown in Figure 9. At high speeds, the predicted amplitude difference in different modes increases. In nonlinear systems, it is necessary to consider more modes to model the systems until the response is convergent. The speed limit of 11 differences is limited but then increases.

In Figure 10, the convergence is greater for the  $\beta$  value, and the fourth mode is well responsive. Therefore, less modes are required for  $\beta$  in modeling.

In both Figures 11 and 12, the range of the studied velocity is from the beginning of the critical velocity to twice the critical velocity. The range of motion for a conical tube with different internal angles and with different  $\beta_T$  coefficients is plotted in the following figures.

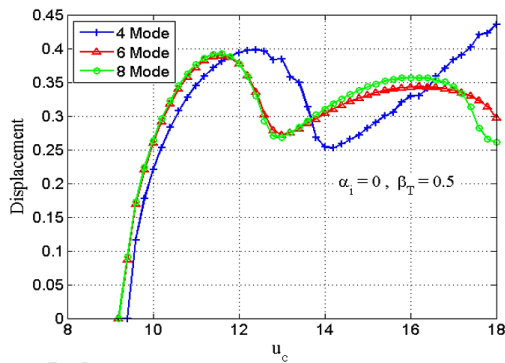


Figure 9. The Effect of velocity on changes in the amplitude of displacement ( $\alpha_i = 0, \beta_T = 0.5$ )

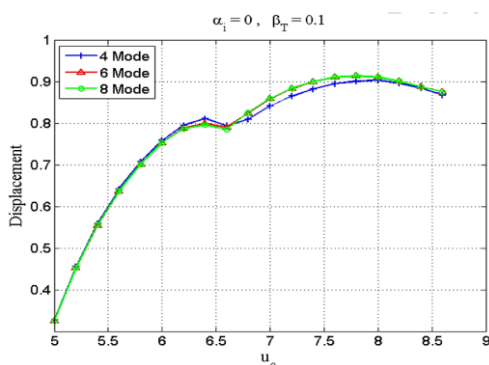


Figure 10. The Effect of velocity on changes in the amplitude of displacement ( $\alpha_i = 0, \beta_T = 0.1$ )

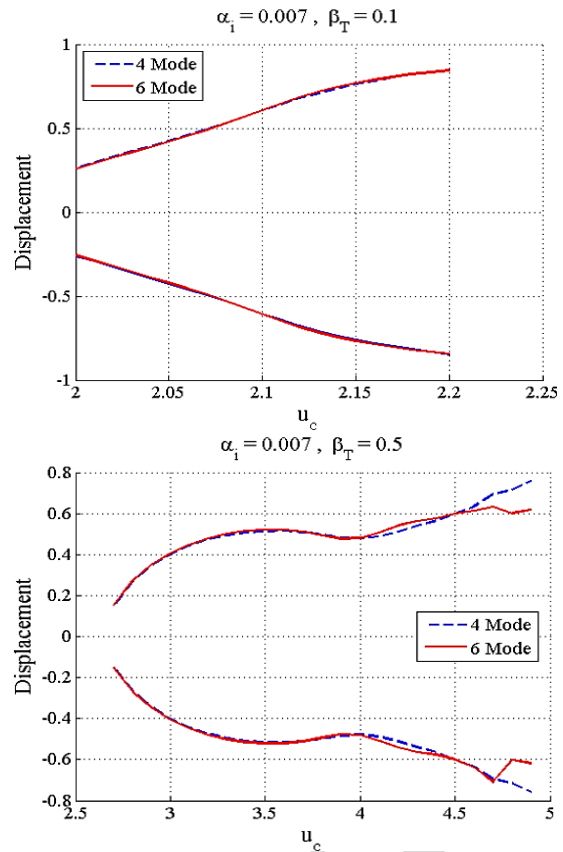


Figure 11. The Effect of velocity on changes in the amplitude of displacement ( $\alpha_i = 0.007, \beta_T = 0.1$  and  $0.5$ )

According to Figure 12, the difference in response between the upper and lower modes in  $\beta_T$  is further increased. The effect of changing the internal slope angle of the conical, the diagram shows the maximum velocity displacement for different interior angles in Figure 13.

In Figures 14 and 15, the wider the internal angle of the wall, the lower the range of oscillations, and the narrower the internal angle, the higher the rate of growth of the oscillation range. Also, in lower beta coefficients, the scales obtained after instability have a larger size than more beta. Figure 16 shows the natural frequency of the system in terms of fluid velocity at different  $L/h$  ( $h$  is the shell thickness ( $R_s - r_s$ )). As the parameter increases, the lateral ratio of the natural frequency of the system decreases and the damping frequency of the system increases. The critical velocity of the fluid is reduced and the system becomes prone to buckling.

Weight percentage of carbon nanotubes is another parameter of this study, which is its effect on the Dimensionless frequency shown in Figure 17. increasing the Weight percentage of carbon nanotubes increases the frequency of the tube. Increasing the carbon nanotubes increases the strength of the tube and thus reduces the displacement amplitude.

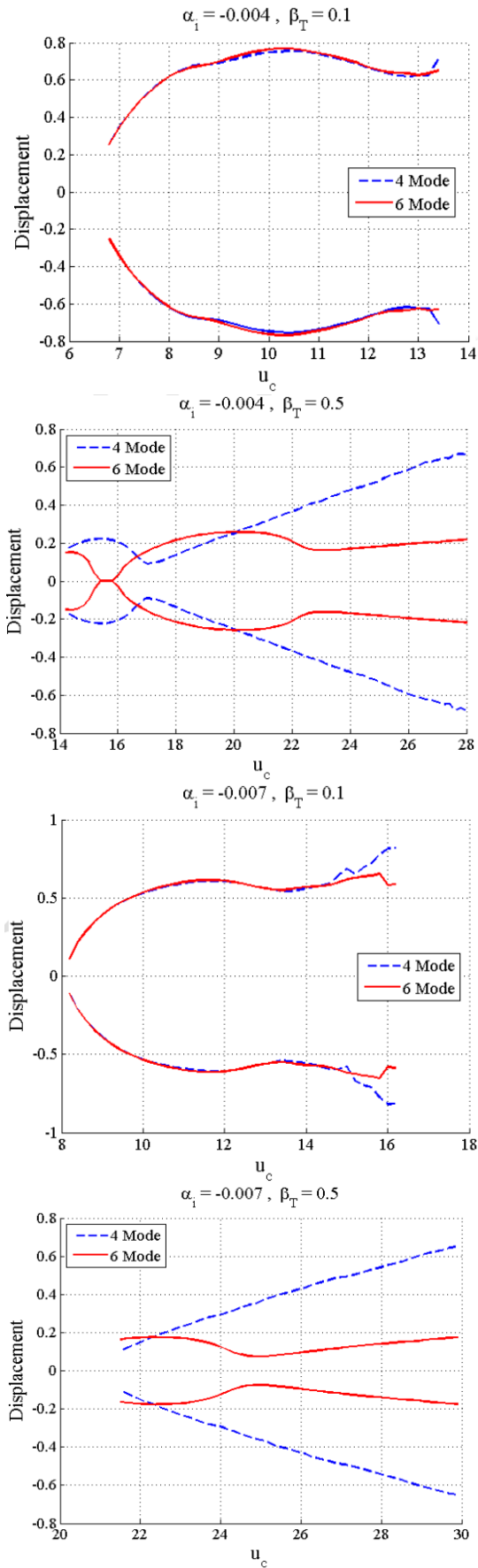


Figure 12. The difference in response between high and low modes in  $\beta_T$ .

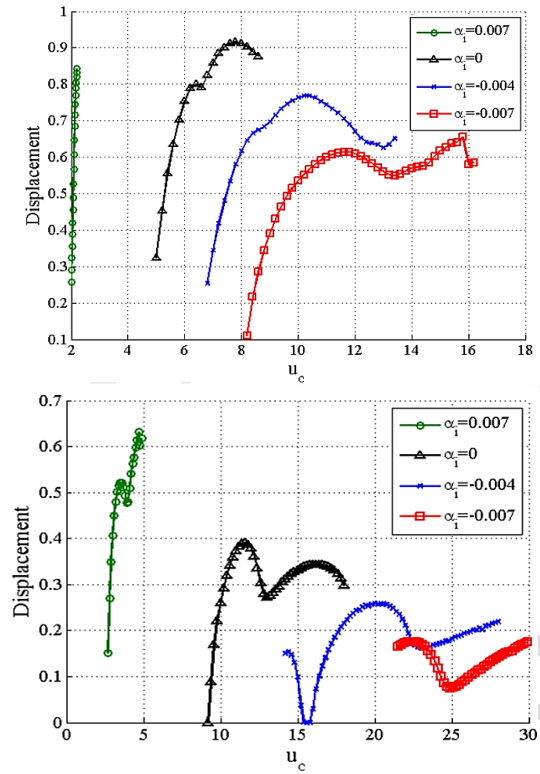


Figure 13. Maximum velocity displacement for different interior angles.

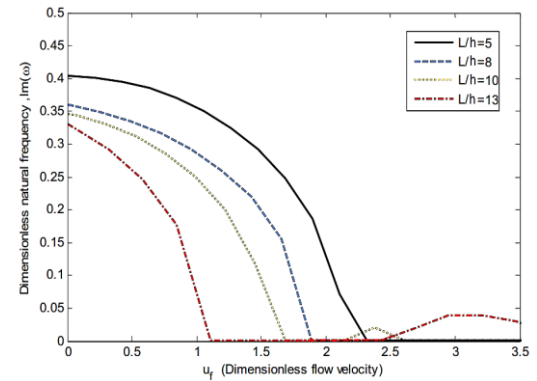


Figure 14. Dimensionless natural frequency relative to flow rate.

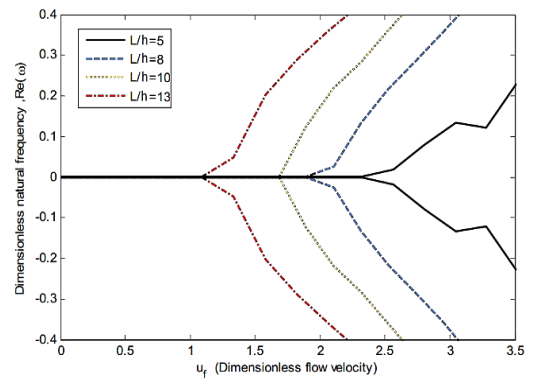


Figure 15. Dimensionless natural frequency relative to flow rate.

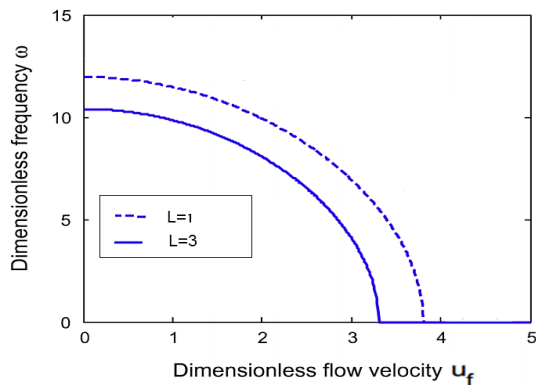


Figure 16. Natural frequency of the fluid velocity at different  $L/h$ .

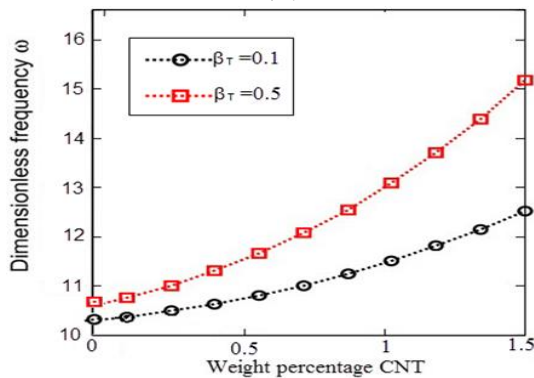


Figure 17. Frequency change by CNT weight percentage change.

#### 4. Conclusions

In all sections and by changing all the parameters, it has been observed that by increasing the fluid velocity, the natural frequency of the system decreases in all vibration modes and reaches zero. At this point, the critical velocity of the fluid is defined. From this velocity onwards the system becomes unstable and prone to buckling. In addition, as the fluid velocity increases, the amplitude of the vibration increases and the nonlinear effects of the system increase, so more modes are needed to converge the responses. As the internal angle progresses toward the opening of the inner wall, the range of oscillations decreases. It also has oscillation amplitude in lower  $\beta$  ranges and higher growth rates. The Runge-Kutta method is done with Matlab-Simulink software and a comparison between the results of this method with the solution methods used by other researchers is shown to be a good match. In a conical tube, the  $\beta T$  coefficient increases with increasing inner diameter along the tube and the system becomes more stable. Increasing the length of the pipe makes the opening conical pipe more stable and the closing conical pipe more unstable. The change in length has no effect on the stability of the cylindrical tube.

#### Declaration

The author(s) declared no potential conflicts of interest with respect to the research, authorship, and/or publication of this article. The author(s) also declared that this article

is original, was prepared in accordance with international publication and research ethics, and ethical committee permission or any special permission is not required.

#### References

1. Webster, Aaron, Frank Vollmer, and Yuki Sato. *Probing biomechanical properties with a centrifugal force quartz crystal microbalance*. Nature communications, 2014. 5(1): p. 1-8.
2. Lu, Ze-Qi, Kai-Kai Zhang, Hu Ding, and Li-Qun Chen. *Internal resonance and stress distribution of pipes conveying fluid in supercritical regime*. International Journal of Mechanical Sciences, 2020. 186 (2020): 105900.
3. Ge, Xinbo, Yiping Li, Xilin Shi, Xiangsheng Chen, Hongling Ma, Chunhe Yang, Chang Shu, and Yuanxi Liu. *Experimental device for the study of liquid–solid coupled flutter instability of salt cavern leaching tubing*. Journal of Natural Gas Science and Engineering, 2019. 66: p. 168-179.
4. Amabili, M., K. Karagiozis, M. P. Païdoussis. *Effect of geometric imperfections on non-linear stability of circular cylindrical shells conveying fluid*. International Journal of Non-Linear Mechanics, 2009. 44(3): p. 276-289.
5. Liao-Liang, K. Wang, Y. *Flow-induced vibration and instability of embedded double-walled carbon nanotubes based on a modified couple stress theory*. Physica E: Low-dimensional Systems and Nanostructures, 2011. 43(5): 1031-1039.
6. Sadeghi, M. *Dynamics of cantilevered pipes conveying fluid. Part 3: Three-dimensional dynamics in the presence of an end-mass*. Journal of Fluids and Structures, 2007. 23(4): p. 589-603.
7. Ghayesh, Mergen H., Michael P. Païdoussis, M. Amabili. *Nonlinear dynamics of cantilevered extensible pipes conveying fluid*. Journal of Sound and Vibration, 2013. 332(24): 6405-6418.
8. Farajpour, A. *Nonlinear mechanics of nanotubes conveying fluid*. International Journal of Engineering Science, 2018. 133: p. 132-143.
9. Liang, F. *Dynamical modeling and free vibration analysis of spinning pipes conveying fluid with axial deployment*. Journal of Sound and Vibration, 2018. 417: p. 65-79.
10. Lu, Ze-Qi. *Nonlinear vibration effects on the fatigue life of fluid-conveying pipes composed of axially functionally graded materials*. Nonlinear Dynamics, 2020. 100: p. 1091-1104.
11. Mohammadi, N., H. Asadi, M. M. Aghdam. *An efficient solver for fully coupled solution of interaction between incompressible fluid flow and nanocomposite truncated conical shells*. Computer Methods in Applied Mechanics and Engineering, 2019. 351: p. 478-500.
12. Ninh, D., Nguyen D. T. *Investigation for electro-thermo-mechanical vibration of nanocomposite cylindrical shells with an internal fluid flow*. Aerospace Science and Technology, 2019. 92: p. 501-519.
13. Khudayarov, B. A., Kh M. Komilova, F. Zh Turaev. *Numerical simulation of vibration of composite pipelines conveying fluids with account for lumped masses*. International Journal of Pressure Vessels and Piping, 2020. 179: 104034.
14. Sedighi, H.M. *Divergence and flutter instability of magneto-thermo-elastic C-BN hetero-nanotubes conveying fluid*. Acta Mechanica Sinica, 2020. 36(2): p. 381-396.
15. Bahaadini, R., M. Hosseini, M. Amiri. *Dynamic stability of viscoelastic nanotubes conveying pulsating magnetic*



- nanoflow under magnetic field*. Engineering with Computers, 2020. p. 1-13.
16. Li, Q., Liu, W., Lu, K. and Yue, Z. *Nonlinear Parametric Vibration of a Fluid-Conveying Pipe Flexibly Restrained at the Ends*. Acta Mechanica Solida Sinica, 2019. 33(3): p. 327-346.
  17. Prince, Peter J., John R. Dormand. *High order embedded Runge-Kutta formulae*. Journal of Computational and Applied Mathematics, 1981. 7(1): p. 67-75.
  18. Rahmani, M., A. Moslemi Petrucci. *Analytical Investigation of the Vibrational and Dynamic Response of Nano-Composite Cylindrical Shell Under Thermal Shock and Mild Heat Field by DQM Method*. Journal of Modeling and Simulation of Materials, 2020. 3(1): p. 22-36.
  19. Zhu, P., Lei, Z.X., Liew, K.M. *Static and free vibration analyses of carbon nanotube-reinforced composite plates using finite element method with first order shear deformation plate theory*. Composite Structures, 2012. 94(4): p. 1450-1460.
  20. Morovvati, M. R., & Mollaei-Darjani, B. *The formability investigation of CNT-reinforced aluminum nano-composite sheets manufactured by accumulative roll bonding*. The International Journal of Advanced Manufacturing Technology, 2018. 95(9-12): 3523-3533.
  21. Benjamin, T.B. *Dynamics of a system of articulated pipes conveying fluid*. I. Theory. Proceedings of the Royal Society of London. Series A, 1961. 261: p. 457-486.
  22. Stoker, J. J. *Nonlinear elasticity*. Gordon, Breach, 1968.
  23. Gregory, R. W., and M. P. Paidoussis. *Unstable oscillation of tubular cantilevers conveying fluid II. Experiments*. Proceedings of the Royal Society of London. Series A. Mathematical and Physical Sciences, 1966. 293(1435): p. 528-542.
  24. Wang, L., Z. Y. Liu, A. Abdelkefi, Y. K. Wang, and H. L. Dai. *Nonlinear dynamics of cantilevered pipes conveying fluid: towards a further understanding of the effect of loose constraints*. International Journal of Non-Linear Mechanics, 2017. 95: p. 19-29.

**Research Article**

## Effect of spring mid-support condition on the vibrations of the axially moving string

Saim Kural <sup>a,\*</sup> 

<sup>a</sup>Manisa Celal Bayar University, Faculty of Engineering, Department of Mechanical Engineering, 45140, Yunussemre, Manisa, Turkey

**ARTICLE INFO***Article history:*

Received 24 June 2020

Revised 29 August 2020

Accepted 05 September 2020

*Keywords:*

Axially moving string

Perturbation method

Spring supported string

Vibration analysis

**ABSTRACT**

In this study, the axially moving string with spring-loaded middle support is discussed. The supports assumed as simple support on the string both ends. The intermediate support shows the characteristics of the spring. The string velocity is accepted as harmonically varying around a mean value. The Hamiltonian principle is used to find the equations of motion. The equations of motion become nonlinear, considering the nonlinear effects caused by string extensions. The equations of motion and boundary conditions are become dimensionless by nondimensionalization. Approximate solutions were found by using multiple time scales which is one of the perturbation methods. By solving the linear problem that is obtained by the first terms of the perturbation series, the exact natural frequencies were calculated for the different locations of the mid-support, various spring coefficients, and various axial velocity values. The second-order nonlinear terms reveal the correction terms for the linear problem. Stability analysis is carried out for cases where the velocity change frequency is away from zero and two times the natural frequency. Stability boundaries are determined for the principal parametric resonance case.

© 2020, Advanced Researches and Engineering Journal (IAREJ) and the Author(s).

**1. Introduction**

Because of their low bending stiffness, products such as paper sheets, plastic films, power transmission belts, magnetic tapes, and textile fibers can be modeled as an axially moving string. Determining the dynamic behavior of these systems is very important for a stable and durable design. Fundamental studies about the subject can be found in references [1-3]. Wickert investigated the response problem for the vibration of an axially moving string that resting on an elastic foundation [4]. Nayfeh et al. [5] investigated solutions for quadratic and cubic nonlinearity problem and they concluded that the direct-perturbation method is better for these problems. Pellicano and Zirilli [6] have researched axially moving beam vibrations under nonlinear effects. The string-beam transition problem was investigated in [7] for axially moving media. An axially moving string with various non-ideal boundary conditions under nonlinear effects are investigated in [8]. Pellicano analyzed the dynamic properties of axially moving systems to explain the

complex dynamic behavior observed in experimental and numerical research [9].

Also, Bağdatlı et al. investigated continuous media as an axially moving beam with middle support [10]. The combined longitudinal-transverse nonlinear dynamics of an axially moving beam were described in Ghayesh et al. [11] and they discussed the stability of an axially moving beam that has middle spring support. Two dimensional movements of an axially moving string were described in [12]. Similarly, the moving string system is modeled by using Hamilton's principle [13]. An experimental study of the nonlinear characteristics of an axially moving string investigated in [14]. An alternative analytical method was investigated in [15] for the nonlinear vibration behavior of conical cantilever beams. To reduce vibration for a nonlinear drilling system a boundary control scheme was studied by He [16]. A new mathematical model studied in [17] to determine dynamic behavior for a beam or strip moving in a certain axial direction along a given area. Chen et al. [18] studied a nonlinear equation describing the transverse vibration of an axially moving string with

\* Corresponding author. Tel.: +90 236 201 2380.

E-mail addresses: [saimkural@gmail.com](mailto:saimkural@gmail.com)

ORCID: 0000-0003-1722-6252

DOI: 10.35860/iarej.757503

constant and time-dependent length. Zhao et al. [19] discussed the global balancing of an axially moving system under the input saturation nonlinearity circumstances. Zhang et al. [20] present numerical simulations for vibration reduction. Yilmaz et al. [21] used vibration analysis with FFT for determine the misalignment fault detection.

In this study, the effect of spring mid-support condition on the nonlinear vibrations of the axially moving string was discussed. The equations of motion were obtained by using the Hamiltonian principle. To solve the equations of motion; multiple time scale perturbation method was used. This method is a semi-analytical method used to obtain approximate solutions of systems with differential equations that are difficult or impossible to solve. Natural frequency analysis was performed depending on spring constant, string velocity, and position of the center support and the obtained results are given in graphics. Considering the effects of string elongation, the system became nonlinear, and then, the solution of the equations of motion was discussed. The effects of nonlinearities on solutions were investigated. The different vibration structures for different states of the string velocity change frequency are examined. By making stability analysis was made and the stable and unstable areas were identified.

**2. The Equations of Motion and Solution**

Figure 1 shows the basic model of the axially moving string with mid-supported spring.  $x^*$ ,  $z^*$  and  $t^*$  are coordinate and time variables, respectively.  $w^*$  is the transverse and  $u^*$  is axial displacement, and  $v^*$  is the axial string velocity. In this section, the equations of motion were derived for axially moving spring mid-supported strings. Both ends were defined as simple-supported.

The Lagrangian for the system can be written the extended form of Hamiltonian Principle as:

$$\begin{aligned} \mathcal{L} = T - V = & \frac{1}{2} \rho A \int_0^{x_s} \{(\dot{w}_1^* + w_1^{*'} v^*)^2 \\ & + (v^* + \dot{u}_1^* + u_1^{*'} v^*)^2\} dx^* \\ & + \frac{1}{2} \rho A \int_{x_s}^L \{(\dot{w}_2^* + w_2^{*'} v^*)^2 \\ & + (v^* + \dot{u}_2^* + u_2^{*'} v^*)^2\} dx^* \\ & - \frac{1}{2} EA \int_0^{x_s} \left(u_1^{*'} + \frac{1}{2} w_1^{*'}{}^2\right)^2 dx^* \\ & - \frac{1}{2} EA \int_{x_s}^L \left(u_2^{*'} + \frac{1}{2} w_2^{*'}{}^2\right)^2 dx^* \\ & - \int_0^{x_s} P \left(u_1^{*'} + \frac{1}{2} w_1^{*'}{}^2\right) dx^* \\ & - \int_{x_s}^L P \left(u_2^{*'} + \frac{1}{2} w_2^{*'}{}^2\right) dx^* \\ & - \int k w_1^* dx^* @ x = x_s \end{aligned} \tag{1}$$

where  $(\dot{\phantom{x}})$  means time derivative  $\left(\frac{d}{dt^*}\right)$  and  $(\phantom{x})'$  means coordinate variable derivative  $\left(\frac{d}{dx^*}\right)$ . Euler-Bernoulli beam theory was used to obtain Equation (1). In this equation, the first two integrals on the right-hand side are kinetic energy between supports, the next four integrals are elastic potential energy due to elongation, and axial force (P), and last term is spring potential energy on mid-support location( $x_s$ ). After using the Hamiltonian principle into Equation (1), that can be expressed as follows:

$$\begin{aligned} & \rho A (\ddot{w}_{1,2}^* + 2\dot{w}_{1,2}^{*'} v^* + w_{1,2}^{*'} \dot{v}^* + w_{1,2}^{*''} v^{*2}) \\ & - EA \left(u_{1,2}^{*''} w_{1,2}^{*'} + u_{1,2}^{*'} w_{1,2}^{*''} + \frac{3}{2} w_{1,2}^{*'}{}^2 w_{1,2}^{*''}\right) \\ & - P w_{1,2}^{*''} = 0 \end{aligned} \tag{2}$$

$$\begin{aligned} & \rho A (\ddot{u}_{1,2}^* + 2\dot{u}_{1,2}^{*'} v^* + u_{1,2}^{*'} \dot{v}^* + \dot{v}^* + u_{1,2}^{*''} v^{*2}) \\ & - EA \left(u_{1,2}^{*'} + \frac{1}{2} w_{1,2}^{*'}{}^2\right)' = 0 \end{aligned} \tag{3}$$

$$\begin{aligned} & \rho A v^{*2} [w_1^{*'}(x_s) - w_2^{*'}(x_s)] - EA [u_1'(x_s) w_1'(x_s) + \\ & \frac{1}{2} w_1'^3(x_s) - u_2'(x_s) w_2'(x_s) - \frac{1}{2} w_2'^3(x_s)] - \\ & P [w_1^{*'}(x_s) - w_2^{*'}(x_s)] - k w_1(x_s) = 0 \end{aligned} \tag{4}$$

$$\begin{aligned} & \rho A v^{*2} [u_1'(x_s) - u_2'(x_s)] - EA [u_1'(x_s) - u_2'(x_s) + \\ & \frac{1}{2} w_1'^2(x_s) - \frac{1}{2} w_2'^2(x_s)] = 0 \end{aligned} \tag{5}$$

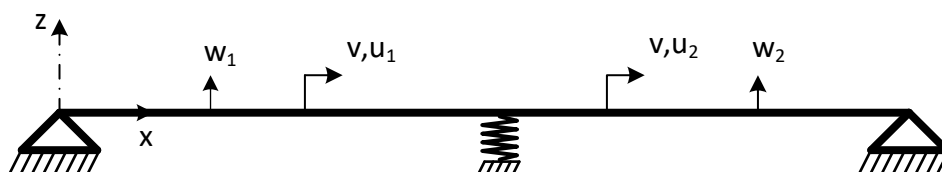


Figure 1. Axially moving string with intermediate spring support

Equations (2) and (3) obtained from double integrals and Equations (4) and (5) from single integrals. To simplify the future parametric analysis, let us define the dimensionless parameters as follows,

$$v_b^2 = \frac{EA}{P}, v_k = \frac{kL}{P}, \eta = \frac{x_s^*}{L}, x = \frac{x^*}{L}, t = \frac{t^*}{\sqrt{\frac{\rho AL^2}{P}}} \tag{6}$$

$$w_{1,2} = \frac{w_{1,2}^*}{L}, u_{1,2} = \frac{u_{1,2}^*}{L}, v = \frac{v^*}{\sqrt{\frac{P}{\rho A}}} \tag{7}$$

After all the operations were done and the necessary simplifications were made, the equations of motion and boundary conditions are obtained as follows,

$$(\ddot{w}_{1,2} + 2\dot{w}'_{1,2}v + w'_{1,2}\dot{v}) + w''_{1,2}(v^2 - 1) = \frac{1}{2}v_b^2 \left[ \int_0^\eta w_1'^2 dx + \int_\eta^1 w_2'^2 dx \right] w''_{1,2} \tag{7}$$

$$w_1(0, t) = 0, w_2(1, t) = 0$$

$$w_1(\eta, t) =$$

$$\frac{1}{v_k} \left\{ 1 + \frac{1}{2}v_b^2\varepsilon \left[ \int_0^\eta w_1'^2 dx + \int_\eta^1 w_2'^2 dx \right] \right\} (w_2'(\eta, t) - w_1'(\eta, t)) \tag{8}$$

The right-hand side of the Equation (7) represents the nonlinear terms from string elongation.  $\ddot{w}_{1,2}$  represents local,  $2\dot{w}'_{1,2}v$  represents Coriolis, and  $v_b^2 w''_{1,2}$  represents centripetal acceleration.  $\eta$  is the location of center spring. The displacement in Equations (7) and (8) can be assumed as  $w_{1,2} = \sqrt{\varepsilon} y_{1,2}$  ( $\varepsilon \ll 1$ ) to ensure that the displacement due to nonlinear effects appear in the higher-order in perturbation method. Also, the string velocity can be assumed as varying harmonically around a fixed average value,

$$v = v_0 + \varepsilon v_1 \sin \Omega t \tag{9}$$

Thus, the equations of motion and boundary conditions are,

$$\ddot{y}_{1,2} + 2\dot{y}'_{1,2}v_0 + 2\dot{y}'_{1,2}\varepsilon v_1 \sin \Omega t + y'_{1,2}\varepsilon v_1 \Omega \cos \Omega t + (v_0^2 + \varepsilon^2 v_1^2 \sin^2 \Omega t + 2\varepsilon v_0 v_1 \sin \Omega t - 1)y''_{1,2} = \frac{1}{2}v_b^2\varepsilon \left[ \int_0^\eta y_1'^2 dx + \int_\eta^1 y_2'^2 dx \right] y''_{1,2} \tag{10}$$

$$y_1(0, t) = 0, y_2(1, t) = 0$$

$$y_1(\eta, t) = \frac{1}{v_k} \left\{ 1 + \frac{1}{2}v_b^2\varepsilon \left[ \int_0^\eta y_1'^2 dx + \int_\eta^1 y_2'^2 dx \right] \right\} (y_2'(\eta, t) - y_1'(\eta, t)) \tag{11}$$

### 3. Perturbation Analysis

For approximate solutions of Equation (10), multiple scales perturbation method was used. The displacement functions can be expanded as,

$$y_1(x, t; \varepsilon) = y_{11}(x, T_0, T_1) + \varepsilon y_{12}(x, T_0, T_1) + \dots \tag{12}$$

$$y_2(x, t; \varepsilon) = y_{21}(x, T_0, T_1) + \varepsilon y_{22}(x, T_0, T_1) + \dots \tag{13}$$

where  $T_0=t$  is the slow,  $T_1=\varepsilon t$  is the fast time scales, and time derivatives can be explained as follows:

$$\frac{d}{dt} = D_0 + \varepsilon D_1 + \dots, \frac{d^2}{dt^2} = D_0^2 + 2\varepsilon D_0 D_1 + \dots \tag{14}$$

where  $D_n = d/dT_n$  Substituting Equations (12), (13), and (14) into Equation (10) yields,

The left-hand side ( $0 < x_s < \eta$ )

$$(D_0^2 + 2\varepsilon D_0 D_1)(y_{11} + \varepsilon y_{12}) + 2v_0(D_0 + \varepsilon D_1)(y'_{11} + \varepsilon y'_{12}) + (v_0^2 - 1)(y''_{11} + \varepsilon y''_{12}) + \varepsilon(2v_1 \sin \Omega T_0 (D_0 + \varepsilon D_1)(y'_{11} + \varepsilon y'_{12}) + 2v_0 v_1 \sin \Omega T_0 (y''_{11} + \varepsilon y''_{12}) + v_1 \Omega \cos \Omega T_0 (y'_{11} + \varepsilon y'_{12})) + \varepsilon^2 v_1^2 \sin^2 \Omega T_0 (y''_{11} + \varepsilon y''_{12}) = \frac{1}{2}v_b^2\varepsilon \left[ \int_0^\eta (y'_{11} + \varepsilon y'_{12})^2 dx + \int_\eta^1 (y'_{21} + \varepsilon y'_{22})^2 dx \right] (y''_{11} + \varepsilon y''_{12}) \tag{15}$$

The right-hand side ( $\eta < x_s < 1$ )

$$\begin{aligned}
 & (D_0^2 + 2\varepsilon D_0 D_1)(y_{21} + \varepsilon y_{22}) \\
 & + 2v_0(D_0 + \varepsilon D_1)(y'_{21} + \varepsilon y'_{22}) \\
 & + (v_0^2 - 1)(y''_{21} + \varepsilon y''_{22}) \\
 & + \varepsilon(2v_1 \sin \Omega T_0 (D_0 + \varepsilon D_1)(y'_{21} + \varepsilon y'_{22}) \\
 & + 2v_0 v_1 \sin \Omega T_0 (y''_{21} + \varepsilon y''_{22}) \\
 & + v_1 \Omega \cos \Omega T_0 (y'_{21} + \varepsilon y'_{22})) \\
 & + \varepsilon^2 v_1^2 \sin^2 \Omega T_0 (y''_{21} + \varepsilon y''_{22}) \\
 & = \frac{1}{2} v_b^2 \varepsilon \left[ \int_0^\eta (y'_{11} + \varepsilon y'_{12})^2 dx \right. \\
 & \left. + \int_\eta^1 (y'_{21} + \varepsilon y'_{22})^2 dx \right] (y''_{21} + \varepsilon y''_{22})
 \end{aligned} \tag{16}$$

If we make order arrangement to these equations and neglect the higher-order terms;

Order (1)

The equations of motion,

$$\begin{aligned}
 D_0^2 y_{11} + 2v_0 D_0 y'_{11} + (v_0^2 - 1)y''_{11} &= 0 \\
 D_0^2 y_{21} + 2v_0 D_0 y'_{21} + (v_0^2 - 1)y''_{21} &= 0
 \end{aligned} \tag{17}$$

And boundary conditions,

$$\begin{aligned}
 y_{12}(0, t) = 0, y_{22}(1, t) = 0, y_{12}(\eta, t) = y_{22}(\eta, t), \\
 y_{11}(\eta, t) = \frac{1}{v_k} [y'_{21}(\eta, t) - y'_{11}(\eta, t)]
 \end{aligned} \tag{18}$$

Order (ε)

The equations of motion,

$$\begin{aligned}
 & D_0^2 y_{12} + 2v_0 D_0 y'_{12} + (v_0^2 - 1)y''_{12} \\
 & = -2D_0 D_1 y_{11} - 2v_0 D_1 y'_{11} - 2v_1 \sin \Omega T_0 D_0 y'_{11} \\
 & - 2v_0 v_1 \sin \Omega T_0 y''_{11} - v_1 \Omega \cos \Omega T_0 y'_{11} \\
 & + \frac{1}{2} v_b^2 \left[ \int_0^\eta y'_{11}{}^2 dx + \int_\eta^1 y'_{21}{}^2 dx \right] y''_{11} \\
 & D_0^2 y_{22} + 2v_0 D_0 y'_{22} + (v_0^2 - 1)y''_{22} \\
 & = -2D_0 D_1 y_{21} - 2v_0 D_1 y'_{21} - 2v_1 \sin \Omega T_0 D_0 y'_{21} \\
 & - 2v_0 v_1 \sin \Omega T_0 y''_{21} - v_1 \Omega \cos \Omega T_0 y'_{21} \\
 & + \frac{1}{2} v_b^2 \left[ \int_0^\eta y'_{11}{}^2 dx + \int_\eta^1 y'_{21}{}^2 dx \right] y''_{21}
 \end{aligned} \tag{19}$$

And boundary conditions,

$$\begin{aligned}
 y_{12}(0, t) = 0, y_{22}(1, t) = 0, \\
 y_{12}(\eta, t) = y_{22}(\eta, t), \\
 y_{12}(\eta, t) = \frac{1}{2} v_b^2 \left[ \int_0^\eta y'_{11}{}^2 dx \right. \\
 \left. + \int_\eta^1 y'_{21}{}^2 dx \right] y_{11}(\eta, t)
 \end{aligned} \tag{20}$$

We can get the solution function for the linear order (O(1)),

$$\begin{aligned}
 y_{11}(x, T_0, T_1; \varepsilon) &= A_n(T_1) e^{i\omega_n T_0} Y_1(x) \\
 &+ \bar{A}_n(T_1) e^{-i\omega_n T_0} \bar{Y}_1(x) \\
 y_{21}(x, T_0, T_1; \varepsilon) &= A_n(T_1) e^{i\omega_n T_0} Y_2(x) \\
 &+ \bar{A}_n(T_1) e^{-i\omega_n T_0} \bar{Y}_2(x)
 \end{aligned} \tag{21}$$

Substituting Equations (21) into Equation (17), one obtains,

$$\begin{aligned}
 (v_0^2 - 1)Y_1'' + 2iv_0 \omega_n Y_1' - \omega_n^2 Y_1 &= 0 \\
 (v_0^2 - 1)Y_2'' + 2iv_0 \omega_n Y_2' - \omega_n^2 Y_2 &= 0
 \end{aligned} \tag{22}$$

and boundary conditions,

$$\begin{aligned}
 Y_1(0, t) = 0, Y_2(1, t) = 0, Y_1(\eta, t) = Y_2(\eta, t), \\
 Y_1(\eta, t) = \frac{1}{v_k} [Y_2'(\eta, t) - Y_1'(\eta, t)]
 \end{aligned} \tag{23}$$

For the approximate solution, the following functions are proposed,

$$\begin{aligned}
 Y_1(x) &= c_1 e^{\beta_1 x} + c_2 e^{\beta_2 x} \\
 Y_2(x) &= c_3 e^{\beta_1 x} + c_4 e^{\beta_2 x}
 \end{aligned} \tag{24}$$

By applying boundary conditions, a matrix is created with obtained four equations. By taking the determinant of this matrix, the frequency equation obtained in a general form as follows.

$$\begin{aligned}
 & \frac{1}{2} \{-2(e^{\eta\beta_1} - e^{\eta\beta_2})(e^{\eta\beta_1 + \beta_2} - e^{\beta_1 + \eta\beta_2})v_k \\
 & + e^{\eta(\beta_1 + \beta_2)}(e^{\beta_1} - e^{\beta_2})(\beta_1 - \beta_2)\} \\
 & = 0
 \end{aligned} \tag{25}$$

The natural frequencies against mean velocity ( $v_0$ ) and spring coefficient ( $v_k$ ) are given in the following figures. Figure 2 was obtained for the middle support at the  $\mu = 0.1$  location. The variations of  $v_k$  between 0 and 30, and  $v_0$  between 0 and 1 were examined. Natural frequencies drop to zero while mean velocity increasing. The natural frequencies increase directly proportional to  $v_k$ . The effect of the spring coefficient on the natural frequencies decreases as the mean velocity increases.

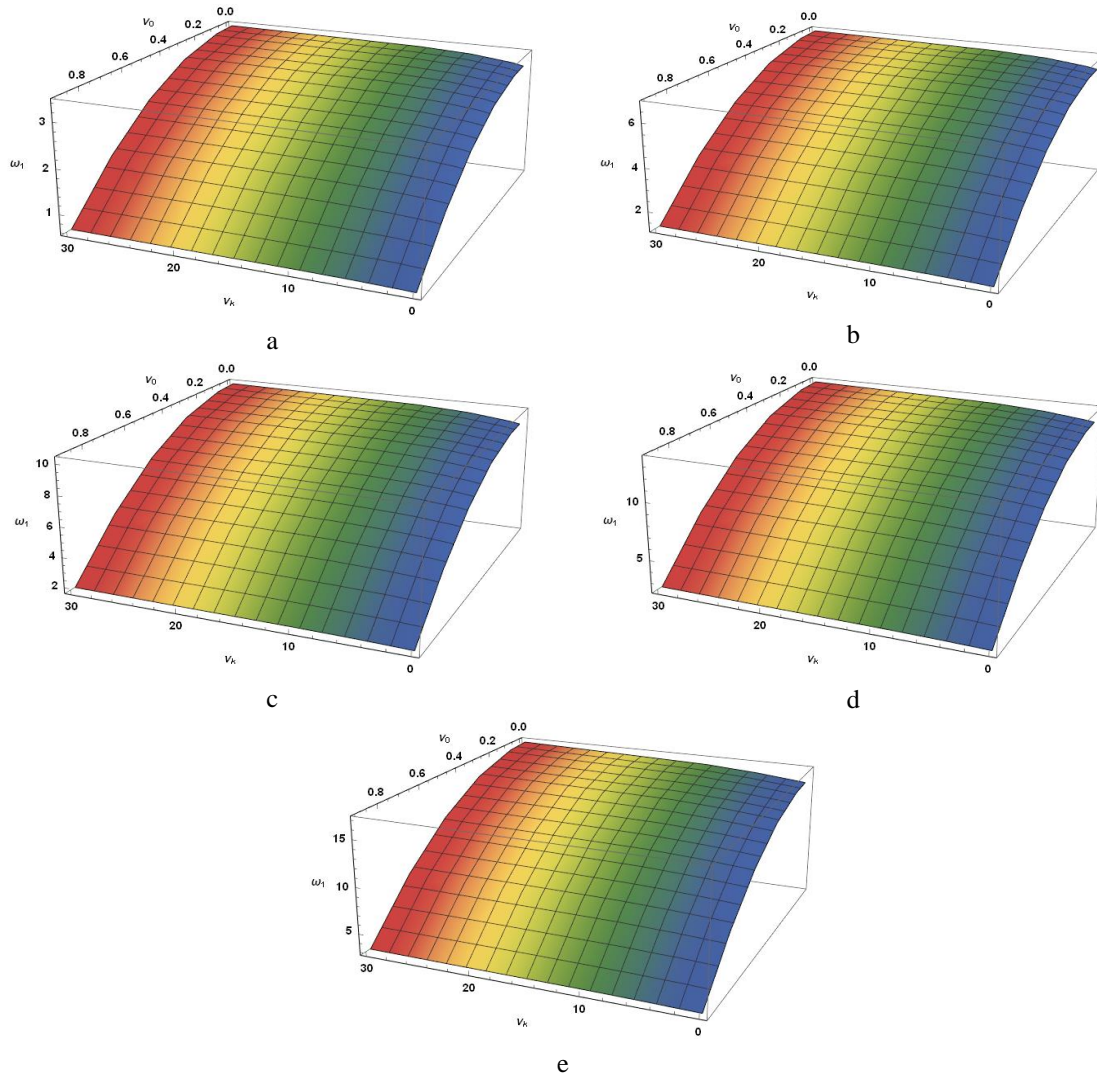


Figure 2. Variation of the natural frequency values with axial velocity and spring coefficient ( $\mu = 0.1$  location) (a; first mode, b; second mode, c; third mode, d; fourth mode, e; fifth mode)

The first natural frequencies for  $\mu = 0.1$ ,  $\mu = 0.3$  and  $\mu = 0.5$  locations compared in Figure 3. As expected  $\mu = 0.1$  location has the smallest natural frequency values, and  $\mu = 0.5$  location has the highest. When  $v_k = 0$  all 3 locations have the same values. While  $v_0$  increases the effect of the

spring coefficient on the natural frequency values decreases, again. In Figure 2 all five natural frequency shapes are similar, but for  $\mu = 0.3$  and  $\mu = 0.5$  positions  $v_k$  has more effect on natural frequency.

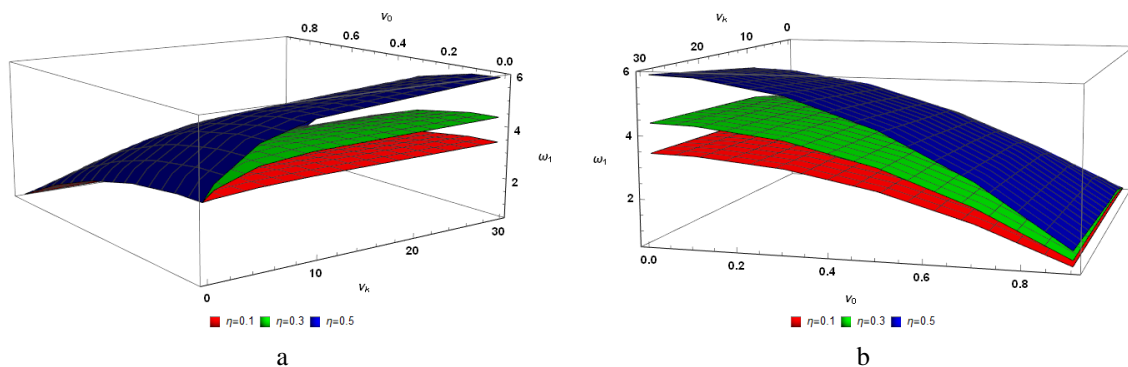


Figure 3. Comparison of the first mode natural frequency values for different  $\mu$  locations (a; left-hand side, b; right-hand side)

We can get the solution function for the linear order (O(1));

$$\begin{aligned}
 y_{12}(x, T_0, T_1) &= \phi_1(x, T_1)e^{i\omega_n T_0} \\
 &+ W_1(x, T_0, T_1) + c.c. \\
 y_{22}(x, T_0, T_1) &= \phi_2(x, T_1)e^{i\omega_n T_0} \\
 &+ W_2(x, T_0, T_1) + c.c.
 \end{aligned}
 \tag{26}$$

The first term ( $\phi$ ) refers to the secular terms of the function, the second term ( $W$ ) to the non-secular terms of the function, and last term (c.c.) means complex conjugate.

$$\begin{aligned}
 \cos \Omega T_0 &= \frac{e^{i\Omega T_0} + e^{-i\Omega T_0}}{2} \\
 \sin \Omega T_0 &= \frac{e^{i\Omega T_0} - e^{-i\Omega T_0}}{2i}
 \end{aligned}
 \tag{27}$$

Following equations are obtained by doing above trigonometric transformations and write them together with the proposed solutions to the nonlinear order equations,

$$\begin{aligned}
 e^{i\omega_n T_0} &[-\omega_n^2 \phi_1 + 2iv_0 \omega_n \phi_1' + (v_0^2 - 1)\phi_1''] = \\
 &-2(i\omega_n Y_1 + v_0 Y_1') A' e^{i\omega_n T_0} \\
 &+ v_1 \left(-\omega_n Y_1' - \frac{\Omega}{2} Y_1' + iv_0 Y_1''\right) A e^{i(\Omega + \omega_n) T_0} \\
 &+ v_1 \left(\omega_n \bar{Y}_1' - \frac{\Omega}{2} \bar{Y}_1' + iv_0 \bar{Y}_1''\right) \bar{A} e^{i(\Omega - \omega_n) T_0} \\
 &+ \frac{1}{2} v_b^2 \left[ \begin{aligned} &2Y_1'' \left( \int_0^\eta Y_1' \bar{Y}_1' dx + \int_\eta^1 Y_2' \bar{Y}_2' dx \right) \\ &+ \bar{Y}_1'' \left( \int_0^\eta Y_1'^2 dx + \int_\eta^1 Y_2'^2 dx \right) \end{aligned} \right] A^2 \bar{A} e^{i\omega_n T_0} \\
 &+ N.S.T. + c.c.
 \end{aligned}
 \tag{28}$$

$$\begin{aligned}
 e^{i\omega_n T_0} &[-\omega_n^2 \phi_2 + 2iv_0 \omega_n \phi_2' + (v_0^2 - 1)\phi_2''] = \\
 &-2(i\omega_n Y_2 + v_0 Y_2') A' e^{i\omega_n T_0} \\
 &+ v_1 \left(-\omega_n Y_2' - \frac{\Omega}{2} Y_2' + iv_0 Y_2''\right) A e^{i(\Omega + \omega_n) T_0} \\
 &+ v_1 \left(\omega_n \bar{Y}_2' - \frac{\Omega}{2} \bar{Y}_2' + iv_0 \bar{Y}_2''\right) \bar{A} e^{i(\Omega - \omega_n) T_0} \\
 &+ \frac{1}{2} v_b^2 \left[ \begin{aligned} &2Y_2'' \left( \int_0^\eta Y_1' \bar{Y}_1' dx + \int_\eta^1 Y_2' \bar{Y}_2' dx \right) \\ &+ \bar{Y}_2'' \left( \int_0^\eta Y_1'^2 dx + \int_\eta^1 Y_2'^2 dx \right) \end{aligned} \right] A^2 \bar{A} e^{i\omega_n T_0} \\
 &+ N.S.T. + c.c.
 \end{aligned}
 \tag{29}$$

$$\begin{aligned}
 \phi_1(0) &= 0, \phi_2(1) = 0, \\
 \phi_1(\eta) &= \phi_2(\eta) \\
 \phi_1(\eta) &= \frac{1}{2} v_b^2 \left[ \begin{aligned} &2Y_1(\eta) \left( \int_0^\eta Y_1' \bar{Y}_1' dx + \int_\eta^1 Y_2' \bar{Y}_2' dx \right) \\ &+ \bar{Y}_1(\eta) \left( \int_0^\eta Y_1'^2 dx + \int_\eta^1 Y_2'^2 dx \right) \end{aligned} \right] A^2 \bar{A}
 \end{aligned}
 \tag{30}$$

The different vibration structures for different states of the string velocity change frequency ( $\Omega$ ) are examined separately below.

i)  $\Omega$ ; away from  $2\omega_n$  and 0:

In this case, the solvability condition is obtained from Equations (28) and (29) as follows.

$$D_1 A - k_3 A^2 \bar{A} = 0
 \tag{31}$$

The amplitude A can be defined as follows,

$$A = \frac{1}{2} a_n e^{i\theta}
 \tag{32}$$

Inserting Equation (32) into Equation (31) and separate the real and imaginary parts.

where  $k_3$  is;

$$\begin{aligned}
 k_3 &= \frac{1}{4} v_b^2 \left( \frac{2 \left( \int_0^\eta Y_1' \bar{Y}_1' dx + \int_\eta^1 Y_2' \bar{Y}_2' dx \right) \left( \int_0^\eta Y_1'' \bar{Y}_1 dx + \int_\eta^1 Y_2'' \bar{Y}_2 dx \right)}{i\omega_n \left( \int_0^\eta Y_1 \bar{Y}_1 dx + \int_\eta^1 Y_2 \bar{Y}_2 dx \right) + v_0 \left( \int_0^\eta Y_1' \bar{Y}_1 dx + \int_\eta^1 Y_2' \bar{Y}_2 dx \right)} \right. \\
 &+ \left. \frac{\left( \int_0^\eta Y_1'^2 dx + \int_\eta^1 Y_2'^2 dx \right) \left( \int_0^\eta \bar{Y}_1'' \bar{Y}_1 dx + \int_\eta^1 \bar{Y}_2'' \bar{Y}_2 dx \right)}{i\omega_n \left( \int_0^\eta Y_1 \bar{Y}_1 dx + \int_\eta^1 Y_2 \bar{Y}_2 dx \right) + v_0 \left( \int_0^\eta Y_1' \bar{Y}_1 dx + \int_\eta^1 Y_2' \bar{Y}_2 dx \right)} \right)
 \end{aligned}
 \tag{33}$$

$$\begin{aligned} a_n' &= 0 \\ \theta' &= \frac{1}{4} k_{3I} a_n^2 \end{aligned} \tag{34}$$

Hence,

$$\begin{aligned} a_n &= a_{0n} \text{ (a is continuous)} \\ \theta &= \frac{1}{4} k_{3I} a_{0n}^2 T_1 + \theta_0 \end{aligned} \tag{35}$$

The real part of  $k_3$  is small enough to be neglected compared to its imaginary part.

$$k_3 = ik_{3I} \tag{36}$$

Nonlinear frequency equation from here,

$$(\omega_n)_{nl} = \omega_n + \varepsilon \frac{1}{4} k_{3I} a_{0n}^2 \tag{37}$$

The relationship between nonlinear natural frequency and amplitudes is shown in Figures. 4 to 7. The effect of the axial mean velocity for the first mode is shown in Figs 6 and 7 for  $\mu = 0.3$  and  $\mu = 0.5$ , respectively. These comparisons are again shown for  $v_k = 1$  in Fig. 8 and for the second mode in Fig. 9. Nonlinearities increase directly proportional to mean velocity. When  $v_k$  increase, nonlinearity decreases. When the mid-spring location is at  $\mu = 0.5$ , nonlinearity is increase according to  $\mu = 0.3$ .

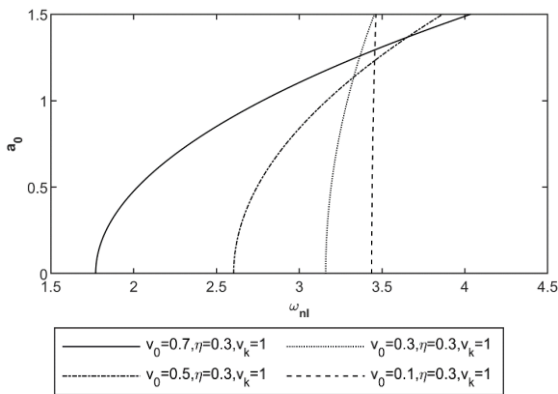


Figure 4. Nonlinear frequency-amplitude variation for axial mean velocity (mode 1).

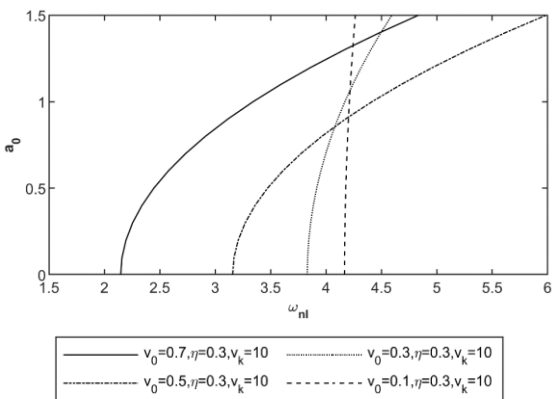


Figure 5. Nonlinear frequency-amplitude variation for axial mean velocity (mode 1).

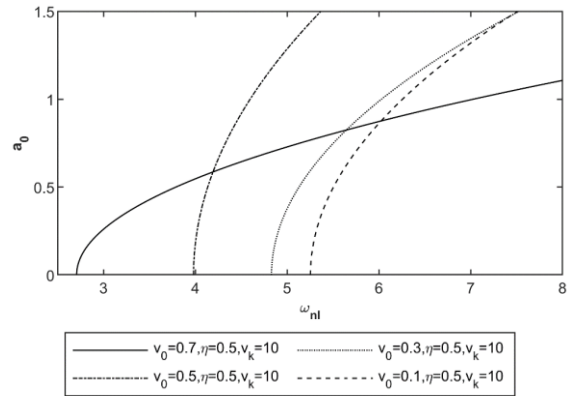


Figure 6. Nonlinear frequency-amplitude variation for axial mean velocity (mode 1).

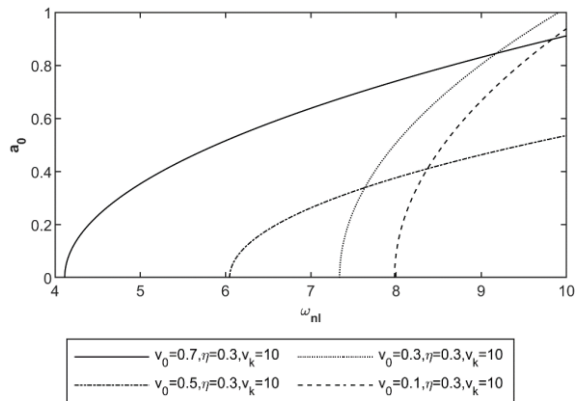


Figure 7. Variation of the amplitude with nonlinear frequency values for axial velocity (mode 2).

ii) *Principal parametric resonance:*

In this case, the velocity change frequency can be defined as follows;

$$\Omega = 2\omega_n + \varepsilon\sigma \tag{38}$$

From Equations. (28) and (29) solubility condition is obtained as follows

$$D_1 A + k_0 \bar{A} e^{i\sigma T_1} - k_3 A^2 \bar{A} = 0 \tag{39}$$

By inserting the amplitude definition in Equation (39) and divide it into real and imaginary parts.

$$\begin{aligned} a'_n &= a_n(k_{0I} \sin\gamma_n - k_{0R} \cos\gamma_n) \\ \gamma'_n &= \sigma + 2(k_{0R} \sin\gamma_n + k_{0I} \cos\gamma_n) - \frac{1}{2} k_{3I} a_n^2 \\ k_0 &= k_{0R} + ik_{0I}, \gamma_n = \sigma T_1 - 2\theta_n \end{aligned} \tag{40}$$

For stable regime  $a'_n$  and  $\gamma'_n$  can be assumed zero and hence;

$$\sigma_1 = \frac{1}{2} k_{3I} a_n^2 - 2\sqrt{k_{0R}^2 + k_{0I}^2} \tag{41}$$

$$\sigma_2 = \frac{1}{2} k_{3I} a_n^2 + 2\sqrt{k_{0R}^2 + k_{0I}^2} \tag{42}$$



where  $k_0$  is;

$$k_0 = \frac{1}{4} v_1 \frac{(\Omega - 2\omega_n) \left( \int_0^\eta \bar{Y}_1' \bar{Y}_1' dx + \int_\eta^1 \bar{Y}_2' \bar{Y}_2' dx \right) - 2iv_0 \left( \int_0^\eta \bar{Y}_1'' \bar{Y}_1 dx + \int_\eta^1 \bar{Y}_2'' \bar{Y}_2 dx \right)}{i\omega_n \left( \int_0^\eta Y_1 \bar{Y}_1 dx + \int_\eta^1 Y_2 \bar{Y}_2 dx \right) + v_0 \left( \int_0^\eta Y_1' \bar{Y}_1 dx + \int_\eta^1 Y_2' \bar{Y}_2 dx \right)} \quad (43)$$

We can write the complex amplitude in the form below (Equation (44)), inserting it into Equation (39) and divide it into real and virtual parts gives Equations (45) and (46);

$$A_n = \frac{1}{2} (p_n + iq_n) e^{i(\sigma T_1/2)} \quad (44)$$

$$p'_n = -k_{0R} p_n + \left( \frac{\sigma}{2} - k_{0I} \right) q_n - \frac{1}{4} k_{3I} q_n (p_n^2 + q_n^2) \quad (45)$$

$$= F_1(p_n, q_n)$$

$$q'_n = k_{0R} q_n - \left( \frac{\sigma}{2} + k_{0I} \right) p_n + \frac{1}{4} k_{3I} p_n (p_n^2 + q_n^2) \quad (46)$$

$$= F_2(p_n, q_n)$$

Hence the Jacobian matrix.

$$\begin{bmatrix} \partial F_1 / \partial p_n & \partial F_1 / \partial q_n \\ \partial F_2 / \partial p_n & \partial F_2 / \partial q_n \end{bmatrix}_{p_n=q_n=0} \quad (47)$$

and eigenvalues.

$$\lambda_{1,2} = \pm \sqrt{k_{0R}^2 + k_{0I}^2 - \frac{\sigma^2}{4}} \quad (48)$$

From here, the stability limits yields;

$$\sigma > 2\sqrt{k_{0R}^2 + k_{0I}^2}, \sigma < -2\sqrt{k_{0R}^2 + k_{0I}^2} \quad (49)$$

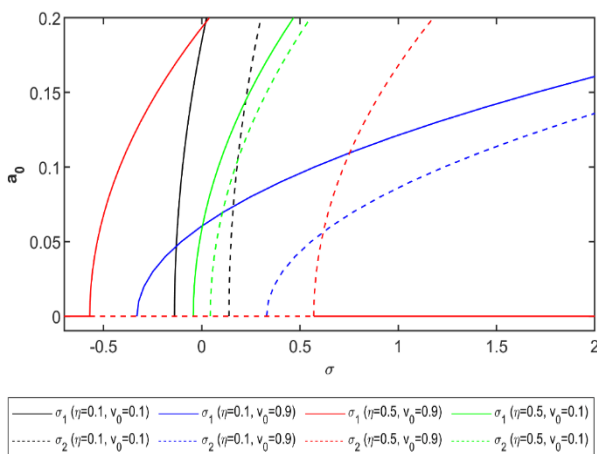


Figure 8. Variation of the aptitude with detuning parameter for different  $\mu$  locations and axial velocity.

In Figure 10, the changes of amplitudes depending on the detuning parameter are given comparatively. The unstable region increases with the spring velocity increase.  $\mu = 0.5$  has a smaller unstable region according to  $\mu = 0.1$  for low spring velocities but while spring velocity increasing this unstable region increases much more according to case  $\mu = 0.1$ .

### 4. Conclusions

The transverse vibrations of an axially moving string with spring-loaded middle support are discussed. From this study, we can see there is no perfect design for all conditions. The design of Spring mid-supported string must be made specifically for the location where it will be used, and selections should be made according to the following criteria.

- Increasing rigidity of the spring coefficient also increases the natural frequency of the string.
- While the string velocity increasing, the natural frequency decrease.
- When mid-support moves right, natural frequencies increase more significantly with the rigidity of the spring coefficient increase until center location.
- When  $v_k$  increase, nonlinearity decreases.
- When the mid-spring location is at  $\mu = 0.5$ , nonlinearity is increase according to  $\mu = 0.3$ .
- The unstable region increases with the velocity increase.
- The unstable region is smaller for  $\mu = 0.5$  according to  $\mu = 0.1$  for smaller low spring velocities but while spring velocity increasing this unstable region increases much more for  $\mu = 0.5$ .

### Declaration

The author(s) declared no potential conflicts of interest with respect to the research, authorship, and/or publication of this article. The author(s) also declared that this article is original, was prepared in accordance with international publication and research ethics, and ethical committee permission or any special permission is not required.

### Nomenclature

- $\mathcal{L}$  : Lagrangian.
- T : Kinetic energy.
- V : Potential energy.
- L : String Length.

$\rho$	: Constant density.
$A$	: Cross-section of string.
$E$	: Young's modulus.
$v_b$	: Longitudinal rigidity.
$v_k$	: The effect of the rigidity of the spring coefficient.
N.S.T.	: Non-secular terms.
$\sigma$	: The detuning parameter.

## References

1. Thurman, A. L., Mote, C.D., *Free, Periodic, Nonlinear Oscillation of an Axially Moving Strip*. Journal of Applied Mechanics, 1969. **36**(1): p. 83-91.
2. Ulsoy, A.G., Mote, C.D. Jr., and Syzmani, R., *Principal developments in band saw vibration and stability research*. Holz als Roh- und Werkstoff, 1978. **36**(7): p. 273-280.
3. Wickert, J.A., Mote, C.D. Jr., *Current research on the vibration and stability of axially moving materials*. Shock and Vibration Digest, 1988. **20**(5): p. 3-13.
4. Wickert, J.A., *Response solutions for the vibration of a traveling string on an elastic foundation*. Journal of Vibration and Acoustics, 1994. **116**(1): p. 137-139.
5. Nayfeh, A.H., Nayfeh, J.F., Mook, D.T., *On methods for continuous systems with quadratic and cubic nonlinearities*. Nonlinear Dynamics, 1992. **3**: p. 145-162.
6. Pellicano, F., Zirilli, F., *Boundary layers and non-linear vibrations in an axially moving beam*. International Journal of Non-Linear Mechanics, 1998. **33**(4): p. 691-711.
7. Kural, S., Özkaya, E., *Vibrations of an axially accelerating, multiple supported flexible beam*. Structural Engineering and Mechanics, 2012. **44**(4): p. 521-538.
8. Yurddaş, A., Özkaya, E., Boyacı, H., *Nonlinear vibrations and stability analysis of axially moving strings having nonideal mid-support conditions*. Journal of Vibration and Control, 2012. **20**(4): p. 518-534.
9. Pellicano F., *On the dynamic properties of axially moving system*. Journal of Sound and Vibration, 2005. **281**(3-5): p. 593-609.
10. Bağdatlı, S.M., Özkaya, E., Öz, H.R., *Dynamics of Axially Accelerating Beams with an Intermediate Support*. Journal of Vibration and Acoustics, 2011. **133**(3): 031013, 10 pages.
11. Ghayesh, M. H., Amabili, M. Païdoussis, M. P., *Nonlinear vibrations and stability of an axially moving beam with an intermediate spring support: two-dimensional analysis*. Nonlinear Dynamics, 2012. **70**(1): p. 335-354.
12. Nguyen, Q. C., Hong, K.S., *Simultaneous control of longitudinal and transverse vibrations of an axially moving string with velocity tracking*. Journal of Sound and Vibration, 2012. **331**(13): p. 3006-3019.
13. He, W., Ge, S. S., Huang, D., *Modeling and vibration control for a nonlinear moving string with output constraint*. IEEE/ASME Transactions on Mechatronics, 2015. **20**(4): p. 1886-1897.
14. Xia, C., Wu, Y., Lu, Q., *Experimental study of the nonlinear characteristics of an axially moving string*. Journal of Vibration and Control, 2015. **21**(16): p. 518-534.
15. Sun, W., Sun, Y., Yu, Y., Zheng, S., *Nonlinear vibration analysis of a type of tapered cantilever beams by using an analytical approximate method*. Structural Engineering and Mechanics, 2016. **59**(1): p. 1-14.
16. He, W., Nie, S., Meng, T., Liu, Y.-J., *Modeling and vibration control for a moving beam with application in a drilling riser*. IEEE Transactions on Control Systems Technology, 2017. **25**(3): p. 1036-1043.
17. Vetyukov, Y., *Non-material finite element modelling of large vibrations of axially moving strings and beams*. Journal of Sound and Vibration, 2018. **414**(3): p. 299-317.
18. Chen, E. , Li, M., Ferguson, N., Lu, Y., *An adaptive higher order finite element model and modal energy for the vibration of a traveling string*. Journal of Vibration and Control, 2018. **25**(5): p. 996-1007.
19. Zhao, Z., Ma, Y., Liu, G., Zhu, D., Wen, G., *Vibration Control of an Axially Moving System with Restricted Input*. Complexity, 2019. **2019**: Article ID 2386435, 10 pages.
20. Zhang, X., Pipeleers, G., Hengster-Movrić, K., Faria, C., *Vibration reduction for structures: distributed schemes over directed graphs*. Journal of Vibration and Control, 2019. **25**(14): p. 2025-2042.
21. Yılmaz, Ö , Aksoy, M , Kesilmiş, Z ., *Misalignment fault detection by wavelet analysis of vibration signals*. International Advanced Researches and Engineering Journal, 2019. **3**(3): p. 156-163.



## Research Article

# Turkish sign language digits classification with CNN using different optimizers

Onur Sevli <sup>a,\*</sup>  and Nazan Kemalöglü <sup>b</sup> 

<sup>a</sup>Burdur Mehmet Akif Ersoy University, Faculty of Engineering, Computer Engineering Department, 15030, Burdur, Turkey

<sup>b</sup>Burdur Mehmet Akif Ersoy University, Center of Information Technologies, 15030, Burdur, Turkey

### ARTICLE INFO

#### Article history:

Received 08 March 2020

Revised 25 May 2020

Accepted 10 July 2020

#### Keywords:

Convolutional neural networks

Sign language recognition

Turkish sign language

### ABSTRACT

Sign language is a way for hearing-impaired people to communicate among themselves and with people without hearing impairment. Communication with the sign language is difficult because few people know this language and the language does not have universal patterns. Sign language interpretation is the translation of visible signs into speech or writing. The sign language interpretation process has reached a practical solution with the help of computer vision technology. One of the models widely used for computer vision technology that mimics the work of the human eye in a computer environment is deep learning. Convolutional neural networks (CNN), which are included in deep learning technology, give successful results in sign language recognition as well as other image recognition applications. In this study, the dataset containing 2062 images consisting of Turkish sign language digits was classified with the developed CNN model. One of the important parameters used to minimize network error of the CNN model during the training is the learning rate. The learning rate is a coefficient used to update other parameters in the network depending on the network error. The optimization of the learning rate is important to achieve rapid progress without getting stuck in local minimums while reducing network error. There are several optimization techniques used for this purpose. In this study, the success of four different training and test processes performed with SGD, RMSprop, Adam and Adamax optimizers were compared. Adam optimizer, which is widely used today with its high performance, was found to be the most successful technique in this study with 98.42% training and 98.55% test accuracy.

© 2020, Advanced Researches and Engineering Journal (IAREJ) and the Author(s).

## 1. Introduction

Sign language is a unique communication method that enables hearing-impaired people to communicate with each other and people with no hearing impairment. Contrary to popular belief, there are no universal patterns of sign language that a limited number of people know today. Each society has its national sign language and differs from nation to nation [1]. This makes communication difficult. Hearing and speech impaired people have less writing skills, so choosing to write instead of sign language is not comfortable [2]. Sign languages are translated into spoken or written languages by other people who know that sign language. However, it becomes difficult due to the low number of people who know sign language and differences between sign languages. It is

necessary to translate sign languages among themselves and into normal speaking and writing languages practically and accurately.

Sign language translation process based on seeing with the human eye and interpreting has become feasible by computers with technological developments. This method, also known as computer vision, is a technology that provides fast results by imitating the work of the human eye in a computer environment [3]. The most preferred of the models using this technology today is deep learning, which is a sub-branch of machine learning. Deep neural networks are mathematical models of the human nervous system and consist of millions of configurable parameters. Convolutional neural networks (CNN), which is a sub-branch of deep learning, produce extremely successful results in image recognition and classification problems

\* Corresponding author. Tel.: +90-248-213-4130

E-mail addresses: [onursevli@mehmetakif.edu.tr](mailto:onursevli@mehmetakif.edu.tr) (O. Sevli), [nkemaloglu@mehmetakif.edu.tr](mailto:nkemaloglu@mehmetakif.edu.tr) (N. Kemalöglü)

ORCID: 0000-0002-8933-8395 (O. Sevli), 0000-0002-6262-4244 (N. Kemalöglü)

DOI: 10.35860/iarej.700564

and have been applied successfully in the recognition of human movements in recent years. The number of studies using CNN in the field of sign language recognition has been increasing recently.

Bheda and Radpour proposed a classifier CNN model for American Sign Language and achieved 82.5% accuracy [4]. Koller et al. presented a deep learning model that interprets sign language mouth shapes [5]. Huang et al. proposed a 3D CNN model for sign language recognition [6]. Pigou et al. achieved 91.7% accuracy in their CNN-based classification study for Italian sign language [7]. Hasan and Ahmad achieved 96.4% accuracy in their machine learning-based study on the Bengali sign language database consisting of 11 digits and 16 words [8]. Agarwal and Thakur classified the sign language dataset consisting of digits 0-9 using support vector machines [9]. Oyewole et al. used Principal Component Analysis and Artificial Neural Networks in their classification study for Nigerian sign language [10]. Besides, previous studies include classifications for Chinese [11], Korean [12], Albanian [13], Arabic [14-15], Mexican [16] and Tamil [17] sign languages.

Aran et al. ; developed a tool that teaches Turkish sign language. The system can recognize complex signs including both hand gestures and head gestures and expressions, and verbal and animated feedback is provided to the user. In performance tests, it was observed that the system showed 99% success in recognizing hand signals and 85% in recognizing head and facial expressions [21].

Beşer et al. classified the sign language dataset consisting of digits 0-9 that created by Ankara Ayrancı Anatolian High School students. The data was divided into 70% education and 30% test. In the study using Capsule

Neural Network for classification, a success of 94.52% was achieved [22].

Particle swarm optimization, artificial bee colony, and genetic algorithm were used for classification in the study with the same data set. As a result of the experimental studies, it was seen that the artificial bee colony gave the highest accuracy with a success of 98.09% [23].

In this study, a CNN model was developed for Turkish sign language analysis, and the dataset created by Ankara Ayrancı Anatolian High School students was classified. The dataset contains 2062 images of 10 different digits between 0 and 9. Four different optimizers were used to optimize the learning rate used in updating the parameters of the CNN network model, and the accuracy values of the four separate learning processes were compared. The following sections describe data set features, CNN architecture, learning rate optimization methods, experimental studies, and results.

## 2. Material and Method

### 2.1 Dataset

The dataset was created by 218 students studying at Ankara Ayrancı Anadolu High School and shared publicly [18]. The dataset contains 2062 images consisting of 10 digits between 0 and 9. Image examples from the data set are shown in Figure 1.

The main features of the dataset:

- Image sizes: 64x64
- Color space: Grayscale
- Number of classes: 10 (Digits: 0-9)



Figure 1. Image examples from the dataset

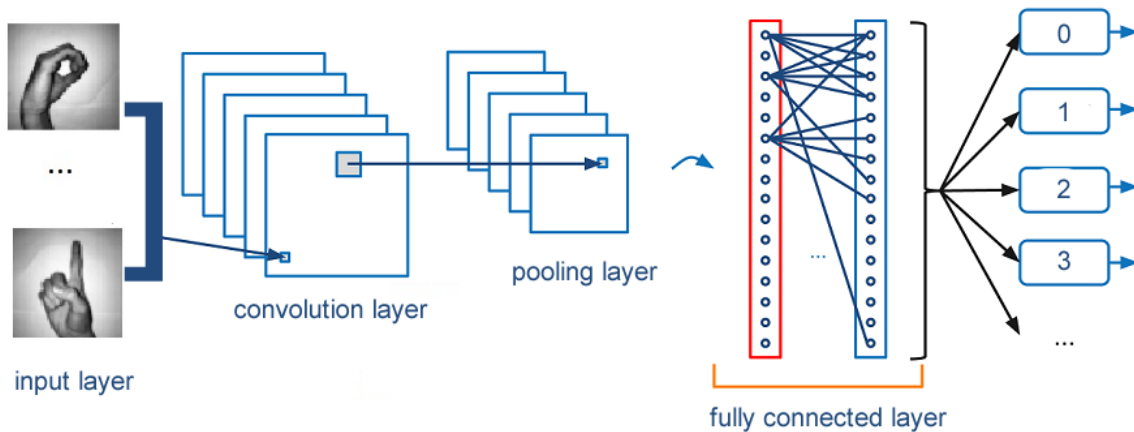


Figure 2. The general structure of CNN

## 2.2 Convolutional Neural Networks (CNN)

Machine learning is a sub-branch of artificial intelligence and it is a technique that enables machines to produce new solutions based on previous solutions. Artificial neural networks are mathematical models based on the functioning of the human brain. Deep learning is the processing of data in deep neural networks for feature extraction. One of the deep learning methods, CNN is used in computer vision, classification, recognition, regression, and many other fields. They are deep neural networks that have gained popularity with their success in image classification.

CNN is a computer vision technique that allows us to automatically extract and define features from images. It contains input, convolution, pooling, fully connected, and prediction layers. The general structure of CNN is shown in Figure 2.

The input layer consists of images to be processed. Convolution is the process of applying special filters on the image pixels and multiplying the input pixel values by the filter values. The image features are extracted with the help of the filters applied to the input.

Pooling is the reduction process performed on the input image matrix. It is carried out by taking the average or maximum values. A large number of pixels in the pool are reduced to a single value. The size of the image is reduced by moving the pool over all the image pixels. In this way, the image can be processed more efficiently. The average and maximum pooling processes with a 2x2 pool on the 4x4 input matrix are shown in Figure 3.

One of the other important parameters in neural networks is the activation function. The activation function increases the nonlinearity of the inputs and produces a stable result for the next layer. An appropriate activation function should be selected according to the procedure performed on the neural network.

The fully connected layer provides the transition to the neural network that will make the classification. The number of neurons in the output of the classification layer

must be the same as the number of classes in the dataset.

## 2.3 Learning Rate Optimization

One of the methods used to increase the CNN model performance is learning rate optimization. The learning rate is a coefficient used in updating the network parameters depending on the amount of error that occurs in the learning process of the network. If the learning rate is too small, network parameters are updated in very small steps and the process takes a long time. The high learning rate can cause the network to miss the optimum point that minimizes the error. Therefore, learning rate optimization is very important.

The learning rate is a dynamically adjusted parameter depending on the situation. Different optimization algorithms are used to optimize the learning rate. Stochastic Gradient Descent (SGD), RMSprop, Adam, and AdaMax are some of these optimizers.

SGD performs a parameter update for each training sample. It is usually a fast technique. It makes an update at every step. The high variance caused by frequent updates causes oscillations in the loss function. While this helps to find better local minimums, it can sometimes lead to missing the global minimum.

RMSprop is a gradient-based optimization technique. It offers a solution to the problem of reducing the learning rate excessively.

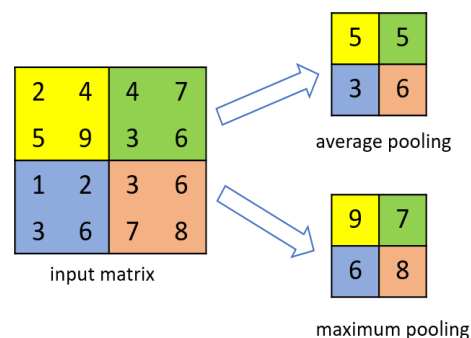


Figure 3. The pooling process

Instead of using all the values obtained from the squares of the past slopes, it restricted the amount [19]. RMSprop helps to reduce oscillations in the loss function.

Adam [20], is an adaptive learning rate optimization technique designed specifically to train deep neural networks. Adam is a combination of RMSprop and SGD, which are two other methods used in this field, with momentum. It is widely used because of the performance it provides.

AdaMax is the version of Adam optimizer that replaces the root mean square (RMS) feature with the infinity norm of previous gradients. AdaMax is generally suitable for infrequent parameter updates and noisy gradients.

Optimizers can perform differently for various situations, such as the data set used, the structure of the model created, and the classification type. It is necessary to choose the optimizer that gives the fastest and most accurate results according to the processed data and the model used.

### 3. Experimental Study

In this study, the performance of the CNN model created was evaluated comparatively using four different optimizers, namely SGD, RMSprop, Adam, and AdaMax, on the dataset consisting of digits in the Turkish sign language. 2602 images used were divided into 80% training and 20% test set. There were 1649 images in the training set and 413 images in the test set.

In this study, all models were coded with Python and run with GPU acceleration. The study was carried out on hardware with 32 GB RAM, Intel Core i7-9750H processor, NVIDIA GeForce RTX 2070 graphics card.

#### 3.1 The CNN Model

The CNN model created consists of 16 layers. The first layer is the input layer containing a total of 4096 pixels in 64x64 size for each image. The second layer is the convolution layer and contains 8 filters of 5x5 size. The third layer is the pooling layer with a pool size of 2x2. The fourth layer is the dropout layer that makes 25% of the neurons randomly passive. The fifth layer is the convolution layer and contains 16 filters of 3x3 size. The sixth layer is the pooling layer with a pool size of 2x2. The seventh layer is the dropout layer that makes 25% of the neurons randomly passive. The eighth layer is the convolution layer and contains 32 filters of 3x3 size. The ninth layer is the pooling layer with a pool size of 2x2. The tenth layer is the dropout layer that makes 25% of the neurons randomly passive. The eleventh layer is the convolution layer and contains 64 filters of 3x3 size. The twelfth layer is the pooling layer with a pool size of 2x2. The thirteenth layer is the dropout layer that makes 25% of the neurons randomly passive. The ReLU activation

function was used in all mentioned layers. The maximum pooling method was used in all the pooling layers.

The fully connected layer provides the transition to a 3-layer artificial neural network. The first layer consists of 128, the second layer 64, and the last layer, the output layer, consists of 10 neurons. The ReLU activation function was used in the first two layers, the softmax activation function was used in the output layer.

The summary of the CNN model created is shown in Table 1.

The model includes a total of 164,618 trainable parameters.

#### 3.2 Training and Results

In a neural network, the difference between predicted and actual values is called the error rate. Network parameters are updated depending on the error rate and in this way, the most accurate result is tried to be reached. The update parameters are multiplied by the learning rate to quickly reduce the error during the training process. The learning rate should be changed dynamically depending on the current error rate in the network. There are several optimization methods used for this job and it is important to choose the most ideal one.

The developed CNN model was trained four times, each using a different optimizer namely SGD, RMSprop, Adam, and AdaMax. Each training process took 100 epochs. The input batch size was 250 images. Accuracy and losses at the end of each training were reported.

*SGD optimizer:* As a result of 100 epochs, the training accuracy achieved with the SGD optimizer was 13% and the test accuracy was 7.7%. The confusion matrix obtained at the end of the training is shown in Figure 4.

Table 1. Summary of the CNN model created

Layer	Output Shape	Parameter
conv2d_1 (Conv2D)	(None, 64, 64, 8)	208
max_pooling2d_1	(None, 32, 32, 8)	0
dropbox_1 (Dropout)	(None, 32, 32, 8)	0
conv2d_2 (Conv2D)	(None, 32, 32, 16)	1168
max_pooling2d_2	(None, 16, 16, 16)	0
dropout_2 (Dropout)	(None, 16, 16, 16)	0
conv2d_3 (Conv2D)	(None, 16, 16, 32)	4640
max_pooling2d_3	(None, 8, 8, 32)	0
dropout_3 (Dropout)	(None, 8, 8, 32)	0
conv2d_4 (Conv2D)	(None, 8, 8, 64)	18496
max_pooling2d_4	(None, 4, 4, 64)	0
dropout_4 (Dropout)	(None, 4, 4, 64)	0
flatten_1 (Flatten)	(None, 1024)	0
dense_1 (Dense)	(None, 128)	131200
dense_2 (Dense)	(None, 64)	8256
dense_3 (Dense)	(None, 10)	650

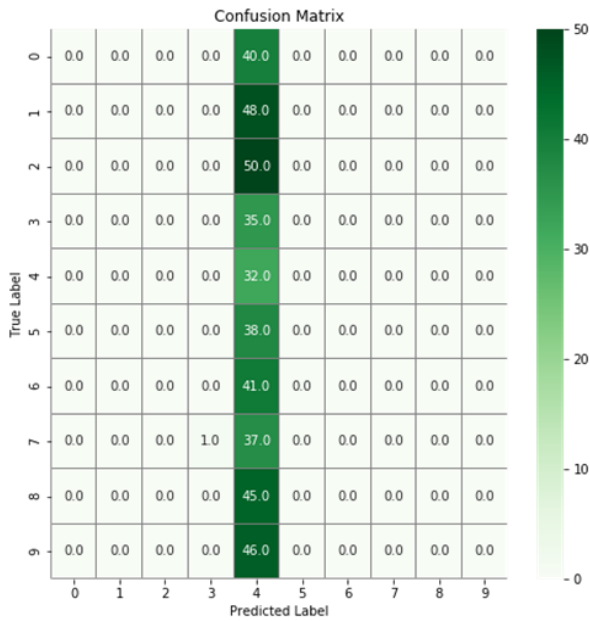


Figure 4. The confusion matrix of the SGD optimizer

As seen from the confusion matrix, the classification success of the model was extremely low. The accuracy and the loss graphics obtained with the SGD optimizer are shown in Figures 5 and 6.

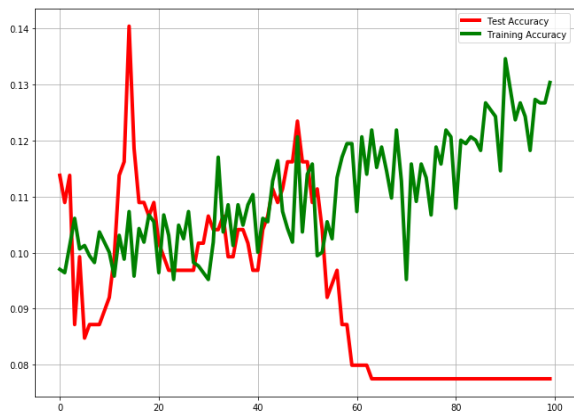


Figure 5. The accuracy graphics of the SGD optimizer

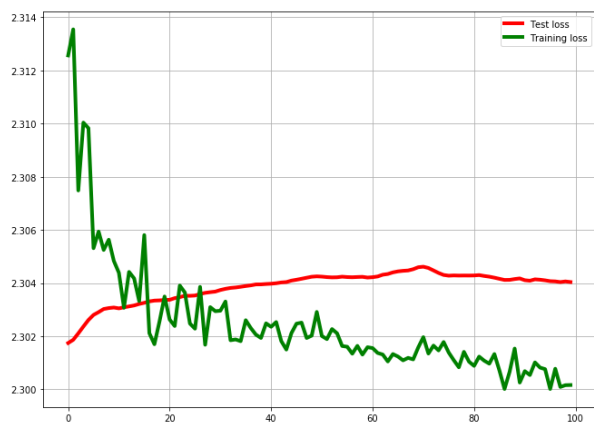


Figure 6. The loss graphics of the SGD optimizer

High variance arising from the frequent updating of the SGD optimizer is seen as an oscillation in the graphics. SGD often got stuck in local minimums. As a result of 100 epochs, it could not raise the accuracy and reduce the error quickly. Its performance was insufficient compared to the other optimizers used with an equal number of epochs.

*RMSprop:* As a result of 100 epochs, the training accuracy achieved with the RMSprop optimizer was 95.45% and the test accuracy was 96.85%. The confusion matrix obtained at the end of the training is shown in Figure 7.

As seen from the matrix, the model made quite accurate predictions. The accuracy and the loss graphics obtained with the RMSprop optimizer are shown in Figures 8 and 9.

RMSprop significantly increased success compared to SGD. There were still oscillations in the graphics, but they were greatly reduced. RMSprop quickly reduced the error while increasing accuracy.

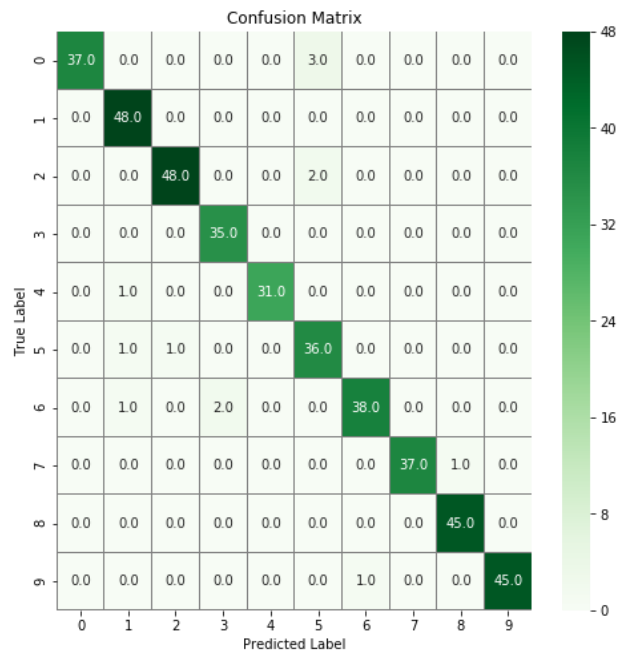


Figure 7. The confusion matrix of the RMSprop optimizer

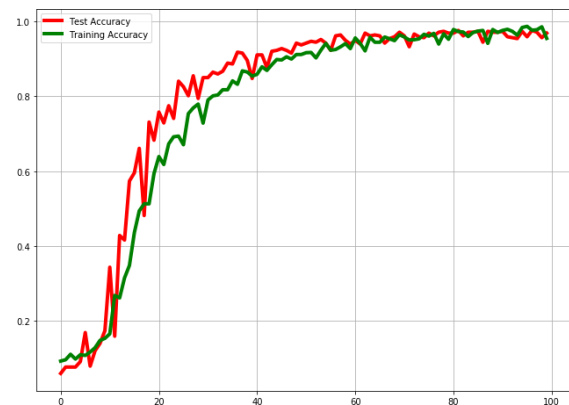


Figure 8. The accuracy graphics of the RMSprop optimizer



Figure 9. The loss graphics of the RMSprop optimizer

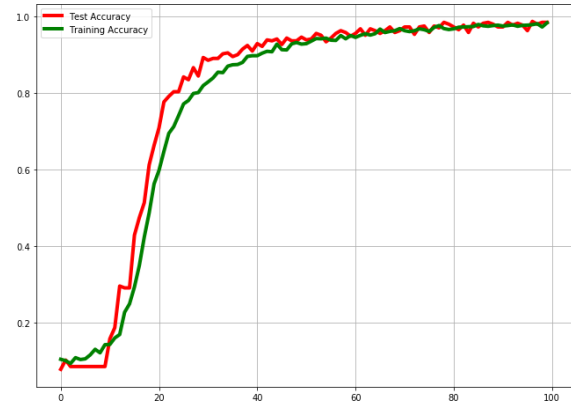


Figure 11. The accuracy graphics of the Adam optimizer

*Adam:* As a result of 100 epochs, the training accuracy achieved with the Adam optimizer was 98.42% and the test accuracy was 98.55%. The confusion matrix obtained at the end of the training is shown in Figure 10.

As can be seen from the matrix, the discrimination ability of the model with the Adam optimizer was quite high and the model made highly accurate predictions. The accuracy and the loss graphics obtained with the Adam optimizer are shown in Figures 11 and 12.

As seen from the graphics, the accuracy of the model with the Adam optimizer increased faster than the other optimizers. The error showed a faster descent with fewer oscillations.

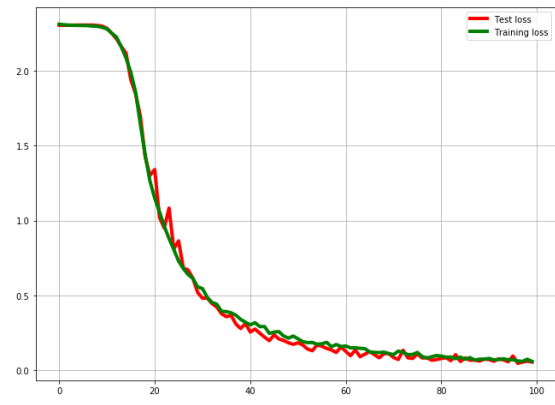


Figure 12. The loss graphics of the Adam optimizer

*Adamax:* As a result of 100 epochs, the training accuracy achieved with the Adamax optimizer was 89.81% and the test accuracy was 91.53%. The confusion matrix obtained at the end of the training is shown in Figure 13.

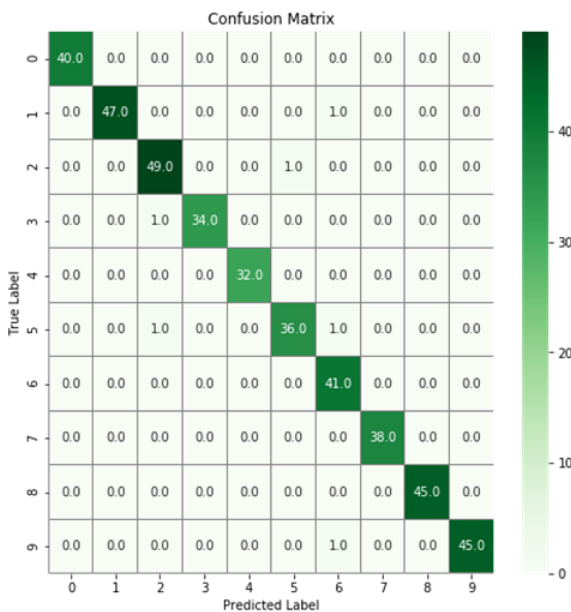


Figure 10. The confusion matrix of the Adam optimizer

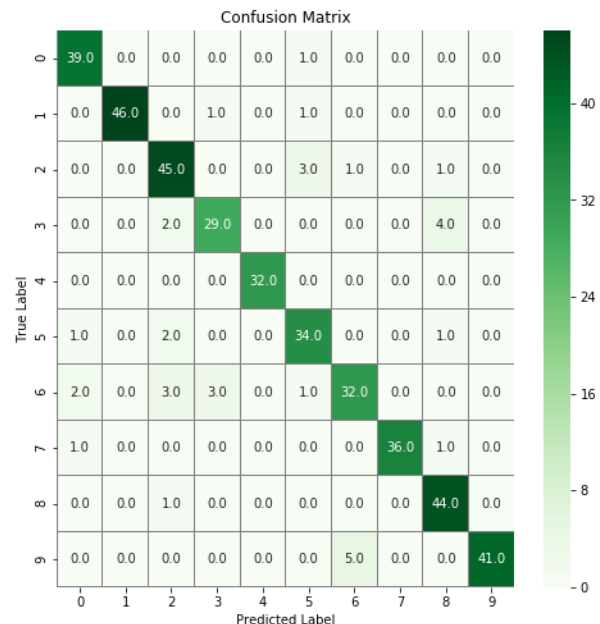


Figure 13. The confusion matrix for the Adamax optimizer

According to the matrix, Adamax had a successful discrimination and classification accuracy, although it was lower than Adam and RMSprop. The accuracy and the loss graphics obtained with the Adamax optimizer are shown in Figures 14 and 15.



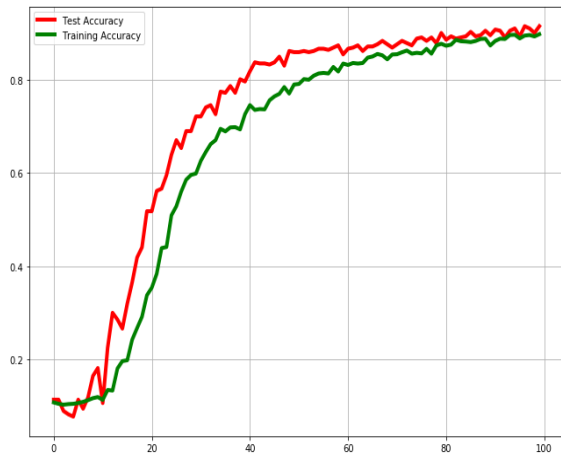


Figure 14. The accuracy graphics for the Adamax optimizer

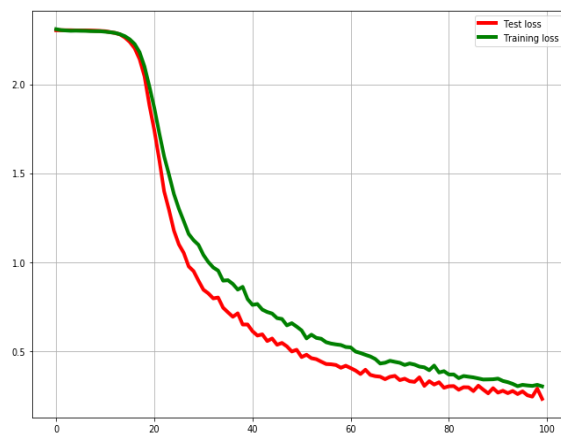


Figure 15. The loss graphics for the Adamax optimizer

Table 2. Accuracy values of the CNN model with different optimizers

Optimizer	Training Accuracy	Test Accuracy
SGD	% 13	% 7.7
RMSprop	% 95.45	% 96.85
Adam	% 98.42	% 98.55
Adamax	% 89.81	% 91.53

According to the graphs, although Adamax provides partially lower accuracy compared to Adam and RMSprop, the graphics oscillated less than RMSprop. Adamax has reached similar accuracy levels in a longer period than Adam.

As a result of 100 epochs, the training and test accuracies of the CNN model created with different optimizers are summarized in Table 2.

The Adam optimizer provided higher accuracy in both training and test stages than the other three optimizers used. The Adam optimizer, which is widely used in the field of deep learning due to its performance, also showed the highest performance in this study. There was also consistency between the training and test accuracies of Adam optimizer. The SGD optimizer got stuck in local

minimums at the stage of minimizing the error with frequent updates and performed lower than other optimizers at equal epoch values. The RMSprop optimizer provided a close performance to Adam and less oscillation than SGD. The Adamax optimizer performed lower than RMSprop in terms of accuracy values but it was more consistent with fewer oscillations.

#### 4. Conclusions

Sign language plays an important role in the communication of hearing-impaired people among themselves and with people without hearing impairments. However, there are problems in communication due to the differences between sign languages and the low number of people who know sign language. Sign language interpretation is done by converting visible body signs into speech or written language. Computer vision applications imitating the human eye offer a technological solution in this field.

CNN, which is a deep learning technology, has great success, especially in image classification. CNN models are trained with existing images, allowing them to predict different situations in the future. To reduce the estimation error, the parameters used in the CNN network need to be finely adjusted. One of these parameters is the learning rate. The learning rate is a coefficient used to update network parameters depending on the error that occurs in a neural network. Optimization is required so that the learning rate does not get stuck in the local minimum points while reducing the network error. There are various optimizers used for this purpose that perform different performances on different models and datasets.

With the CNN model developed in this study, 2062 images consisting of the digits in Turkish sign language were classified. The CNN model was trained four times using four different optimizers and the performance of each stage was evaluated. The optimizers used are SGD, RMSprop, Adam, and Adamax. In terms of training and test accuracy, Adam optimizer performed best. The CNN model we have established has achieved a remarkable success among the studies conducted on the same dataset with a 98.55% success rate. In the following studies, a larger database including gestures related to Turkish sign language will be created and model success will be tested with a similar CNN model and different optimizers.

#### Declaration

The author(s) declared no potential conflicts of interest with respect to the research, authorship, and/or publication of this article. The author(s) also declared that this article is original, was prepared in accordance with international publication and research ethics, and ethical committee permission or any special permission is not required.

## References

1. Oral, A. Z., *Türk işaret dili çevirisi*. 2016, Ankara.
2. Van Herreweghe, M. *Prelingual dove jongeren en nederlands: een syntactisch onderzoek*. 1996. PhD Thesis. Ghent University.
3. Alkoffash, M. S., Bawaneh, M. J., Muaidi, H., Alqrainy, S., and Alzghool, M. *A survey of digital image processing techniques in character recognition*. International Journal of Computer Science and Network Security (IJCSNS), 2014. 14(3): p. 65.
4. Bheda, V., and Radpour, D., *Using deep convolutional networks for gesture recognition in American sign language*. arXiv preprint arXiv:1710.06836, 2017.
5. Koller, O., Ney, H., and Bowden, R., *Deep learning of mouth shapes for sign language*. In Proceedings of the IEEE International Conference on Computer Vision Workshops, 2015. p. 85-91.
6. Huang, J., Zhou, W., Li, H., and Li, W., *Sign language recognition using 3d convolutional neural networks*. In 2015 IEEE international conference on multimedia and expo (ICME), 2015. p. 1-6.
7. Pigou, L., Dieleman, S., Kindermans, P. J., and Schrauwen, B., *Sign language recognition using convolutional neural networks*. In European Conference on Computer Vision, 2014. p. 572-578.
8. Hasan, S. K., and Ahmad, M., *A new approach of sign language recognition system for bilingual users*. In 2015 International Conference on Electrical & Electronic Engineering (ICEEE), 2015. p. 33-36.
9. Agarwal, A., and Thakur, M. K., *Sign language recognition using Microsoft Kinect*. In 2013 Sixth International Conference on Contemporary Computing (IC3), 2013. p. 181-185.
10. Oyewole, O. G., Nicholas, G., Oludele, A., and Samuel, O., *Bridging Communication Gap Among People with Hearing Impairment: An Application of Image Processing and Artificial Neural Network*. International Journal of Information and Communication Sciences, 2018. 3(1): p. 11.
11. Wang, C., Gao, W., and Xuan, Z., *A real-time large vocabulary continuous recognition system for chinese sign language*. In Pacific-Rim Conference on Multimedia, 2001. p. 150-157.
12. Kim, J. S., Jang, W., and Bien, Z., *A dynamic gesture recognition system for the Korean sign language (KSL)*. IEEE Transactions on Systems, Man, and Cybernetics, Part B (Cybernetics), 1996. 26(2): p. 354-359.
13. Gani, E., & Kika, A., *Albanian Sign Language (AlbSL) Number Recognition from Both Hand's Gestures Acquired by Kinect Sensors*. arXiv preprint arXiv:1608.02991, 2016.
14. Assaleh, K., and Al-Rousan, M., *Recognition of Arabic sign language alphabet using polynomial classifiers*. EURASIP Journal on Advances in Signal Processing, 2005. 13: p. 507614.
15. Assaleh, K., Shanableh, T., Fanaswala, M., Bajaj, H., and Amin, F., *Vision-based system for continuous Arabic Sign Language recognition in user dependent mode*. In 2008 5th International Symposium on Mechatronics and Its Applications, 2008. p. 1-5.
16. Solís, F., Martínez, D., and Espinoza, O., *Automatic mexican sign language recognition using normalized moments and artificial neural networks*. Engineering, 2016. 8(10): p. 733-740.
17. Rajam, P. S., and Balakrishnan, G., *Recognition of tamil sign language alphabet using image processing to aid deaf-dumb people*. Procedia Engineering, 2012. 30: p. 861-868.
18. Turkey Ankara Ayrancı Anadolu High School's Sign Language Digits Dataset, <https://www.kaggle.com/ardamavi/sign-language-digits-dataset>. Web. 10 Jan 2020.
19. Gazel, S. E. R., and batı, C. T., *Derin Sinir Ağları ile En İyi Modelin Belirlenmesi: Mantar Verileri Üzerine Keras Uygulaması*. Yüzcüncü Yıl Üniversitesi Tarım Bilimleri Dergisi, 29(3): p. 406-417.
20. Kingma, D. P., and Ba, J., *Adam: A method for stochastic optimization*. arXiv preprint arXiv:1412.6980, 2014.
21. Aran, O., Keskin, C., and Akarun, L., *Sign language tutoring tool*. In 2005 13th European Signal Processing Conference, 2005. pp. 1-4.
22. Beşer, F., Kızrak, M. A., Bolat, B., and Yildirim, T., *Recognition of sign language using capsule networks*. In 2018 26th Signal Processing and Communications Applications Conference (SIU), 2018. p. 1-4.
23. Ozcan, T., and Basturk, A., *Transfer learning-based convolutional neural networks with heuristic optimization for hand gesture recognition*. Neural Computing and Applications, 2019. 31(12): p. 8955-8970.

**Research Article****Analysis of parameter changes of a neuronal network model using transfer entropy****Sevgi Şengül Ayan <sup>a,\*</sup> and Deniz Gençağa <sup>b</sup>** <sup>a</sup>*Department of Industrial Engineering, Antalya Bilim University, Antalya 07190, Turkey*<sup>b</sup>*Department of Electrical and Electronics Engineering, Antalya Bilim University, Antalya 07190, Turkey*

## ARTICLE INFO

*Article history:*

Received 02 June 2020

Revised 20 July 2020

Accepted 29 July 2020

*Keywords:*

Hodgkin-huxley network

Parameter analysis

Transfer entropy

## ABSTRACT

Understanding the dynamics of coupled neurons is one of the fundamental problems in the analysis of neuronal model dynamics. The transfer entropy (TE) method is one of the primary analyses to explore the information flow between the neuronal populations. We perform the TE analysis on the two-neuron conductance-based Hodgkin-Huxley (HH) neuronal network to analyze how their connectivity changes due to conductances. We find that the information flow due to underlying synaptic connectivity changes direction by changing conductances individually and/or simultaneously as a result of TE analysis through numerical simulations.

© 2020, Advanced Researches and Engineering Journal (IAREJ) and the Author(s).

**1. Introduction**

Neuronal action potentials are the basic units of brain activity but how millions of neurons adjust their interactions remains an open problem. Different patterns of synchronization behavior have been observed by the excitable cells after an applied stimulation or during spontaneous activity [1-3]. These synchronizations have been observed in different sensory tasks including visual [4], auditory [5] as well as in the motor system [6]. Some pathological conditions in brain activity are related to the disturbance of the synchronization patterns [7]. Once the dynamics of the synchronization changes, the pattern activity between neurons change mostly due to the communication between the ion channels. However, the effects of the ion channels on the information transfer are still unclear. We approach this question with a statistical measure called transfer entropy.

Transfer entropy is a non-parametric statistical measure capable of capturing nonlinear source-destination relations between multi-variate time series [8-9]. Data recorded from neurons involve generally one or more variables and the interactions between these variables are highly nonlinear. So, applying the transfer entropy method is fit

to analyze these types of neuronal data. Directed information methods like transfer entropy reveal an analytical difference between the direction of the information flow between the neurons in a network. We perform the TE analysis on the two-neuron conductance-based Hodgkin-Huxley (HH) neuronal network to obtain how their connectivity changes due to conductances.

It has been shown that the relationship between the parameters including ionic conductances, applied current, or coupling constant of a neuron affects the pattern of synchronization [10-11]. However, analyzing the roles of intrinsic ionic conductances in information transfer is limited. Most neurons involve voltage-gated currents together with background ‘passive’ currents and we will be focusing on their influence on information flow [12]. To the best of our knowledge there have been no works detailing how ionic conductances can tune the direction of information flow between the neurons in a neuronal network.

Conductance-based models have been used to generate the spiking activity of electrically excitable cells including heart cells, pancreatic-beta cells and neurons and it has proved itself as a very successful tool to mimic the spiking activity and analyze the systems deeply [13-15].

\* Corresponding author. Tel.: +90-242-245-00-00.

E-mail addresses: [sevgi.sengul@antalya.edu.tr](mailto:sevgi.sengul@antalya.edu.tr) (S. Şengül), [deniz.gençaga@antalya.edu.tr](mailto:deniz.gençaga@antalya.edu.tr) (D. Gençağa)

ORCID: 0000-0003-0083-4446 (S. Şengül), 0000-0003-0065-172X (D. Gençağa)

DOI: 10.35860/iarej.747142

Mathematical models of the neurons can contain many free parameters that drive the activity pattern such as the maximal conductances of the different ionic currents, applied current, the coupling constant, or noise strength [16]. These parameters should be determined either by experimental measurements or by simulations of complex optimization problems until the model performs truly. However, conductances of real neurons are not constant parameter, they can change with the changing activity of the cell according to the intrinsic dynamics of the currents [17]. We focus on the effects of the maximal conductances in a coupled Hodgkin-Huxley neuronal network that we defined. In our model, the coupling is defined from Neuron 1 to Neuron 2 and in the system, while Neuron 1 is spiking due to the applied current, Neuron 2 is spiking due to the coupling from Neuron 1. In this network, there are two negative feedback variables for each neuron. The activation of a  $K^+$  current (n) responsible for the upstroke of an impulse together with the inactivation of the  $Na^+$  currents (h) provides negative feedback to the system. On the other hand,  $Na^+$  current activation (m) responsible for starting the spiking activity provides positive feedback for each neuron in our network model.

Here, we explore the activities of voltage-gated  $Na^+$ ,  $K^+$  channels, and passive leak ion channels using a Hodgkin-Huxley-type model network. For a coupled HH model, we show that the activities due to the changes in the conductance parameters of these channels manifest themselves as variations of the synchrony of the action potentials and the spike intervals of the coupled system. Due to these changes, the roles of the affecting and the affected neurons can easily switch, causing a change of direction in coupling. In order to explore this phenomenon from data, we propose the utilization of transfer entropy, which is a non-parametric information theoretic quantity used to detect the direction of the statistical interactions between two variables, even if they are nonlinearly dependent as in this application. We show that we can detect any change in the direction between the affected and the affecting neurons and demonstrate this as a function of changing conductance values.

Our findings are important in terms of understanding the changes in channel activation/inactivation properties as a result of changes in channel densities which can reveal the physiological or pathological situations affecting the neuronal network activity in the way neurons respond to changes in conductances.

## 2. Methods

In this work, we focus on the analysis of a network of two coupled neurons using the HH model system and apply the transfer entropy method to this model with changing maximal conductances. We studied the effects of varied potassium, sodium, and leak conductances on

transfer entropy in two populations of conductance-based model neurons.

### 2.1 Transfer Entropy

An effective mathematical modeling of a physical phenomenon is of utmost importance to better understand and describe the factors and their relationships causing it. In statistics and machine learning, many methods, such as regression and neural networks, have been utilized in science and engineering for this purpose. In addition to modeling, information theory has let us to quantify the interactions between different variables and/or model parameters using data. In particular, Shannon entropy is an information theoretical quantity to describe the average uncertainty of a system, model or a parameter and it is defined by the following equation:

$$H(V) = -\sum_{v \in V} p(v) \log(p(v)). \quad (1)$$

where  $H$  denotes the entropy of a random variable “ $V$ ” and  $p(v)$  represents its probability density function (pdf). Using this main concept, other information theoretical quantities, like the Shannon entropy, Mutual Information (MI), Kullback-Leibler divergence and Transfer Entropy (TE), are defined in the literature [18-19]. Among these, MI is used to quantify the "amount of information" obtained about one random signal through observing the other random signal, which can be expressed by the following equation:

$$MI(V_1, V_2) = \sum_{v_1 \in V} \sum_{v_2 \in V} p(v_1, v_2) \log \frac{p(v_1, v_2)}{p(v_1)p(v_2)}, \quad (2)$$

where  $MI(V_1, V_2)$  denotes the mutual information between random variables  $V_1$  and  $V_2$ . Above, it is observed that this quantity is defined in terms of the pdf of random variables and becomes zero for the statistical independence case, i.e.  $p(v_1, v_2) = p(v_1)p(v_2)$ . MI can be utilized to identify nonlinear relationships among random variables, whereas the correlation coefficient  $\rho$  is optimal as long as there is a linear relationship. MI between two variables can also be expressed as a summation of Shannon entropies as shown below:

$$MI(V_1, V_2) = H(V_1) + H(V_2) - H(V_1, V_2), \quad (3)$$

where  $H(V_1, V_2)$  is the joint Shannon entropy. Here, we note that  $MI(V_1, V_2) = MI(V_2, V_1)$ , meaning that MI is a symmetric measure. Therefore, if we would like to identify the direction of information flow from one variable to another, MI is not a sufficient approach. Instead, Schreiber [19] proposed another information theoretical quantity, called Transfer Entropy, which is capable of detecting the direction, i.e. either  $V_1$  effects  $V_2$ , or  $V_2$  effects  $V_1$ , for two variables. In the literature, the affecting variable is generally known as the “source” and the affected variable is known as the “target” variable. The TE in two directions are calculated from data by using the following equations:

$$TE_{V_1 V_2} = T(V_{2(i+1)} | V_{2(i)}^{(k)}, V_{1(i)}^{(l)}) = \sum_{v_{2(i+1)}, v_{2(i)}^{(k)}, v_{1(i)}^{(l)}} p(v_{2(i+1)}, v_{2(i)}^{(k)}, v_{1(i)}^{(l)}) \log_2 \frac{p(v_{2(i+1)} | v_{2(i)}^{(k)}, v_{1(i)}^{(l)})}{p(v_{2(i+1)} | v_{2(i)}^{(k)})} \quad (4)$$

$$TE_{V_2 V_1} = T(V_{1(i+1)} | V_{1(i)}^{(k)}, V_{2(i)}^{(l)}) = \sum_{v_{1(i+1)}, v_{1(i)}^{(k)}, v_{2(i)}^{(l)}} p(v_{1(i+1)}, v_{1(i)}^{(k)}, v_{2(i)}^{(l)}) \log_2 \frac{p(v_{1(i+1)} | v_{1(i)}^{(k)}, v_{2(i)}^{(l)})}{p(v_{1(i+1)} | v_{1(i)}^{(k)})} \quad (5)$$

where  $(i + 1)$  is an index for the leading time instant and  $(i)$  is an index for the current time. Above,  $v_{1(i)}^{(k)} = \{v_{1(i)}, \dots, v_{1(i-k+1)}\}$  shows the vector including the value of  $V_1$  at time instant  $(i)$  and its values at  $(k - 1)$  preceding time instants. Similarly,  $v_{2(i)}^{(l)} = \{v_{2(i)}, \dots, v_{2(i-l+1)}\}$  denotes the vector including the value of  $V_2$  at time instant  $(i)$  and its values at  $(l - 1)$  leading time instants. Here,  $V_1$  shows the  $k$ -th order and  $V_2$  shows the  $l$ -th order Markov processes. In the literature,  $k$  and  $l$  are also referred as the embedding dimensions. In our simulations, one past value of each signal is taken into consideration by assuming  $k = l = 1$  during TE analysis. In this case, TE can be estimated by the marginal and joint Shannon entropies as follows:

$$TE_{V_2 V_1} = T(V_{1(i+1)} | V_{1(i)}, V_{2(i)}) = H(V_{1(i)}, V_{2(i)}) - H(V_{1(i+1)}, V_{1(i)}, V_{2(i)}) + H(V_{1(i+1)}, V_{1(i)}) - H(V_{1(i)}) \quad (6)$$

In order to analyze the effect of change in conductance parameters, we utilize TE as defined above. In these equations, we note that the pdf's of variables need to be estimated from data first. Here, utilized histogram based estimations to infer the multivariate pdf's given above. To do this, both source and target data are separated into certain number of bins and the frequency of data in each volume element is used as the pdf estimate [20-21]. As an example, we illustrate the joint probability density estimate,  $\hat{p}(V_{1(i)}, V_{2(i)})$ , of two action potential data, using 10 and 100 bins for the marginal and joint histograms, respectively, in Figure 1. In order to judge if the estimated values are significant, we utilize a surrogate data testing with a p-value of 0.05.

The rest of the approach proceeds as follows: The probability density function of each term in (6) is estimated by the illustrated histogramming given above and the following entropy terms are obtained using (1) and its multivariate versions:

$H(V_{1(i)}, V_{2(i)}), H(V_{1(i+1)}, V_{1(i)}, V_{2(i)}), H(V_{1(i+1)}, V_{1(i)}), H(V_{1(i)})$ . Finally, TE from  $V_2$  to  $V_1$  is computed by the substitution of these in (6). The procedure is shown in the Figure 2.

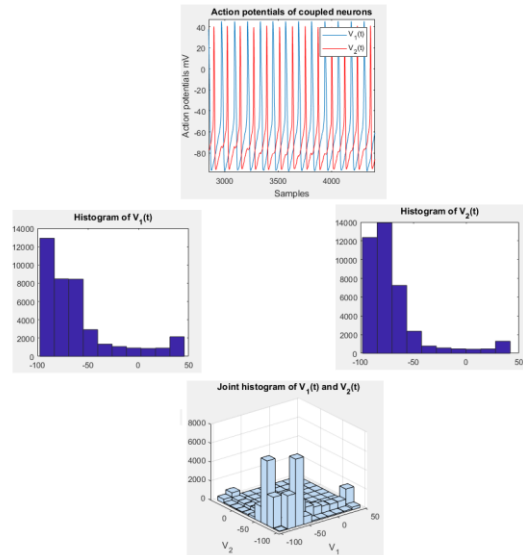


Figure 1. Probability density estimation from neuron action potential data using histograms.

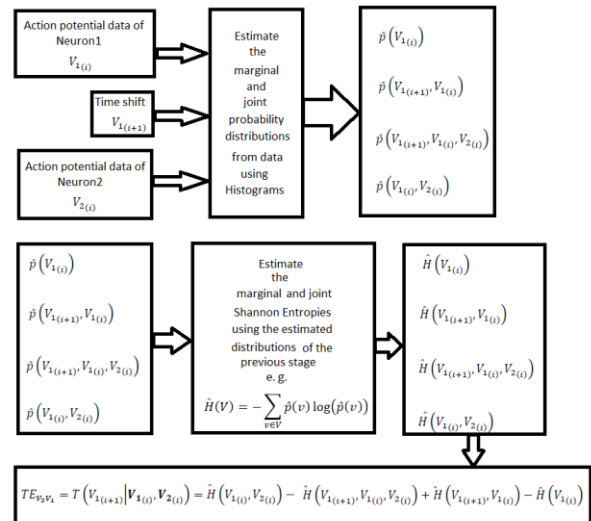


Figure 2. The block diagram of the proposed approach.

### 2.2 Model

Neurons are electrically excitable cells and responsible for the information transfer in our body through electrical signals called action potentials or spikes. Hodgkin and Huxley (HH) defined a first mathematical model that explains the generation of spikes using a nonlinear differential equation system [22].  $K^+$  and  $Na^+$  ions together with the  $Cl^-$  ions are mainly responsible for the electrical behavior of the HH system. We consider a Hodgkin-Huxley type model describing the activity of two coupled neuronal network with coupling corresponds to that of an electrical synapse as shown in Figure 3. Electrical synapses are specific sites where gap junction channels bridge the plasma membrane of two neurons. Gap junction is a gap between the pre- and post-synaptic neurons and impulse in here are transmitted in both directions [23]. So we define the coupling is proportional to the difference between the pre-synaptic and postsynaptic membrane potentials.

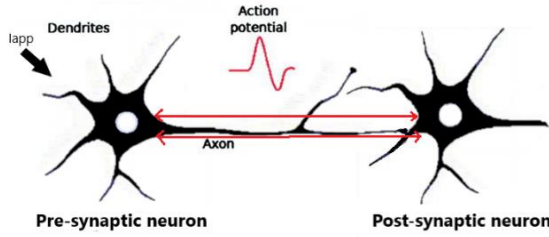


Figure 3. Model configuration for two-neuron Hodgkin-Huxley network

The differential equations for the rate of change of voltage  $V_1$  and  $V_2$  for these neurons are given as follows:

$$C_m \frac{dV_1}{dt} = I_{app} - I_{Na,1} - I_{K,1} - I_{L,1}, \quad (7)$$

$$C_m \frac{dV_2}{dt} = -I_{Na,2} - I_{K,2} - I_{L,2} - k(V_1 - V_2) \quad (8)$$

where  $C_m$  is the membrane capacitance,  $I_{app}$  is the applied current. Here,  $I_{Na,i}$  is the fast sodium current,  $I_{K,i}$  is the delayed rectifying potassium current and  $I_{L,i}$  is the leak current that all measured in  $\frac{\mu A}{cm^2}$  for  $i = 1, 2$ . Coupling between the two neurons is simply defined by voltage difference as  $k(V_1 - V_2)$  and coupling strength is  $k$ .

In our HH network model, ionic currents for each neuron  $x = 1, 2$  are defined as follows:

$$I_{Na,x} = \bar{g}_{Na,x} m^3 h (V_x - V_{Na}), \quad (9)$$

$$I_{K,x} = \bar{g}_{K,x} n^4 (V_x - V_K), \quad (10)$$

$$I_{L,x} = \bar{g}_{L,x} (V_x - V_L). \quad (11)$$

$V_{Na}$ ,  $V_K$ ,  $V_L$  are the reversal potentials associated with the currents. Here  $m$  represents the  $Na^+$  activation and  $h$  represents the inactivation of the channel.  $n$  is the activation variable of the  $K^+$  current. Here  $\bar{g}_x$  denotes the maximal conductances. Gating functions of the ion channels defined with activation and inactivation dynamics and changing with time according to the differential equations below:

$$\frac{dx}{dt} = \frac{x_\infty(V) - x}{\tau_x(V)}, \quad x = m, h, n. \quad (12)$$

The equilibrium activation and inactivation functions are defined as follows;

$$x_\infty(V) = \frac{\alpha_x(V)}{\alpha_x(V) + \beta_x(V)}, \quad x = m, h, n, \quad (13)$$

where ( $\tau_x$ ) shows the time that the channel needs to reach the equilibrium. Time constants in our network model are defined as:

$$\tau_x(V) = \frac{1}{\alpha_x(V) + \beta_x(V)}, \quad x = m, h, n. \quad (14)$$

Table 1 contains the information on the transition rates  $\alpha_x$  and  $\beta_x$  and the parameter values used to simulate the network.

Table 1. Transition rates and parameter values for the coupled two-neuron network model.

Transition rates ( $ms^{-1}$ )		
$\alpha_m$	$0.1(40 + V)/(1 - \exp(-(55 + V)/10))$	
$\beta_m$	$4 \exp(-(65 + V)/18)$	
$\alpha_h$	$0.07 \exp(-(65 + V)/20)$	
$\beta_h$	$1/(1 + \exp(-(35 + V)))$	
$\alpha_n$	$0.01(55 + V)/(1 - \exp(-(10V + 55)))$	
$\beta_n$	$0.125 \exp(-(V + 65)/80)$	
Parameter values		
$C_m = 1 \mu F$	$V_{Na} = 50 mV$	$g_{Na} = 120 \mu S$
$I_{app} = 8 mA$	$V_K = -77 mV$	$g_K = 36 \mu S$
$k = 0.25$	$V_L = -54.4 mV$	$g_L = 0.3 \mu S$

### 2.3 Simulation:

Model network is solved by XPPAUT software [24] using a 4th order Runge-Kutta solver with a time step of 0.001ms and the application of the transfer entropy method is simulated by the MATLAB software. Initial values for the simulations are considered as:  $V_1 = V_2 = -65$ ,  $m_1 = m_2 = 0.05$ ,  $h_1 = h_2 = 0.6$  and  $n_1 = n_2 = 0.317$ .

## 3. Results

Varying ionic conductances have an effect on the cell's electrical activity and understanding the underlying reason is biologically crucial. Here, we investigate this by focusing on three conductances that are available in the Hodgkin-Huxley neuronal network model. Here, the defined coupled neurons show phase-locked spiking. By definition, the Neuron 1 is spiking due to applied current and the Neuron 2 is spiking due to the coupling from Neuron 1. So originally the direction of the information flow is defined from Neuron 1 to Neuron 2 (1-to-2). We both independently change the conductances of each current separately and the same currents' conductances simultaneously under the observation of the amount of information flow. For all cases, we simulate transfer entropy analysis over the ranges of  $g_x$  parameters for which the model network exhibits tonic spiking and analyzes whether the order of the information flow changes due to the strength of the maximal conductances or not.

### 3.1 The effects of changing maximal potassium conductances in the model

Altering the kinetic properties of  $K^+$  current in the HH model is known to alter the spike duration and interspike interval [15]. And the maximal  $K^+$  conductances  $g_{K1}$  and  $g_{K2}$  in our coupled two-neuron network model measures the amount of subtractive feedback to the system from each neuron. So here we ask whether the information flow changes the direction by changing the amount of subtractive feedback with altering the conductances separately ( $g_{K1}$  or  $g_{K2}$ ) and simultaneously ( $g_{K1}$  and  $g_{K2}$ ).

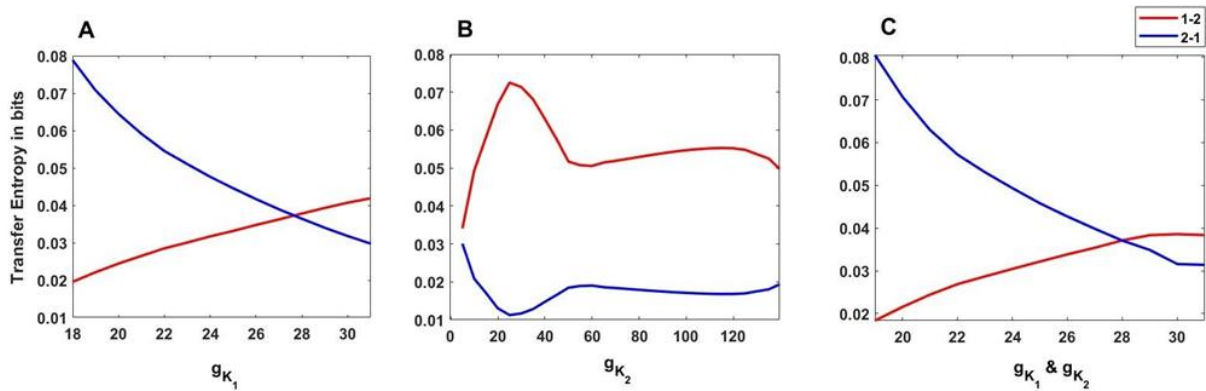


Figure 4. Transfer entropy results with changing a)  $g_{K1}$ , maximal conductance of  $K^+$  current for Neuron 1 b)  $g_{K2}$ , maximal conductance of  $K^+$  current for Neuron 2 and c)  $g_{K1}$  &  $g_{K2}$ , maximal conductances of  $K^+$  currents for Neuron 1 and Neuron 2 simultaneously with the same ratio.

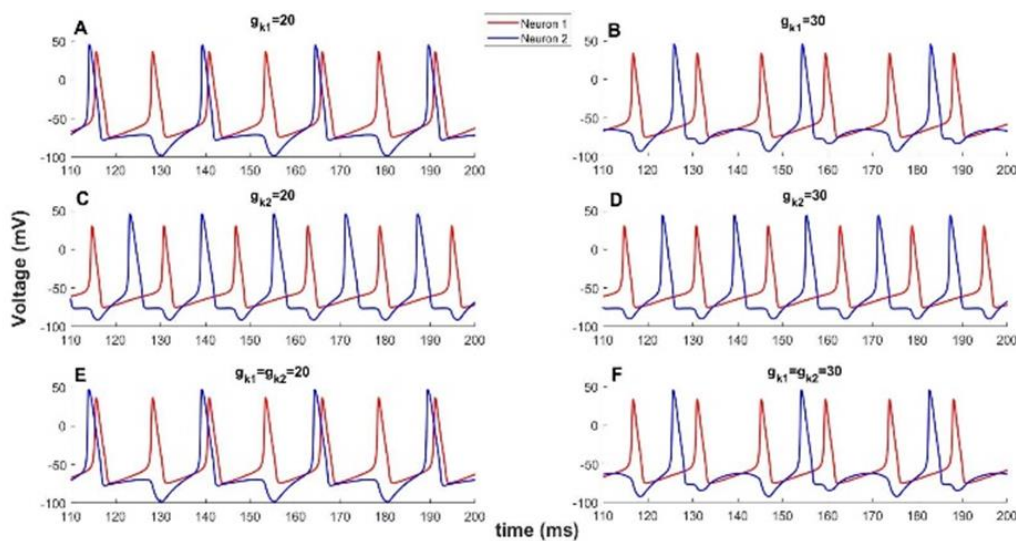


Figure 5. Pattern of spiking activity of Neuron 1 and Neuron 2 when A)  $g_{K1}=20, g_{K2}=36$ ; B)  $g_{K1}=30, g_{K2}=36$ ; C)  $g_{K1}=36, g_{K2}=20$ ; D)  $g_{K1}=36, g_{K2}=30$ ; E)  $g_{K1} = g_{K2} = 20$ ; F)  $g_{K1} = g_{K2} = 30$ .

Figure 4 shows the effects of changing  $g_{K1}$  (panel A), changing  $g_{K2}$  (panel B), and changing  $g_{K1}$  and  $g_{K2}$  together (panel C) on information flow as a result of transfer entropy simulation. Information flow from Neuron 1 to Neuron 2 is shown as 1-to-2 and the information flow from Neuron 2 to Neuron 1 is shown as 2-to-1. Figure 5 shows the effect of the changing maximal conductances on the output signal in terms of the synchrony, spike duration, and interspike interval. We can see that, the direction of flow changes with the increasing  $g_{K1}$  conductance in Figure 4A. Even though our coupling is defined as 1-to-2, before  $g_{K1}$  around 27, the TE results of 2-to-1 is higher. This can be explained as the  $g_{K1}$  arranges the amount of the subtractive feedback and when the amount of subtractive feedback is high enough for Neuron 1, the frequency of Neuron 1 is decreasing by increasing the interspike interval as shown in Figures 5A and 5B.

As a result, input coming to Neuron 2 from Neuron 1 dominates the information flow and causes the change of the

direction from 1-to-2 to 2-to-1 (Figure 4A).

The characteristic of the TE curves for varying  $g_{K2}$  does not cross each other meaning that the information flow does not change direction according to the strength of the subtractive feedback due to  $K^+$  current of Neuron 2 [25]. To be able to change the information flow in this coupled system, we should support Neuron 2, but increasing  $g_{K2}$  will do the inverse and the phase locked system is not affected as illustrated in Figure 5C&5D.

Once we start to increase the  $K^+$  conductance of each neuron together with the same ratio, we observe a similar effect of increasing the  $K^+$  conductance of Neuron 1. For lower values of maximal  $K^+$  conductances ( $g_{K1}$  and  $g_{K2}$ ) information is transferred from Neuron 2 to Neuron 1. But there is a threshold value around  $g_{K1} = g_{K2} = 28$ , that the information changes the direction to 1-to-2. Figure 5E and 5F shows the spiking behavior and how the phase-locked system is affected by the changes of both  $K^+$  conductances.

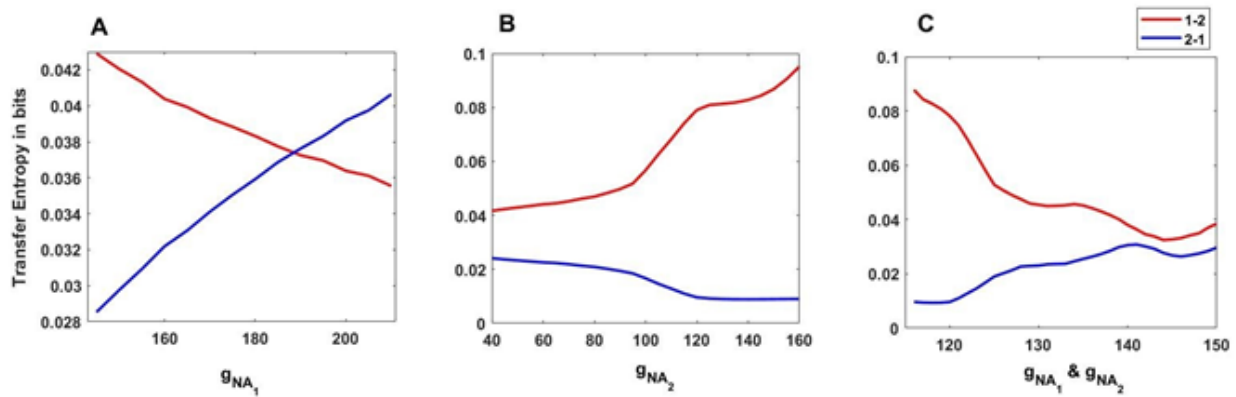


Figure 6. Transfer entropy results with changing a)  $g_{Na1}$ , maximal conductance of  $Na^+$  current for Neuron 1 b)  $g_{Na2}$ , maximal conductance of  $Na^+$  current for Neuron 2 and c)  $g_{Na1}$  &  $g_{Na2}$ , maximal conductances of  $Na^+$  currents for Neuron 1 and Neuron 2 simultaneously with the same ratio.

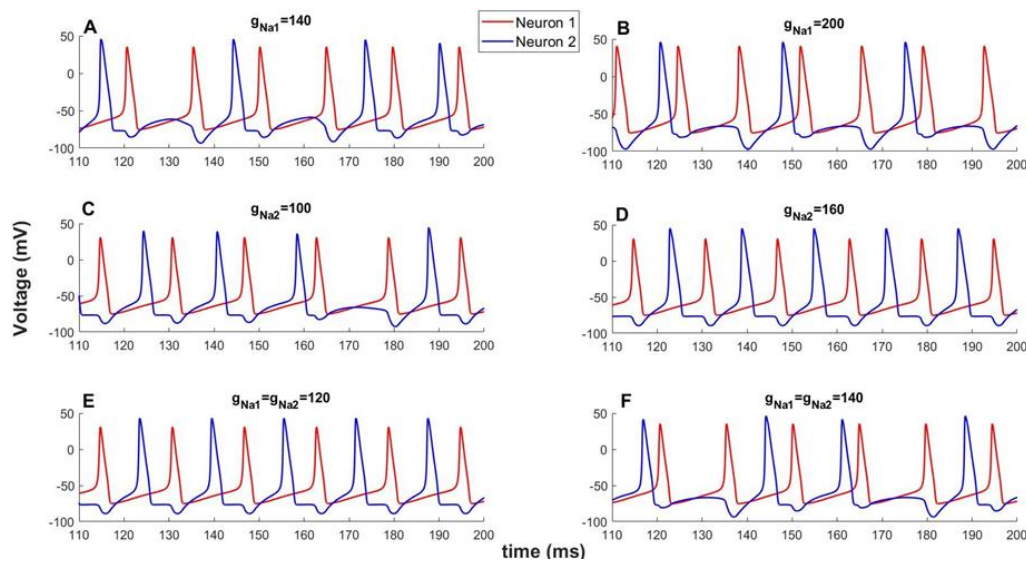


Figure 7. Pattern of spiking activity of Neuron 1 and Neuron 2 when A)  $g_{Na1}=140$ ,  $g_{Na2}=120$ ; B)  $g_{Na1}=200$ ,  $g_{Na2}=120$ ; C)  $g_{Na1}=120$ ,  $g_{Na2}=100$ ; D)  $g_{Na1}=120$ ,  $g_{Na2}=160$ ; E)  $g_{Na1} = g_{Na2} = 120$ ; F)  $g_{Na1} = g_{Na2} = 140$ .

Since the system is highly nonlinear, forecasting the direction of the flow according to current strength is almost impossible without further analysis like we applied here with Transfer Entropy.

### 3.2 The effects of changing maximal sodium conductances in the model

The activity pattern that our model network displays are also controlled by  $Na^+$  conductances  $g_{Na1}$  and  $g_{Na2}$  providing positive feedback to the related neurons. Additional  $Na^+$  conductance supports the neuron to act more profoundly to equivalent input current as we can see in Figure 7.

Increasing the  $Na^+$  current for Neuron 1 without increasing the  $K^+$  current can cause the model network to drive into a more depolarized state and that is why information transfer changes direction from 1-to-2 to 2-to-1 (Figure 6A).

Once we compare the results of  $Na^+$  and  $K^+$  conductance

effect on the TE as shown in the Figure 6A and Figure 4A, we observe an opposite behavior since they support the system adversely. On the other hand, increases in  $g_{Na2}$  conductance only have an inverse effect against the  $g_{Na1}$  results. The amount of information flow builds up from Neuron 1 to Neuron 2 and the direction of the information flow stays stable (Figure 6B). Increasing both  $Na^+$  currents by increasing the maximal conductances  $g_{Na1}$  and  $g_{Na2}$  together have a similar effect in our coupled network and transfer entropy curves do not cross each other and the information flow stays the same.

The gating dynamics responsible for channel activations and inactivations are highly nonlinear especially for the  $Na^+$  conductance.  $Na^+$  channel simulates the dynamics with two gates; activation and inactivation. While the activation of the  $Na^+$  channel supports the system positively, inactivation of the channel provides negative feedback to the system [26].



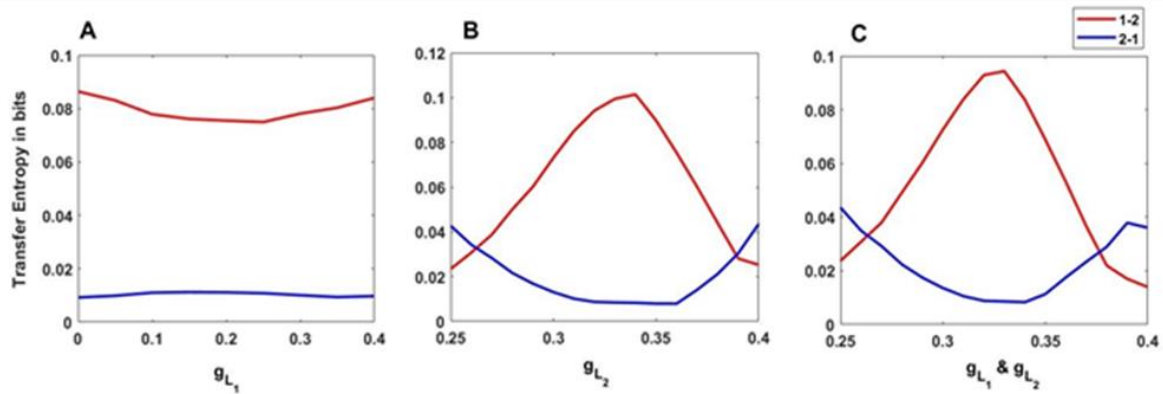


Figure 8: Transfer entropy results with changing a)  $g_{L1}$ , maximal conductance of leak current for Neuron 1 b)  $g_{L2}$ , maximal conductance of leak current for Neuron 2 and c)  $g_{L1}$  &  $g_{L2}$ , maximal conductances of leak currents for Neuron 1 and Neuron 2 simultaneously with the same ratio.

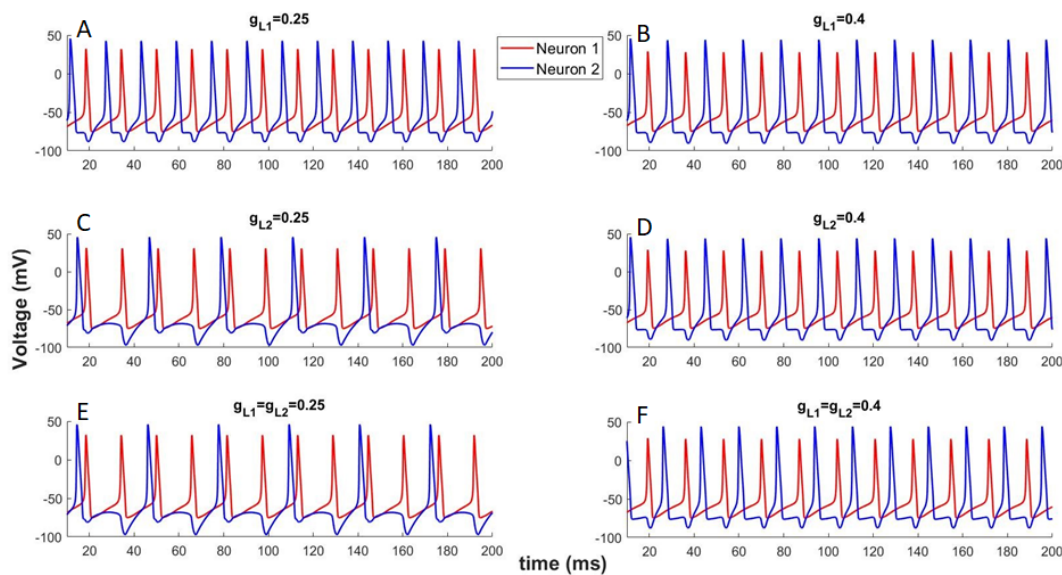


Figure 9: Pattern of spiking activity of Neuron 1 and Neuron 2 when A)  $g_{L1}=0.25$ ,  $g_{L2}=0.3$ ; B)  $g_{L1}=0.4$ ,  $g_{L2}=0.3$ ; C)  $g_{L1}=0.3$ ,  $g_{L2}=0.25$ ; D)  $g_{L1}=0.3$ ,  $g_{L2}=0.4$ ; E)  $g_{L1}=g_{L2}=0.25$ ; F)  $g_{L1}=g_{L2}=0.4$ .

So, our study reveals unexpected information transfer changes following changes in sodium conductance.

### 3.3 The effects of changing maximal Leak conductances in the model

Leak channels provide a background synaptic activity and how they influence the information flow for the coupled system is also important to analyze. Altering the leak conductance by changing the  $g_L$  parameters also alter the intrinsic cell dynamics. However, it is not yet established if it changes the information flow. To analyze the change in information flow, we simply increase the maximal leak conductances of each neuron separately and together in the network model.

The presence of the added leak conductance for Neuron 1 does not have any impact on the flow of information as we can see in Figure 5A. Transfer entropy results for both directions are not affected by the changes in  $g_{L1}$ . The phase-locked system is not affected by the changes in  $g_{L1}$  as shown in Figure 9A&9B that supports the stability in TE results.

Neuron 2 does not have an applied input and excitability

is due to the coupling from Neuron 1. So increasing or decreasing the leak conductance causes a corresponding increase/decrease in the frequency of action potentials affecting the direction of the information flow as we can see in Figure 9B and 9C.

Interspike interval for Neuron 2 decreases as  $g_{L2}$  increases and 2-to-1 coupling turns to the 1-to-2 coupling between neurons. During this change in the coupling, the direction of the information flow also changes. Similar results are observed once both the leak conductances are perturbed as shown in Figure 8C and Figure 9E&F. So conductance-based networks can show both ways of information flow according to the strength of the leak conductance.

While the information flow occurs from Neuron 2 to Neuron 1 for smaller  $g_L$  values, the direction oscillates with an increasing  $g_{L2}$  value. These results suggest that the interaction between the coupled network dynamics critically changes by the effects of leak conductance by changing the interspike variability and as a result the direction of the information flow changes between the neurons.

#### 4. Conclusion

The objective of this study is to determine the effects of changing conductances on the two –neuron HH network by using the transfer entropy which is an information-theoretical quantity. Our defined model involves two synchronized neurons due to the coupling defined from Neuron 1 to Neuron 2. Firstly, we observe a strong correlation between the maximal conductances of the ion channels  $g_{Na}$ ,  $g_K$  and  $g_L$ , the action potential duration and interspike interval. Once we perturb these parameters, the pattern of synchronization for the neuronal networks also changes dramatically. That is why it is crucial to analyze the ambiguity of the parameters in the network model. In order to understand the population behavior of neurons, we should understand the relations under the nonlinear dynamics involved in the AP network. Here, to understand how neural systems integrate, encode, and compute information, we use transfer entropy, which is capable of catching the nonlinear interactions between the variables. For the two-neuron HH network, the TE analysis reveals that information transfer changes direction with the maximum conductances against the coupling defined originally. This coupling between neurons is modeled by the nonlinear equation system of (7) and (8), where it is not obvious that the first neuron can also be affected by the second. However, using TE, we show that the latter statement can also come true as a result of changing conductances. For example, from Figure 2A, we can conclude that the direction of coupling (information flow) is from neuron 2 to neuron 1 for conductance levels up to  $g_{K1} \cong 27$  as the probability of predicting the current values of neuron 2's action potential by using its own past values and the past values of neuron 1 is higher than the probability of the predictability of that of neuron 1 from its own past and neuron 2's past. In other words, for this conductance zone,  $TE_{V_2V_1} > TE_{V_1V_2}$ . Similarly, we note that this directionality is reversed as the conductance values exceed 27 for this case.

We observe these changes with each maximal conductance including the leak channel. Either having a very strong or very weak leak for Neuron 2 changes the information flow. We observe that there is an interval for  $g_{L2}$  that holds the network stable as is defined. On the other hand,  $Na^+$  channel activation provides a positive feedback to the network and once we increase the maximal conductance of the Neuron 1 there is a threshold that changes the information flow from 1-to-2 to 2-to-1 due to the strong positive feedback flows from Neuron 1 to Neuron 2.  $K^+$  channel activation, on the other hand, provides negative feedback to the system and we observe an opposite behavior once we perturb the  $K^+$  maximal conductance as we expect. This time, for lower values of the  $g_{K1}$ , information flow changes direction from 1-to-2 to 2-to-1 due to the strong negative feedback flow from Neuron 1 to Neuron 2.

Depending on the ion channels property, changing the maximal conductance of either each neuron separately or together, can change the amount of information flow against the coupling. This result highlights that since different data sets can closely optimize the experimental data and the flow of the direction changes with the changing maximal conductances, the chosen parameter set is matter even though it can mimic the data well.

The main effect of the perturbation of conductances is to change the synchrony with either changing the interspike interval or spike duration. According to the perturbed parameter we observe the disruption of the synchronized network. The TE analysis is defined for inspecting the information transfer between the signals. For neuronal spikes simulated by our defined network, TE analysis reveals useful information about the parameters of the involved ion channels. Since the network is highly nonlinear, the effect of adding or subtracting a conductance can change the different intrinsic properties like the values of other parameters. That is why we need deeper analysis to better understand the underlying behavior of neuronal networks.

This work presents a complementary analysis to our previous effort on the full network investigation of a coupled two neuron HH model where the effects of additional noise are examined.

#### Declaration

The author(s) declared no potential conflicts of interest with respect to the research, authorship, and/or publication of this article. The author(s) also declared that this article is original, was prepared in accordance with international publication and research ethics, and ethical committee permission or any special permission is not required.

#### Acknowledgement

This work is supported by the Scientific and Technological Research Council of Turkey (TÜBİTAK) with project number 118E765.

#### References

1. Pournaki, A., Merfort, L., Ruiz, J., Kouvaris, N. E., Hövel, P., & Hizanidis, J., *Synchronization patterns in modular neuronal networks: A case study of C. elegans*. Frontiers in Applied Mathematics and Statistics, 2019.
2. Zhou, Y., Qiu, L., Wang, H., & Chen, X., *Induction of activity synchronization among primed hippocampal neurons out of random dynamics is key for trace memory formation and retrieval*. The FASEB Journal, 2019. **34**(3): p. 3658-3676.
3. Nikitin, D., Omelchenko, I., Zakharova, A., Avetyan, M., Fradkov, A. L., & Schöll, E., *Complex partial synchronization patterns in networks of delay-coupled neurons*. Philosophical Transactions of the Royal Society A: Mathematical, Physical and Engineering Sciences, 2019.

- 377(2153) 20180128, p. 1-19.
4. Gray, C. M., König, P., Engel, A. K., & Singer, W., *Oscillatory responses in cat visual cortex exhibit inter-columnar synchronization which reflects global stimulus properties*. Nature, 1989. **338**(6213): p. 334-337.
  5. Leiber, S., Lutzenberger, W., & Kaiser, J., *Effects of memory load on cortical oscillatory activity during auditory pattern working memory*. Brain Research, 2006. **1120**(1): p. 131-140.
  6. Fernando, C., & Sojakka, S., *Pattern recognition in a bucket*. Advances in Artificial Life, ECAL 2003. p. 588-597.
  7. Timofeev, I., Bazhenov, M., Seigneur, J., & Sejnowski, T., *Neuronal synchronization and Thalamocortical rhythms during sleep, wake, and epilepsy*. Jasper's Basic Mechanisms of the Epilepsies, 2012 p. 157-175.
  8. Timme, N. M., & Lapish, C., *A tutorial for information theory in neuroscience*. Eneuro. ENEURO, 2018. **5**(3), <https://doi.org/10.1523/eneuro.0052-18.2018>.
  9. Gençağa, D., Şengül Ayan, S., Farnoudkia, H., & Okuyucu, S., *Statistical approaches for the analysis of dependency among neurons under noise*. Entropy, 2020. **22**(4): 387.
  10. Jæger, K. H., Wall, S., & Tveito, A., *Detecting undetectables: Can conductances of action potential models be changed without appreciable change in the transmembrane potential?*. Chaos: An Interdisciplinary Journal of Nonlinear Science, 2019. **29**(7): 073102.
  11. Liu, Z., Golowasch, J., Marder, E., & Abbott, L. F., *A model Neuron with activity-dependent conductances regulated by multiple calcium sensors*. The Journal of Neuroscience, 1998. **18**(7): p. 309-2320.
  12. Fernandez, F. R., & White, J. A., *Reduction of spike Afterdepolarization by increased leak conductance alters Interspike interval variability*. Journal of Neuroscience, 2009. **29**(4): p. 973-986.
  13. Şengül Ayan, S., Sircan, A. K., Abewa, M., Kurt, A., Dalamam, U., & Yaraş, N., *Mathematical model of the ventricular action potential and effects of isoproterenol-induced cardiac hypertrophy in rats*. European Biophysics Journal, 2020. **49**(5): p. 323-342.
  14. Duncan, P. J., Sengul, S., Tabak, J., Ruth, P., Bertram, R., & Shipston, M. J., *Large conductance  $Ca^{2+}$ -activated  $K^{+}$  channels (BK) promote secretagogue-induced transition from spiking to bursting in murine anterior pituitary corticotrophs*. The Journal of Physiology, 2014. **593**(5): p. 1197-211.
  15. Patel, A. X., & Burdakov, D., *Mechanisms of gain control by voltage-gated channels in intrinsically-firing neurons*. Plos One, 2015. **10**(3), e0115431.
  16. Gençağa, D., & Ayan, S. Ş., *Effects of neuronal noise on neural communication*. Proceedings of The 39th International Workshop on Bayesian Inference and Maximum Entropy Methods in Science and Engineering, 2019. **33**(1): p. 2.
  17. Lane, B. J., Samarth, P., Ransdell, J. L., Nair, S. S., & Schulz, D. J., *Synergistic plasticity of intrinsic conductance and electrical coupling restores synchrony in an intact motor network*. eLife, 2016. 5. <https://doi.org/10.7554/elife.16879>.
  18. Cover, T. M., Thomas, J. A., *Information theory and portfolio theory*. Elements of Information Theory, 2005. p:613-656. USA: John Wiley & Sons, Inc.
  19. Schreiber, T., *Measuring information transfer*. Physical Review Letters, 2000. **85**(2): p. 461-464.
  20. Scott, D. W., *Multivariate density estimation*. 2012, USA: Wiley Series in Probability and Statistics.
  21. Gençağa, D., *Transfer entropy*. Entropy, 2018. **20**(4): p. 288. <https://doi.org/10.3390/e20040288>.
  22. Hodgkin, A. L., & Huxley, A. F., *A quantitative description of membrane current and its application to conduction and excitation in nerve*. The Journal of Physiology, 1952. **117**(4): p.500-544.
  23. Dhanya E, Pradhan, N., Sunitha R, & Sreedevi, A., *Modelling and implementation of two coupled Hodgkin-Huxley Neuron model*. 2015 International Conference on Computing and Network Communications (CoCoNet).
  24. Ermentrout, B., *Simulating, analyzing, and animating dynamical systems*. 2002, USA: Society for Industrial and Applied Mathematics.
  25. Şengül, S., Clewley, R., Bertram, R., & Tabak, J., *Determining the contributions of divisive and subtractive feedback in the Hodgkin-Huxley model*. Journal of Computational Neuroscience, 2014. **37**(3): p. 403-415.
  26. Bezanilla, F., Rojas, E., & Taylor, R. E., *Sodium and potassium conductance changes during a membrane action potential*. The Journal of Physiology, 1970. **211**(3): p. 729-751.



## Research Article

## CCII current conveyor and dormand-prince-based chaotic oscillator designs for secure communication applications

Murat Alçın <sup>a</sup> , Murat Tuna <sup>b,\*</sup> , İhsan Pehlivan <sup>c</sup>  and İsmail Koyuncu <sup>d</sup> 

<sup>a</sup>Afyon Kocatepe University, Faculty of Technology, Department of Mechatronics, Afyonkarahisar 03200, Turkey

<sup>b</sup>Kırklareli University, Technical Sciences Vocational High School, Department of Electrical and Energy, Kırklareli 39000, Turkey

<sup>c</sup>Sakarya University of Applied Sciences, Faculty of Technology, Department of Electrical and Electronics Engineering, Sakarya 54187, Turkey

<sup>d</sup>Afyon Kocatepe University, Faculty of Technology, Department of Electrical and Electronics Engineering, Afyonkarahisar 03200, Turkey

## ARTICLE INFO

## Article history:

Received 13 June 2020

Revised 05 August 2020

Accepted 05 September 2020

## Keywords:

CCII

Dormand-Prince algorithm

FPGA

Nonlinear oscillator

VHDL

## ABSTRACT

Chaos is one of the important research areas in recent years. The chaotic signal generator is one of the most basic structure in the chaos-based researches and applications. In this study, Sundarapandian-Pehlivan Chaotic Oscillator (SPCO) designs have been implemented in 2 different platforms as analog-based using Second-Generation Current Controlled Current Conveyor (CCII) and FPGA-based with one of the chaotic oscillator that has been presented to the literature namely Sundarapandian-Pehlivan system. The structure used for the design of CCII-based chaotic oscillator and the results obtained from the study have been presented. In the second phase, the design of SPCO has been realized in order to utilize for running in FPGA chips using Dormand-Prince (DP) numeric algorithm. The design has been coded in VHDL using 32-bit IEEE-754-1985 floating point representation. The designed system has been tested by synthesizing it in Xilinx ISE Design Tools program. Then, the test results obtained from DP-based SPCO structure have been presented. In the last phase, the designed system has been synthesized for VIRTEX-7 FPGA. FPGA chip resource consumption values that obtained after the Place-Route process are presented. According to the results, the maximum operating frequency of DP-based SPCO unit on FPGA is obtained as 362.608 MHz. In future studies, the designs of Pseudo Random Number Generator (RNG) and True RNG can be performed using DP-based SPCO unit implemented successfully in this study.

© 2020, Advanced Researches and Engineering Journal (IAREJ) and the Author(s).

### 1. Introduction

Chaotic systems (CSs) are one of the areas that have been studied extensively in recent years [1–3]. CSs can be defined as nonlinear systems that exhibit an infinite number of non-periodic oscillations with a specific order within certain intervals [4,5]. The sensitivity to the initial conditions (ICs) and the system parameters are among the important characteristics of the CSs [6,7]. For this reason, in CSs, the slight changes in the parameter values or the ICs of the system may significantly affect the dynamic behavior of the system in time domain [8,9].

The chaotic signal generator is one of the basic structures used in chaos-based studies and applications

[10–13]. Nowadays, the chaotic signal generators and Chaotic Oscillators (COs) can be created by using different platforms. The circuits constructed by using analog electronic circuit elements can be given as examples for one of the most basic structures of CO structures [14,15]. In these circuits, active circuit elements are used together with basic elements such as resistors and capacitors, which are passive circuit elements [15,16]. Operational Amplifier (Op-Amp), Operational Transconductance Amplifier (OTA) and Second-Generation Current Controlled Current Conveyor (CCII) can be given as examples for the analog circuit elements that used in the CO designs [17–19]. The Op-

\* Corresponding author. Tel.: +90-288-214-1845; Fax: +90-288-214-1495.

E-mail addresses: [muratalcin@aku.edu.tr](mailto:muratalcin@aku.edu.tr) (M. Alçın), [murat.tuna@klu.edu.tr](mailto:murat.tuna@klu.edu.tr) (M. Tuna), [ipehlivan@subu.edu.tr](mailto:ipehlivan@subu.edu.tr) (İ. Pehlivan),

[ismailkoyuncu@aku.edu.tr](mailto:ismailkoyuncu@aku.edu.tr) (İ. Koyuncu)

ORCID: 0000-0002-2874-7048 (M. Alçın), 0000-0003-3511-1336 (M. Tuna), 0000-0001-6107-655X (İ. Pehlivan), 0000-0003-4725-4879 (İ. Koyuncu)

DOI: 10.35860/iarej.752321

Amp has high-gain and it is a direct coupling element that can perform many linear/non-linear signal processing operations. Today, there are Op-Amp elements operating at frequencies higher than 100 MHz and higher power values than 100 W. Although it is quite difficult to integrate Op-Amp elements with other analog or digital structures on the same chip, it is very suitable for integrating OTA element with analog or digital structures on the same chip. Besides, OTA elements have very high bandwidths compared to Op-Amp elements [20,21]. CCII elements can operate in a wider frequency band than Op-Amp and OTA elements. Also, CCII elements are active circuit elements that have more flexible use in terms of circuit synthesis [22,23].

Another method used for CO design is the structure of Artificial Neural Network (ANN)-based CO design [24–26]. ANN is a mathematical modeling process of the thinking and decision making feature of the human brain. In this method, ANN is first trained by using the training set obtained from the CO [27]. Then ANN model is implemented on a digital platform by taking the weight and bias values obtained from the training as reference [28]. In ANN-based CO designs, many digital sources have been used, and since they contain non-linear transfer functions, their operating frequencies are generally low [28–32].

One of the most preferred methods in the literature is that the COs, which is given in a continuous time, is implemented on a digital platform in discrete time using numerical algorithms [33,34]. For this purpose, Euler, Heun, 4th order Runge-Kutta, Runge-Kutta-Butcher and Dormand-Prince are the numerical algorithms used in the literature [28,35,36]. Among these algorithms, the algorithm that can show the most characteristic of the CSs and produce the closest results is the Dormand-Prince (DP) algorithm [37,38].

In the literature, there are different chaotic oscillator designs implemented using ANN-based and different numerical algorithms on FPGA, which is one of the digital platforms in recent years (Table 1). Alçın et al. [24] implemented the Pehlivan-Uyaroglu chaotic system based on ANN on FPGA and obtained the operating frequency as 266 MHz. They discussed the chip statistics and simulation results of the design and presented them to the literature. Yu et al. [22] designed the 4-D Chua chaotic system in 32-bit IEEE-754-1985 floating point number format with VHDL on FPGA using RK4 numerical algorithm and present the operating frequency of the system as 180 MHz. Rajagopal et al. [33] designed a new 3-D chaotic system on FPGA using Runge-Kutta Butcher (RK5B) numerical algorithm in 32-bit IEEE-754-1985 floating point number format. Koyuncu et al. [37] designed the SEA chaotic oscillator as 16I-16Q, 14I-14Q, 12I-12Q, 10I-10Q, 8I-8Q fixed point based on

FPGA using DP numerical algorithm and obtained the operating frequencies of the systems in the range of 344–366 MHz. Seker et al. [36] carried out the DP numerical algorithm-based design of the chaotic oscillator on FPGA in 32-bit IEEE-754-1985 floating point number format and present the operating frequency of the design as 316 MHz. Senouci et al. [39] transformed multiple chaotic systems they designed under Matlab/Simulink into FPGA code using MATLAB HDL Coder and Fixed Point Toolbox and realized their designs on the digital platform. Operating frequencies of systems embedded on FPGAs vary between 27-72 MHz. Kizmaz et al. [40] carried out the designs and chaos analysis of Memristor-Based Simplest Chaotic system based on DP numerical algorithm in their study. Koyuncu et al. [41] performed the Dormand-Prince based chaotic oscillator design with golden proportion balance point on FPGA. In this study, SPCO chaotic system was designed on Xilinx Virtex-7 FPGA using DP numerical algorithm in 32-bit IEEE 754-1985 floating point number format. The operating frequency of the system designed in VHDL was obtained as 362 MHz.

In this presented study, Sundarapandian-Pehlivan CS has been implemented using two different platforms: CCII-based as analog and numerically as DP-based on FPGA chip. In the second part of this study, information about Sundarapandian-Pehlivan CS is given. In the third part, CCII-based SPCO design is presented. In the fourth part, DP-based CO structure and FPGA chip statistics are presented. In the last part, the results obtained from the study were evaluated.

## 2. SPCO System

CSs or oscillators are divided into two groups, continuous time and discrete time. Examples of continuous-time COs are Sprott A, Burke-Shaw, Lorenz, Chua, Rössler, Pehlivan-Uyaroglu and Pehlivan-Wei COs [39,43,44]. Continuous-time COs are expressed by differential equations. The differential equations of the nonlinear autonomous SPCO used in this study are given below [42].

$$\begin{aligned}\dot{x} &= a \cdot y - x \\ \dot{y} &= -b \cdot x - z \\ \dot{z} &= c \cdot z + x \cdot y^2 - x\end{aligned}\quad (1)$$

The parameters a, b and c in these equations can take different values according to the design. In this study, the ICs for Dormand-Prince-based SPCO are taken as  $x(0) = 0$ ,  $y(0) = 0$  and  $z(0) = 0.1$  and the parameters of the system are taken as  $a = 1.5$ ,  $b = 0.4$  and  $c = 0.4$ . The change in system parameters and oscillator ICs in COs completely changes the dynamic behavior of the system.

Table 1. Technical characteristics of FPGA-based COs designs in the literature in recent years.

Paper	Method	Number Format	Clock (MHz)
[1]	Euler numerical algor.	Fixed (7;25)	-----
[2]	Heun-RK4 numerical algor.	Floating	390
[3]	RK4 numerical algor.	Fixed (16;16)	373
[13]	RK4 numerical algor.	Fixed (8;24)	112
[22]	RK4 numerical algor.	Floating	180
[24]	ANN-based design	Floating	266
[26]	ANN-based design	Floating	231
[27]	ANN-based design	Floating	240
[28]	ANN-based design	Floating	272
[31]	ANN-based design	Floating	231
[33]	RK5B numerical algor.	Floating	-----
[34]	3-D COs, Forward Euler and RK4	Fixed (8;24)	-----
	4-D Hyper-COs, Forward Euler and RK4	Fixed (8;24)	-----
[34]	3-D COs, Simulink HDL-Coder	Fixed (8;24)	48
	4-D Hyper-COs, Simulink HDL-Coder	Fixed (8;24)	41
[37]	DP numerical algor.	Fixed (16;16)	344-366
[38]	DP numerical algor.	Floating	316
[39]	Simulink HDL-Coder	Fixed	27-72
[40]	DP numerical algor.	Fixed	-----
[41]	DP numerical algor.	Floating	316
[42]	RK4 numerical algor.	Floating	293
This	DP numerical algor.	Floating	362

There are many methods developed in the literature for the chaos analysis of COs. One of the most preferred methods of these methods are chaotic phase portraits and time series methods. Phase portraits of x-y, y-z, x-z and x-y-z obtained using the DP numerical algorithm for the SPCO used in this study are given in Figure 1, Figure 2, Figure 3 and Figure 4, respectively. Besides, the x-y-z time series obtained using the DP numerical algorithm for the SPCO is presented in Figure 5.

### 3. CCII-based SPCO Design

In this section, SPCO has been modeled using OTA elements and the circuit design of the modeled system has been realized with ORCAD PSPICE program.

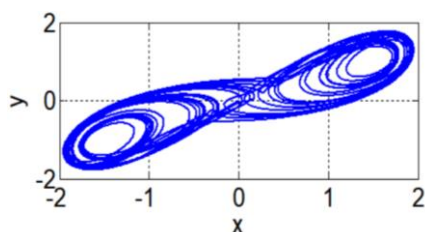


Figure 1. x-y phase portrait of Dormand-Prince-based SPCO

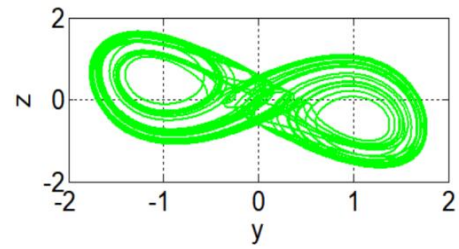


Figure 2. y-z phase portrait of Dormand-Prince-based SPCO

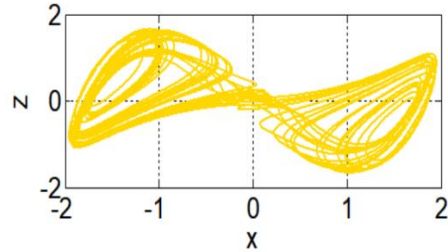


Figure 3. x-z phase portrait of Dormand-Prince-based SPCO

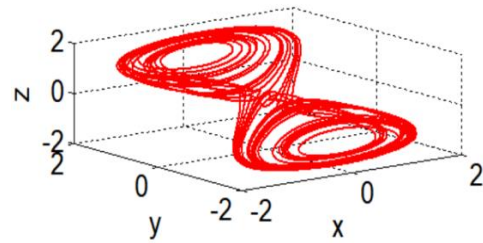


Figure 4. x-y-z phase portrait of Dormand-Prince-based SPCO

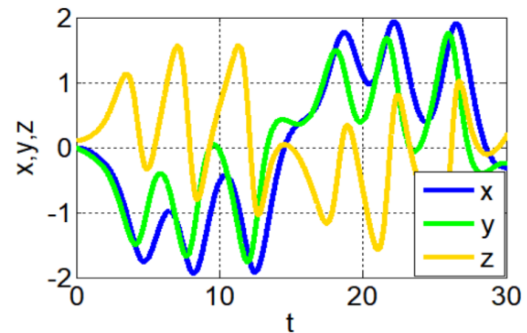


Figure 5. x-y-z time series of Dormand-Prince based SPCO

In the circuit, 14 AD844 CCII, 2 AD633 multiplier, three capacitors and 10 resistance elements with different values have been used. Below is the CO circuit diagram performed with OTA in Figure 6 using the ORCAD PSPICE program.

In Figure 7, x-y, y-z and x-z phase portraits obtained from ORCAD are given, according to the ICs of the CCII-based CO, as  $x(0) = 0$ ,  $y(0) = 0$  and  $z(0) = 0.1$  and the system parameters as  $a=1.5$ ,  $b=0.4$  and  $c=0.4$ , between the time intervals from 0 to 100ms. In addition, Fast Fourier Transformation (FFT) analysis results of the signals obtained from CCII-based SPCO are presented in Figure 8.

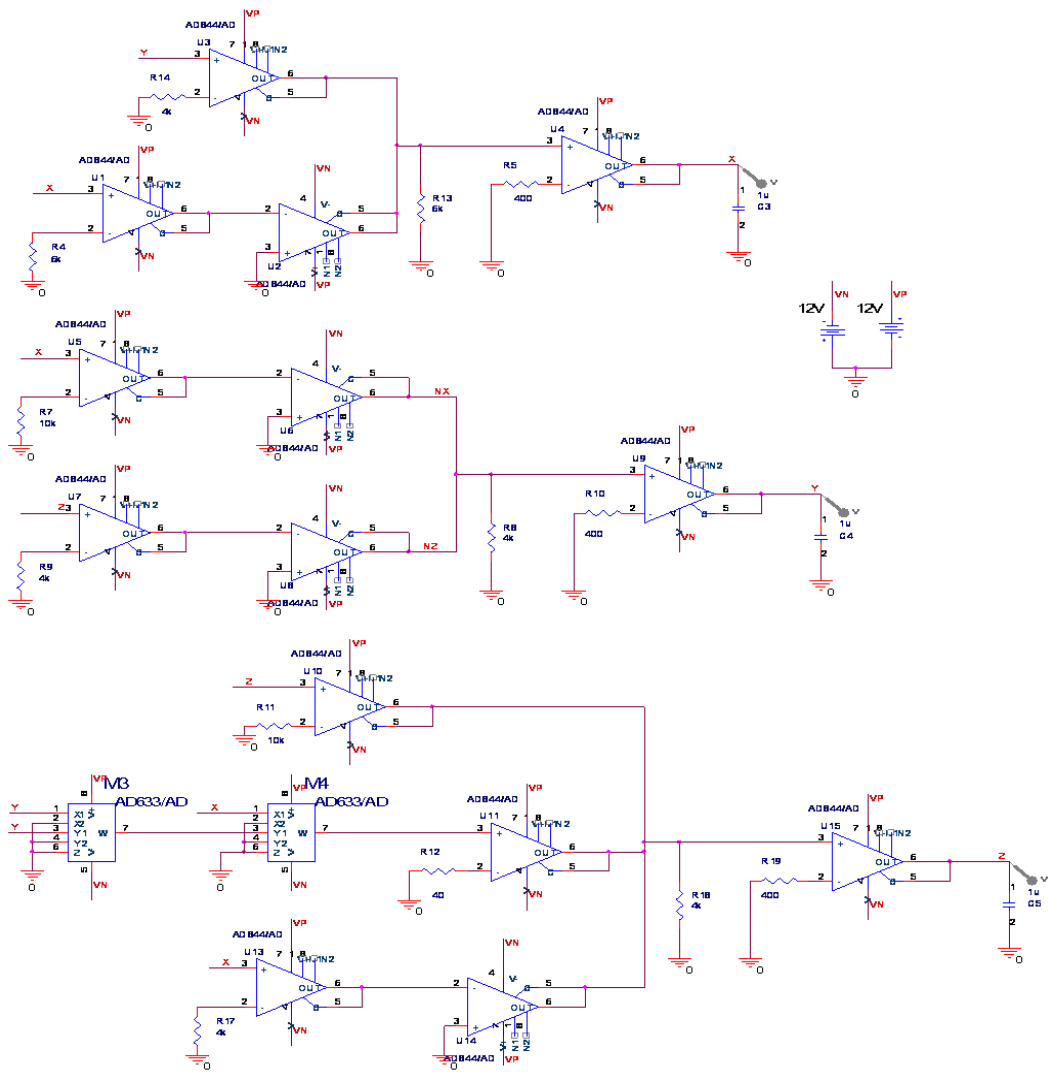


Figure 6. Circuit schema of CCII-based SPCO design using ORCAD-Pspice program

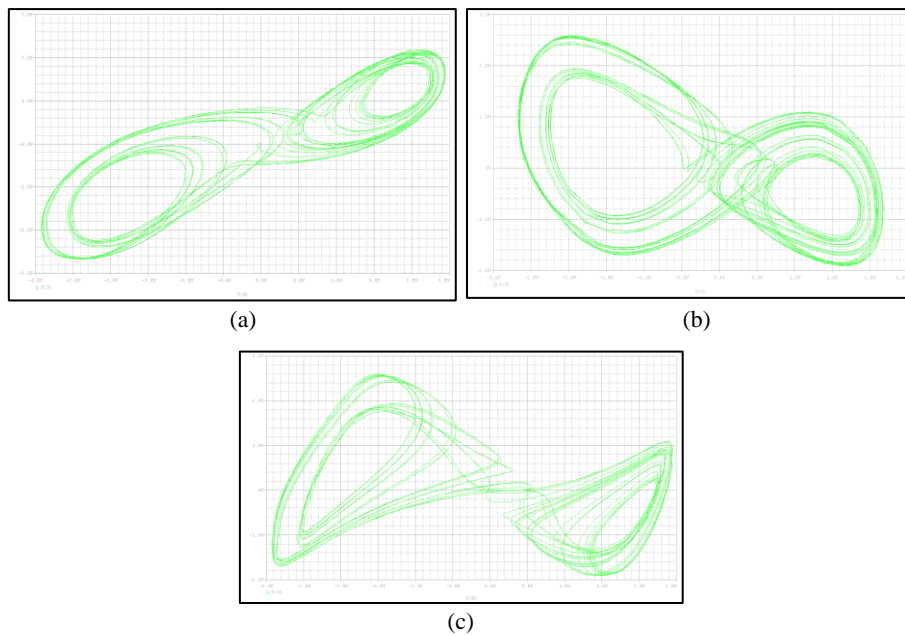


Figure 7. (a) x-y, (b) y-z and (c) x-z phase portraits of CCII-based SPCO designed using ORCAD-Pspice program

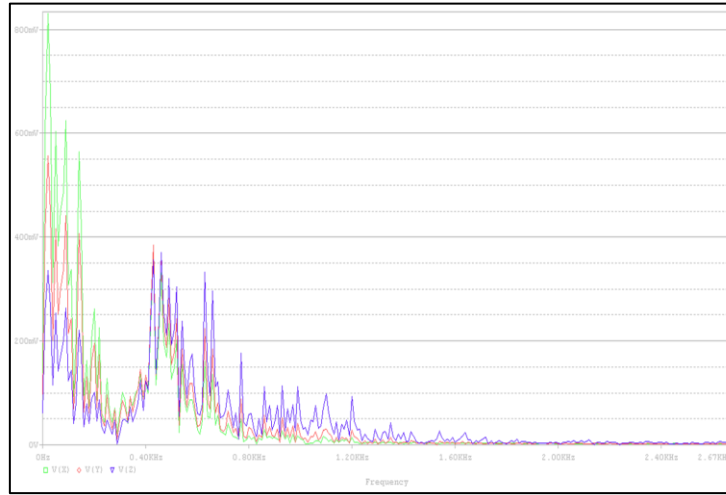


Figure 8. FFT analysis results of the CCII-based SPCO designed using ORCAD-Pspice program

#### 4. Dormand-Prince-based SPCO on FPGA

In this part of the study, the SPCO is modeled to work on FPGA using the DP. DP is given in Equation (2). DP consists of seven steps of  $k_1$ ,  $k_2$ ,  $k_3$ ,  $k_4$ ,  $k_5$ ,  $k_6$  and  $k_7$ . IEEE-754-1985 32-bit floating point representation was used for the design and the design was coded in VHDL. Xilinx ISE Design Tools (ISE-DTs) program was used for the design synthesis, testing and Place-Route operations. Xilinx IP-Core Generator is used for the basic arithmetic operations including division, addition etc. used in the design. The first-order block diagram of DP based SPCO unit designed to work on FPGA chip is given in Figure 9.

$$\begin{aligned}
 y_{i+1} &= y_i + h \left( \frac{35}{384} k_1 + \frac{500}{1113} k_3 + \frac{125}{192} k_4 - \frac{2187}{6784} k_5 + \frac{11}{84} k_6 \right) \\
 k_1 &= F(x_i, y_i) \\
 k_2 &= F \left( x_i + \frac{h}{5}, y_i + \frac{h}{5} k_1 \right) \\
 k_3 &= F \left( x_i + \frac{3}{10} h, y_i + \frac{3}{40} k_1 + \frac{9}{40} k_2 \right) * h \\
 k_4 &= F \left( x_i + \frac{4}{5} h, y_i + \frac{44}{45} k_1 - \frac{56}{15} k_2 + \frac{32}{9} k_3 \right) * h \\
 k_5 &= F \left( x_i + \frac{8}{9} h, y_i + \frac{19372}{6561} k_1 - \frac{25360}{2187} k_2 + \frac{64448}{6561} k_3 - \frac{212}{729} k_4 \right) * h \\
 k_6 &= F \left( x_i + h, y_i + \frac{9017}{3168} k_1 - \frac{355}{33} k_2 + \frac{46732}{5247} k_3 + \frac{49}{176} k_4 - \frac{5103}{18656} k_5 \right) * h \\
 k_7 &= F \left( x_i + h, y_i + \frac{35}{384} k_1 + 0 * k_2 + \frac{500}{1113} k_3 + \frac{125}{192} k_4 - \frac{2187}{6784} k_5 + \frac{11}{84} k_6 \right) * h
 \end{aligned} \quad (2)$$

Dormand-Prince-based SPCO unit on FPGA has 1-bit Clk and 1-bit Run input signals. The design has 32-bit  $X_{out}$ ,  $Y_{out}$ ,  $Z_{out}$  and 1-bit  $R_{ready}$  output signals. Clk signal allows the units in the design to work synchronously.

Run signal is used to provide the first run. When the '1' signal arrives to the Run input of the design, the  $X_{out}$ ,  $Y_{out}$  and  $Z_{out}$  outputs start to produce their initial values as a result of the 360 clock pulse. At this moment, the value of  $R_{Ready}$  becomes '1'. In cases where there is no output in the  $X_{out}$ ,  $Y_{out}$  and  $Z_{out}$ , the  $R_{ready}$  signal produces a '0' output.

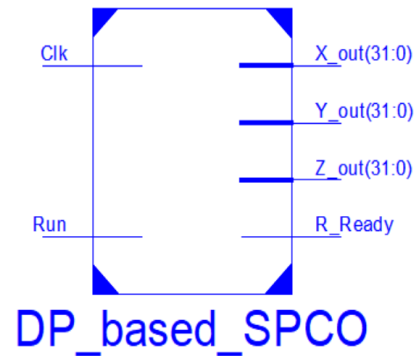


Figure 9. The first-order block diagram of Dormand-Prince based SPCO unit

The second-order block diagram of DP based SPCO unit designed to work on the FPGA chip is given in Figure 10. There are 10 units in the design, 6X3MUX,  $K_1$ ,  $K_2$ ,  $K_3$ ,  $K_4$ ,  $K_5$ ,  $K_6$ ,  $K_7$ ,  $y_s$ , and Filter. The 6X3MUX unit is designed to choose between the initial values assigned by the designer and the value produced when the system starts producing results. When the design first starts working, it sends the initial values of the 6X3MUX unit to the system.

When the system starts producing the first results, it sends these values to the system as the initial value for the system to produce the next results. The  $K_1$ ,  $K_2$ ,  $K_3$ ,  $K_4$ ,  $K_5$ ,  $K_6$  and  $K_7$  units are designed to calculate the values found in the DP algorithm. The  $y_s$  unit calculates the values of the DP algorithm using the values produced by the  $K_1$ ,  $K_2$ ,  $K_3$ ,  $K_4$ ,  $K_5$ ,  $K_6$  and  $K_7$  units. It then sends these values to the Filter unit. Since the designed system produces results in a 360 clock pulse period, the Filter unit is used to filter the values that come before this moment. When it comes to the 360th clock pulse, it transfers the values received to the output of the designed DP-based SPCO unit. At the same time, the unit sends a '1' signal to the  $R_{Ready}$  output.



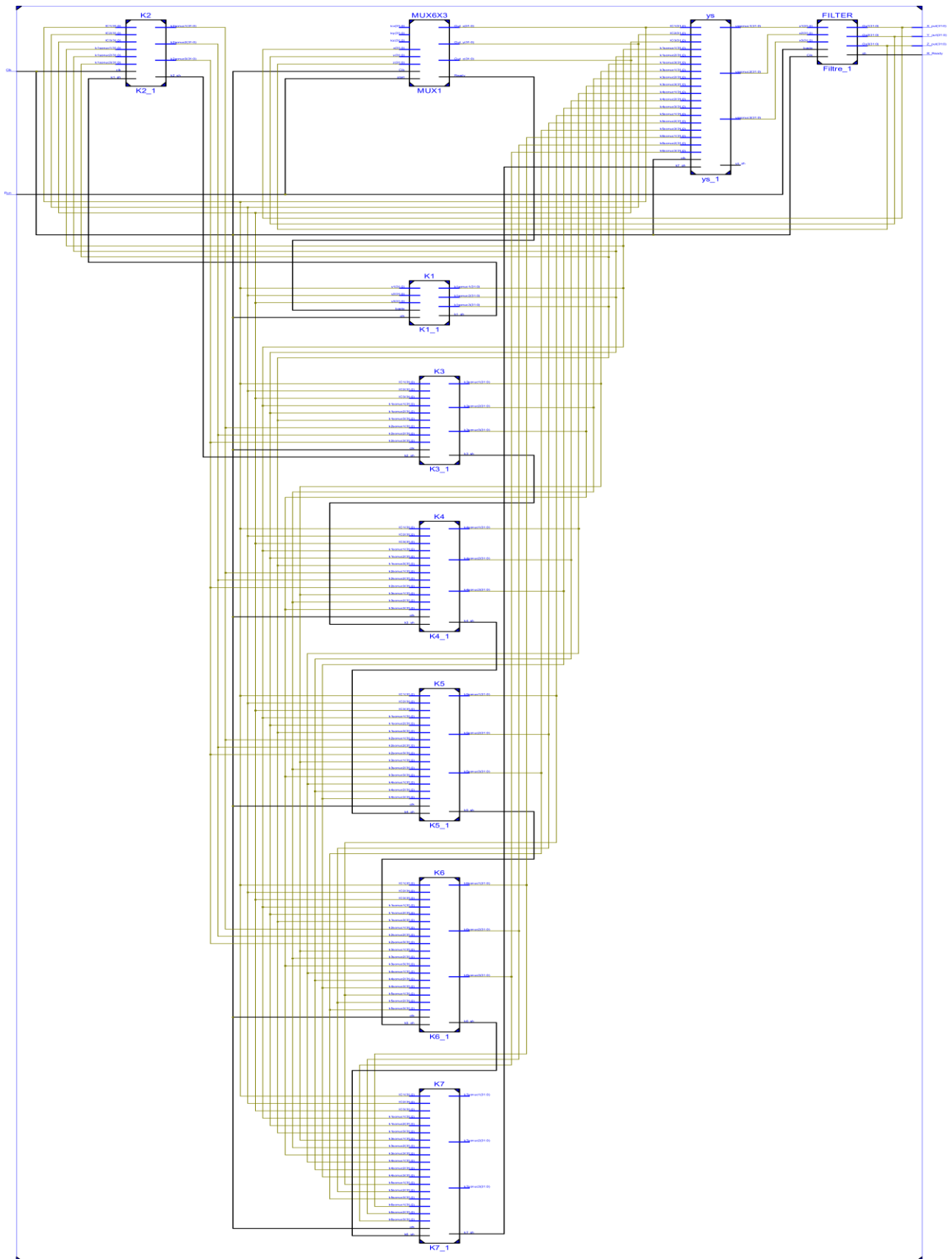


Figure 10. The second-order block diagram of Dormand-Prince based SPCO unit

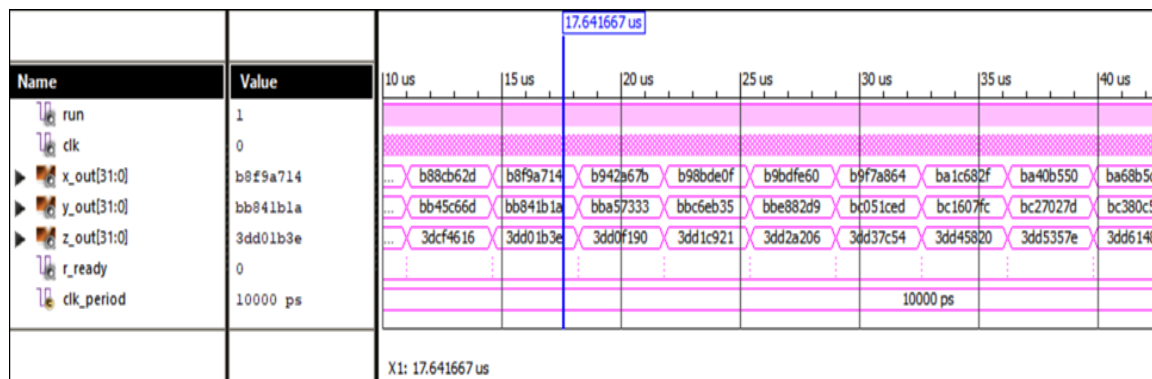


Figure 11. The results of Dormand-Prince based SPCO unit using Xilinx ISE-DTs

Table 2. The usage statistics for VIRTEX-7 chip of DP based SPCO unit

Logic Utilization	Used	Available	Utilization (%)
Number of Slice Registers	154,979	607,200	25
Number of DSP48E1s	150	2,800	5
Number of Slice LUTs	156,371	303,600	51
Number of bonded IOBs	99	700	14

Dormand-Prince based SPCO unit, which was designed to work on FPGA chip, has been tested by using Xilinx ISE-DTs. The test results of DP based SPCO unit using Xilinx ISE-DTs are given in Figure 11. A clock pulse signal and Run input signal generated at 10 ns intervals were sent as '1' to the design. After receiving the Run signal, the presented design produces the first results after 360 clock pulse interval. After this clock pulse, it continues to produce results in every 360 clock pulse. The design works according to the 32-bit IEEE-754-1985 floating point standard. However, in order to evaluate the design results more easily, the results are shown in hexadecimal format.

The Place & Route process was performed for the VIRTEX-7 XC7VX485T-2FFG1761 FPGA chip to be utilized in the designed DP based SPCO unit using Xilinx ISE-DTs program. After the Place+Route process, the obtained FPGA chip resource utilization report is presented in Table 2. The maximum operating frequency of the presented design on the Virtex-7 FPGA chip was obtained as 362.608 MHz. In other words, the minimum clock period of the design is 2.758 ns.

#### 4. Conclusions

In this study, using the SPCO, which is one of the CSs presented to the literature, CO designs have been implemented to be utilized in chaos-based engineering applications on two separate platforms with CCII analog electronic circuit element and FPGA chip. The structure used for the CCII-based CO design and the results of the

study are presented. Then SPCO was designed to work on FPGA chips using the DP. The design uses 32-bit floating point representation. The design was coded in VHDL and the designed system was synthesized in Xilinx ISE-DTs program. The designed system has been tested by preparing a test bench in VHDL. In the study, test results obtained from DP based SPCO structure are given. The SPCO unit designed in the last part of the study was synthesized for the VIRTEX-7 FPGA. Source usage values of FPGA chip obtained after the Place+Route of the unit are presented in the study. According to the obtained results, the maximum operating frequency of DP-based SPCO unit on FPGA is approximately 362 MHz. The chaotic signal generator is one of the basic structures used in chaos-based studies and applications. In this study, SPCO designs have been successfully implemented in 2 different platforms as analog-based using CCII and digital-based using FPGA chip. Synchronization, secure communication and Pseudo/True RNG applications can be implemented with DP based SPCO unit proposed in this study in future studies.

#### Declaration

The author(s) declared no potential conflicts of interest with respect to the research, authorship, and/or publication of this article. The author(s) also declared that this article is original, was prepared in accordance with international publication and research ethics, and ethical committee permission or any special permission is not required.

#### References

- Chang, D., Li, Z., Wang, M., and Y. Zeng, *A Novel Digital Programmable Multi-Scroll Chaotic System and Its Application in FPGA-Based Audio Secure Communication*, AEU-International Journal of Electronics and Communications, 2018. **88**(2018): p. 20–29.
- Tuna, M., and C.B. Fidan, *Electronic Circuit Design, Implementation and FPGA-Based Realization of a New 3D Chaotic System with Single Equilibrium Point*, Optik - International Journal for Light and Electron Optics, 2016. **127**(24): p. 11786–11799.

3. Alçın, M., Tuna, M., and İ. Koyuncu, *IQ-Math Based Designing of Fourth Order Runge-Kutta Algorithm on FPGA and Performance Analysis According to ANN Approximation*, International Journal of Advanced Research in Science, Engineering and Technology, 2018. **5**(8): p. 6523–6530.
4. Tuncer, T., *The Implementation of Chaos-Based PUF Designs in Field Programmable Gate Array*, Nonlinear Dynamics, 2016. **86**(2): p. 975–986.
5. Id, A., Shaukat Id, S., Id, A.A., Id, A.E., Aziz, S., Id, S., and J. Ahmad Id, *Chaos Theory and Its Application: An Essential Framework for Image Encryption*, Chaos Theory and Applications, 2020. **2**(1): p. 17–22.
6. Tuna, M., and C.B. Fidan, *A Study on the Importance of Chaotic Oscillators Based on FPGA for True Random Number Generating (TRNG) and Chaotic Systems*, Journal of the Faculty of Engineering and Architecture of Gazi University, 2018. **33**(2): p. 469–486.
7. Bonny, T., and Q. Nasir, *Clock Glitch Fault Injection Attack on an FPGA-Based Non-Autonomous Chaotic Oscillator*, Nonlinear Dynamics, 2019. **96**(3): p. 2087–2101.
8. Avaroğlu, E., Tuncer, T., Özer, A.B., Ergen, B., and M. Türk, *A Novel Chaos-Based Post-Processing for TRNG*, Nonlinear Dynamics, 2015. **81**(1–2): p. 189–199.
9. Akgul, A., Moroz, I., Pehlivan, I., and S. Vaidyanathan, *A New Four-Scroll Chaotic Attractor and Its Engineering Applications*, Optik - International Journal for Light and Electron Optics, 2016. **127**(13): p. 5491–5499.
10. Avaroğlu, E., *Pseudorandom Number Generator Based on Arnold Cat Map and Statistical Analysis*, Turkish Journal of Electrical Engineering & Computer Sciences, 2017. **25**(1): p. 633–643.
11. Garipcan, A.M., and E. Erdem, *A TRNG Using Chaotic Entropy Pool as a Post-Processing Technique: Analysis, Design and FPGA Implementation*, Analog Integrated Circuits and Signal Processing, 2020. **103**(2020): p. 391–410.
12. Akgül, A., Zahid Yıldız, M., Faruk Boyraz, Ö., Güler, E., Kaçar, S., and B. Gürevin, *Microcomputer-Based Encryption of Vein Images with a Non-Linear Novel System*, Journal of the Faculty of Engineering and Architecture of Gazi University, 2020. **35**(3): p. 1369–1385.
13. Bonny, T., Al Debsi, R., Majzoub, S., and A.S. Elwakil, *Hardware Optimized FPGA Implementations of High-Speed True Random Bit Generators Based on Switching-Type Chaotic Oscillators*, Circuits, Systems, and Signal Processing, 2019. **38**(3): p. 1342–1359.
14. Çam Taşkiran, Z.G., and H. Sedef, *Memristör Tabanlı Kaotik Rössler Devresi Gerçeklemesi*, Gazi Üniversitesi Mühendislik-Mimarlık Fakültesi Dergisi, 2019. **35**(2): p. 765–774.
15. Sundarapandian, V., and I. Pehlivan, *Analysis, Control, Synchronization, and Circuit Design of a Novel Chaotic System*, Mathematical and Computer Modelling, 2012. **55**(7–8): p. 1904–1915.
16. Akgul, A., Hussain, S., and I. Pehlivan, *A New Three-Dimensional Chaotic System, Its Dynamical Analysis and Electronic Circuit Applications*, Optik-International Journal for Light and Electron Optics, 2016. **127**(18): p. 7062–7071.
17. Lin, Y., Wang, C., and H. He, *A Simple Multi-Scroll Chaotic Oscillator Employing CCII*s, Optik-International Journal for Light and Electron Optics, 2015. **126**(7–8): p. 824–827.
18. Munoz-Pach, J.M., Campos-Lop, W., Tlelo-Cuau, E., and C. Sanchez-Lo, *OpAmp-, CFOA- and OTA-Based Configurations to Design Multi-Scroll Chaotic Oscillators*, Trends in Applied Sciences Research, 2012. **7**(2): p. 168–174.
19. Bulut, G.G., Emin Şahin, M., and H. Güler, *An Implementation of Chaotic Circuits with Multisim-LabVIEW*, International Advanced Researches and Engineering Journal, 2018. **02**(03): p. 304–308.
20. Dar, M.R., Kant, N.A., and F.A. Khanday, *Realization of Fractional-Order Double-Scroll Chaotic System Using Operational Transconductance Amplifier (OTA)*, Journal of Circuits, Systems and Computers, 2018. **27**(1): p. 1850006.
21. Singh, J.P., Koley, J., Akgul, A., Gurevin, B., and B.K. Roy, *A New Chaotic Oscillator Containing Generalised Memristor, Single Op-Amp and RLC with Chaos Suppression and an Application for the Random Number Generation*, European Physical Journal: Special Topics, 2019. **228**(10): p. 2233–2245.
22. Yu, F., Shen, H., Liu, L., Zhang, Z., Huang, Y., He, B., Cai, S., Song, Y., Yin, B., Du, S., and Q. Xu, *CCII and FPGA Realization: A Multistable Modified Fourth-Order Autonomous Chua's Chaotic System with Coexisting Multiple Attractors*, Complexity, 2020. **5212601**: p. 1–17.
23. Hasan, S., and I.A. Khan, *Multi-Scroll Chaos Generator Using Current Conveyors*, 2009 International Multimedia, Signal Processing and Communication Technologies, 2009. Aligarh, India. p. 229–232.
24. Alçın, M., Pehlivan, İ., and İ. Koyuncu, *Hardware Design and Implementation of a Novel ANN-Based Chaotic Generator in FPGA*, Optik - International Journal for Light and Electron Optics, 2016. **127**(13): p. 5500–5505.
25. Alçın, M., *The Modelling Performance Evolution of Recurrent Neural Networks Having Different Training Functions for Modelling Sprott H Chaotic System*, International Journal on Research Innovations in Engineering Science and Technology(IJRIEST), 2017. **2**(10): p. 563–568.
26. Koyuncu, İ., Oğuz, Y., Çimen, H., Özer, T., and M. Tuna, *Design and Implementation of Artificial Neural Network-Based 3-D Novel Jerk Chaotic Oscillator on FPGA*, 3rd International Conference on Engineering Technology and Applied Sciences, 2018. Skopje, Macedonia. p. 1–6.
27. Alcin, M., Erdogmus, P., and I. Koyuncu, *Artificial Neural Network-Based 4-D Hyper-Chaotic System on Field Programmable Gate Array*, International Journal of Intelligent Systems and Applications in Engineering, 2020. **8**(2): p. 102–108.
28. Vaidyanathan, S., Pehlivan, I., Dolvis, L.G., Jacques, K., Alcin, M., Tuna, M., and I. Koyuncu, *A Novel ANN-Based Four-Dimensional Two-Disk Hyperchaotic Dynamical System, Bifurcation Analysis, Circuit Realisation and FPGA-Based TRNG Implementation*, International Journal of Computer Applications in Technology, 2020. **62**(1): p. 20–35.
29. Koyuncu, İ., Şahin, İ., Gloster, C., and N.K. Sartekin, *A Neuron Library for Rapid Realization of Artificial Neural Networks on FPGA: A Case Study of Rössler Chaotic System*, Journal of Circuits, Systems and Computers, 2017. **26**(01): p. 1750015.
30. Dalkiran, I., and K. Danis, *Artificial Neural Network*

- Based Chaotic Generator for Cryptology*, Turkish Journal of Electrical Engineering & Computer Sciences, 2010. **18**(2): p. 225–240.
31. Alçın, M., Koyuncu, I., Tuna, M., Varan, M., and I. Pehlivan, *A Novel High Speed Artificial Neural Network–Based Chaotic True Random Number Generator on Field Programmable Gate Array*, International Journal of Circuit Theory and Applications, 2019. **47**(3): p. 365–378.
  32. Tuna, M., Karthikeyan, A., Rajagopal, K., Alçın, M., and İ. Koyuncu, *Hyperjerk Multiscroll Oscillators with Megastability: Analysis, FPGA Implementation and A Novel ANN-Ring-Based True Random Number Generator*, AEU-International Journal of Electronics and Communications, 2019. **112**(2019): p. 152941–10.
  33. Rajagopal, K., Akgul, A., Jafari, S., Karthikeyan, A., and I. Koyuncu, *Chaotic Chameleon: Dynamic Analyses, Circuit Implementation, FPGA Design and Fractional-Order Form with Basic Analyses*, Chaos, Solitons & Fractals, 2017. **103**(2017): p. 476–487.
  34. Bonny, T., *Chaotic or Hyper-Chaotic Oscillator? Numerical Solution, Circuit Design, MATLAB HDL-Coder Implementation, VHDL Code, Security Analysis, and FPGA Realization*, Circuits, Systems, and Signal Processing, 2020. p. 1–28.
  35. Dursun, M., and E. Kaşifoğlu, *Design and Implementation of the FPGA-Based Chaotic van Der Pol Oscillator*, International Advanced Researches and Engineering Journal, 2018. **02**(03): p. 309–314.
  36. Karakaya, B., Turk, M.A., Turk, M., and A. Gulen, *Selection of Optimal Numerical Method for Implementation of Lorenz Chaotic System on FPGA*, International Advanced Researches and Engineering Journal, 2018. **02**(02): p. 147–152.
  37. Koyuncu, İ., and H.İ. Seker, *Implementation of Dormand-Prince Based Chaotic Oscillator Designs in Different IQ-Math Number Standards on FPGA*, Sakarya University Journal of Science, 2019. **23**(5): p. 859–868.
  38. Şeker, H.İ., Koyuncu, İ., Tuna, M., and M. Alçın, *Implementation of Dormand Prince Based SEA Chaotic Oscillator Design on FPGA*, V. Science Technology and Innovation Congress, 2019. Alanya, Turkey. p. 303–310.
  39. Senouci, A., Bouhedjeur, H., Tourche, K., and A. Boukabou, *FPGA Based Hardware and Device-Independent Implementation of Chaotic Generators*, AEU-International Journal of Electronics and Communications, 2017. **82**(2017): p. 211–220.
  40. Kizmaz, H., Kocamaz, U.E., and Y. Uyaroğlu, *Control of Memristor-Based Simplest Chaotic Circuit with One-State Controllers*, Journal of Circuits, Systems, and Computers, 2019. **28**(1): p. 1950007.
  41. Koyuncu, İ., Şeker, H.İ., Tuna, M., and M. Alçın, *Dormand-Prince Tabanlı Kaotik Osilatör Tasarımının FPGA Üzerinde Gerçeklenmesi*, International Eurasian Conference on Science, Engineering and Technology, 2018. Ankara, Turkey. p. 1059–1065.
  42. Koyuncu, İ., and A.T. Özcerit, *The Design and Realization of a New High Speed FPGA-Based Chaotic True Random Number Generator*, Computers & Electrical Engineering, 2017. **58**(2017): p. 203–214.
  43. Pehlivan, I., and Y. Uyaroglu, *A New Chaotic Attractor from General Lorenz System Family and Its Electronic Experimental Implementation*, Turkish Journal of Electrical Engineering & Computer Sciences, 2010. **18**(2): p. 171–184.
  44. Pehlivan, İ., and Z. Wei, *Analysis, Nonlinear Control, and Chaos Generator Circuit of Another Strange Chaotic System*, Turkish Journal of Electrical Engineering & Computer Sciences, 2012. **20**(2): p. 1229–1239.

**Research Article**

## Design of polyrod antenna having isoflux radiation characteristic for satellite communication systems

Volkan Akan <sup>a,\*</sup> 

<sup>a</sup>TUBITAK Space Technologies Research Institute, Microwave and Antenna Systems Group, ODTU, Ankara, TR-06800, Turkey

## ARTICLE INFO

*Article history:*

Received 26 May 2020

Revised 25 July 2020

Accepted 12 August 2020

*Keywords:*

Antenna  
Communication  
Satellite

## ABSTRACT

In satellite communication, link margin and therefore antenna radiation characteristics are key factors to ensure providing a robust communication link between space and ground segment. For telemetry/telecommand and payload data transfer, isoflux antennas are employed widely in satellite communication systems to direct electromagnetic wave efficiently. To decrease complexity and manufacturing cost, simple antenna structures are preferred. In this study, after a detailed literature survey, a polyrod antenna has been designed to use in the space segment of Low Earth Orbit satellite communication subsystem. The proposed polyrod antenna has maximum gain at about  $60^\circ$  elevation angle of the antenna. Moreover, its impedance bandwidth is 750MHz (11%) that is fairly adequate to use in high data rate transmitters. By using CST Microwave Studio™ which is a commercially available 3-D electromagnetic time-domain solver, directivity, gain, axial ratio for elevation plane at X-Band, and return loss characteristic have been presented. Based on the obtained results, the designed polyrod antenna can be used where a conical shaped beam radiation pattern is needed.

© 2020, Advanced Researches and Engineering Journal (IAREJ) and the Author(s).

### 1. Introduction

Communication systems on satellites take on various tasks. Those are telemetry/telecommand (TM/TC) transmit and receive tasks, payload data transfer to a ground station, inter-satellite communication, broadcasting service, mobile communication service, etc. as mentioned by Imbriale in [1] and Akan in [2]. Due to this fact, a satellite communication subsystem for the space segment can require different kinds of antennas. Moreover, these antennas should meet harsh space requirements like atomic oxygen, vibration loads during the launch phase, ionizing radiation, extensive temperature differences as explained by Imbriale and Akan et al. in their studies [1-2].

As it is well known, in a communication subsystem, antennas are initial or final elements for a receiver or transmitter, respectively. Due to the requirement of directing electromagnetic energy into the desired area or receiving a coming electromagnetic wave more directive and effectively in a specific way, these electromagnetic energy transducers are key elements for wireless telecommunication systems. As known, artificial satellites have limited power budget and therefore, required high

effective isotropic power (EIRP) for RF transmitters and G/T for receivers should be generally compensated by the antenna on the satellite platform. Furthermore, communication systems should provide a positive link margin to enhance vigorous communication link and link budget.

To compensate for increasing free space loss at the edge coverage (EoC) communication system of the satellite platform, an antenna having isoflux radiation characteristic or steerable antennas are employed. To avoid complexity, additional power consumption, and lower reliability, passive isoflux antennas are usually preferred. Therefore, there are many studies for antennas that have isoflux radiation characteristics in the open literature [3-12]. Huang presented that one can obtain a conical shaped beam using higher-order mode excitation of circular microstrip antenna in [7]. In that study, to obtain a circular polarization two probes with  $90^\circ$  phase difference are used. However, Nakano suggested a simple version of this higher-order mode excited circular patch antenna with a circular polarization feature in [8]. In this antenna, there are two perturbation notches to get a

\* Corresponding author. Tel.: +90-312-210-1310 ; Fax: +90-312-210-1315.  
E-mail address: [volkanakan@hotmail.com](mailto:volkanakan@hotmail.com) (V. Akan)  
ORCID: 0000-0001-7774-8752  
DOI: 10.35860/iarej.742702

circularly polarized electromagnetic wave. There are also antennas that have higher circular polarization purity i.e. lower axial ratio compared to microstrip antennas. Two of them are bifilar and quadrifilar helix antennas as presented by Zackrisson, Choi et al. and Colantonio [4-6]. Despite they have wide beamwidth, maximum gain values of them are generally low. Therefore, they are often used for TM/TC communication subsystems of LEO satellites. Moreover, the production stages of these antennas are quite difficult, since their radiation characteristic strictly depends on the physical parameters of the helix structure. Another important point is that some mechanical reinforcement can be required to enhance their strength against to vibration loads of the launch phase. Because in some applications, helix length can be long while its diameter is quite small which can make this antenna vulnerable to the vibration loads. In [11], X-Band choke ring horn antenna was designed and manufactured to use on SWOT mission of NASA as indicated by Chahat et al. The designed antenna has isoflux radiation pattern with circular polarization at X-Band. Another X-Band isoflux antenna design was presented by Fallahzadeh et al. in [12] to obtain a maximum gain at  $62.5^{\circ}$  elevation angle of the antenna.

Polyrod or dielectric rod antennas have been widely used for different applications like wireless communication, since 1939 as stated by Abumunshar and Sertel in [13]. They can also be employed at millimeter-wave integrated circuits to utilize the surface waves [13]. Kobayashi et al. designed a tapered dielectric rod antenna operating at 81.5GHz as indicated in [14]. In another study, a dielectric rod antenna was designed and used for chip to chip communication at W-Band by Ghassemi and Wu in [15]. 3-D printing technique which is a today's technology, can also be applied easily to manufacture polyrod antennas as presented by Huang et al. in their studies [16]. In that paper, the authors designed a wideband circularly polarized dielectric rod antenna that operates between 4.05GHz and 7.55GHz. Then it was manufactured using 3-D printer Zortrax M200 and Flashforge Guider IIs. Polyrod antennas are not only used as single element radiator but also used to form antenna arrays. By Shokouhi and Firouzeh, linear array of dual polarized slot coupled dielectric rod radiators was proposed in their study [17].

Polyrod antennas excited by a circular horn antenna support  $TE_{11}$  antenna as mentioned by Milligan [18]. This  $TE_{11}$  mode also excites the hybrid mode of  $HE_{11}$ . In [19], a rectangular dielectric rod antenna fed by parallel strip line was proposed by Hou et al. The operating frequency band of the antenna was 5.4 to 6.6GHz as mentioned by the authors. Therefore, this study indicates that dielectric rod antennas can be fed by different types of transmission lines. The dielectric rod antennas are also utilized for pulsed power systems as highlighted by Petrella et al. in [20]. In their study, they designed a polyrod antenna that can generate 500 ps pulse with an amplitude of 600 V/cm

for a 25 kV input from the pulse transformer to stimulate biological tissues. There are different techniques to enhance bandwidth of a dielectric rod antenna. One of them is presented by Abumunshar and Sertel in [13]. In that study, feed and radiation tapering sections were used in order to get 5:1 impedance and radiation bandwidth that covers 6-30GHz as shown in [13]. So the designed polyrod antenna has an ultra-wide bandwidth. However, there are very limited published study in the literature about polyrod or dielectric rod antennas to use in satellite communication systems as isoflux radiator. The best known study was published by King et al. [21].

To benefit high radiation efficiency, wide bandwidth, and stable radiation pattern characteristic of the polyrod antenna, in this study a modified polyrod antenna design is proposed where a horn antenna structure can be used with a simple geometry of dielectric to maximize the directivity at high elevation angles of the antenna. As it is well known that a horn antenna and conical dielectric part can be easily manufactured today on a computer numerical control (CNC) milling machine. Furthermore, due to its proportional structure, this antenna is quite robust against vibration load. Another advantage of the polyrod antenna is that its maximum gain elevation angle can be modified by altering the geometry of the conical dielectric part. Thus, an isoflux polyrod antenna that has a maximum gain at about  $\pm 60^{\circ}$  elevation angles has been designed to get an isoflux radiation characteristic to satisfy the link budget requirements of LEO satellite communication systems that operate at X-Band.

First of all, in part two, the importance and the reason of isoflux radiation pattern requirement for LEO satellite communication link are discussed. Afterwards in part three, polyrod antenna has been explained and a basic study and its results are presented. In addition, how the radiation characteristic changes with respect to some varying physical dimensions is studied in this part. Then an optimized polyrod antenna which has maximum gain at higher elevation angle has been proposed and its directivity and axial ratio pattern results are presented. The obtained results are promising to use in space segment for satellite communication, particularly for payload data transfer.

## 2. Importance of Isoflux Radiation Pattern for Satellite Communication

As mentioned in the previous section, at the EoC more EIRP is needed to reimburse increasing free space loss. For this recompense, increasing output RF power can cost too much, since there would be needed more expensive RF signal amplifying section like Travelling Wave Tube Amplifier (TWTA) or solid-state amplifier component and also it leads to more DC power consumption. Instead of increasing RF output power, there is a passive solution: this is to use an antenna that has isoflux radiation pattern. A

simple geometrical calculation can be given to define change of range with respect to the elevation angle of a satellite. As shown in Figure 1, slant range relation between satellite and ground station can be evaluated using earth radius  $R$  (equals to about 6378km), satellite altitude  $h$ , antenna elevation angle  $\theta$ , and satellite elevation angle with respect to horizon  $\alpha$ .

Then utilizing cosine law on this geometry Slant Range can be approximated for the EoC assuming the ground station is in line of sight of the satellite as below

$$Slant\ Range = [R^2 + (R + h)^2 - 2R(R + h) \cos \gamma]^{1/2} \quad (1)$$

Furthermore, using sine law, the relation between the antenna elevation angle (on satellite) and elevation angle of the satellite can be given as

$$\frac{R}{\sin \theta} = \frac{R+h}{\sin(90+\theta)} \quad (2)$$

Based on these relations, change of the antenna elevation angle (on satellite) versus the elevation angle of the satellite can be demonstrated as given in Figure 2. From Figure 2, it is obvious that the antenna elevation angle equals zero when the ground station is at the nadir point of the satellite i.e. the satellite is exactly on the ground station. Besides, free space loss can be calculated from the Friis transmission equation using slant range relation. It is written as;

$$FSL = \left( \frac{4\pi\ Slant\ Range}{\lambda} \right)^2 \quad (3)$$

In this equation,  $\lambda$  is the wavelength for operating frequency of the communication link between the satellite and the ground station. Using Equation (3) and Equation (2) free space loss has been evaluated with respect to the elevation angle of the satellite as presented in Figure 3.

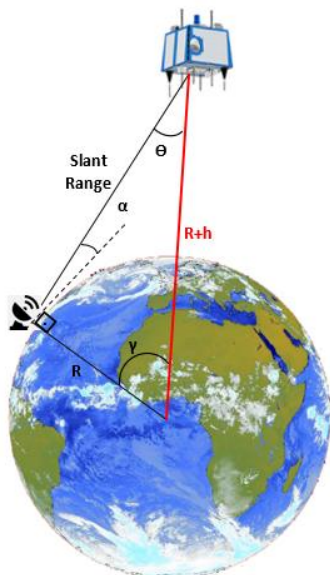


Figure 1. Geometrical illustration of slant range, antenna elevation angle, and satellite elevation angle

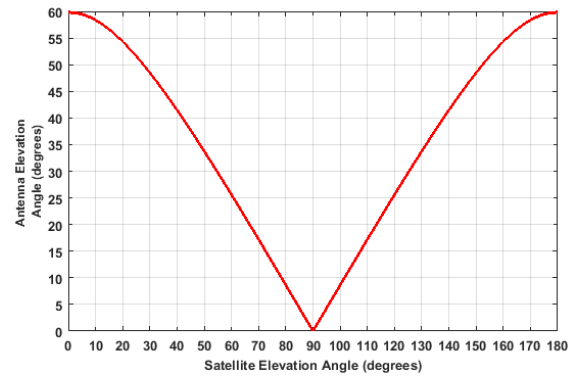


Figure 2. Evaluated antenna elevation angle for the given satellite elevation angle

As expected minimum free space loss occurs at 90° value of the satellite elevation angle, since the distance between the satellite and ground station is minimum. However, it is the maximum at 0° and 180° values of the satellite elevation angle where the distance reaches its maximum value.

### 3. Polyrod Antenna

In this study, a polyrod antenna has been designed and analyzed to get isoflux coverage for satellite communication systems. Comprehensive experimental studies have been carried out by Mueller and Mallack as given in [22, 23] for the analysis of the polyrod antenna. A polyrod antenna that has cross-sectional dimensions in the order of a wavelength behaves like a dielectric lens. Particularly, assured laws of this behavior have been found by King et al. and Wilkes who are the researchers of the Applied Physics Laboratory of the Johns Hopkins University [21, 24]. Besides, in [22], King obtained a shaped beam radiation pattern to use on satellite platforms by using Silver’s analytical beam synthesis approach for circular aperture antenna given in [25]. In [21], the easiness of manufacturing polyrod antenna is especially highlighted. For this antenna, a dielectric rod exceeds the flare of a conical horn antenna and then its diameter is decreased gradually down to the defined value as indicated in Figure 4. The dielectric material is chosen as polystyrene that is a kind of aromatic hydrocarbon polymer for the rod part of this antenna structure.

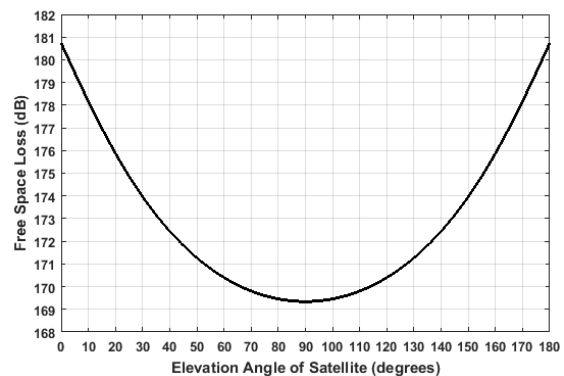


Figure 3 Evaluated free space vs. Elevation angle of the satellite at operating frequency of 7GHz

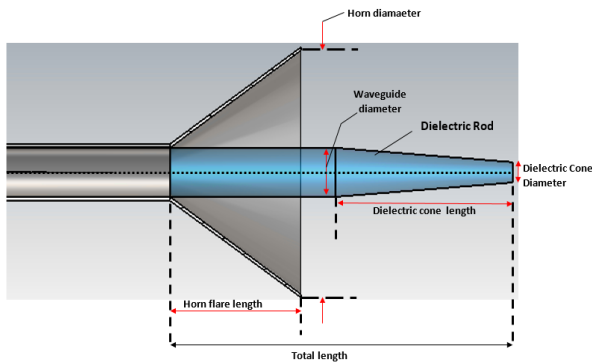


Figure 4. Shaped beam dielectric rod antenna [21]

The dimensional parameters of the antenna are shown in Figure 4.

Related physical dimensions of the polyrod antenna studied by King et al. are given in Table 1 [21]. Polystyrene’s dielectric permittivity and loss tangent are 2.5 and 0.00033, respectively.

Using the suggested dimensions given in [21] simulation result for normalized directivity of the antenna at 7.3GHz is given in Figure 5 by utilizing circularly polarized wave excitation. Nonetheless, the same results could not be obtained. The obtained directivity values are about 10.6dBi and 10.1dBi at  $\theta = \pm 20^\circ$  by simulation. Given directivity values are about 12.42dBi, in [21]. It is considered that the reasons for these discrepancies are tolerances of manufacturing and dielectric material permittivity.

For different physical dimensions, simulations have been realized to see the effects of them onto antenna radiation characteristics. Foremost, effect of flare has been studied. For different values of horn radius simulations have been carried out and results are presented in Figure 3. But, as shown in Figure 6, the effect of horn dimension is poor to widen the beamwidth.

Table 1. Polyrod antenna dimensions given in [21]

Dimensions	Inch (mm)
Horn Diameter (Flare Diameter)	5.1 (129.54)
Waveguide Diameter	1.35 (34.29)
Dielectric Cone Diameter	0.564 (14.33)
Horn Flare Length	3.72 (94.49)
Total Length	9.72 (246.89)

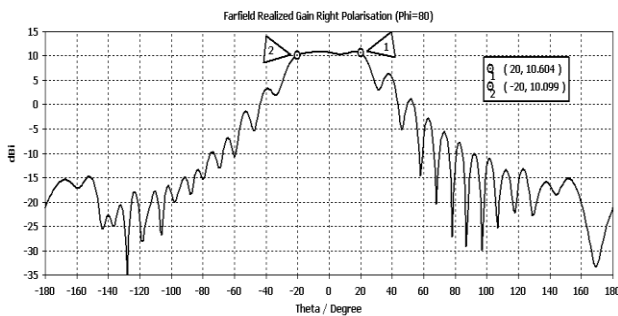


Figure 5. Simulation result for directivity pattern of shaped beam dielectric rod antenna at 7.3GHz using physical dimensions in [21]

Secondly, simulations have been iterated by changing the dielectric rod length, since it is apparent that the dielectric rod is dominant to shape the beam from the study given in [24].

According to these simulations, dielectric rod length is seemingly effective to shape the beam as shown in Figure 7.

#### 4. Design of Polyrod Antenna having Wider Beamwidth

Depending upon orbit height of a satellite elevation angle where the maximum gain is obtained can be a different value. For example, for (Low Earth Orbit) LEO and Middle Earth Orbit (MEO) satellites, this elevation angle will be higher. According to an example of link budget where 800km orbit height, it will be required a maximum directivity at approximately  $60^\circ$ . Therefore, after many parameter sweeps and optimization process maximum directivity at  $\theta = 58^\circ$  has been accomplished. The cross-sectional view and dimension parameters of the designed polyrod antenna are shown in Figure 8. As dielectric material, another low loss substance PTFE (Teflon) has been selected. Its dielectric permittivity and loss tangent are 2.1 and 0.0002, respectively. In addition, a septum polarizer or dual feed with  $90^\circ$  phase difference can be used to form a circularly polarized wave at output of the antenna. Throughout the simulations a septum polarizer has been utilized. Nonetheless, for the sake of brevity its design is not given in this article.

In this structure, the dielectric rod consists of two parts. The first one which is inside the flare follows shape of the cone of horn and then the second part which is outside the horn and its circular area becomes smaller gradually.

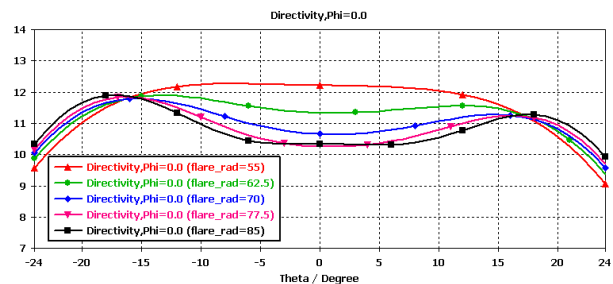


Figure 6. Directivity pattern of polyrod antenna for different flare radius values obtained by simulation at 7GHz

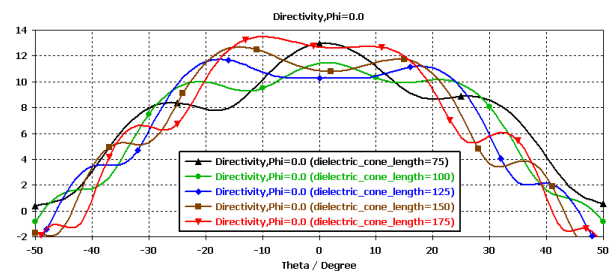


Figure 7. Directivity pattern of polyrod antenna for different dielectric cone lengths at 7GHz



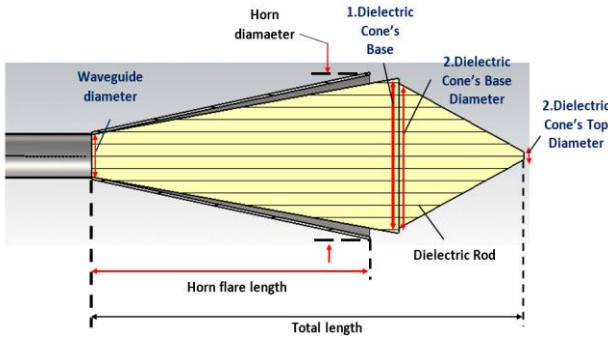


Figure 8. Longitudinal cross-section view and dimensions of the designed polyrod antenna in this study

As stated by Mueller and Wilkes [22, 24], the geometrical transition between first and second dielectric cone is effective to shape the beam of the antenna and it behaves similar to lens antennas. The physical dimensions of the designed antenna are tabulated in Table 2.

The acquired circularly polarized radiation pattern is presented in Figure 9 for the operating frequency of 7GHz. As shown in this figure second maximum (after the boresight) directivity value is 4.96dBic obtained at  $\theta = -58^\circ$  for  $\phi=0^\circ$  cut plane.

However, a tolerable asymmetry is determined again with respect to  $\theta = 0^\circ$ . It's tolerable because the directivity at  $\theta = 58^\circ$  is about 4.1dBic. It is evident that once beamwidth widens then the maximum directivity decreases as expected. In Figure 10, the variation of axial ratio with respect to  $\theta$  at  $\phi=0^\circ$  cut is seen. Particularly, for  $\theta$  values where maximum directivity is obtained, axial ratio values are lower than 1.5dB. Moreover, between  $\theta$  angle values where the maximum directivity is obtained, the axial ratio value is almost smaller than 10dB. In that manner, its axial ratio purity is at a reasonable level as a circularly polarized antenna.

Table 2. Dimensions of the designed polyrod antenna in this study

Dimensions	(mm)
Horn Diameter	130
Waveguide Diameter	34.29
1 <sup>st</sup> Dielectric Cone Base Diameter	124.286
2 <sup>nd</sup> Dielectric Cone Base Diameter	116.286
2 <sup>nd</sup> Dielectric Cone Top Diameter	6
Horn Flare Length	240
Total Length	373

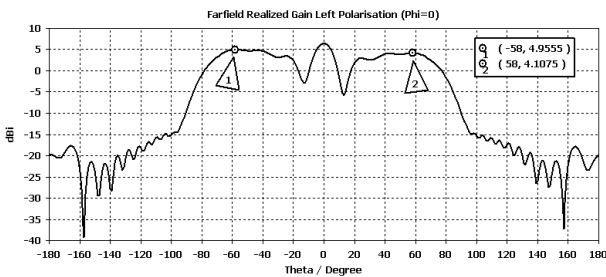


Figure 9. Directivity of the designed antenna at  $\phi=0^\circ$  cut plane.

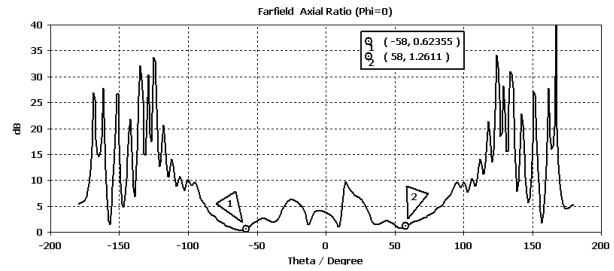


Figure 10. Axial ratio of the designed antenna at  $\phi=0^\circ$  cut plane

Besides, 3-D radiation pattern for directivity is seen in Figure 11. According to this figure conical shaped beam is obvious.

The return loss of the antenna has also been obtained by the simulation and it is given in Figure 12. This result demonstrates 10dB return loss bandwidth of the antenna is at a good value range for the defined frequency band of 7-7.5GHz.

In Table 3, obtained antenna characteristics have been compared to results of some studies available in the literature. As seen from Table 3, in [11, 12] choke ring horn antenna was employed to get isoflux pattern which have a maximum directivity/gain at  $60^\circ$  and  $62.5^\circ$  elevation angle, respectively.

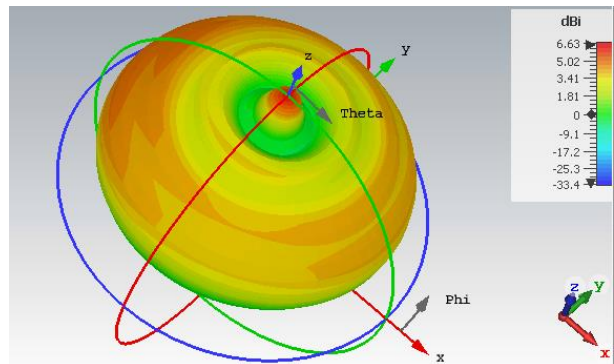


Figure 11. 3-D radiation directivity pattern of the designed antenna

Table 3. Comparison of the proposed polyrod antenna with the studies available in the literature

	This Study	[21]	[11]	[12]
Antenna Type	Polyrod	Polyrod	Choke ring horn	Choke ring horn
Radiation Characteristic	Isoflux	Isoflux	Isoflux	Isoflux
Elevation angle where the max directivity obtained	$58^\circ$	$20^\circ$	$60^\circ$	$62.5^\circ$
Operating Frequency Band	X-Band	X-Band	X-Band	X-Band
Maximum Gain	3.8dBic	Not available	4.9dBic	2.5dBic
Polarization	Circular	Circular	Circular	Circular

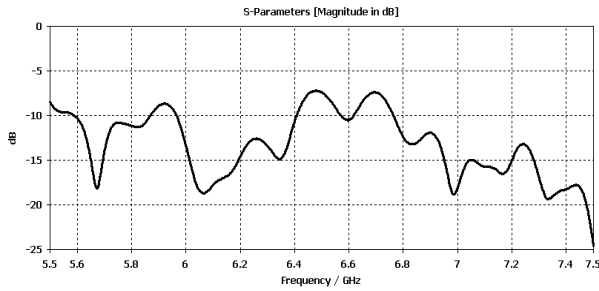


Figure 12. Return loss of the designed antenna.

There is a slightly difference of the elevation angles where the maximum gain is obtained for this study and the antennas given in [11, 12]. Furthermore, the choke ring antenna studied in [11] has maximum gain of 4.9dBic. The proposed polyrod antenna has 3.8dBic maximum gain in this study. This is higher than maximum gain of the antenna presented in [12].

In this paper, a shaped beam polyrod antenna having maximum directivity at about  $60^\circ$  has been designed and presented. According to the author's best knowledge there is only one study about isoflux polyrod antenna in the literature. This is the paper published by King et al. [21]. Hence, a direct comparison couldn't be realized for obtained results of the proposed antenna structure in this paper. However, it should be noted that the proposed polyrod antenna's maximum directivity has been obtained at a higher elevation angle value compared to the angle obtained in King's study [21]. Therefore, the proposed antenna is appropriate to utilize it for LEO satellite communication subsystem. Its 10dB return loss bandwidth is about 750MHz (about 11%) and it keeps the radiation pattern stable through this frequency band. Since microstrip patch, bifilar and quadrifilar helix antennas have resonant characteristic, their operating frequency bands are limited approximately 1.5% without an impedance matching. Colantonio et al. [6] designed a stepped coaxial matching circuit to enhance the operating bandwidth of the bifilar antenna. However, in this study there is no need to an additional matching circuit like that.

## 5. Conclusions

As mentioned in the previous parts of this paper, to widen coverage area of antennas on satellite platforms isoflux radiation characteristic is needed for TM/TC and high throughput payload data transfer communication systems. In this way, link margin of a communication link between satellite and the ground station can be kept above 0dB.

In the open literature, there are many different types of antennas to reach this goal. One of them is polyrod antenna but the given results are only for narrow beamwidth specification i.e. for higher satellite orbits. In this paper, a polyrod antenna that has an isoflux radiation characteristic has been designed and analyzed using CST Microwave Studio<sup>TM</sup> which is a commercially available 3-D electromagnetic solver, approximately at  $\theta = 60^\circ$ . This antenna can radiate circularly polarized electromagnetic

wave at 7GHz and it has a conical-shaped pattern. By changing the physical parameters of the dielectric rod and the horn, its theta value where maximum directivity need can be varied. Compared to the designed polyrod antenna by King [21], the proposed antenna has maximum directivity at higher elevation angle (for the antenna) which is subtended to lower elevation angle for the satellite as evaluated in Figure 2. In this way, the coverage area of polyrod antenna has been increased to use on satellites which orbit in lower altitudes. In addition, the proposed polyrod antenna has been compared to choke ring horn antennas available in the literature. Based on these comparisons, the proposed antenna has promising electrical characteristic. It should be also noted that manufacturing process of a choke ring horn antenna is more difficult than the polyrod antenna and this is an important factor which can lead higher manufacturing costs. As future work, manufacturing of prototype, and measurements of the designed antenna will be realized to verify the simulation results. Then, it will be employed for the next satellites to be designed and manufactured at TUBITAK Space Technologies Research Institute.

## Declaration

The author declared no potential conflicts of interest with respect to the research, authorship, and/or publication of this article. The author also declared that this article is original, has been prepared in accordance with international publication and research ethics, and ethical committee permission or any special permission is not required.

## Nomenclature

$\alpha$	: Elevation angle of satellite
C-Band	: Frequency band between 4 and 8GHz
DC	: Direct Current
EIRP	: Effective Isotropic Radiated Power
EoC	: Edge of Coverage
FSL	: Free Space Loss
G/T	: Receiver gain over noise temperature ratio
$\gamma$	: Central angle
$h$	: Altitude of satellite
$\lambda$	: Wavelength of RF signal at the operating frequency
$R$	: Radius of the Earth
$\theta$	: Elevation angle of the antenna on a satellite
S-Band	: Frequency band between 2 and 4GHz
TM/TC	: Telemetry and Telecommand
W-Band	: Frequency band between 75 and 110GHz
X-Band	: Frequency band between 8 and 12GHz

## References



1. Imbriale, W.A., S. Gao, and L. Boccia., *Space Antenna Handbook*. 2012, USA: John Wiley & Sons, Inc.
2. Akan, V., and E. Yazgan, *Antennas for Space Applications: A Review*. Book chapter in *Advanced Radio Frequency Antennas for Modern Communication and Medical Systems* (Ed. A. Saban), 2020, UK: IntechOpen. p. 139-171.

3. Akan, V. and E. Yazgan, *Analysis and design of circularly polarized and frequency tunable microstrip antenna having conical radiation pattern characteristic*, in 32nd ESA Antenna Workshop on Antennas for Space Applications 2010: Noordwijk, Netherlands, p.175-177.
4. Zackrisson, J., *RUAG space activities in the TT&C, GNSS and data-downlink antenna field*, in 11th European Conference on Antennas and Propagation EUCAP2017: Paris, France, p.529-533.
5. Choi, E.C, J. W. Lee, and T.K. Lee, *Modified S-band satellite antenna with isoflux pattern and circularly polarized wide beamwidth*. IEEE Antennas and Wireless Propagation Letters, 2013.**12**(10), p. 1319-1322.
6. Colantonio, D. and C. Rosito, *A spaceborne telemetry loaded bifilar helical antenna for LEO satellites*, in SBMO/IEEE MTT-S International Microwave and Optoelectronics Conference (IMOC) 2009: Belem, Brazil, p.741-745.
7. Huang, J., *Circularly polarized conical patterns from circular microstrip antennas*. IEEE Transactions on Antennas and Propagation, 1984.**32**(9), p. 991-994.
8. Nakano, H., *Singly-fed patch antenna radiating a circularly polarized conical beam*. Electronics Letters 1990.**26**(10), p. 638-640.
9. Cahill, R., I. Cartmell, G. Dooren, K. Clibbon, and C. Sillence, *Performance of shaped beam quadrifilar antennas on the METOP spacecraft*. IEE Proceedings - Microwaves, Antennas and Propagation, 1998.**145**(1), p.19-24.
10. Akan, V. *Electrically small printed antenna for applications on CubeSat and nano-satellite platforms*. Microwave Opt Technol Lett 2015.**57**(4), p.891-896.
11. Chahat, N., L. R. Amaro, J. Harrell, C. Wang, P. Estabrook, and S. A. Butman, *X-Band Choke Ring Horn Telecom Antenna for Interference Mitigation on NASA's SWOT Mission*, IEEE Transactions on Antennas and Propagation, 2016.**64**(6), p.2075-2082.
12. Fallahzadeh, M., H. Aliakbarian, A. Haddadi, and S. Radiom, *Beam shaping of X-band stepped choke ring antenna for LEO satellite applications*. IEEE Aerospace and Electronic Systems Magazine, 2018.**33**(10), p.34-39.
13. Abumunshar, A. J. and K. Sertel, *5:1 Bandwidth dielectric rod antenna using a novel feed structure*. IEEE Transactions on Antennas and Propagation, 2017.**65**(5), p. 2208-2214.
14. Kobayashi, S. R. Mittra, and R. Lampe, *Dielectric tapered rod antennas for millimeter-wave applications*, IEEE Transactions on Antennas and Propagation, 1982.**30**(1), p.54-58.
15. Ghassemi, N. and K. Wu, *Planar dielectric rod antenna for gigabyte chip-to-chip communication*, IEEE Transactions on Antennas and Propagation, 2012.**60**(10), p.4924-4928.
16. Huang, J., S. J. Chen, Z. Xue, W. Withayachumnankul, and C. Fumeaux, *Wideband circularly polarized 3-D printed dielectric rod antenna*, IEEE Transactions on Antennas and Propagation, 2020.**68**(2), p.745-753.
17. Shokouhi, F. and Z. H. Firouzeh, *Linear array of dual-polarised slot-coupled dielectric-rod elements for wireless applications*, IET Microwaves, Antennas & Propagation, 2019.**13**(13), p.2284-5474.
18. Milligan, T.A., Modern Antenna Design. 2005, USA: IEEE Press and Wiley Interscience.
19. Hou, Y. Li, Z. Zhang, and Q. Xue, *Rectangular dielectric rod antenna fed by air-substrate parallel strip line*. IEEE Transactions on Antennas and Propagation, 2019.**67**(10), p. 6308-6316.
20. Petrella, R. A., K. H. Schoenbach, and S. Xiao, *A dielectric rod antenna driven by a pulsed power system*. IEEE Transactions on Dielectrics and Electrical Insulation, 2017.**24**(4), p. 2157-2163.
21. King, H., J. Wong, and C. Zamites, *Shaped-beam antennas for satellites*. IEEE Transactions on Antennas and Propagation 1966.**14**(5), p. 641-643.
22. Mueller, G. E. and W. A. Tyrrell, *Polyrod antennas*. The Bell System Technical Journal, 1947.**26**(4), p.837-851.
23. Mallach, P., *Dielectric radiators for dm and cm waves*. Intelligence Interrogation Report, Berlin, Combined Intelligence Objectives Subcommittee 1947: Berlin Germany, p.1567-1589.
24. Wilkes, G., *Wavelength lenses*. Proceedings of the IRE, 1948.**36**(2), p.206-212.
25. Silver, S., *Microwave Antenna Theory and Design*. 1949, New York: McGraw-Hill.



## Research Article

# PAPR reduction using selective mapping scheme in universal filtered multicarrier waveform

Şakir Şimşir <sup>a,\*</sup>  and Necmi Taşpınar <sup>b</sup> 

<sup>a</sup>Nevşehir Hacı Bektaş Veli University, Department of Electrical and Electronics Engineering, Nevşehir, 50300, Turkey

<sup>b</sup>Erciyes University, Department of Electrical and Electronics Engineering, Kayseri, 38039, Turkey

### ARTICLE INFO

#### Article history:

Received 30 April 2020

Revised 31 May 2020

Accepted 06 July 2020

#### Keywords:

Peak to average power ratio

Selective mapping

Solid state power amplifier

Universal filtered multicarrier

5G

### ABSTRACT

In this paper, the selective mapping (SLM) technique possessing the powerful and distortionless peak to average power ratio (PAPR) reduction capability was employed in universal filtered multicarrier (UFMC) waveform that is considered as one of the most promising fifth generation (5G) waveform candidates in order to provide a solution to the PAPR issue encountered in the related waveform. Owing to our SLM-based PAPR reduction implementation performed by employing the SLM scheme between the quadrature amplitude modulation (QAM) mapping and bandwidth-subdivision operations at the transmitter side, successful PAPR reduction results were achieved in a straightforward and effective manner. In the simulations, the effect of the related way of SLM application on alleviating the PAPR and spectral leakages of the UFMC signal amplified via the solid state power amplifier (SSPA) was investigated for various number of phase factor combinations. Besides, the impact of SLM on the bit error rate (BER) of the UFMC waveform was analyzed for varied values of SSPA parameters called smoothness ( $p$ ) and input back off (IBO) controlling the linearity and operation point of the SSPA, respectively.

© 2020, Advanced Researches and Engineering Journal (IAREJ) and the Author(s).

## 1. Introduction

Universal filtered multicarrier (UFMC) [1] is a newly proposed waveform having the potential to replace the conventional orthogonal frequency division multiplexing (OFDM) which is unable to provide the next generation telecommunication standards. The disadvantages such as the requirement of synchronization, sensitivity to frequency offsets and the problem of high side lobes posing a real obstacle for OFDM to be employed in the fifth generation (5G) systems were successfully resolved by the UFMC while maintaining the key features of the conventional OFDM. In the UFMC scheme, the whole bandwidth is divided into multiple sub-bands to be filtered, fragmentally. Thanks to the filtering per sub-band operation, it is possible to use low length filters making the UFMC suitable for short burst communication. Moreover, the out of band (OOB) radiation which makes any waveform vulnerable to the problem of inter carrier interference (ICI), can be alleviated significantly by the UFMC scheme. Having the low side lobes enhances the

suitability of UFMC waveform to be used in the fragmented spectrum. As well as these superior features, possessing the fundamental OFDM features makes the UFMC waveform quite flexible to be used in multiple services [2-4].

Due to the fact that UFMC is a kind of waveform using multicarrier transmission strategy as the OFDM waveform, the aforementioned superior features don't prevent the UFMC from being exposed to the high peak to average power ratio (PAPR) problem. As known, a nonlinear high power amplifier (HPA) is employed at the transmitter end in order to amplify the signals prior to the transmission process and such amplifiers which are preferred in real applications cannot perform a healthy amplification out of a certain range. Therefore, the high PAPR signals which push the related type of amplifiers to exceed the linear amplification range and reach to the saturation region cannot be amplified without any degradation which results in the increase of both OOB radiation and bit error rate (BER). In order to minimize

\* Corresponding author. Tel.: +90 (384) 228 1000 - 15066; Fax: +90 (384) 228 11 23.

E-mail addresses: [sakirsimsir@nevsehir.edu.tr](mailto:sakirsimsir@nevsehir.edu.tr) (Ş. Şimşir), [taspinar@erciyes.edu.tr](mailto:taspinar@erciyes.edu.tr) (N. Taşpınar)

ORCID: 0000-0002-1287-160X (Ş. Şimşir), 0000-0003-4689-4487 (N. Taşpınar)

DOI: 10.35860/iarej.730126

such signal distortions, many type of PAPR reduction algorithms such as tone injection (TI) [5], active constellation extension (ACE) [6], selective mapping (SLM) [7, 8], tone reservation (TR) [9], clipping and filtering [10], coding [11], partial transmit sequence (PTS) [12, 13] and interleaving [14] were suggested in the literature.

In case of considering the aforementioned classical PAPR reduction algorithms given in [5-14], SLM technique takes part in the most prominent ones with its significant PAPR reduction capability. The SLM technique provides an efficient and distortionless PAPR reduction by multiplying the original quadrature amplitude modulation (QAM) modulated data sequence with the certain number of alternative phase rotation factor combinations to generate different candidate signals to be transmitted and picking the one with minimal PAPR for transmission [7, 8]. In this study, the SLM technique which was primarily suggested for the conventional OFDM was flawlessly applied to the UPMC waveform.

Some of the works handling the PAPR issue in the UPMC signal are as follows [15-18]: Baig et al. [15] embedded a type of linear precoder based on discrete Hartley transform to the transmitter side of the UPMC scheme to eliminate its PAPR problem. Taşpınar and Şimşir [16] suggested a practical and effective way of implementing PTS-based PAPR alleviation in the UPMC transmitter. In the related paper, they gave detailed mathematical expressions clarifying the operations performed in the PAPR minimization process. Tipan et al. [17] compared some types of clipping techniques to each other on the basis of their achievements on the amount of PAPR improvement in the UPMC transmission signal. In the same paper, an investigation regarding how much effect each of the related clipping methods has on the BER results of the UPMC waveform was also carried out. Rong et al. [18] applied the PTS to the UPMC waveform in a high complex manner and the complexity of the related application was reduced without causing almost any performance lost in the PAPR reduction process.

The outline of our paper is as follows: In Section 2, the acquisition of UPMC signal was described and the PAPR definition of the related signal was given. In Section 3, the PAPR improvement using SLM technique in the UPMC waveform was explained in detail. In Section 4, the simulation results were investigated and at last, the article was finished by yielding the conclusions of our study in Section 5.

## 2. UPMC Signal Acquisition and PAPR Definition

The UPMC signals are produced by fulfilling the transmitter operations demonstrated in Figure 1 via the block diagram [1-4].

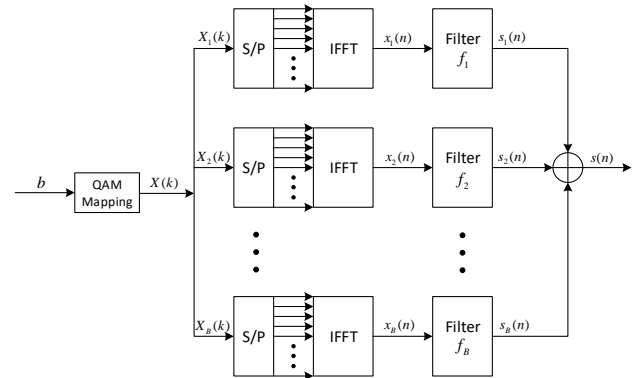


Figure 1. Signal generation at the UPMC transmitter

As clearly understood from the Figure 1, the UPMC transmitter operations start with modulating the information bits by the QAM modulator. Then the QAM symbols obtained from the modulator output is allocated to the certain positions in the multiple sub-bands that are acquired by dividing the whole band into the multiple parts with certain sizes. Subsequent to the inverse fast Fourier transform (IFFT) operation performed on each symbol group, the time domain signal belonging to the  $b$ th sub-band is obtained as follows [16]:

$$x_b(n) = \frac{1}{\sqrt{N}} \sum_{k=0}^{N-1} X_b(k) e^{j2\pi kn/N} \quad (1)$$

$$; 0 \leq n \leq N-1; \quad 1 \leq b \leq B$$

In Equation (1),  $X_b(k)$  represents the  $b$ th sub-band frequency domain signal.  $N$ ,  $k$  and  $B$  denote the subcarrier number, subcarrier indices and the total sub-band number, respectively. Following the operation of cyclic prefix to the time domain signals  $x_b(n)$ , the related signals are filtered one by one through the finite impulse response (FIR) filters and then added together to generate the UPMC signal specified by  $s(n)$ . Hereby, the PAPR definition of the time domain signal acquired from the UPMC transmitter output is expressed in the following manner [16]:

$$PAPR(dB) = 10 \log_{10} \frac{\max_{0 \leq n \leq N+L_{CP}+L_f-1} |s(n)|^2}{E[|s(n)|^2]} \quad (2)$$

where  $L_{CP}$  and  $L_f$  represent the lengths of cyclic prefix and FIR filter, respectively.

## 3. SLM-Based PAPR Improvement in UPMC Signal

Our way of applying the SLM technique [7, 8] to the UPMC transmitter was expressed visually in Figure 2. As demonstrated in Figure 2, in the first instance, the

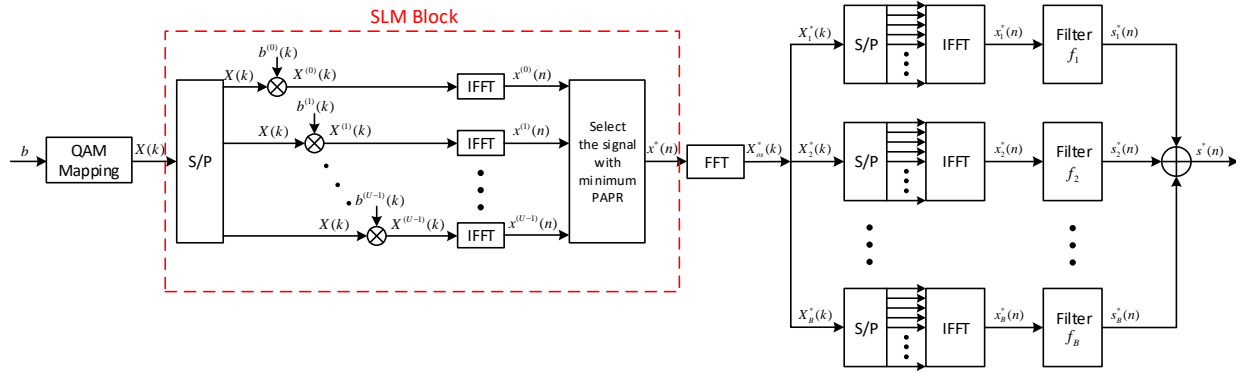


Figure 2. The block diagram of PAPR reduction process employing SLM technique in the UPMC waveform

information data acquired from the output of QAM modulator is given to the input of SLM block. The signals optimized by the SLM algorithm are then subjected to the fast Fourier transform (FFT) process in order to make the related signals suitable for being applied to the UPMC transmitter input. The frequency domain data sequence acquired from the output of FFT block are given to the input of UPMC transmitter. Finally, the signals achieved from the UPMC transmitter output will possess the minimized PAPR values. The operations performed for achieving the UPMC signal with minimum PAPR employing the SLM technique are clarified below:

At first, the information bits are subjected to any type of QAM modulation and in consequence of this, the following data sequence consisting of QAM symbols is obtained:

$$X(k) = [X(0), X(1), \dots, X(N-1)] \quad (3)$$

The sequence of  $X(k)$  is then multiplied by the  $N$  length alternative phase rotation factor sequences  $b^{(u)}(k) = [b^{(u)}(0), b^{(u)}(1), \dots, b^{(u)}(N-1)]$  generated randomly where  $b^{(u)}(k) \in \{1, -1\}$ ,  $u = 0, 1, \dots, U$ .  $U$  specifies the number of randomly generated phase factor combinations. Following the multiplication process, the phase rotated data sequence denoted by  $X^{(u)}(k)$  can be expressed as follows:

$$\begin{aligned} X^{(u)}(k) &= [X(0) \cdot b^{(u)}(0), X(1) \cdot b^{(u)}(1), \dots, X(N-1) \cdot b^{(u)}(N-1)] \\ &= [X^{(u)}(0), X^{(u)}(1), \dots, X^{(u)}(N-1)] \end{aligned} \quad (4)$$

Later on,  $X^{(u)}(k)$  is oversampled via the zero padding process in which  $(L-1)N$  zeros are inserted into the related  $N$  length sequence:

$$X_{os}^{(u)}(k) = \left[ \underbrace{0, 0, \dots, 0}_{(L-1)N/2}, \underbrace{X^{(u)}(0), X^{(u)}(1), \dots, X^{(u)}(N-1)}_N, \underbrace{0, 0, \dots, 0}_{(L-1)N/2} \right] \quad (5)$$

where  $L$  corresponds to the oversampling factor. The oversampled phase rotated data vector is subjected to the IFFT operation to attain the following signal in time domain:

$$\begin{aligned} x^{(u)}(n) &= IFFT(X_{os}^{(u)}(k)) \\ &= \frac{1}{\sqrt{N}} \sum_{k=0}^{N-1} X(k) \cdot b^{(u)}(k) \cdot e^{\frac{j2\pi kn}{LN}}, \quad 0 \leq n \leq LN-1 \end{aligned} \quad (6)$$

The optimum phase rotation combination  $b^*(k)$  minimizing the PAPR of  $x^{(u)}(n)$  signal can be found as follows:

$$b^*(k) = \arg \min_{b^{(u)}(k)} \left\{ \max_{0 \leq n \leq LN-1} \left| \frac{1}{\sqrt{N}} \sum_{k=0}^{N-1} X(k) \cdot b^{(u)}(k) \cdot e^{\frac{j2\pi kn}{LN}} \right|^2 \right\} \quad (7)$$

where the  $\arg \min \{ \}$  operator finds the optimum  $b^{(u)}(k)$  minimizing the value of expression in the brackets. Subsequent to finding the optimum phase rotation sequence  $b^*(k)$ , the optimized signal in time domain is acquired from the SLM output in the following way:

$$x^*(n) = \frac{1}{\sqrt{N}} \sum_{k=0}^{N-1} X(k) \cdot b^*(k) \cdot e^{\frac{j2\pi kn}{LN}}, \quad 0 \leq n \leq LN-1 \quad (8)$$

After that,  $x^*(n)$  is subjected to the FFT operation for being able to be used as an input data sequence in the UPMC transmitter.  $X_{os}^*(k)$  data sequence acquired from the FFT output corresponds to the zero inserted frequency

domain optimal data sequence  $X^*(k)$  which is equal to the multiplication of  $X(k)$  by the optimum phase factor combination  $b^*(k)$ . After the FFT process, the resulting data vector  $X_{os}^*(k)$  is allocated to  $B$  sub-bands. The frequency domain data sequence belonging to the sub-band  $b$  is denoted by  $X_b^*(k)$ . Subsequent to fulfilling the next operation which is performing the IFFT process for every sub-band, two more operations called cyclic prefix and filtering are applied to the time domain signal  $x_b^*(n)$ , respectively and after that, the resulting signals on the multiple sub-bands are combined. Finally, the optimal UFGC signal denoted by  $s^*(n)$  with minimized PAPR is acquired from transmitter end. Exhaustive mathematical expressions of the operations performed after the acquisition of  $x^*(n)$  to achieve the  $s^*(n)$  can be found from [16].

#### 4. Simulation Results

The SLM technique initially suggested for the OFDM was optimally integrated to the transmitter of UFGC scheme in order to get the maximum PAPR reduction performance from the related technique. In the simulations, the efficiency of SLM scheme on minimizing the PAPR of UFGC waveform was analyzed for varied number of phase sequence vectors each of which are generated in a random way. The complementary cumulative distribution function (CCDF =  $\Pr[ \text{PAPR} > \text{PAPR}_0 ]$ ) was utilized in the simulations for the analysis of PAPR reduction achievement. Following the analyses made on the PAPR improvements achieved in the UFGC signal, the effect of SLM technique on the level of side lobes and BER belonging to the UFGC signal amplified by one of the most commonly used nonlinear HPAs called solid state power amplifier (SSPA) [19], was investigated for various SLM and SSPA parameters such as the number of randomly generated phase factor combinations ( $U$ ), input back off (IBO) value and the value of smoothness ( $p$ ) coefficient. The parameters appointed for the simulations are yielded in Table 1.

In Figure 3, an investigation on the SLM's ability to reduce the PAPR of UFGC signal was carried out for various number of phase sequences. Figure 3 clearly demonstrates that the PAPR of original UFGC signal can be reduced significantly by increasing the value of  $U$ . For instance, since the performance of SLM technique escalates with the increase in the number of alternative phase sequences, the enhancement in the value of  $U$  from 4 to 256 provides 5.8 dB PAPR improvement at CCDF =  $10^{-3}$ .

Table 1. Simulation parameters

Number of subcarriers	32
Type of modulation	4-QAM
Value of oversampling factor	$L=8$
Size of FFT	256
Number of sub-band	2
Type of filter	Dolph-Chebyshev
Length of cyclic prefix	$L_{CP}=16$
Frequency of sampling	3.84 MHz
Type of HPA	SSPA
Type of channel	AWGN

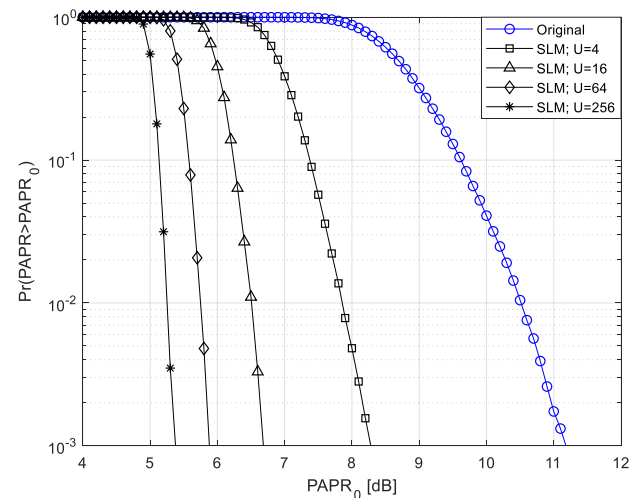


Figure 3. The PAPR improvements achieved by the SLM scheme for different values of  $U$

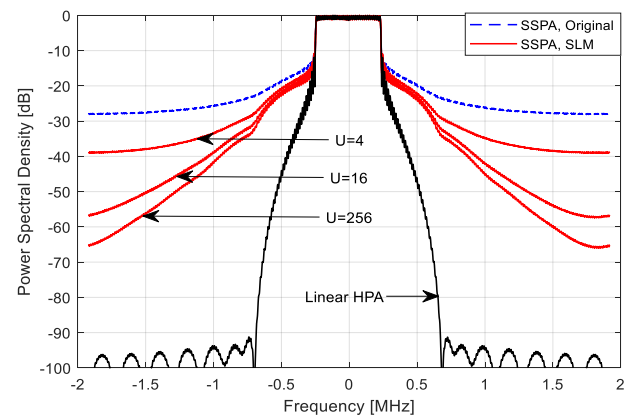


Figure 4. The performance of SLM technique on suppressing the SSPA originated side lobe escalation in the UFGC waveform for several  $U$  values (IBO = 7,  $p = 1$ )

In Figure 4, the SLM performance on suppressing the side lobe escalation arisen from the usage of SSPA for amplifying the UFGC signal with high PAPR before the transmission process, was analyzed via the power spectral density (PSD) graph for several  $U$  values. As can be seen from the Figure 4, the side lobes of the original UFGC

signal were reduced from above the level of  $-30$  dB to approximately  $-65$  dB by enhancing the value of  $U$  from 4 to 256. Since the signals with high PAPR are exposed to nonlinear amplification originated distortion by the SSPA, reducing the signal PAPR through the SLM technique leads to less distortion while amplifying the signal and consequently, high level side lobes arisen from the signal distortions are reduced as well.

In Figure 5, the capability of the SLM procedure was evaluated with regard to its effect on the BER of the UPMC waveform for several IBOs. As distinctly viewed from the Figure 5, for each of the IBO values determined for this simulation, in case of increasing the number of phase sequences, the PAPR of UPMC is further improved and depending on this, the amplification of the related

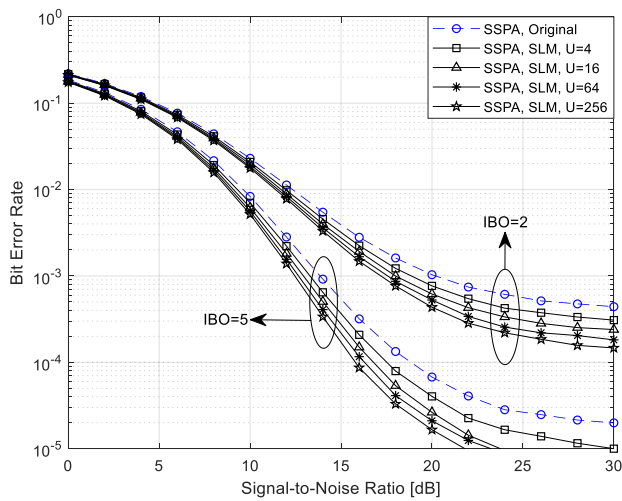


Figure 5. Performance of SLM procedure on reducing the SSPA originated BER increase in the UPMC waveform for different IBO values ( $p = 2$ )

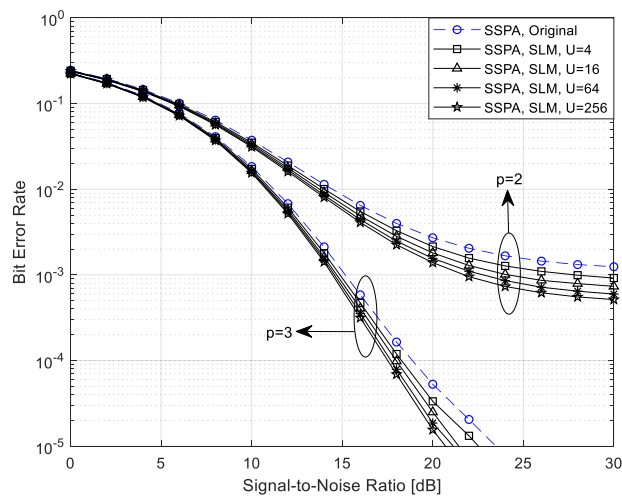


Figure 6. Performance of SLM scheme on reducing the SSPA originated BER increase in the UPMC waveform for different smoothness values ( $IBO = 0$ )

signal via the SSPA is carried out with less degradation which results in a significant improvement in the BER performance. For instance, if the BER results at 20 dB signal-to-noise ratio (SNR) value for  $IBO = 5$  dB are taken into consideration, the BER values achieved for 4, 16, 64 and 256 phase sequences are equal to  $4 \times 10^{-5}$ ,  $2.64 \times 10^{-5}$ ,  $2.1 \times 10^{-5}$  and  $1.66 \times 10^{-5}$ , respectively while the BER of the original signal is equal to  $6.75 \times 10^{-5}$ . Apart from this, increasing the value of IBO corresponding to the parameter that determines the distance of the operating point to the threshold value beyond which the SSPA reaches the saturation, gives rise to BER improvement in the UPMC waveform since the frequency of reaching the saturation region leading to signal distortions during the amplification process decreases.

In Figure 6, the BER graph of the UPMC waveform utilizing the SLM technique for PAPR reduction was obtained with respect to the varied smoothness values. As can be easily realized from the Figure 6, the value of BER belonging to the UPMC waveform scales down with the increase in the number of alternative phase factor combinations generated for minimizing the PAPR of transmission signal. Besides, the enhancement in the value of smoothness coefficient symbolized by  $p$  escalates the linearity of SSPA. With an increased linearity of SSPA, the amount of degradation on the signals during the amplification process decreases and depending on this, a significant BER decrement occurs in the UPMC waveform. For instance, with the increase of coefficient  $p$  from 2 to 3, the BERs acquired by the SLM scheme for 4, 16, 64 and 256 phase sequences at 20 dB SNR value decrease from  $2.14 \times 10^{-3}$ ,  $1.81 \times 10^{-3}$ ,  $1.56 \times 10^{-3}$  and  $1.39 \times 10^{-3}$  to  $3.34 \times 10^{-5}$ ,  $2.5 \times 10^{-5}$ ,  $1.87 \times 10^{-5}$  and  $1.56 \times 10^{-5}$ , respectively.

### 5. Conclusions

In this paper, optimal integration of SLM technique initially suggested for OFDM was carried out in order to exploit full of its potential PAPR alleviation capability in the UPMC waveform. The amount of PAPR improvement carried out by the SLM scheme was demonstrated via the  $PAPR_0 - CCDF(Pr[ PAPR > PAPR_0])$  graph in the simulations. From the related graph, the probability that the PAPR of the signal taken from the output of UPMC transmitter is greater than a certain PAPR value ( $PAPR_0$ ) can be easily seen. Besides, the capability of SLM strategy on lowering the SSPA originated spectral regrowth and BER increase was evaluated for different values of  $U$ , IBO and  $p$  via the PSD and BER graphs, respectively. The simulation results obviously demonstrates that it is possible to achieve serious improvements through the SLM technique in the PAPR, spectral characteristic and BER performance of the UPMC waveform.



## Declaration

The author(s) declared no potential conflicts of interest with respect to the research, authorship, and/or publication of this article. The author(s) also declared that this article is original, was prepared in accordance with international publication and research ethics, and ethical committee permission or any special permission is not required.

## Acknowledgment

This study was supported by the Scientific Research Projects Coordination Unit of Erciyes University [Grant No: FDK-2018-8463].

## References

- Vakilian, V., T. Wild, F. Schaich, S.T. Brink, and J.F. Frigon, *Universal-filtered multi-carrier technique for wireless systems beyond LTE*, in GC Wkshps 2013: Atlanta. p. 223-228.
- Li, Y., B. Tian, K. Yi, and Q. Yu, *A novel hybrid CFO estimation scheme for UFMC-based systems*. IEEE Communications Letters, 2017. **21**(6): p. 1337-1340.
- Wu, M., J. Dang, Z. Zhang, and L. Wu, *An advanced receiver for universal filtered multicarrier*. IEEE Transactions on Vehicular Technology, 2018. **67**(8): p. 7779-7783.
- Duan, S., X. Yu, and R. Wang, *Performance analysis on filter parameters and sub-bands distribution of universal filtered multi-carrier*. Wireless Personal Communications, 2017. **95**(3): p. 2359-2375.
- Chen, J.C. and C.K. Wen, *PAPR reduction of OFDM signals using cross-entropy-based tone injection schemes*. IEEE Signal Processing Letters, 2010. **17**(8): p. 727-730.
- Krongold, B.S. and D.L. Jones, *PAR reduction in OFDM via active constellation extension*. IEEE Transactions on Broadcasting, 2003. **43**(3): p. 258-268.
- Bauml, R.W., R.F.H. Fischer, and J.B. Huber, *Reducing the peak-to-average power ratio of multicarrier modulation by selected mapping*. Electronics Letters, 1996. **32**(22): p. 2056-2057.
- Wang, C.L. and Y. Quyang, *Low-complexity selected mapping schemes for peak-to-average power ratio reduction in OFDM systems*. IEEE Transactions on Signal Processing, 2005. **53**(12): p. 4652-4660.
- Liang, H., H.C. Chu, and C.B. Lin, *Peak-to-average power ratio reduction of orthogonal frequency division multiplexing systems using modified tone reservation techniques*. International Journal of Communication Systems, 2016. **29**(4): p. 748-759.
- Li, X. and L.J. Cimini, *Effect of clipping and filtering on the performance of OFDM*. IEEE Communications Letters, 1998. **2**(5): p. 131-133.
- Jones A.E., T.A. Wilkinson, and S.K. Barton, *Block coding scheme for reduction of peak to mean envelope power ratio of multicarrier transmission scheme*. Electronics Letters, 1994. **30**(25): p. 2098-2099.
- Cimini, L.J. and N.R. Sollenberger, *Peak-to-average power ratio reduction of an OFDM signal using partial transmit sequences*. IEEE Communications Letters, 2000. **4**(3): p. 86-88.
- Bozkurt, Y.T. and N. Taşpınar, *PAPR reduction performance of bat algorithm in OFDM systems*. International Advanced Researches and Engineering Journal, 2019. **3**(3): p. 150-155.
- Jayalath, A.D.S. and C. Tellambura, *Reducing the peak-to-average power ratio of orthogonal frequency division multiplexing signal through bit or symbol interleaving*. Electronics Letters, 2000. **36**(13): p. 1161-1163.
- Baig, I., U. Farooq, N.U. Hasan, M. Zghaibeh, A. Sajid, and U.M. Rana, *A low PAPR DHT precoding based UFMC scheme for 5G communication systems*, CoDIT 2019: Paris. p. 425-428.
- Taşpınar, N. and Ş. Şimşir, *PAPR reduction based on partial transmit sequence technique in UFMC waveform*, in CISTI 2019: Coimbra. p. 1-6.
- Tipan, M.N., J. Caceres, M.N. Jimenez, I.N. Cano, and G. Arevalo, *Comparison of clipping techniques for PAPR reduction in UFMC systems*, LATINCOM 2017: Guatemala City. p. 1-4.
- Rong, W., J. Cai, and X. Yu, *Low-complexity PTS PAPR reduction scheme for UFMC systems*. Cluster Computing, 2017. **20**(11): p. 3427-3440.
- Ryu, H.G., J.S. Park, and J.S. Park, *Threshold IBO of HPA in the predistorted OFDM communication system*. IEEE Transactions on Broadcasting, 2004. **50**(4): p. 425-428.



## Research Article

## Performing reactive power compensation of three-phase induction motor by using parallel active power filter

Ömer Ali Karaman <sup>a</sup> , Ahmet Gündoğdu <sup>b,\*</sup>  and Mehmet Cebeci <sup>c</sup> 

<sup>a</sup>Batman University, Department of Electric, Vocational School, Batman, 72000, Turkey

<sup>b</sup>Batman University, Department of Electrical and Electronic Engineering, Batman, 72000, Turkey

<sup>c</sup>Firat University, Department of Electrical and Electronic Engineering, Elazığ, 23000, Turkey

## ARTICLE INFO

## Article history:

Received 03 May 2020

Revised 11 June 2020

Accepted 05 July 2020

## Keywords:

Harmonics

Parallel active power filter

Power factor correction

3-phase induction motor

## ABSTRACT

Nowadays, the problem of power quality increases day by day. Harmonic current and reactive power are the important factors disturbing the power quality. The induction motors draw both harmonic current and reactive power from the grid. Reactive power and harmonic current lead to heat losses and decrease in the efficiency of the transmission lines. Passive and active filter applications have been used to solve these problems. There are some disadvantages of passive filters. Large physical dimensions and resonance with load can be shown as examples for these disadvantages. Therefore, the application areas of Active Power Filter (APF) are rapidly developing due to the fact that they can be applied together with harmonic and reactive power compensation as appropriate control methods. This paper proposes a MATLAB/Simulink simulation to perform power factor correction and reactive power compensation of three-phase induction motor by using three-phase Parallel Active Power Filter (PAPF). In order to generate PAPF's reference currents the Sine Multiplication Technique (SMT) is used. Simulation studies are presented to be able to assess the performances under different motor operating conditions. The proposed hysteresis controller based PAPF filter makes the power factor up to 1 and the reactive power compensation of the three-phase induction motor.

© 2020, Advanced Researches and Engineering Journal (IAREJ) and the Author(s).

### 1. Introduction

Induction motors are widely utilized in many different applications [1]. An important percentage of the energy generated in an industrialized country is consumed by induction motors [2]. However, the main disadvantages of them are that they require reactive power and draw harmonic currents. Reactive power leads to heat losses and decrease in the efficiency of the power systems. To reduce or solve many of the problems related to the power quality, the optimal control of the reactive power can be applied [3]. It is also possible to make significant financial saving with the reactive power compensation. The circulation of reactive power in the grid in a system without reactive power compensation is shown in Figure1.

In terms of controlling power systems, one of the important problems is reactive power compensation. In the power systems, to increase the current carrying

capacity and to reduce the size of the transmission line conductor, reactive power compensation is required. Thus, it leads to the reduction of losses. Also, the production cost of the transmission system is reduced [4]. There are many advantages of producing reactive power at the point close to the load and giving it to the grid in order to prevent excessive current circulation caused by the reactive power requirement in the grid. This application is known as the conventional reactive power compensation method. It is also called "power factor correction". Figure2 shows the reactive power circulation in the grid after the compensation is performed.

Therefore, the reactive power should be reduced by correcting the power factor. Passive filter applications have long been used to solve these problems. Nevertheless, it is possible to mention many disadvantages of passive filters, such as settling to certain frequency values, resonance with load, and large physical

\* Corresponding author. Tel.: +90 488 217 41 06.

E-mail addresses: [omer.ali.karaman@batman.edu.tr](mailto:omer.ali.karaman@batman.edu.tr) (Ö.A. Karaman), [ahmet.gundogdu@batman.edu.tr](mailto:ahmet.gundogdu@batman.edu.tr) (A. Gündoğdu), [mcebeci@firat.edu.tr](mailto:mcebeci@firat.edu.tr) (M.Cebeci)

ORCID: 0000-0003-1640-861X (Ö.A. Karaman), 0000-0002-8333-3083 (A.Gündoğdu), 0000-0002-2971-6788 (M.Cebeci)

DOI: 10.35860/iarej.731187

dimensions. Because conventional compensation systems can not immediately respond to the reactive power demand that a load needs in a moment, correcting the loads' power factor, which is powerful and has the ability to enter and leave the circuit swiftly, cannot be achieved by applying the conventional electromechanical compensation arrangements. The rapid increase in technology has also increased the importance of compensation realized by using modern methods.

When the compensation of power systems is done with semiconductor switches, the voltage collapses can be avoided and it can improve transient and dynamic stability [5,6]. Besides, reactive power compensation should be used to reduce current harmonics [7]. In electrical systems, nonlinear loads draw nonlinear current from the grid. In power systems, voltage harmonics are generated by nonlinear currents. Then, all system elements are affected by spreading of these voltage harmonics to the entire power system. Due to current and voltage harmonics, overheating of transformers, increasing of losses, reduction in the power factor, and decreasing of the system efficiency are experienced [8]. In terms of the Point of Common Connection (PCC), there are some limitations brought by the IEEE Standards 519 to the voltage and current harmonics. The above-mentioned standards recommend that the determined value of the Total Harmonic Distortion (THD %) should be 3% for the voltage and 5% for the current. Because the power systems' receivers are affected negatively by harmonic currents, these standards have been prepared to ensure that the harmonic currents are kept within the determined limits [9].

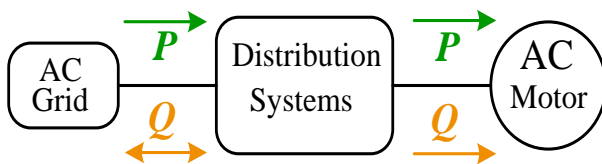


Figure 1. Reactive power circulation in the grid.

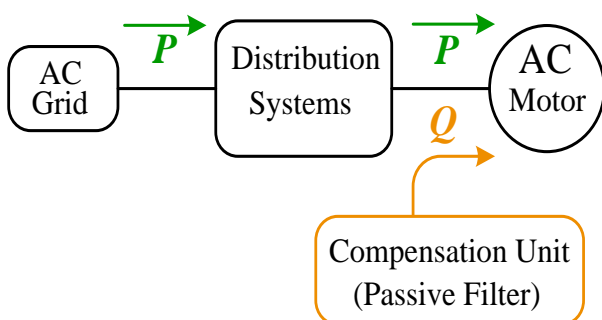


Figure 2. Conventional compensation system

Active power filters (APF) are called devices that both compensate and eliminate harmonics by using semiconductor switches. Due to the switching capabilities of the power switches at very high frequencies, active power filters can also filter high frequency current and voltage harmonics, perform reactive power compensation, reduce neutral line currents and eliminate imbalance emerging in three-phase systems.

Nowadays, various active power filters (e.g., serial, parallel, hybrid and combined power quality regulators) are used to find solutions for power quality problems. The most common and widely utilized active power filter method in the industry is the parallel active power filter (PAPF) [10,11].

For example, in distribution systems, to be able to ensure the optimal reactive power compensation, an optimal phase angle model and allocation method of multiple Distribution-STATCOM (DSTATCOM) was proposed. The proposed method is more influential in compensation of the reactive power for the reduction of the power loss [12].

One of the effective methods of performing reactive power compensation in industrial applications is the hybrid active power filter because it allows low-cost high power applications [13].

For different compensations in a system that had static and dynamic loads, a 3-phase DSTATCOM was applied and its performance analysis was carried out. In this study, to generate the reference signal, the synchronous reference frame theory was used and the hysteresis pulse width modulation switching was applied for the firing pulse generation, and these were realized in the field-programmable gate array (FPGA) [14].

A model to correct the power factor, and digital implementation of various loops of a circuit (e.g., hysteresis controller for current loop and PI controller for voltage loop) were presented. Fixed, sinusoidal and variable bands were implemented and they were verified through simulation. Compared to other hysteresis control methods, the variable band hysteresis control gave lower THD value for the input current in the current loop [15]. For the shunt active power filter depending on the predictive direct power control through the space vector modulation, a powerful control design was proposed. The problem of the variable switching frequency of the predictive control method was solved by the proposed design, and it offered simple and powerful hardware application [16]. Instead of conventional compensation systems, PAPF ensures dynamic and rapid reactive power compensation even under very changeable load conditions [17].

A simple controller structure with minimal feedback that ensured the open-ended winding induction motor (OEWM), used in the Dual inverter drive (DID) system,

to operate under constant power factor under different load and speed conditions was proposed [18].

Reactive power compensation of an induction motor with nine switching elements and fed through an AC-DC-AC converter was performed. A PI controller was developed to achieve the desired power factor within the closed-loop control structure [19].

The effects of the active power filter (APF) on power quality at the output of a synchronous generator with a distorted back-EMF waveform were examined. In simulation and experimental studies conducted using APF, it was observed that THD was significantly reduced [20].

A new adaptive fuzzy-based hysteresis current control technique was proposed to reduce current harmonics and switching losses in a system using the hybrid active power filter (HAPF). Experimental studies showed that switching losses were reduced by 9% [21].

In addition to having a fast dynamic response, the “bipolar hysteresis current control technique” used in two-stage photovoltaic (PV) micro-inverters has high efficiency even at high switching frequencies. To reduce switching losses at high switching frequencies, the unipolar hysteresis current control technique is preferred. However, in also this control technique, zero-crossing distortions and low-frequency harmonics occur in the grid current. To solve this problem, the technique of proportional resonant (PR) and hybrid hysteresis current control was proposed [22].

Electric motors and other inductive loads need reactive power. They draw the power they need either from the grid or from fixed-capacity compensation units called passive filters. The active power filters developed as an

alternative system both meet the reactive power requirement of the system and make the power factor of the system one (1) at each load stage. In the literature, there are different studies on the reactive power compensation of parallel active power filter (PAPF) and 3-phase induction motor. However, studies that SMT, which is the reference current prediction technique, and HBCC, which is the hysteresis controller structure, are used together has not been encountered. In order to contribute to this area, a model in which the Sine Multiplication Technique (SMT) and Hysteresis Band Current Controller (HBCC) structure were used together was created. With this model created in MATLAB/Simulink environment, reactive power compensation of a 3-phase induction motor was performed. With simulation studies for no-load and loaded operating conditions, the power factor of the system was successfully increased to 1. In this respect, this study is different from other studies that have been conducted and it partly contains originality.

## 2. Entire System and Proposed Filter

As seen in Figure 3, the system simulation consists of three-phase induction motor, the sine multiplication technique control block to determine the reference current, dc-link capacitor, 3-wired two-level voltage source inverter, hysteresis band current controller (HBCC), and a coupling inductance to connect the inverter to the grid.

Although the literature includes a lot of complex control algorithms, the use of the simple structure hysteresis controller with the Sine Multiplication Technique has the advantages of being easy-applicable and easy to perform with low speed microprocessors.

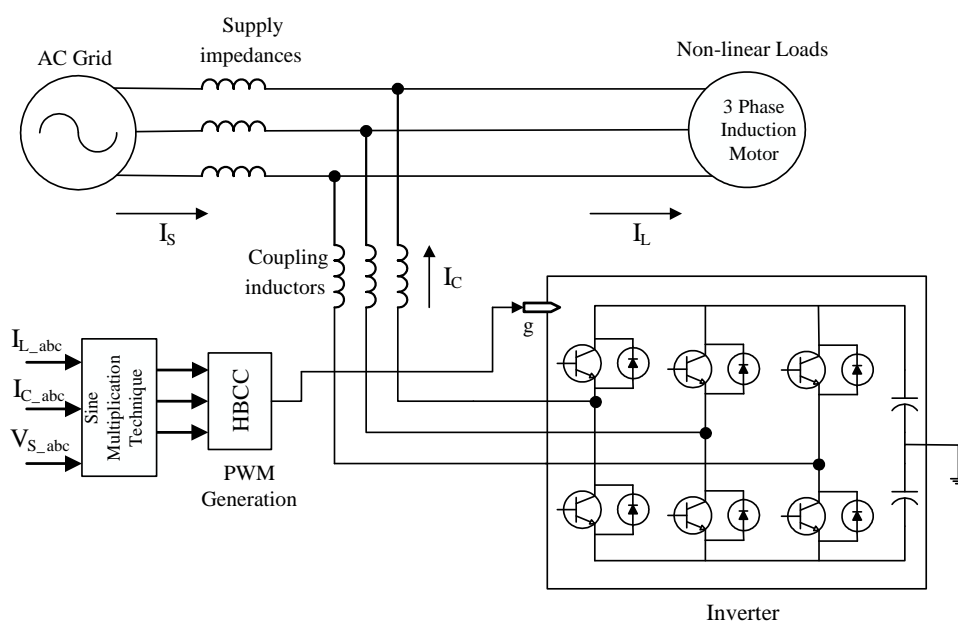


Figure 3. Block diagram of the PAPF

**2.1 Parallel Active Power Filter (PAPF)**

Among the active power filters, the one that is the most commonly utilized in the industry is the parallel active power filter [23]. Figure 4 shows the general structure of the PAPF's voltage source [26]. A PAPF consist of an inverter, a DC link capacitor, a connection inductance that provides connection to the grid and a controller unit. The inverter generates the compensation current. The duty of the connection inductance used on the AC side of the inverter is to prevent the switching parasites generated by the inverter, and the switching signals for the inverter are generated by the controller.

Injecting currents as equal magnitude and in reverse phase to the grid to be able to get rid of load current's harmonics and performing reactive power compensation can be shown as the primary principles of the PAPF. In this way, the harmonics are eliminated and the source currents start to oscillate sinusoidally. For successful application of PAPF, extracting the correct reference current values and generating gate signals are important. Therefore, it is needed to determine the reactive and harmonic components that are drawn by the load currents in order to extract the reference currents. In the literature, there are various techniques for the extraction of reference currents; some of these are shown in Figure 5 [26].

For the extraction of the harmonic current/voltage components in APF practices, a lot of methods that can be performed both in frequency and time domains have been proposed and assessed.

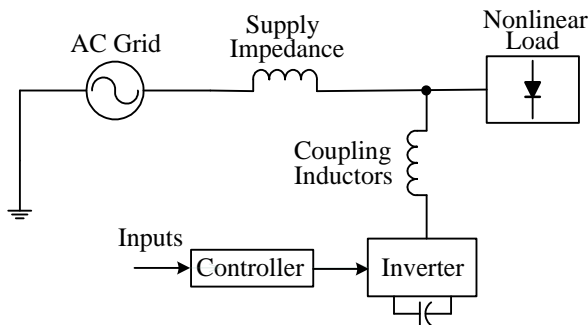


Figure 4. Voltage source PAPF.

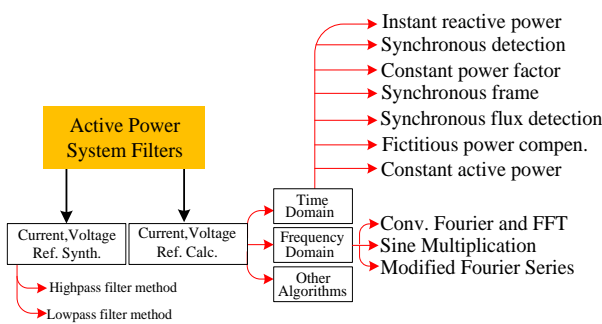


Figure 5. Methods for reference current/voltage extraction

When these methods are examined, it is seen that the most widely used are frequency and time domain based methods [24]. Though there are some distinctive limitations of the techniques used to extract reference current, most of them run stably under fixed loads. Nevertheless, various load circumstances affect their performance significantly. In order to mitigate these effects, different approaches such as Fourier, Artificial Neural Network (ANN) have been proposed in the literature [25,26].

However, these methods presented have some disadvantages. For example, in the method used to extract reference current by depending on the artificial neural networks, a huge amount of data is needed for the training of the network. In this study, for the generation of the active power filter reference currents, the sine multiplication method is used [27].

**2.2 Reference Current Estimation**

The most important part of the PAPF is the reference current extraction part. In this study, the Sine Multiplication Technique was used to find the reference current. SMT is a widely used technique for the determination of the reference compensation currents of PAPFs [28]. However, in power systems where the source voltage is not in ideal sinusoidal form, sine multiplication technique loses effectiveness [27]. Figure 6 shows the block diagram of SMT.

By injecting the predicted reference current into the grid in the opposite phase and with equal amplitude, elimination of the harmonics and realization of the reactive power compensation are achieved. If we assume that the grid is pure (in other words, it does not have harmonics and reactive component), the grid voltage is in the ideal form. Eq. (1) expresses this situation.

$$V_s(t) = V_m \sin \omega t \tag{1}$$

If we assume that a non-linear load is fed by this grid, then the current drawn from the grid can be expressed as shown in Eq. (2).

$$I_L(t) = \sum_{n=1}^{\infty} I_{nm} \sin(n\omega t + \phi_n) = I_{nm} \sin(\omega t + \phi_1) + \sum_{n=2}^{\infty} I_{nm} \sin(n\omega t + \phi_n) \tag{2}$$

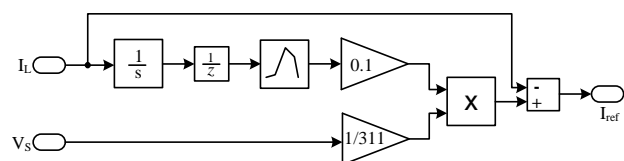


Figure 6. MATLAB/Simulink block diagram of SMT

As seen in the Eq. (2), the fundamental component is the maximum value of the first-order harmonic and  $I_m$  refers to the maximum load current value. Independently from capacitive or inductive load conditions, the sign of the phase angle ( $\varphi_1$ ) of the load is written as a general expression. We can express the instantaneous power that is drawn from the grid as follows;

$$P(t) = V_s(t) \cdot I_L(t) \tag{3}$$

The following power components were obtained by placing Eq. (1) and Eq. (2) in their places at Eq. (3);

$$P(t) = V_m I_m \sin^2 \omega t \cdot \cos \varphi_1 + V_m I_m \cdot \cos \omega t \cdot \sin \omega t \cdot \sin \varphi_1 + V_m \sin \omega t \sum_{n=2}^{\infty} I_{nm} \sin(n\omega t - \varphi_n) \tag{4}$$

It is understood from Eq. (4) that active power as well as infinite number of harmonics and reactive power are drawn from the grid. By separating it from Eq. (4), the active power can be expressed as follows;

$$P_{active} = V_m I_m \cdot \sin^2 \omega t \cdot \cos \varphi_1 \tag{5}$$

As a result of its withdrawal from the active power, the instantaneous power value shown in Eq. (4) and the harmonic and reactive power components are obtained. Reactive power can be shown as;

$$P_{reactive} = V_m I_m \cdot \cos \omega t \cdot \sin \omega t \cdot \sin \varphi_1 \tag{6}$$

The remaining part in Eq. (4) is the harmonic power components. If the active power can be removed in Eq. (4), the remaining reactive and harmonic component power can be compensated with PAPF. Similarly, the reactive and harmonic current components are obtained by subtracting the real current from the total current given in Eq. (2). Therefore real current can be written as;

$$I_s(t) = I_m \sin(\omega t + \varphi_1) \tag{7}$$

Finally, by subtracting the actual current component from the total load current, the reference compensation current of the parallel active power filter given in Eq. (8) can be calculated;

$$I_c(t) = I_L(t) - I_s(t) \tag{8}$$

### 2.3 Hysteresis Band Current Control (HBCC)

Various current control methods have been applied to generate switching signals in active power filters [29]. In this paper, in order to obtain switching signals, HBCC

was used as a control method. It has been proven that HBCC is an effective technique to generate gate signals in all applications of active power filters that have voltage source inverters. Furthermore, this is a consistent and fast method that has a high accuracy rate [30]. HBCC is widely applied in APF for current harmonic compensation [31]. In HBCC as a control method, in order for generating switching signals, actual compensation current and reference compensation current are combined on a hysteresis band. With this non-linear current controlling technique, the continuous tracking of the output current of the inverter within a certain band is ensured [32].

In the block diagram given in Figure 9, the reference currents generated by SMT and the motor currents drawn from the grid are compared to be able to control the inverter current. The obtained current error is applied as input to the two-level hysteresis controller in order to generate switching signals. The block structure of the two-level hysteresis controller is shown in Figure 7. This block structure represents only one phase. Because the system is three-phase, three separate hysteresis controllers were used.

The current controller bandwidth is  $2\Delta I$ . The actual motor current ( $I$ ) varies in such a way that it stays within the  $\pm\Delta I$ -valued band around the reference currents ( $I_{ref}$ ). Therefore, in the actual motor current, the amount of deviation allowed in positive and negative directions is as much as the maximum  $I_{ref} \pm \Delta I$ . Controller outputs are digital outputs and take 0 and 1 values. If the controller output is 0, the S2 switching signal is generated and if the controller output is 1, the S1 switching signal is generated. The variations of S1 and S2 switching signals are shown in Figure 8.

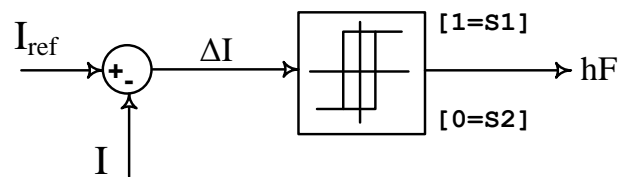


Figure 7. Hysteresis controller block diagram.

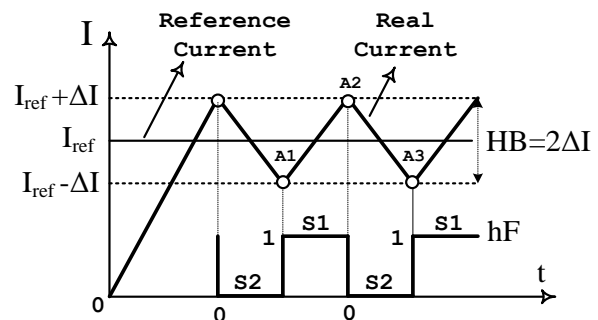


Figure 8. Structure of hysteresis band.

The  $I_{ref}-\Delta I$  value is the lower bound value of the hysteresis band and is shown in Figure 8 with the point A1. The A1 point is the lowest value where the actual motor current allowed by the controller can decrease. When it reaches to point A1, it is no longer allowed the actual motor current to decrease further, and at this point, the controller output becomes  $hF=1$  in order to produce the S1 switching signal that will increase the current. With the selection of the S1 switching signal at point A1, the actual motor current continues to increase with a positive slope up to point A2. The controller output at point A2 becomes  $hF=0$  and the S2 switching signal which will reduce the current is selected. Motor current continues to decrease with negative slope up to A3 point. In the hysteresis bandwidth determined in this way, switching signals that will allow the motor current to change in positive and negative directions are obtained. The current controller output according to the current error is mathematically expressed by Eq. (9).

$$hF = \begin{cases} 1 = S1 & I \leq I_{ref} - \Delta I \\ 0 = S2 & I \geq I_{ref} + \Delta I \end{cases} \quad (9)$$

Hysteresis bandwidth  $HB=2\Delta I$  directly affects the switching frequency of the inverter. Small bandwidth causes high switching frequency, while large bandwidth causes low switching frequency. Therefore, the switching frequency of the inverter should not be exceeded by

keeping the bandwidth at the optimum value. The switching frequencies obtained for 3 different hysteresis band values in the conducted simulation studies is given in Table 1 below.

### 3. Simulation Results

Figure 9 shows the Simulink block diagram for the entire system. In this simulation study, MATLAB/Simulink package program was utilized to perform the reactive power compensation of induction motor with PAPF. The source voltage and frequency were set to 311 volt and 50 Hz, respectively. DC-link voltage and coupling inductance were determined 311 V and 3 mH. Induction motor parameters were 4 kW for power, 400 V for voltage and 1430 rpm for speed.

The three-phase induction motor is supplied with a source voltage with a balanced 311 V amplitude. It is important that this voltage signal is pure sinusoidal because the unit sinusoidal signal used to create the reference current is derived from the source voltage.

Table 1. Switching frequency for different hysteresis bands.

Hysteresis Band (HB)	Switching Frequency ( $f_{sw}$ )
$2\Delta I = 1$	$f_{sw} = 5.082$ kHz
$2\Delta I = 0.5$	$f_{sw} = 7.342$ kHz
$2\Delta I = 0.1$	$f_{sw} = 12.540$ kHz

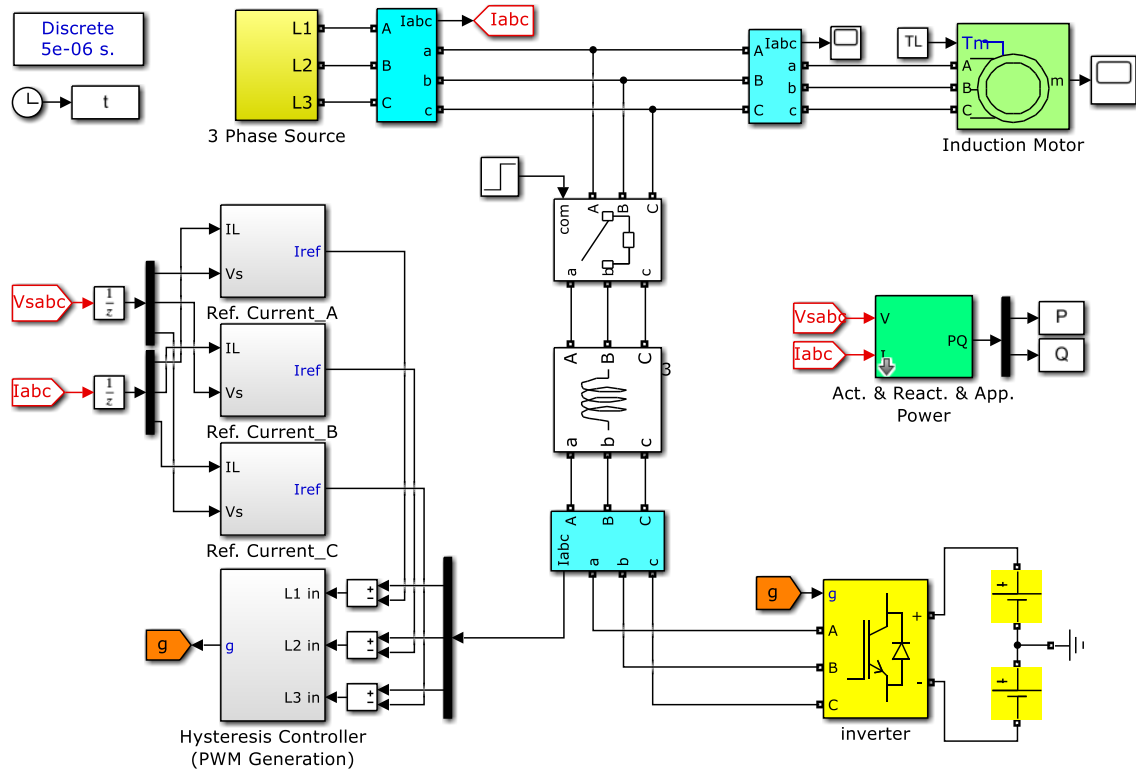


Figure 9. All system MATLAB/Simulink block diagram.

Figure 10 shows that there is a phase difference between voltage and current due to the reactive component before 0.16<sup>th</sup> of a second. In the same way, PAPF activates at 0.16<sup>th</sup> second. Therefore it makes reactive power compensation and eliminates the phase difference between the voltage and current.

Figure 11 shows that when PAPF enabled, the reactive power drawn from three-phase source by the induction motor is decreases to zero. In this way successful reactive power compensation is made. In terms of power signals, P, Q, and S refer to active, reactive, and apparent powers, respectively.

Figure 12 shows, motor power factor with filter and no filter at no-load conditions. After the filter is activated at 0.16<sup>th</sup> second than the power factor becomes 1.

The phase difference between current and voltage is

shown in Figure 13 when the induction motor is loaded with 2 Nm. At 0.16<sup>th</sup> second the PAPF is enabled. In this case, the phase difference observed between the voltage and the current disappears. Thus, PAPF successfully performs reactive power compensation even when the motor is loaded with 2 Nm.

Figure 14 shows that when PAPF is enabled, the reactive power drawn from the three-phase source by the induction motor decreases to zero. In this way, successful reactive power compensation is realized.

Figure 15 shows the motor power factor with filter and without filter at loaded conditions. After the filter is activated at 0.16<sup>th</sup> second, the PAPF performs a successful reactive power compensation by raising the power factor from 0.89 to 1.

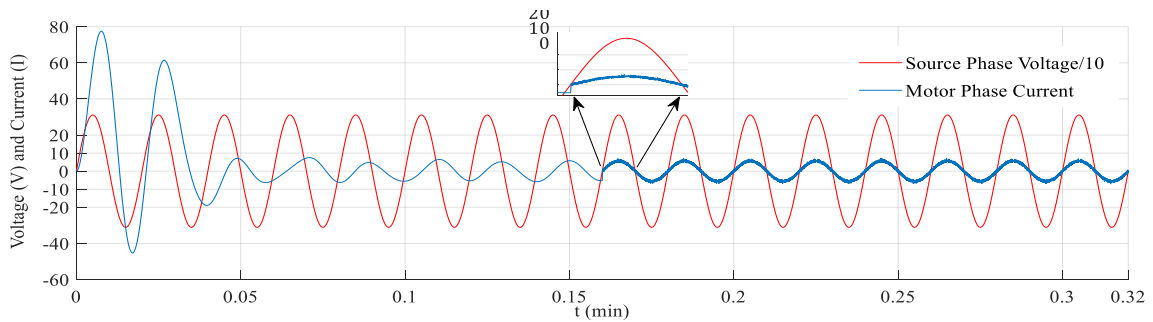


Figure 10. Source voltage and phase current of motor (no-load).

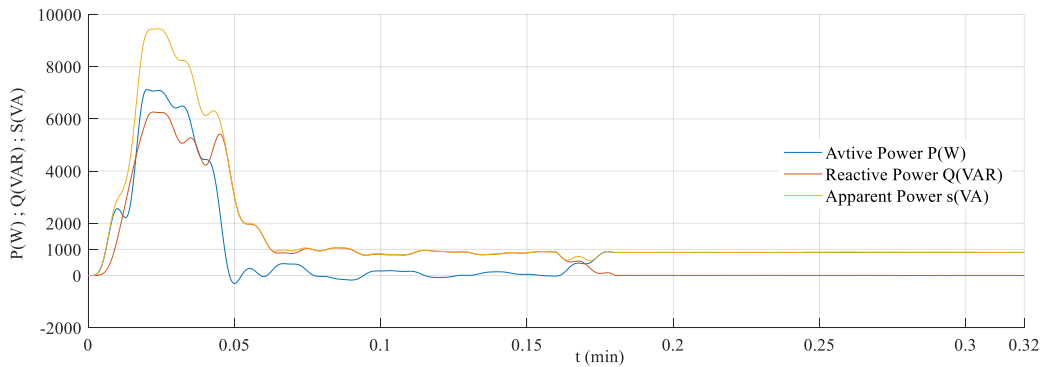


Figure 11. Active, reactive and apparent power signals.

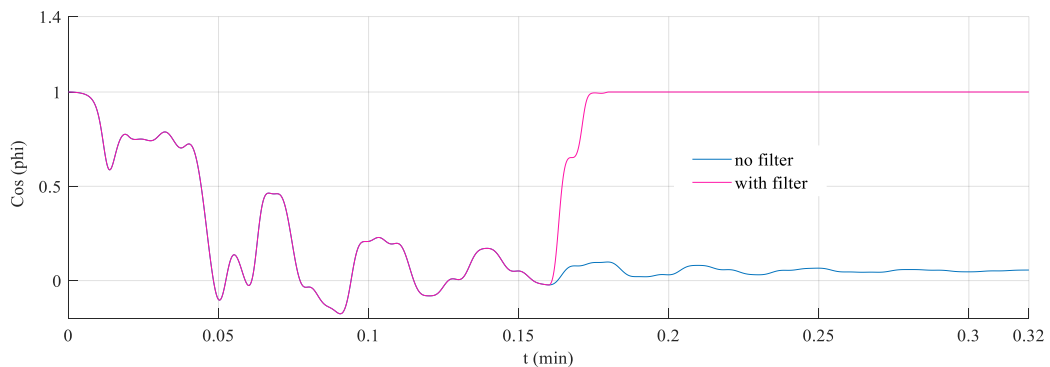


Figure 12. Power factor with filter and no filter at no-load conditions.



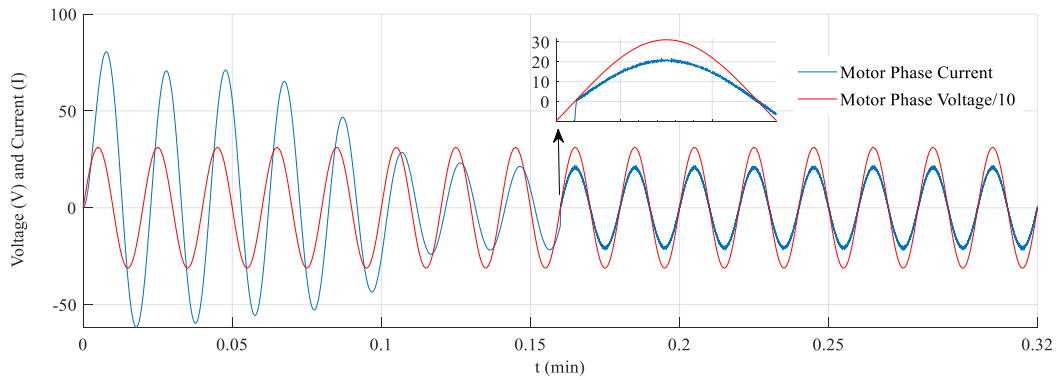


Figure 13. Source voltage and phase current of motor (loaded with 2 Nm).

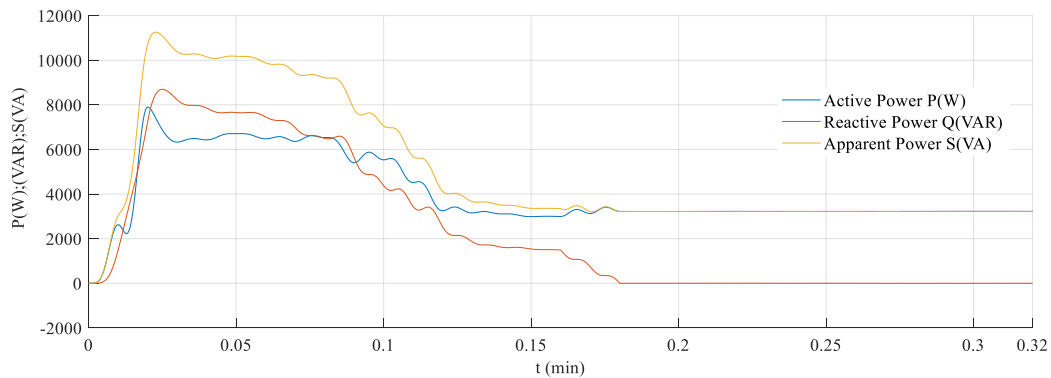


Figure 14. Active, reactive and apparent power signals (loaded with 2 Nm).

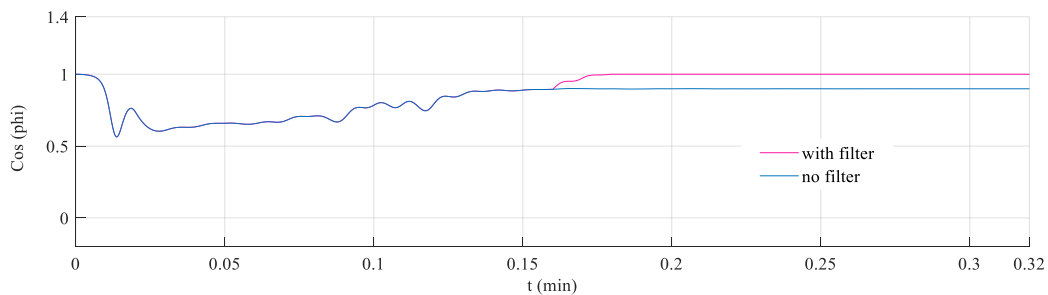


Figure 15. Power factor with filter and no filter at loaded conditions.

According to the block diagram given in Figure 9, the induction motor is directly connected to the 3-phase grid. There is no any switched power supply, such as inverter and converter, between the grid and the motor. Therefore, the current drawn from the grid by the motor running as an open loop is in pure sinusoidal form. However, there is a phase difference between the current drawn from the grid and the voltage. With the enabling of the Parallel Active Power Filter (PAPF), the motor draws the reactive energy, it needs, through the inverter connected to the DC bus. In this case, the phase difference between motor current and voltage becomes zero, but motor current loses its pure sinusoidal form. That is, it becomes a harmonic structure. Harmonics occur in all switched electronic circuits. The distortions to be caused by these harmonics vary according

to the switching frequency. In this respect, the total THD to occur in the current with the enabling of PAPF is found naturally higher than the situation before the compensation. This is because the currents drawn by the motor from the grid before compensation are pure sinusoidal and their THD is lower. In this respect, by considering that THD analysis of conditions before and after compensation could be a different study subject, no harmonic analysis was performed in this study.

#### 4. Conclusions

In the literature, there are different studies related to the reactive power compensation of the 3-phase induction motor with the parallel active power filter (PAPF). However, studies in which SMT, which is the reference current prediction

technique, and HBCC, which is the hysteresis controller structure, are used together have not been encountered much. In this study, in order to contribute to this area, a model in which the sine Multiplication Technique (SMT) and Hysteresis Band Current Controller (HBCC) structure were used together was created. With this model created in MATLAB/Simulink environment, reactive power compensation of a 3-phase induction motor was performed and the power factor was corrected. In this respect, this study is different from other studies that have been conducted and it partly contains originality.

Performance of a PAPF using the sine multiplication technique was investigated. Reference currents were estimated via sine multiplication technique. While the induction motor was running both no-load and loaded, the PAPF successfully performed reactive power compensation and power factor correction. Simulation studies were presented to evaluate the performance under different motor operating conditions. It was observed that PAPF performed a successfully reactive power compensation by increasing the power factor.

## Declaration

The author(s) declared no potential conflicts of interest with respect to the research, authorship, and/or publication of this article. The author(s) also declared that this article is original, was prepared in accordance with international publication and research ethics, and ethical committee permission or any special permission is not required.

## References

1. Yılmaz, Ö., Aksoy, M., Kesilmiş, Z. *Misalignment fault detection by wavelet analysis of vibration signals*. International Advanced Researches and Engineering Journal. 2019. 3(3), p.156-163.
2. Gundogdu, A., Dandil, B., Ata, F. *Direct Torque Control Based on Hysteresis Controller of Asynchronous Motor*. Science and Eng. J of Firat Univ. 2017. 29(1), p.197-205.
3. Ferreira, S.C., Gonzatti, R.B., Pereira, R.R., Silva, C.H., Silva, L. E. B., Torres, L.G. *Finite Control Set Model Predictive Control For Dynamic Reactive Power Compensation With Hybrid Active Power Filters*. IEEE Trans. On Industrial Electronics. 2018. 65(3),p.2608–2617.
4. Ye, J., Gooi, H.B., *Phase Angle Control Based Three-phase DVR with Power Factor Correction at Point of Common Coupling*. in Journal of Modern Power Systems and Clean Energy. 2020. 8(1), p. 179-186.
5. Roy, R.B., Cros,J., Basher, E., Akhter, S. *Power Compensation by DSTATCOM Plus SCESS*. Proceedings of the 2017 4th International Conference on Advances in Electrical Engineering (ICAEE). 2017. 28-30, p.100-108.
6. Wang, Y., Xu, Q., Chen, G. *Simplified Multi-Modular Shunt Active Power Filter System and its Modelling*. IET Power Electronic, 2015. 8(6), p. 967–976.
7. Cetin, S. *Power Factor Corrected and Fully Soft Switched PWM Boost Converter*. IEEE Transactions on Industry Applications, 2018. 54(4), p.3508–3517.
8. Badoni, M., Singh, A., Singh, B. *Adaptive Recursive Inverse-Based Control Algorithm for Shunt Active Power Filter*. IET Power Electronic, 2016. 9(5), p.1053–1064.
9. IEEE Std 519-1992. *Recommended Practices and Requirements for Harmonic Control in Electrical Power Systems*. IEEE Std, 1993. p.85-87.
10. Carlos, J., Gil, A., Pérez, E., Ariño, C., Beltran, H. *Optimization Algorithm for Selective Compensation in a Shunt Active Power Filter*. IEEE Transactions On Industrial Electronics, 2015. 62(6), p.3351–3361.
11. Fang, Y., Fei, J., Wang, T. *Adaptive Backstepping Fuzzy Neural Controller Based on Fuzzy Sliding Mode of Active Power Filter*.2020. doi:10.1109/ACCESS.2020.2995755, IEEE Access.
12. Sanam, J., Panda, A.K., Ganguly, Sanjib. *Optimal Phase Angle Injection for Reactive Power Compensation of Distribution Systems with the Allocation of Multiple Distribution STATCOM*. Arabian Journal for Science and Engineering, 2017. 42, p.2663–2671.
13. Ferreira, S.C., Gonzatti, R.B., Pereira, R.R., da Silva, C.H., da Silva, L.E.B., Lambert-Torres, G. *Finite Control Set Model Predictive Control for Dynamic Reactive Power Compensation With Hybrid Active Power Filters* in IEEE Transactions on Industrial Electronics. 2018. 65(3), p. 2608-2617.
14. Kandadai V., Sridharan, M., Parvathy, S.M., Pitchaimuthu, R., Kurup, D. *Performance Evaluation of FPGA-Controlled DSTATCOM for Load Compensation*. Arabian Journal for Science and Engineering, 2016. 41, p.3355–3367.
15. Komathi, C., Umamaheswari, M.G. *Erratum to Design of Gray Wolf Optimizer Algorithm-Based Fractional Order PI Controller for Power Factor Correction in SMPS Applications*. in IEEE Transactions on Power Electronics. 2020. 35(5), p.5543-5543.
16. Krama, A., Zellouma, L., Benaissa, A., Rabhi, B., Bouzidi, M., Benkhoris, M.F. *Design and Experimental Investigation of Predictive Direct Power Control of Three-Phase Shunt Active Filter with Space Vector Modulation using Anti-windup PI Controller Optimized by PSO*. Arabian Journal for Science and Engineering, <https://doi.org/10.1007/s13369-018-3611-6>.
17. Xu, Y., Yu, J., Cao, Y., Lu, X., Yu, J. *Double Resonant Output Filter to Eliminating the Tradeoff Between Bandwidth and Switching Ripple in Shunt Active Power Filters*. IET Power Electronics, 2016. 9(4), p.846–854.
18. Smith, I.J., Salmon, J. *High-Efficiency Operation of an Open-Ended Winding Induction Motor Using Constant Power Factor Control*. IEEE Transactions on Power Electronics. 2018. 33(12), p. 10663-10672.
19. Jibhakate, C.N., Chaudhari, M.A., Renge, M.M. *Reactive Power Compensation Using Induction Motor Driven by Nine Switch AC-DC-AC Converter*. IEEE Access. 2018. 6, p. 1312-1320.
20. Abu-Jalala, A.M., Cox, T., Gerada, C., Rashed, M., Hamiti, T., Brown, N. *Power Quality Improvement of Synchronous Generators Using an Active Power Filter*. IEEE Transactions on Industry Applications. 2018. 54(5), p. 4080-4090.

21. Durna, E. *Adaptive fuzzy hysteresis band current control for reducing switching losses of hybrid active power filter*. *IET Power Electronics*. 2018. 11(5), p. 937-944.
22. Zhang, H., Li, X., Xiao, S., Balog, R.S. *Hybrid hysteresis current control and low-frequency current harmonics mitigation based on proportional resonant in dc/ac inverter*. *IET Power Electronics*. 2018. 11(13), p. 2093-2101.
23. Diab, M., El-Habrouk, M., Abdelhamid, T. H., Deghedie, S. *Survey of Active Power Filters Configurations*. 2018 IEEE International Conference on System, Computation, Automation and Networking (ICSCA). Pondicherry, India, 2018. p.1-14.
24. Devassy, S., Singh, B. *Control of solar energy integrated active power filter in weak grid system*. 7th International Conference on Power Systems (ICPS), Pune. 2017. p. 573-578.
25. Yang, Z., Sun, J., Li, S., Huang, M., Zha, X., Tang, Y. *An Adaptive Carrier Frequency Optimization Method for Harmonic Energy Unbalance Minimization in a Cascaded H-Bridge-Based Active Power Filter*. *IEEE Transactions On Power Electronics*, 2018. 33(2), p.1024–1037.
26. Karaman, Ö.A., Erken, F., Cebeci, M. *Decreasing Harmonics via Three Phase Parallel Active Power Filter Using Online Adaptive Harmonic Injection Algorithm*. *Tehnički vjesnik*, 2018. 25(1), p.157-164.
27. Singh, B., AL-Haddad, K., Chandra, A. *A Review of Active Filters for Power Quality Improvement*. *IEEE Transaction on Industrial Electronics*, 1999. 46(5), p.133-138.
28. Terriche, Y., Golestan, S., Guerrero, J.M., Kerdoune, D., Vasquez, J.C. *Matrix Pencil Method-Based Reference Current Generation for Shunt Active Power Filters*. *IET Power Electronic*, 2018. 11(4), p.772-780.
29. Zhang, J., Yang, H., Wang, T., Li, L., Dorrell, D.G., Lu, D.D.C. *Field-Oriented Control Based on Hysteresis Band Current Controller for a Permanent Magnet Synchronous Motor Driven by a Direct Matrix Converter*. *IET Power Electronic*, 2018. 11(7), p.1277-1285.
30. Koya, S., Alsumiri, M. *A Modified Fuzzy Hysteresis Controller For Shunt Active Power Filter*. 2018 Renewable Energies, Power Systems & Green Inclusive Economy (REPS-GIE). Casablanca, Morocco, 2018. p.1-5.
31. Campanhol, L.B.G., Silva, S.A.O., Goedtel, A. *Application of Shunt Active Power Filter for Harmonic Reduction and Reactive Power Compensation in Three Phase Four-Wire Systems*. *IET Power Electronic*, 2014. 7(1), p.2825–2836.
32. Zhang, J., Li, L., Zhang, L., Dorrell, D. G. *Hysteresis Band Current Controller Based Field-Oriented Control for an Induction Motor Driven by a Direct Matrix Converter*. *IECON 2017-43rd Annual Conference of the IEEE Industrial Elect. Society*, Beijing, China, 2017. p.4633-4638.



## Research Article

# Liquid level control with different control methods based on Matlab/Simulink and Arduino for the control systems lesson

Mehmet Yumurtacı <sup>a,\*</sup>  and Özgür Verim <sup>b</sup> 

<sup>a</sup> Afyon Kocatepe University, Faculty of Technology, Department of Electrics and Electronics Engineering, Afyon, 03200, Turkey

<sup>b</sup> Afyon Kocatepe University, Faculty of Technology, Department of Mechanical Engineering, Afyon, 03200, Turkey

### ARTICLE INFO

#### Article history:

Received 10 June 2020

Revised 21 July 2020

Accepted 07 August 2020

#### Keywords:

Arduino

Controller

Embedded systems

Liquid level

Matlab/Simulink

### ABSTRACT

Liquid level control is needed in many areas, from simple to complex, from daily life to industry. With the developed system in this study, it was aimed to ensure the students of the control system course to learn the concepts of a closed-loop control system and to observe the effect of changes in the system in real-time. The system consists of two tanks, a pump, a pressure sensor, a power supply, a regulated voltage source, a computer, and an Arduino Due board. By using the Matlab/Simulink and added Arduino blocks, software of the control system was created without code need. It is possible to control the liquid level system via the control board through the computer, as well as to control it without a computer by the embedded software. Liquid level control is carried out with different types of control methods from basic level to advanced level (On-off, PID, ANN-PID, and Fuzzy-PID controller). It is also possible to record the desired parameters in real-time, such as reference level, actual level, error signal, and control signal, in the liquid level control system. In this study, an interface for a PID controller was prepared using Matlab/Gui. It was concluded that with Matlab/Simulink blocks added to the system, different control methods could be applied easily.

© 2020, Advanced Researches and Engineering Journal (IAREJ) and the Author(s).

## 1. Introduction

Control of the flow between tanks and fluid level is one of the main problems in industrial processes [1]. Liquid level systems are very complex systems, and traditional control approaches are insufficient to solve this complex structure [2]. In industrial applications, the most commonly used controller for closed-loop control is the proportional-integral-derivative (PID) controller. The best performance in the PID controller is obtained by setting the controller parameters according to the nature of the system [3].

Thakur et al. [2] designed PID and Fuzzy logic controllers in Matlab program to control the water level in a tank. They compared the effects of the controllers by conducting a simulation study. They observed that the Fuzzy logic controller performed better by significantly reducing overshoot and steady-state error. Dinesh et al. [4] discussed the selection of appropriate entry and exit

numbers, membership functions, and rules in the Fuzzy logic controller design for non-linear level control of a cone-shaped tank. They compared the results of the classical PID controller with the results of the Fuzzy logic controller. Varghese and Rose [1] simulated the liquid level control of a two-tank system controlled by the first tank in the Matlab program. Ikhlef et al. [5] controlled the tank level with a PID controller over the internet by using a graphical user interface. Artificial neural networks (ANNs), inspired by the human nervous system, have characteristics such as fault tolerance, parallel processing of data, and natural distribution. Kumar et al. [6] modeled an ANN-PID controller in the Matlab/Simulink environment for liquid level control. Since parameters of the PID controller can be set according to the error change by the ANN-PID controller, its properties in the time domain can be improved effectively. Because it is easy to use as open-source and low-cost hardware and software, the Arduino platform is widely preferred.

\* Corresponding author. Tel.: +90 272 218 2550; Fax: +90 272 218 26 93.

E-mail addresses: [mehmetyumurtaci@aku.edu.tr](mailto:mehmetyumurtaci@aku.edu.tr) (M. Yumurtacı), [ozgurverim@hotmail.com](mailto:ozgurverim@hotmail.com) (Ö. Verim)

ORCID: 0000-0001-8528-9672 (M. Yumurtacı), 0000-0002-1575-2630 (Ö. Verim)

DOI: 10.35860/iarej.750664

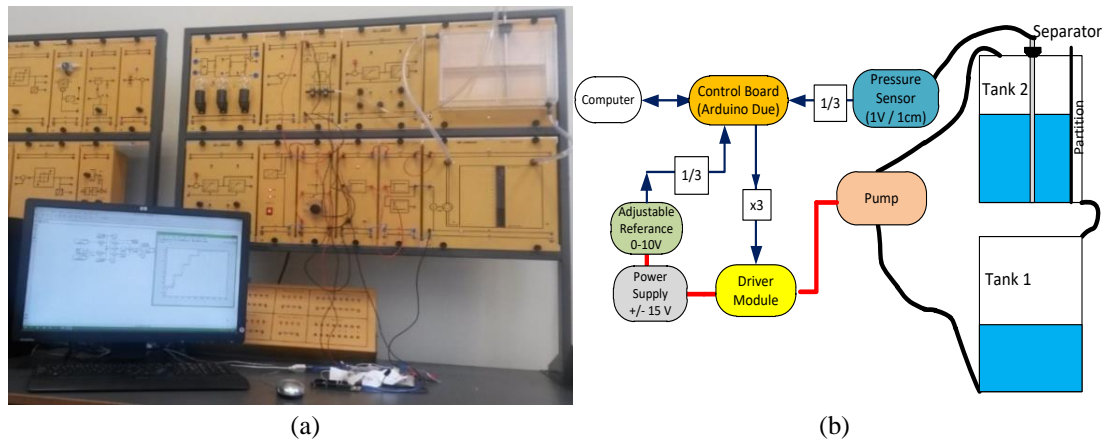


Figure 1. Liquid level control system (a) and experimental setup block diagram (b)

Sheng [7] set the water level inside the cylindrical tank with a PID controller that he designed using the Arduino microcontroller. Zidane [8] carried out the control of a four-tank system.

In this study, liquid level control was realized with different control methods in real-time by using a two-tank liquid level control system in the Delorenzo control system experimental training set. On-off, PID, ANN-PID, and Fuzzy-PID controllers were applied to the existing system, from basic to advance. It is thought that this study will be useful for students who take the control systems course in different engineering fields in terms of observing a closed-loop control system and having the opportunity to apply different control methods. Users can easily apply different control methods by using Matlab/Simulink blocks. Thanks to the created interface, the system is easier to use, observation of results is fast, and the data of the desired parameters can be recorded.

## 2. Material and Method

### 2.1 Experimental Setup

Some of the liquid level control modules in the experimental set of the control systems belonging to the Delorenzo Company were used in this study. The real system is as seen in Figure 1(a). In order to give detailed information about the modules used in the liquid level control system and their connections with each other, the block diagram of the experimental system is given in Figure 1(b). While the tank 1 seen in Figure 1(b) serves as a water tank, the liquid level of the tank 2 is controlled. An adjustable voltage source between 0-10V is used for the reference input of the liquid level system. The pressure sensor works based on the comparison principle. It compares the pressures of inside metal pipe in the tank and ambient. 1V output is taken from the sensor for each 1cm water level in tank 2. The pump operating with 10V empties the tank 1 to tank 2. Since the analog inputs of the Arduino Due board are 3.3V, the potentiometer is used as a voltage divider in two places in order to reduce 10V to this voltage level. Since the board's pulse width modulation (PWM)

output will also deliver a maximum of 3.3V, the power required for the pump is ensured by using an amplifier module and then a drive module is used to increase it to 10V. Due to the compartment in tank 2, there is also the possibility of liquid leakage and creating a disturbance effect.

### 2.2 Control Methods

To control the liquid level, different controllers were designed for a closed-loop control system. On-off and PID controllers were used as the basic level, and ANN-PID and Fuzzy-PID were preferred at the advanced level. Control programs/software were implemented in the Matlab/Simulink environment without using codes. The controller adjusted the power of the pump during operation with the PWM technique. In the block diagrams, reference level, real level, and controller parameters are shown for users in real-time.

#### 2.2.1 On-Off Controller

The pump driven by the on-off controller either runs at full power or does not run at all. If the difference between the desired water level and the actual level in the tank is positive, the pump is active at full power, and if the difference is zero or negative, the pump is disabled. Depending on the error value, the tolerance band is used to prevent the pump from switching on and off continuously. In this way, it is aimed to use both the driver circuit and the pump for a longer period of time. The block diagram designed for the on-off controller is shown in Figure 2.

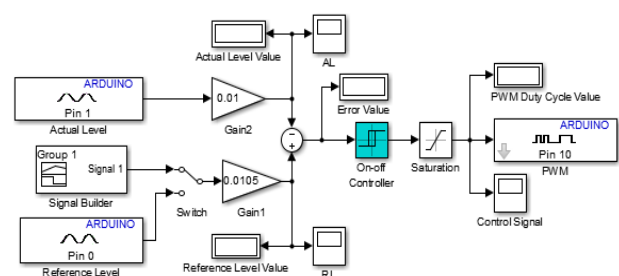


Figure 2. On-off controller block diagram

**2.2.2 PID Controller**

PID is the most preferred controller in industrial applications. The controller adjusts the power of the pump according to the magnitude of the error value between the reference level and the actual level. If the error is large, the pump is driven at full power, and as the error value gets smaller, the power of the pump is reduced by the controller. The PID controller gives the ideal result for a single reference value with which the parameters are set. The block diagram of the PID controller is given in Figure 3.

**2.2.3 ANN- PID Controller**

Artificial neural network (ANN) has been created by taking inspiration from the working logic of the human brain. The neural network is of great interest because it has advantages such as good dynamic performance, nonlinear prediction ability, robustness, and error tolerance capability [9]. The network can be trained, and if it encounters different situations, it generates an idea of the new situation. By taking advantage of this situation, it was attempted to solve the case where the PID controller was ideal for a single point. For different reference values, appropriate PID controller gain parameters were determined in the liquid level control system. With these data, the ANN model was created using Matlab/nftool. While the input of the network is the reference value, the output is proportional, integral, and derivative controller gain parameters. In the ANN model, there is one hidden layer with ten neurons. The Levenberg-Marquardt backpropagation algorithm was used in the training of the network. The gain parameters of the PID controller are estimated by the ANN model based on the reference level selected and automatically changed on the controller. This situation can be monitored instantly from the indicators by the user. The ANN-PID controller not only has the advantages of PID, but also has learning, remembering, and nonlinear prediction capabilities. Matlab/Simulink block diagram of the ANN-PID controller is shown in Figure 4.

With the Matlab/nftool, students can easily create a network model that has a different number of hidden layers and a different number of neurons in the layer and try it in the current system.

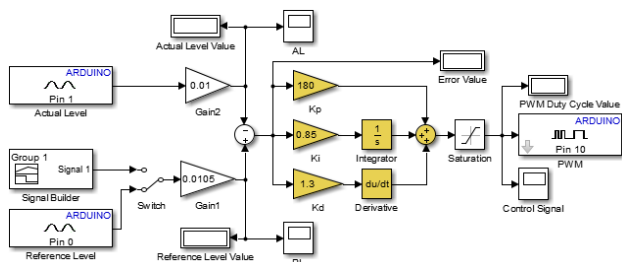


Figure 3. Block diagram of the PID controller

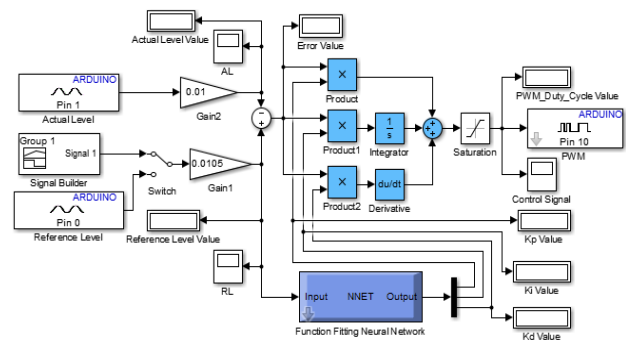


Figure 4. ANN-PID controller block diagram

With the help of Matlab/nntool, they can also use different types of network models in the system.

**2.2.4 Fuzzy- PID Controller**

Fuzzy logic is a controller that has humanoid thoughts and intermediate values. The controller input is mostly numerical values [10]. It is performed by using linguistic variables instead of numerical values and rules instead of complex mathematical expressions. Linguistic variables are very high, high, medium, low, and very low [1]. The fuzzy logic control method includes fuzzification, rule base, interference, and defuzzification operations [11]. Each of these parts plays an important role in the control process and affects the overall system behavior and controller performance. Fuzzification converts numerical data at the input into linguistic terms. The rule base provides the necessary information for all components of the fuzzy controller. Interference is the brain of the controller. At the end of the interference phase, fuzzy values that are not directly used in the control process are obtained. The numerical value is obtained by the defuzzification stage [12].

While creating the controller, first of all, a Fuzzy inference system (FIS) file is created by using the Matlab/fuzzy interface. The input of the fuzzy controller is the error, and the derivative output of the error is determined as the controller parameter. As seen in Figure 5, a separate Fuzzy logic controller was created for each parameter of the PID controller. Here, Mamdani type fuzzy model was preferred.

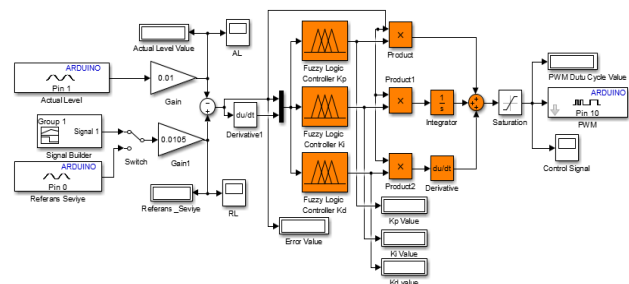


Figure 5. Fuzzy-PID controller block diagram

Seven membership functions for control process precision function were preferred: these were NB (Negative Big), NM (Negative Medium), NS (Negative Small), Z (Zero), PS (Positive Small), PM (Positive Medium), and PB (Positive Big). NB and PB membership functions were selected in gauss, others in triangular. In Figure 6, membership functions of the fuzzy block of the proportional component of the PID controller are given. Membership functions for the error and derivative of the error are similar, and the boundary ranges are between 0-10 and -1 and +1 respectively, while the membership functions of the output control signal are the same and range between 0-255 (8 bits).

Since seven membership functions are used, the rule table consists of 49 rules (Table 1). Different rule tables are used in other components of the PID controller.

The variation of the output control signal against the inputs of the fuzzy logic controller, which will determine the gain value of the proportional component of the PID controller, is given in Figure 7 as three dimensional. As can be seen in the chart, there is a balanced distribution.

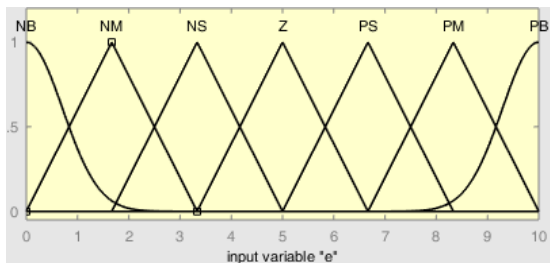


Figure 6. Fuzzy error input membership functions of proportional component of the PID controller

Table 1. The rule table of the fuzzy logic controller, which will determine the proportional parameter of the PID controller [13]

de / e	NB	NM	NS	Z	PS	PM	PB
NB	PB	PB	PM	PM	PS	Z	Z
NM	PB	PB	PM	PS	PS	Z	NS
NS	PM	PM	PM	PS	Z	NS	NS
Z	PM	PM	PS	Z	NS	NM	NM
PS	PS	PS	Z	NS	NS	NM	NM
PM	PS	Z	NS	NM	NM	NM	NB
PB	Z	Z	NM	NM	NM	NB	NB

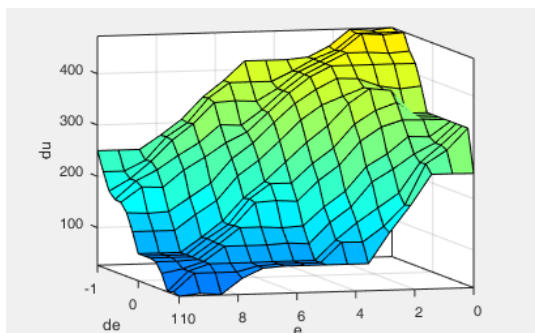


Figure 7. 3D representation of the Fuzzy logic controller

Students can create their own FIS files and use them in the existing system. They can observe their effects by making changes in installed FIS file. They can change the shapes, number, and limits of membership functions and create different rule tables. Our system is able to appeal to users at different levels.

### 3. Discussion and Results

The adjustable voltage source in the experimental setup or the signaling block in Matlab/Simulink can be used as reference input. Figure 8 shows the level change curves according to different controllers for the time-varying reference input created with the signaling block.

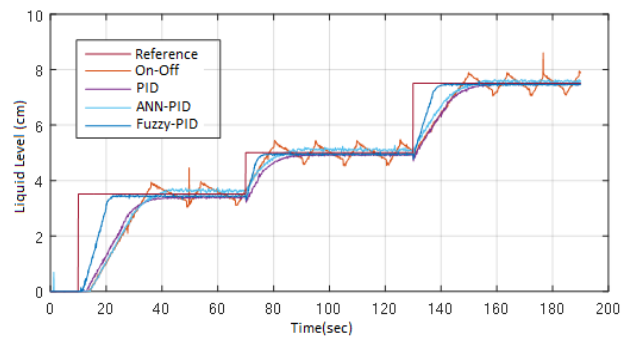


Figure 8. Response curves of controllers for different reference values

In this system, comparison of controllers in terms of parameters such as rise time, overshoot, settling time, permanent status error can be easily made by students. The effects of changes in controller parameters are easily observed in real-time. Any data related to the system can be recorded. As an example, the control signals of the different controllers are shown in Figure 9. The 0-255 range indicates the voltage level of the card the 0-3.3V range. This voltage is raised 3.03 times and applied to the pump. As seen on the on-off controller, the pump is either driven at full power or is disabled. In other controllers, it is observed at intermediate values depending on the error value. It is the Fuzzy-PID controller that gives the fastest response and offers a quick response to the current settings. Our aim is to control the system without the need for codes with different controllers. Thus, it is not the best controller to detect.

With the help of Matlab/Gui, an interface was designed to attract the attention of the students, to learn the concepts about the closed-loop control system in detail, and to observe the parameter changes quickly. From the interface shown in Figure 10, sampling time, simulation time, and PID controller gain parameters are easily determined, and the system is operated. Signals to be plotted in the graphics area can be selected by the user. Here, the set source of voltage on the experiment set is used as a reference input.

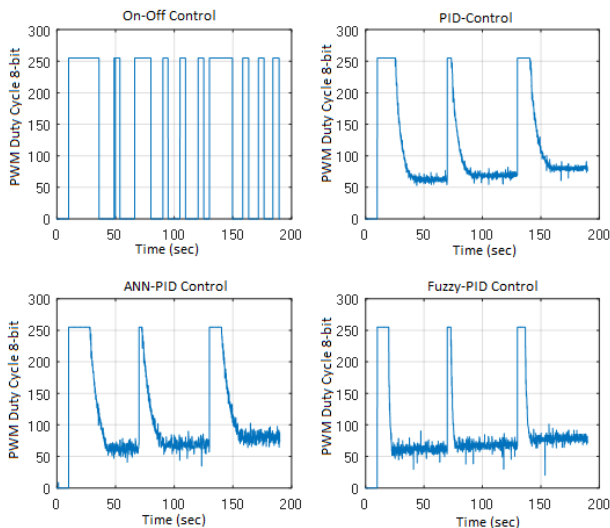


Figure 9. Control signal for different type controllers

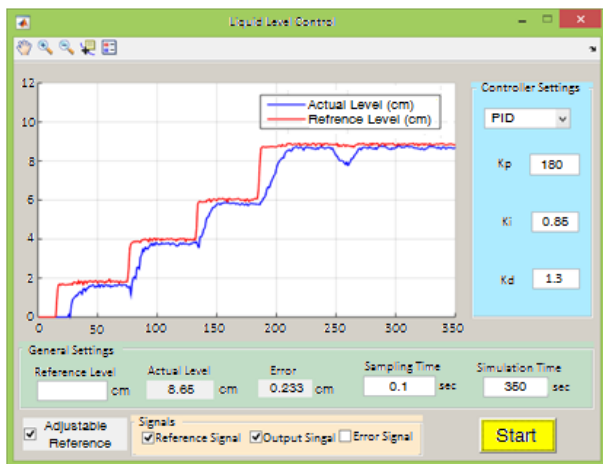


Figure 10. Interface created for PID controller

The system is started by pressing the start button. The graphics drawn with the tools in the menu above the interface can be examined in detail.

#### 4. Conclusions

Liquid level control systems are used widely in the industry and as a result of this, technical personnel with the necessary knowledge and experience are needed. In order to contribute to this need, an experimental setup design and application in which the necessary skills can be gained for liquid level control was realized in this study. Control methods were applied on a two-tank experimental setup, one of which was a water tank and the other was a liquid level control.

The control of the liquid level experimental set was carried out easily by designing basic controllers such as on-off and PID as well as by the advanced controllers such as ANN-PID and Fuzzy-PID. In the application, controllers were designed with Matlab/Simulink and Arduino blocks without the need for codes. Thus, the design was simplified and design time was shortened. The system can be operated in the Matlab/Simulink

environment as well as embedded in the Arduino Due board and can be operated independently. Graphics can be drawn and the values of the desired parameters can be recorded. For the PID controller, an interface was created using Matlab/Gui. Since the instant changes of the selected parameters can be observed, the system is started by entering the simulation time, sampling time, and controller parameters. The graphics can be examined in more detail with the tools available in the interface.

Thanks to the system designed in this study, the students can learn the logic of the closed-loop liquid level control system in detail and select the appropriate controller in line with what is expected from the system.

#### Declaration

The author(s) declared no potential conflicts of interest with respect to the research, authorship, and/or publication of this article. The author(s) also declared that this article is original, was prepared in accordance with international publication and research ethics, and ethical committee permission or any special permission is not required.

#### References

1. Varghese, K.H. and L. Rose, *Comparitive study of various level control techniques for a two tank system*, in IEEE Sponsored 2nd International Conference on Innovations in Information Embedded and Communication Systems (ICIIES) 2015: Coimbatore, India. p. 1-4.
2. Thakur, A.S., H. Singh, and S. Wadhvani, *Designing of fuzzy logic controller for liquid level controlling*. International Journal of u- and e- Service, Science and Technology, 2015. **8(6)**: p. 267-276.
3. Vishnu, V.S., K.A., Aneesa, A. Lal, and A. Nabi, *Real time dc motor speed control using PID in labview with arduino*. Imperial Journal of Interdisciplinary Research (IJIR), 2016. **2(5)**: p. 1757-1759.
4. Dinesh, C., V.V., Manikanta, H.S. Rohini, and K.R. Prabhu, *Real time level control of conical tank and comparison of fuzzy and classical PID controller*. Indian Journal of Science and Technology, 2015. **8(S2)**: p. 40-44.
5. Ikhlef, A., M., Kihel, B., Boukhezzar, N., Mansouri, and F., & Hobar, *Online PID control of tank level system*. IEEE Global Engineering Education Conference (EDUCON) 2016: Abu Dhabi, United Arab Emirates. p. 281-284.
6. Phaneendakumar, G.V., I. Srinu, and K., Satyanarayana, *Design and performance analysis of ANN based hybrid PID controller for liquid level control system*. International Journal of Scientific Research, 2014. **3(9)**: p. 160-165.
7. Sheng, J., *Real time dc water tank level control using arduino mega 2560*. IEEE 28th International Symposium on Industrial Electronics (ISIE) 2019: Vancouver, BC, Canada, Canada. p. 635-640.
8. Zidane, Z., *Constrained model predictive control for the quadruple-tank process*. International Advanced Researches and Engineering Journal, 2019. **03(03)**: p. 175-18.
9. Peng, W., M., Hao, D. Peng, and D., Ri-hui, *Decoupling control based on PID neural network for deaerator and*



- condenser water level control system*. 2015 34th Chinese Control Conference (CCC): Hangzhou, China. p. 3441-3446.
10. Kahraman, M., and F. Pakdamar, *The evaluation on the effect of effective and repetitive vibration to compressive strength with the fuzzy method*. International Advanced Researches and Engineering Journal, 2019. **03(01)**: p. 048-054.
  11. Mondal, B., M.A., Billiha, B. Roy, and R. Saha, *Performance comparison of conventional PID and fuzzy logic controller in the field of over headed water level control system*. International Journal of Computer Sciences and Engineering, 2016. **4(6)**: p. 76-81.
  12. Chabni, F., R., Taleb, A., Benbouali, and M.A., Bouthiba, *The application of fuzzy control in water tank level using arduino*. International Journal of Advanced Computer Science and Applications, 2016. **7(4)**: p. 261-265.
  13. Dib, F., K.B., Meziane, and I., Boumhidi, *Sliding mode control without reaching phase for multimachine power system combined with fuzzy PID based on PSS*. WSEAS Transactions on Systems and Control, 2015. **10**: p. 206-214.



### Research Article

## Estimation of consistency limits of fine-grained soils via regression analysis: A special case for high and very high plastic clayey soils in Istanbul

Zülal Akbay Arama<sup>a</sup> , Muhammed Selahaddin Akın<sup>b</sup> , Said Enes Nuray<sup>a</sup>  and İlknur Dalyan<sup>c,\*</sup> 

<sup>a</sup>Istanbul University-Cerrahpaşa, Engineering Faculty, Civil Engineering Division, Avcılar, Istanbul, 34320, Turkey

<sup>b</sup>Kartal Municipality, Kartal, Istanbul, 34862, Turkey

<sup>c</sup>Disaster and Emergency Management Presidency, Çankaya, Ankara, 06800, Turkey

#### ARTICLE INFO

##### Article history:

Received 12 May 2020

Revised 08 July 2020

Accepted 12 August 2020

##### Keywords:

Clay

Fine-grained soils

Liquid limit

Plasticity index

Regression analysis

#### ABSTRACT

Consistency limits are essential and simple design parameters that are utilized as standard entries of all kinds of soil investigation programs conducted for geotechnical projects which are constructed in/on fine grained soils. These limits also represent mineralogical and physical properties of clayey soils directly and used to estimate their strength and rigidity properties indirectly. However, the consistency tests are assumed as the simple and basic tests of geotechnical engineering investigations, but the effects of operator, calibration of the device and environmental aspects at the tests damage the reliability and correctness of results. In this paper, it is aimed to overcome these challenges by evaluating the consistency characteristics of clayey soils considering only the values of liquid limit of specific clays with the use of simple regression analysis. A database is prepared by using 500 soil investigation reports that are involving the site characterization information, laboratory and field tests of Istanbul Province European side clayey soils, including Avcılar, Esenyurt, Küçükçekmece, Büyükçekmece, Çatalca, Zeytinburnu, Bahçelievler, Bakırköy districts. 1523 liquid limit tests are obtained from the mentioned database for high and very high plastic clays. The regression analyses have been applied to query the parameter effect ratio on the consistent characteristics and relationships have been tried to be developed to evaluate the values of plastic limit and plasticity index directly from only liquid limit test applications. The effects of fine material content, depth and natural water content is also investigated. Verifications of the suggested equations have been done for different cases and comparisons are made with the well-known sources of literature. Consequently, strong equations are acquired to determine the plasticity index value in terms of liquid limit, liquid limit-depth, liquid limit-fine content, natural water content-fine content respectively based on the actual experimental tests conducted in Istanbul.

© 2020, Advanced Researches and Engineering Journal (IAREJ) and the Author(s).

### 1. Introduction

The existence of clay minerals in fine grained soil medium leads soil to be remolded in the presence of some moisture without crumbling. This nature of behavior is represented by cohesion phenomenon that is caused by the adsorbed water which surrounds the clay particles [1]. The mentioned natural behavior trend is initially revealed by Atterberg [2] with the use of a conservative method to describe the consistency of fine grained soils with various water contents.

The relationship between the water contents are specialized as consistency limits and mainly divided into four basic phases such as solid, semisolid, plastic and liquid to classify the physical state of soils [3]. The properties that are obtained with the use of water content values characterize the most prominent physical properties of clays and specific classification systems use the plasticity degree values of clays to identify the dominant characteristics of evaluated soils. In order to determine the typical engineering properties, besides the natural water content value of any type of soil

\* Corresponding author. Tel.: +0-312-258-2323/2114; Fax: +0-312-258-21-02.

E-mail addresses: [zakbay@istanbul.edu.tr](mailto:zakbay@istanbul.edu.tr) (Z. Akbay Arama), [msehahaddinakin@gmail.com](mailto:msehahaddinakin@gmail.com) (M. S. Akın), [enesnuray3@gmail.com](mailto:enesnuray3@gmail.com) (S. E. Nuray),

[ilknurdalyan@gmail.com](mailto:ilknurdalyan@gmail.com) (İ. Dalyan)

ORCID: 0000-0001-8185-7329 (Z. Akbay Arama), 0000-0003-1980-1812 (M. S. Akın), 0000-0002-2333-2687 (S. E. Nuray),

0000-0001-6436-7109 (İ. Dalyan)

DOI: 10.35860/iarej.735529

medium, various boundary water content values should be obtained to identify the physical state that is qualifying consistence. The water content of the soil at the point of transition from solid to semisolid state is described as the shrinkage limit, and from semisolid to plastic state is identified as the plastic limit. In addition to these, the water content of the soil at the point of transition from plastic to liquid state is defined the liquid limit [1]. These three boundary water content values are named as Atterberg limits. The knowledge about the natural water content values that are obtained from the field or laboratory experiments carried out during the design phase of the application projects, is used to find the location of the determined water content value between the Atterberg limits. This application provides only a premise information in terms of the engineering behavior to be exhibited. To acquire the real behavior characteristics of envisaged soil profile, advanced studies were conducted and the concepts of consistency limits were expressed more precisely by Casagrande [4] after 1920 in accordance with the engineering purposes and then the use of the plasticity index in the classification systems was standardized. Plasticity index ( $PI$ ) value is defined as the difference between the liquid limit ( $LL$  or  $w_L$ ) and the plastic limit ( $PL$  or  $w_p$ ) of the inspected soil. The water content degrees between liquid and plastic limits are reflecting the measure of the range of plasticity behavior of especially fine grained soils. Hence the acquirement process of liquid and plastic limit values gains importance to calculate the plasticity index value. In this connection, Casagrande [4], [5] developed the liquid limit test instrument (Casagrande cup) in order to standardize its acquisitions and enabled the experiment to become the least dependent on the practitioner and become repeatable. The proposed technique is based on the preparation step of the different soil samples with various water contents by remolding. The second step of the method includes the application of the test with the Casagrande cup [4], [5]. Although these foreseen experiments seem easy and fast to implement; serious experience, attention and time are required to obtain valid and consistent results. Insufficient remolding effect applied during sample preparation in water contents other than the soils used in the experiments is one of the physical problems that may occur during the limit tests and this may trigger the interpretation errors and cause the wrong limit values to be obtained. Besides, the plastic limit test is shaped entirely based on the experience of the operator who is performing the experiment, and the main reason for the errors related to the experiment is the preparation and testing of the sample depending on the operator. In addition, the ambient temperature and remolding sensitivity of the operator while preparing the sample may cause the sample prepared in a certain water content to lose water and in fact the predicted content value cannot be obtained. This situation makes it difficult to interpret the average water content value and causes the data to be obtained in a wide range. For this

reason, the experiment should be reproducible and interpretation should be made considering the conditions that pose risks in the experiments. In addition, apart from the usage of plasticity index value to classify the fine-grained soils, many engineering features can be calculated in relation to this value. Thus, the prediction of engineering characteristics of soils in terms of index properties has a great applicability in the discipline of geotechnical engineering. Various studies were performed from different points, including experimental, theoretical and empirical relationships to obtain some engineering properties of fine grained soils. In this context, there are many empirical formulas proposed by Skempton [6] based on obtaining the strength and compaction parameters of the soil using the limit water content values. However, the fact that natural soils are not stacked homogeneously as a single formation complicates the issue of which of these empirical expressions can be selected and evaluated for the soil types of the project and also creates a subject that requires expertise. Fall [7] developed a correlation to obtain the plastic limit and plasticity index value by using liquid limit experiments applied on clays. The relevant study is a widely used reference in the literature, and the success of the equations in estimating the plasticity index of low and high plasticity clays is still one of the topics to being evaluated within the studies. Chenari et al. [8] attempted to relate soil compaction characteristics, hydraulic conductivity, and strength and consistency parameters in the study titled obtaining soil geotechnical properties with index parameters. Tanzen et al. [9] used a two-step test procedure for estimating the plastic limit value that was conducted by using a fall cone test. In the first of these studies, the classical fall cone test was applied for eight fields and at the second stage, a test revision with a load value to obtain the plastic limit was proposed. Kuriakose et al. [10] suggested equations using the liquidity index and the water content ratio in estimating the shear strength of clays Naveena et al. [11] were applied the classical consistency limits tests for specific soils that are provided the relationship between simple linear regression analysis and plasticity index and liquid limit value were examined. The correlation obtained as a result of regression analysis has been shown to give results consistent with the results of the Casagrande plastic limit test. Jasim et al. [12] conducted a study based on estimation of the bearing capacity, shear strength angle, cohesion value and plasticity value using artificial intelligence technology. Cantillo and Pajaro [13] have presented a technical note including some correlation equations that are suggested to predict the swelling pressure based on the consistency limits with statistical methods. Spagnoli and Feinendegen [14] have used 40 different clay samples with different mineralogies and have performed some laboratory tests to evaluate the strength and consistency characteristics. Some solutions are conducted with the use of liquidity index depending on the

estimated plastic limit values to verify the suggested relationships. Shimobe and Spagnoli [15] have considered 500 data from both literature and laboratory tests and have compared the undrained shear strength, liquidity index and water content ratio. In addition, it is aimed to acquire the relationship between the strength and liquidity index of remolded specimens. Barnes [16] has suggested a semi-logarithmic relation between the undrained shear strength and liquidity index and has defended to be accurate shear strength values at the liquid and plastic limits can be achieved. Golavska et al. [17] have used the outcomes of the laboratory tests of plastic and liquid limit tests of Eemian gyttja that are characterized by different organic contents. The statistical analyses have been performed to query the effect of the organic content on the single and two-factor relationships obtained between the plastic and liquid limit. Hussain and Atalar [18] have investigated the relationship between the liquid limit and the compaction characteristics with the use of 8 samples of North Nicosia Kythrea group soils in North Cyprus were subjected to Atterberg limits and compaction laboratory tests. Besides, multiple linear regression analyses have been made to obtain the mathematical expression of relationships and the  $R^2$  values of the suggestions have been determined over 75%. Singh and Gupta [19] have enhance a correlation between the strength and the water content ratio and also a correlation between the strength and the liquidity index. Comparisons have been conducted between the obtained relationships with the use of experimental results.

The excessiveness and the actuality of the conducted studies about the evaluation and the derivation process of consistency limits show the importance and actuality of the subject. In addition, the developing information and computer technologies leads researchers to obtain the easy way to calculate all the soil engineering properties by the usage of advanced methods with prediction. So it will be possible to say that the verity of the used prediction method is preliminary depends on the acquirement of the consistency limits. Concordantly, in this study, it is aimed to use the liquid limit test values to predict the representative plasticity index values of high and very high plastic clayey soils that are selected from the European side of Istanbul. For that purpose, a database is generated by the use of different 500 soil investigation reports, including the site characterization information, laboratory and field tests of Istanbul Province European side clayey soils, including Avcılar, Esenyurt, Küçükçekmece, Büyükçekmece, Çatalca, Zeytinburnu, Bahçelievler, Bakırköy districts. Totally, 1523 liquid limit tests are obtained from the mentioned huge database for high and very high plastic clayey soils. Special locations are selected from Istanbul and four zones are arranged depending on the closeness and the wideness of districts to conduct regression analysis with Matlab R2016a. Regression analysis is conducted to query the parameter effect ratio on the consistency characteristics and then regression relationships are tried to be developed to evaluate the values

of plastic limit and plasticity index directly from only liquid limit test applications. On the other hand, the effects of natural water content, depth of the specimen in the field and fine content ratio are also taken into account to acquire more detailed and accurate results to predict the plasticity index value. Verification of the developed equations is conducted for different cases and comparison is done by the well-known sources of literature. Consequently, this study is differentiated from other studies by determining the plasticity index value via liquid limit with the use of characteristic soil types of Istanbul soils because there are not enough literature studies about these kind of soils to correlate their original characteristics. In addition to this, the selected influencer variants of plasticity index are not similar to other conducted studies that exist in the literature. Besides, the present study provides an opportunity for authors to form a huge database to attain novel approaches to define the geotechnical properties of Istanbul.

## 2. Materials and Methods

### 2.1 Application details of consistency limit tests

Liquid limit test device, named Casagrande cup, includes a brass cup and a hard rubber base that can be dropped onto the base by a manually operated by a crank [4]. The soil specimens that are prepared with different moisture contents, placed in the cup to parallel to the horizontal surface. A standard knife is used to cut the specimen and a groove is formed at the vertical axis. Subsequently, the cup is lifted and dropped from 10 mm height. The moisture content of the performed test is specified the required blows to close the distance of approximately 13 mm through the bottom of the groove after  $N$  blows. At least three cup tests have to be experienced to obtain the water content that corresponds to the 25 blows of the cup is identified as liquid limit. The water content of the soil specimens, in percent, and the corresponding number of blows  $N$  is plotted on semi-logarithmic axes. The relationship between the moisture content and  $\log N$  is approximated as a straight line. This straight line is named as the flow curve. The numerical value of the moisture content corresponding to  $N=25$  blows, determined from the drawn flow curve, constitutes the liquid limit of the soil. The procedure for the plastic limit test is defined in ASTM in Test Designation D-4318. The plastic limit is identified as the water content at which the soil crumbles, when rounded into threads of 4.2 mm in diameter. The test is simple and it is conducted by repeated rolling of an ellipsoidal-sized soil mass by manually with the hand on a glass plate. The soil specimens that are prepared to conduct plastic limit test have to be divided into pieces at the length of 3-10 mm. In such a case, if the soil pieces are rolling into smaller sized pieces, it is possible to understand that the specimens are still too wet and the water content is over the plastic limit. But if the soil pieces are crumbed before the diameter size 3 mm, it can be said that the soil specimen is

too dry and the water content is under the plastic limit. Because of this sensitive and operator depended application of the test, it is so hard to obtain accurate results at the first experience. The liquid limit is defined as the upper water content limit and plastic limit is defined as the lower water content limit of the plastic state of the soil. The plastic behavior is occurred between these upper and lower boundaries and taken into consideration in determining a specific parameter *PI* as before mentioned. Special descriptions are given to evaluate the consistency states of clayey soils in the literature. Burminster [20] classifies the *PI* value in a qualitative manner and defines the states of consistency given in Table 1.

Besides, the plasticity index is significant in the classification of the soils and it is fundamental to the Casagrande plasticity chart, which constitutes the basis for the Unified Soil Classification System (*USCS*).

The plasticity chart is given in Figure 1. The A-line drawn in the figure separates the inorganic silts from inorganic clays. The clays are located above and the silts are located under the A-line. The organic silts are also located under the A-line and the liquid limit is existed between 30% and 50%. Organic clays are located in the same region as inorganic silts, under the A-line and the liquid limit value is bigger than 50%. The line that is located above the A-line is U-line. The U-line represents the approximate upper limit of the relationship of the *PI* and *LL* for any envisaged soil.

In this study, all the used soil types are classified according to the *USCS* and liquid limit tests are conducted with Casagrande cup method.

Table 1. Description of soil consistency depended on the *PI* value [1, 20]

Plasticity Index	Description
0	Non-plastic
1-5	Slightly plastic
5-10	Low plasticity
10-20	Medium plasticity
20-40	High plasticity
>40	Very high plasticity

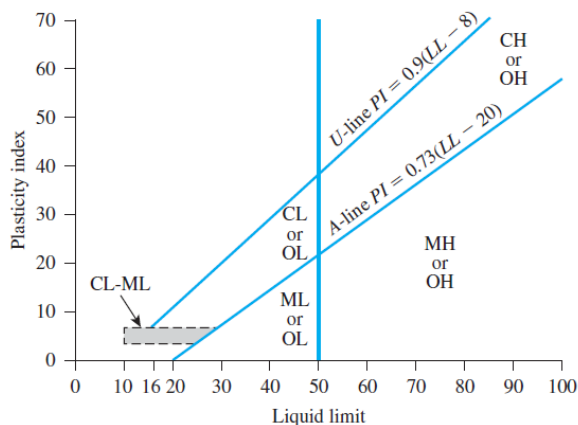


Figure 1. Plasticity chart [1]

### 2.2 Materials and database preparation

In the context of this study, fine-grained soils are taken into consideration to determine their plasticity characteristics via regression analysis. A special database is prepared with the use of 500 soil investigation reports that are supplied with special permission from The Departments of Investment Monitoring and Coordination (DIMCs), Turkey. The soil investigation reports are identifying all the geotechnical soil characteristics of the European side of Istanbul Province. But, the mentioned database is prepared only with the use of the results of natural water content tests, sieve analysis, hydrometer tests, Casagrande cup tests, and plastic limit tests.

Special locations are selected from the European side of Istanbul and four zones are arranged depending on the closeness and the wideness of districts to conduct regression analysis. These districts that are evaluated in the analysis were selected especially from the areas where high and very high plasticity clayey soils that are described in Table 1, are found in the formation. The first zone of the study includes Avcılar, Esenyurt and Küçükçekmece (Zone 1); the second zone includes Büyükçekmece (Zone 2), the third zone includes Çatalca (Zone 3) and the fourth zone includes Zeytinburnu, Bahçelievler, Bakırköy (Zone 4) districts. The locations of the mentioned districts are given in Figure 2. Zone 2 and Zone 3 is formed with the use of only one district due to the existence of huge field volume and attainment of enough soil investigation reports.

Totally 3200 consistency limit tests are used to define the selected districts but only 1523 test results are obtained for high and/or very highly plastic clayey soils (*CH*). The results of 3200 consistency limit tests are illustrated in Figure 3 with the use of Plasticity Chart.

In Figure 3, the high and very highly plastic clays are shown with red dots and named as *CH* according to *USCS*. The distribution of the numbers of consistency limit tests that are used to create the database are given in Table 2 according to the envisaged districts and zones via the regression process variants.

It can be seen from Table 2 that the total number of consistency limit tests conducted for high and very high plastic clays are 249 for Zone 1, 453 for Zone 2, 201 for Zone 3 and 562 for Zone 4 respectively.

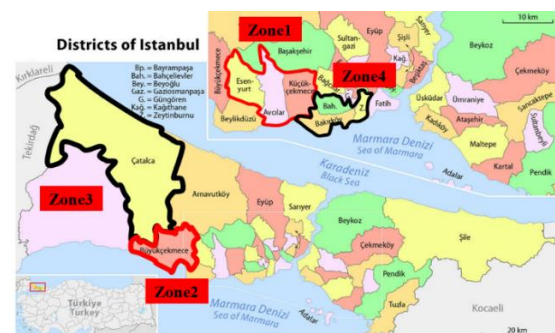


Figure 2. The districts of Istanbul and envisaged zones in the study [21]

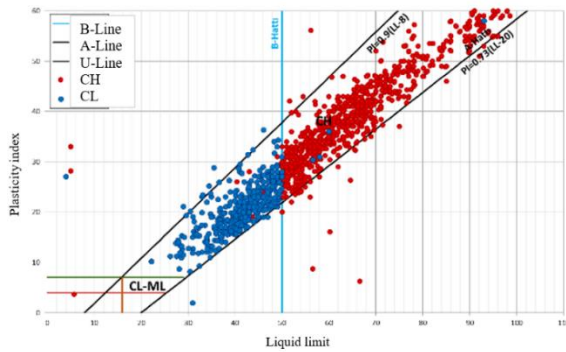


Figure 3. The configurations of liquid limit test results on plasticity chart

Table 2. The number of total consistency limit tests performed for high and very high plastic clays according to the zones

		Objective via variant	PI via LL	PI via LL, h	PI via LL, FC	PI via $w_n$ , FC
Zone 1	Avçılar		23	23	10	10
	Esenyurt		101	101	24	23
	Küçükçekmece		125	125	82	60
Zone 2	Büyükçekmece		453	453	138	368
Zone 3	Çatalca		201	201	229	0
Zone 4	Zeytinburnu		26	26	11	35
	Bahçelievler		110	110	23	376
	Bakırköy		426	426	396	0

The regression analysis is conducted initially to obtain the relationship of the plasticity index in terms of liquid limit. Second step analysis is performed to obtain the relationship of plasticity index in terms of both the specimen depth from the field ( $h$ ) and liquid limit. Third step analysis is conducted to acquire the relationship of plasticity index in terms of liquid limit and fine content of the soil ( $FC$ ). Then the last step is performed to find out the relationship of plasticity index in terms of natural water content ( $w_n$ ) and fine content of soil. The numbers of the tests are reduced due to the increase of the variants of the regression analysis and the number of the tests are also given in Table 2.

### 3. Results and Discussion

Regression analyses are conducted with Matlab R2016a by the use of both 2 and 3 dimensional graph systems to find the most proper expression of plasticity index. Eight different types of functions such as interpolant, linear fitting, polynomial, power, rational, smoothing spline, sum of sine and weibull, are used for 2D analyses and also four different types of functions such as custom equation, interpolant,

lowess and polynomial, are used for 3D analyses to search for the best fitting relationship between the variants in Matlab. Several analyses are performed for each existing method and finally it is found that the proper type of the method is power for 2 dimensional analysis and polynomial for 3 dimensional analyses. In the exploration process of the expression of plasticity index, a two stepped application is conducted. At the first stage, all the envisaged zones are analyzed individually and after, the total evaluations are also conducted for all the existing datasets to find the representative relationship of high and very high plastic clayey soils. At the second stage the equations that are acquired from both 2 and 3 dimensional regression analyses are transferred to Microsoft Excel to search for verification of the result equations. The results obtained by the application of the suggested equations are checked against the actual values of plasticity indexes which are calculated by the application of both experimental liquid and plastic limit tests. Based on the comparison of the results of suggested method and experimental equations, the maximum error, the average error and the percentage of the average errors are achieved. These calculations can provide insight about the probable encountered errors while the use of suggested equation. Therefore, the information about the mentioned details are also added in the content of the results of the analyses.

#### 3.1 Analysis of Zone 1

Regression analyses are conducted for Zone 1 (Avçılar, Esenyurt, Küçükçekmece) with the application of three different conditions arise due to the used variants.

1. *Determination of PI via the use of LL:* This investigation is performed with two dimensional “power” regression analysis. In that case, 249 liquid limit tests are used and the relationship between PI and LL is found by Equation (1).

$$PI = 0.18LL^{1.28} - 1.2 \tag{1}$$

The result curve that is acquired with the calculation of Equation (1) according to the actual values of liquid limit tests are given in Figure 4.

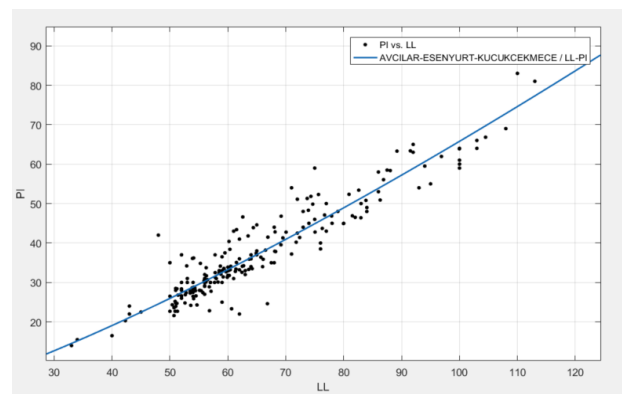


Figure 4. Determination of PI via LL for Zone 1

The outcomes of the analyses are summarized in Table 3. The  $R^2$  value of the most fitting equation is obtained as 0.8918 and the average percent of the errors of the suggested equation is found 7.6%. It can be seen from both Figure 4 and Table 3 that according to the performance values reached in the experimental studies, the regression model shows an effective performance.

2. *Determination of PI via the use of both LL and h:* This investigation is performed with three dimensional “polynomial” regression analysis. In that case, 249 liquid limit tests are used and the relationship between  $PI$  and  $LL$  and  $h$  is found by Equation (2).

$$PI = -13 - 0.01 \times h + 0.77LL \quad (2)$$

The resultant graph that is acquired with the calculation of Equation (2) according to the actual values of liquid limit tests are given in Figure 5.

The outcomes of the analyses are summarized in Table 4. The  $R^2$  value of the most fitting equation is obtained as 0.9304 and the average percent of the errors of the suggested equation is found 7.74%. It can be seen that the addition of the depth factor to the variants of the relationship is strengthening the determination function of  $PI$ . Besides, the average percent of the errors of the suggested equation approximately remain constant.

Table 3. Results of regression analyses for Zone 1 (Condition 1)

Number of the data	249
Value of $R^2$	0.8918
Adjusted $R^2$	0.8909
Average error of the equation	2.8
Average percent of the errors of the equation (%)	7.6

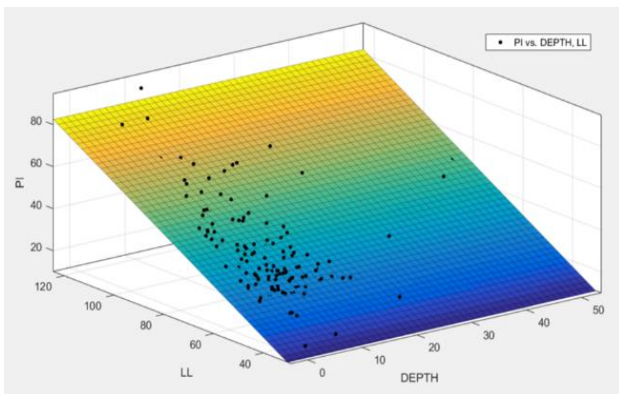


Figure 5. Determination of  $PI$  via  $LL$  and  $h$  for Zone 1

Table 4. Results of regression analyses for Zone 1 (Condition 2)

Number of the data	249
Value of $R^2$	0.9304
Adjusted $R^2$	0.9299
Average error of the equation	2.84
Average percent of the errors of the equation (%)	7.74

3. *Determination of PI via the use of both LL and FC:* This investigation is performed with three dimensional “polynomial” regression analysis. In that case, 116 liquid limit tests are used and the relationship between  $PI$  and  $LL$  and  $FC$  is found by Equation 3.

$$PI = -10 + 0.03 \times FC + 0.75 \times LL \quad (3)$$

The resultant graph that is acquired with the calculation of Equation (3) according to the actual values of liquid limit tests are given in Figure 6.

The outcomes of the analyses are summarized in Table 5. The  $R^2$  value of the most fitting equation is obtained as 0.9464 and the average percent of the errors of the suggested equation is found 5.75%. It can be seen that the addition of the fine content factor to the variants of the relationship is more strengthening the determination function of  $PI$ . In addition to this situation, the average percent of the errors of the suggested equation reduce. Comparison of the analysis performed for  $PI$  via the consideration of  $h$  and  $FC$  individually, demonstrates that the rate of influence of the fine content quantity is relatively bigger than the effect of depth.

### 3.2 Analysis of Zone 2

Regression analyses are conducted for Zone 2 (Büyükçekmece) with the application of three different conditions arise due to the used variants.

1. *Determination of PI via the use of LL:* In that case, 453 liquid limit tests are used and the relationship between  $PI$  and  $LL$  is found by Equation (4). The amount of the laboratory tests is more than Zone 1 for Zone 2.

$$PI = 8.3LL^{0.56} - 46 \quad (4)$$

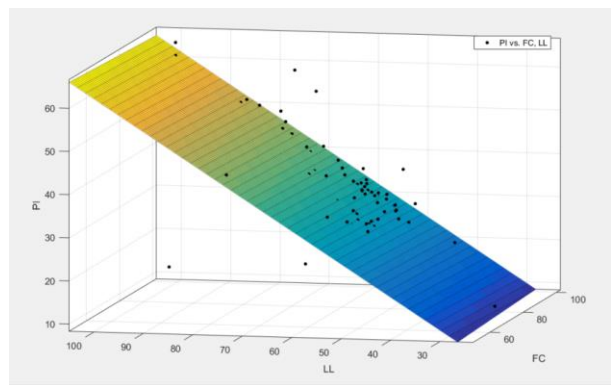


Figure 6. Determination of  $PI$  via  $LL$  and  $FC$  for Zone 1

Table 5. Results of regression analyses for Zone 1 (Condition 3)

Number of the data	116
Value of $R^2$	0.9464
Adjusted $R^2$	0.9454
Average error of the equation	1.86
Average percent of the errors of the equation (%)	5.75

The resultant curve that is acquired with the calculation of Equation (4) according to the actual values of liquid limit tests are given in Figure 7.

The outcomes of the analyses are summarized in Table 6. The  $R^2$  value of the most fitting equation is obtained as 0.9062 and the average percent of the errors of the suggested equation is found 6.40%.

2. *Determination of PI via the use of both LL and h*: In that case, 453 liquid limit tests are used and the relationship between  $PI$  and  $LL$  and  $h$  is found by Equation (5).

$$PI = -6.8 - 0.005 \times h + 0.71 \times LL \quad (5)$$

The resultant graph that is acquired with the calculation of Equation (5) according to the actual values of liquid limit tests are given in Figure 8.

The outcomes of the analyses are summarized in Table 7. The  $R^2$  value of the most fitting equation is obtained as 0.9123 and the average percent of the errors of the suggested equation is found 6.35%. It can be seen that the addition of the depth factor to the variants of the relationship strengthens the determination function of  $PI$ . Besides, the average percent of the errors of the suggested equation approximately remain constant similar with the response of Zone 1.

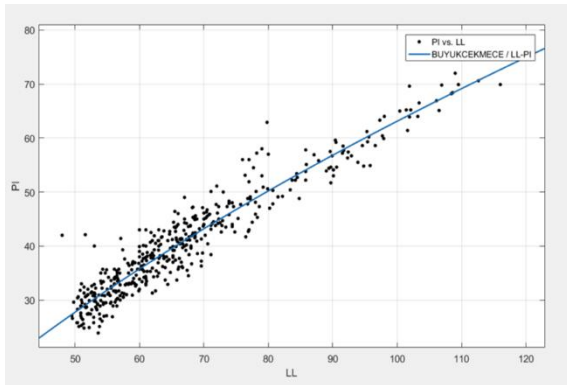


Figure 7. Determination of  $PI$  via  $LL$  for Zone 2

Table 6. Results of regression analyses for Zone 2 (Condition 1)

Number of the data	453
Value of $R^2$	0.9062
Adjusted $R^2$	0.9058
Average error of the equation	2.4
Average percent of the errors of the equation (%)	6.40

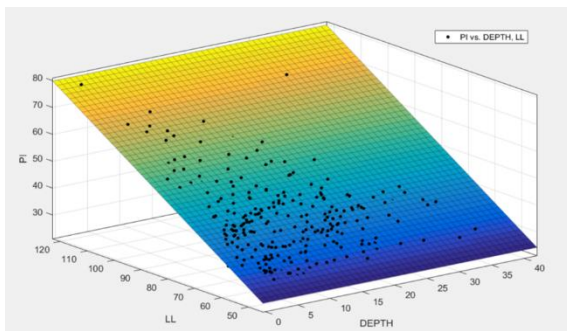


Figure 8. Determination of  $PI$  via  $LL$  and  $h$  for Zone 2

Table 7. Results of regression analyses for Zone 2 (Condition 2)

Number of the data	453
Value of $R^2$	0.9123
Adjusted $R^2$	0.9119
Average error of the equation	2.43
Average percent of the errors of the equation (%)	6.35

3. *Determination of PI via the use of both LL and FC*: In that case, 138 liquid limit tests are used and the relationship between  $PI$  and  $LL$  and  $FC$  is found by Equation (6).

$$PI = -9.4 + 0.06 \times FC + 0.8 \times LL \quad (6)$$

The resultant graph that is acquired with the calculation of Equation (6) according to the actual values of liquid limit tests are given in Figure 9.

The outcomes of the analyses are summarized in Table 8. The  $R^2$  value of the most fitting equation is obtained as 0.7936 and the average percent of the errors of the suggested equation is found 6.7%. In contradistinction to the results of Zone 1 Condition 3, the addition of fine content variant to the solution research, decreases the approximation validity. The effect of depth becomes the significant effective factor for the analyses to establish the actual solution. This situation may be arose due to the evaluated dataset for performing analysis of Condition 3.

### 3.3 Analysis of Zone 3

Regression analyses are conducted for Zone 3 (Çatalca) with the application of three different conditions arise due to the used variants.

1. *Determination of PI via the use of LL*: In that case, 201 liquid limit tests are used and the relationship between  $PI$  and  $LL$  is found by Equation (7).

$$PI = 0.35LL^{1.14} - 4 \quad (7)$$

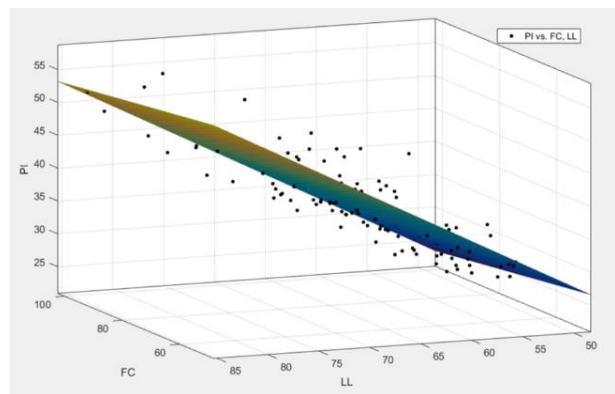


Figure 9. Determination of  $PI$  via  $LL$  and  $FC$  for Zone 2

Table 8. Results of regression analyses for Zone 2 (Condition 3)

Number of the data	138
Value of $R^2$	0.7936
Adjusted $R^2$	0.7902
Average error of the equation	2.42
Average percent of the errors of the equation (%)	6.7



The resultant curve that is acquired with the calculation of Equation (7) according to the actual values of liquid limit tests are given in Figure 10.

The outcomes of the analyses are summarized in Table 9. The  $R^2$  value of the most fitting equation is obtained as 0.8788 and the average percent of the errors of the suggested equation is found 7.13%.

2. *Determination of PI via the use of both LL and h*: In that case, 201 liquid limit tests are used and the relationship between  $PI$  and  $LL$  and  $h$  is found by Equation (8).

$$PI = -11 - 0.09 \times h + 0.72 \times LL \quad (8)$$

The resultant graph that is acquired with the calculation of Equation (8) according to the actual values of liquid limit tests are given in Figure 11.

The outcomes of the analyses are summarized in Table 10. The  $R^2$  value of the most fitting equation is obtained as 0.8815 and the average percent of the errors of the suggested equation is found 6.82%.

It can be seen that the addition of the depth factor to the variants of the relationship strengthens the determination function of  $PI$ . Besides, the average percent of the errors of the suggested equation approximately remain approximately constant similar with the response of Zone 1 and Zone 2.

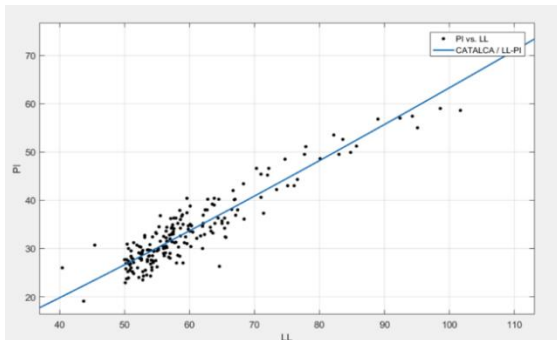


Figure 10. Determination of  $PI$  via  $LL$  for Zone 3

Table 9. Results of regression analyses for Zone 3 (Condition 1)

Number of the data	201
Value of $R^2$	0.8788
Adjusted $R^2$	0.8776
Average error of the equation	2.37
Average percent of the errors of the equation (%)	7.13

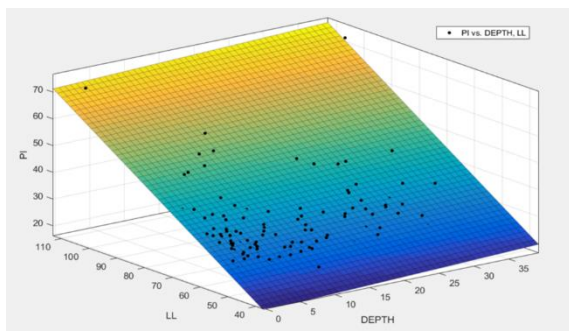


Figure 11. Determination of  $PI$  via  $LL$  and  $H$  for Zone 3

Table 10. Results of regression analyses for Zone 3 (Condition 2)

Number of the data	201
Value of $R^2$	0.8815
Adjusted $R^2$	0.8803
Average error of the equation	2.26
Average percent of the errors of the equation (%)	6.82

3. *Determination of PI via the use of both LL and FC*: In that case, 229 liquid limit tests are used and the relationship between  $PI$  and  $LL$  and  $FC$  is found by Equation (9).

$$PI = -6.7 + 0.04 \times FC + 0.72 \times LL \quad (9)$$

The resultant graph that is acquired with the calculation of Equation (9) according to the actual values of liquid limit tests are given in Figure 12.

The outcomes of the analyses are summarized in Table 11. The  $R^2$  value of the most fitting equation is obtained as 0.8848 and the average percent of the errors of the suggested equation is found 8.2%. The interchange of  $h$  and  $FC$  in the solution function, approximately affects the ultimate result of the suggested method similar but the average percent of the errors of the equation are a little bigger for the effect of  $FC$  rather than the effect of  $h$ .

### 3.4 Analysis of Zone 4

Regression analyses are conducted for Zone 4 (Zeytinburnu, Bahçelievler, Bakırköy) with the application of three different conditions arouse due to the used variants.

1. *Determination of PI via the use of LL*: In that case, 562 liquid limit tests are used and the relationship between  $PI$  and  $LL$  is found by Equation (10).

$$PI = 1,55LL^{0,86} - 17 \quad (10)$$

The resultant curve that is acquired with the calculation of Equation (10) according to the actual values of liquid limit tests are given in Figure 13.

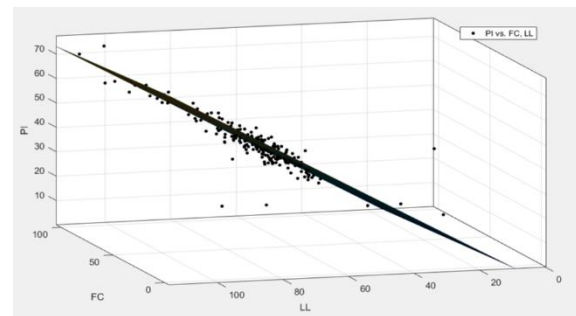


Figure 12. Determination of  $PI$  via  $LL$  and  $FC$  for Zone 3

Table 11. Results of regression analyses for Zone 3 (Condition 3)

Number of the data	229
Value of $R^2$	0.8848
Adjusted $R^2$	0.8836
Average error of the equation	2.37
Average percent of the errors of the equation (%)	8.2

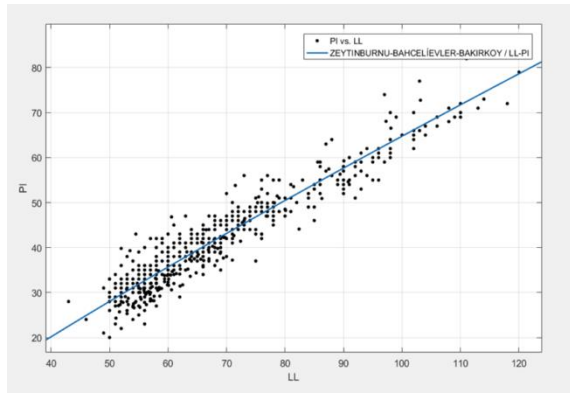


Figure 13. Determination of *PI* via *LL* for Zone 4

The outcomes of the analyses are summarized in Table 12. The  $R^2$  value of the most fitting equation is obtained as 0.9032 and the average percent of the errors of the suggested equation is found 7.10%.

2. Determination of *PI* via the use of both *LL* and *h*: In that case, 562 liquid limit tests are used and the relationship between *PI* and *LL* and *h* is found by Equation (11).

$$PI = -7.8 - 0.03 \times h + 0.73 \times LL \quad (11)$$

The resultant graph that is acquired with the calculation of Equation (11) according to the actual values of liquid limit tests are given in Figure 14.

The outcomes of the analyses are summarized in Table 13. The  $R^2$  value of the most fitting equation is obtained as 0.9057 and the average percent of the errors of the suggested equation is found 7.23%. It can be seen that the addition of the depth factor to the variants of the relationship is not effected the determination function of *PI*.

Table 12. Results of regression analyses for Zone 4 (Condition 1)

Number of the data	562
Value of $R^2$	0.9036
Adjusted $R^2$	0.9032
Average error of the equation	2.8
Average percent of the errors of the equation (%)	7.10

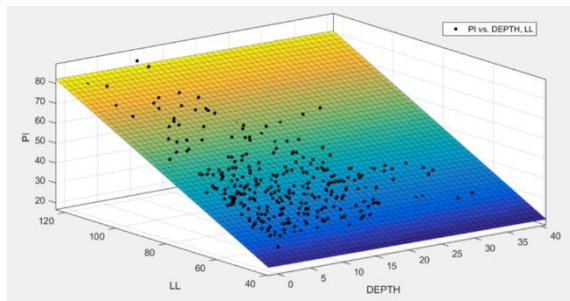


Figure 14. Determination of *PI* via *LL* and *h* for Zone 4

Table 13. Results of regression analyses for Zone (Condition 2)

Number of the data	562
Value of $R^2$	0.9057
Adjusted $R^2$	0.9054
Average error of the equation	2.81
Average percent of the errors of the equation (%)	7.23

3. Determination of *PI* via the use of both *LL* and *FC*: In that case, 430 liquid limit tests are used and the relationship between *PI* and *LL* and *FC* is found by Equation (12).

$$PI = -9.5 + 0.03 \times FC + 0.7 \times LL \quad (12)$$

The resultant graph that is acquired with the calculation of Equation (12) according to the actual values of liquid limit tests are given in Figure 15.

The outcomes of the analyses are summarized in Table 14. The  $R^2$  value of the most fitting equation is obtained as 0.9207 and the average percent of the errors of the suggested equation is found 6.54%. The change of *h* with *FC* affects the accuracy of the suggested equation. The approximation is strengthening and also the average percent of the errors are decreased.

Besides all the investigated cases, the integrated effects of the use of the natural water content and fine content of the soil within the search of proper function to calculate *PI* is studied. But none of the functions defined in Matlab are fitted to obtain the relationship of  $w_n$  and *FC*.

The distribution of the  $w_n$  and *FC* values are shown in Figure 16. Although the illustration shows a convergent relationship between the mentioned values, the calculated values of  $R^2$  are staying between 0.1-0.2. This situation is not a meaning of the ineffectiveness of the parameters on the calculation process of *PI*. Indirect relationships can be obtained if multivariate regression analysis is conducted.

In addition to all these, in order to compare the effect of the data number, common field analyses are conducted with the use of total number of all experimental studies done through all the considered district. The total number of the evaluated dataset is 1532. The similar three conditions, that are mentioned before, about the variants of the solutions for the zones are also taken into account in the analyses. The relationship between plasticity index and liquid limit is obtained by performing two-dimensional analysis and solution result is given in Equation (13) and shown by Figure 17.

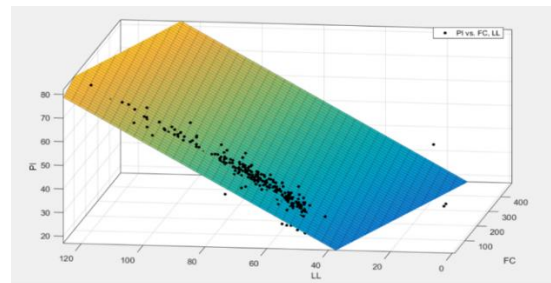


Figure 15. Determination of *PI* via *LL* and *FC* for Zone 4

Table 14. Results of regression analyses for Zone 4 (Condition 3)

Number of the data	430
Value of $R^2$	0.9207
Adjusted $R^2$	0.9203
Average error of the equation	2.5
Average percent of the errors of the equation (%)	6.54

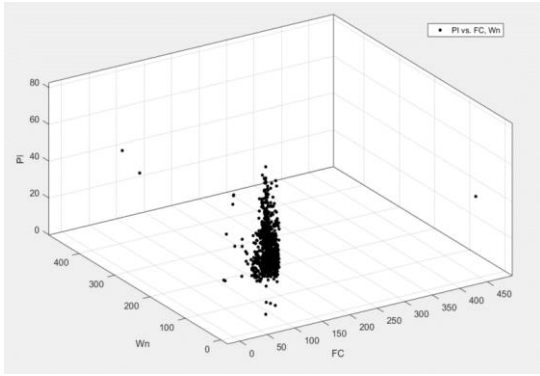


Figure 16. Determination of  $PI$  via  $w_n$  and  $FC$

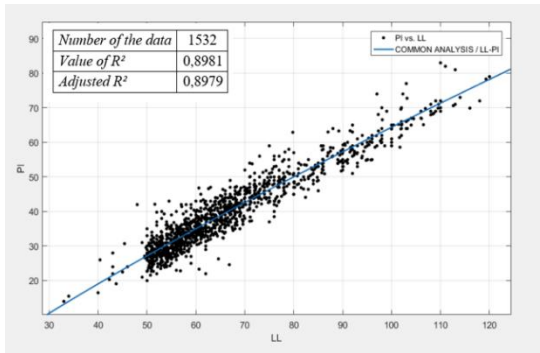


Figure 17. Determination of  $PI$  via  $LL$

$$PI = -1.96LL^{0.82} - 21.6 \quad (13)$$

The  $R^2$  value of the most fitting equation is obtained as 0.8981 for common field analysis.

It is found that the change in plasticity index in terms of  $LL$  and  $h$  can be obtained by Equation (14) and shown by Figure 18.

$$PI = -9.7 + 0.015h + 0.74LL \quad (14)$$

The  $R^2$  value of the most fitting equation is obtained as 0.9062 for common analysis.

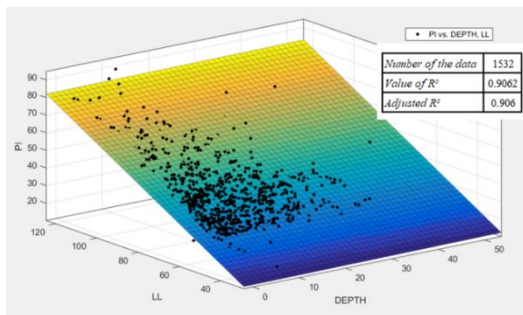


Figure 18. Determination of  $PI$  via  $LL$  and  $h$

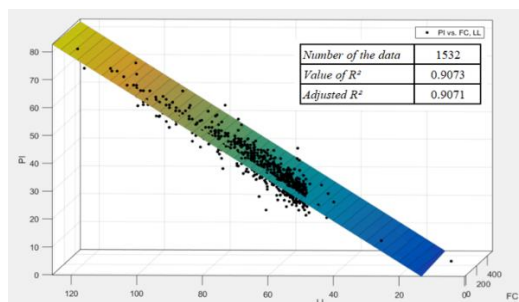


Figure 19. Determination of  $PI$  via  $LL$  and  $FC$

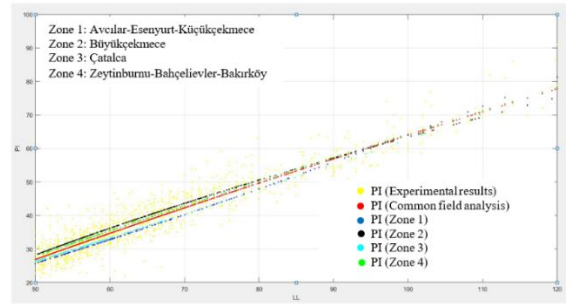


Figure 20. Comparison of the regression analysis of determination of  $PI$  via  $LL$

The regression analysis conducted in the three dimensional “sphere” gives  $PI$  value as a function of  $LL$  and  $FC$  in Equation (15) and shown by Figure 19. The  $R^2$  value of the most fitting equation is obtained as 0.9073 for common analysis.

$$PI = -10 + 0.002FC + 0.73LL \quad (15)$$

According to the  $R^2$  values, it is possible to say that the results of the regression analysis of common evaluation of districts give satisfactory approaches. The compatibility of all the envisaged equations is calculated approximately 90%. When the analysis made for the regions are checked separately, it is seen that the accuracy convergence is lower in the zones with low data compared to common analysis. Consequently, this situation is a direct proof of the data set number effects on the prediction of soil properties.

In Figure 20, an integrated illustration of the experimental test results and the results of the suggested equations are given together. The graph system is arranged to represent the acquirement process of  $PI$  in terms of  $LL$  value. The individual equations of envisaged zones and the equation of common field analysis have been used for the locations that the data are valid. It will be consistent to say that the solution of the common field analysis approximately scans all the experimental test results and the suggested equation of common field analysis may be used as the representative solution function of  $CH$  type soils present at Istanbul. Besides, it is a significant issue that the results of Zone 1-Zone 4 and Zone 2-Zone 3 are close to each other and the curves of solution functions of these mentioned zones constitute the upper and lower  $PI$  boundaries of common filed analysis curve respectively. These close results are arising due to the locations of the districts. The closeness of the districts increases the similarity between the obtained results.

In addition to all these, the comparisons between the suggested equations to determine  $PI$  value, are not be enough to confirm the exact solution function. Therefore, in the context of the study, different comparisons are made to check the accuracy of all the attained relationships. The confirmation process of the equations is continued with two focused ways. Comparisons with actual experimental dataset forms the first way of the confirmation process. In addition,

the discussion with the literature sources creates the second way. The first step of the confirmation process has been studied and explained before, together with the studies of the acquirement of the equation. Therefore, the study is continued with the description of the comparisons between the literature studies. Three different studies are selected from the literature to compare the results of regression analysis. This selection has been done according to the accessibility opportunities of the literature sources. In the selected studies, the determinations are presented for the calculation of  $PI$  in terms of  $LL$ . The first study is suggested by Seed et al. [22]. This study is based on the investigation of the plasticity characteristics of artificial kaolinite-quartz mixtures and Equation (16) is suggested to predict the  $PI$  value of constituted soil specimens.

$$PI = 0.98xLL - 27.5 \quad (16)$$

The second study is proposed by Nagaraj and Jayadeva [23]. Their study is based on the tests of natural clays coming from different depths with heterogeneous mineralogy. Equation (17) is suggested by Nagaraj and Jayadeva [23] to determine  $PI$ .

$$PI = 0.74xLL - 8 \quad (17)$$

The third study is conducted by Spagnoli et al. [24]. Their study is based on the investigation of the plasticity characteristics of smectite and kaolinite types of clay minerals. Equation (18) is suggested for smectite and Equation (19) is suggested for kaolinite type of minerals to calculate the  $PI$  value.

$$PI = 0.97xLL - 37.6 \quad (18)$$

$$PI = 5.94e^{0.023LL} \quad (19)$$

Equation 16-18 is selected to calculate all of the  $PI$  values with the use of the mutual data with common field analysis. In Figure 21, the results of the experimental tests, the common field analysis and the Equation 16-18 is given. The results of the common field analysis are closer with both the experimental test results and the solutions of the equations suggested by Nagaraj and Jayadeva [23]. Besides, the tendency of the behavior of common filed analysis and solutions of Nagaraj and Jayadeva [23] is similar. But especially the solution of Spagnoli et al. [24] differentiates from all appreciated studies and the solutions of Seed et al. [22] presents a different tendency than other relationships. The close similarity between the suggested equation solutions and Nagaraj and Jayadeva [23] arose directly due to the similarity of used kind of soil specimens. Nagaraj and Jayadeva [23] prefers to use natural clays coming from different depths with heterogeneous mineralogy. This preference is in common with the logic of the presented study. Seed et al. [22] and Spagnoli et al. [24] searches for a relationship to determine the plasticity characteristics of special types of minerals.

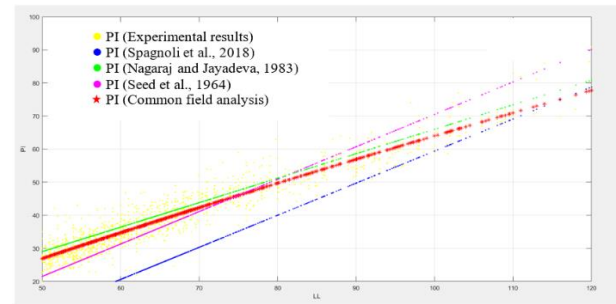


Figure 21. Comparison of the suggested equation with literature sources

This condition zooms out the results of suggested equations and investigated literature sources.

#### 4. Conclusion

This study is conducted to investigate the relationships and effect degrees of parameters on the determination process of the plasticity index in terms of different geotechnical properties. High and very high plastic clay types that are acquired from the special districts of Istanbul province are entreated within the context of the study. Regression analysis is performed for envisaged zones of the investigated field with both the use of two and three dimensional analyses. Individual identifier equations are obtained for each of the defined zones to calculate  $PI$  value and the effect degrees of the parameters are discussed. Common field analysis is also performed to compare the representability of a mutual equation for defining the plasticity parameters of the foreseen zones. Additionally, comparisons are made with the literature sources to verify the suggested equations. Consequently, in this study, these outcomes are obtained:

- Relatively strong equations have been acquired to determine the  $PI$  value in terms of  $LL$ ,  $LL-h$ ,  $LL-FC$ ,  $w_n-FC$  respectively based on the actual experimental tests conducted for Istanbul.
- The comparison process of the suggested relationships with the literature sources also supports the applicability of the envisaged relationships.
- A significant result of the study is to attract attention on the relationships of which are selected to represent the simple geotechnical properties of the investigation site which constitutes the first step of the design.
- In cases where it is not possible to conduct an experimental study, the necessity of checking the validity of the expressions used in the geotechnical parameter estimation for the project sites in question constitutes the final point of view of this study. The parameter prediction methods have to be checked carefully according to the dominant soil type of the research or project.
- Having all those in mind, the current study presents an applicable acquirement process of  $PI$  value for  $CH$  types of clays existed in Istanbul. This situation also paves the way for different parameter estimations that can be made depending on the plasticity index value.

## Declaration

The author(s) declared no potential conflicts of interest with respect to the research, authorship, and/or publication of this article. The author(s) also declared that this article is original, was prepared in accordance with international publication and research ethics, and ethical committee permission or any special permission is not required.

## Acknowledgment

This work supported by Istanbul University Cerrahpaşa under Scientific Research Project (project no: BYP-2020-34856 and FBA-2020-34051) and The Departments of Investment Monitoring and Coordination (DIMCs), Turkey.

## Nomenclature

$CH$	: High plastic clayey soil
$h$	: Depth
$FC$	: Fine content
$LL, w_L$	: Liquid limit
$N$	: Blow number
$PI$	: Plasticity index
$PL, w_p$	: Plastic limit
$USCS$	: Unified soil classification system
$w_n$	: Natural water content

## References

- Das, B.M. and K. Sobhan, *Principles of Geotechnical Engineering*. Eight Edition, Cengage Learning, USA, 2017.
- Atterberg, A., *Über die physikalische Bodenuntersuchung, und über die Plastizität de Tone*, International Mitteilungen für Bodenkunde, 1, 10-43.
- Kollaros, G., *Liquid limit values obtained by different testing methods*. Bulletin of the Geological Society of Greece, 2016. **50**(2): p.778-787.
- Casagrande, A., *Research of Atterberg Limits of soils*. Public Roads, 1932. **13**(8): p.121-136.
- Casagrande, A., *Notes on the design of the liquid limit device*. Géotechnique, 1958. **8** (2): p.84-91.
- Skempton, A. W. and R.D. Northey, *The sensitivity of clays*. Geotechnique, 1953. 3: p.30-53.
- Fall, D., *A Numerical model for repaid determination of plasticity of fine grained soils*, Ground Engineering, 2000.
- Chenari, R. J., P. Tizpa, M.R.G. Rad, S.L. Machado and M.K. Fard, *The use of index parameters to predict soil geotechnical properties*, Arabian Journal of Geosciences, 2014. **8** (7): p.1-13.
- Tanzen, R., T. Sultana, M.S. Islam and A.J. Khan, *Determination of plastic limit using cone penetrometer*. Proceedings of 3rd International Conference on Advances in Civil Engineering, 2016. p. 209-214.
- Kuriakose, B., B.M. Abraham, A. Sridharan and B.T. Jose, *Water content ratio: An effective substitute for liquidity index for prediction of shear strength of clays*. Geotechnical and Geological Engineering, 2017. 35: p.1577-1586.
- Naveena, N., S.J. Sanjay and N.S. Chandanshree, *Establishing relationship between Plasticity Index and Liquid Limit by Simple Linear Regression Analysis*. International Journal for Research in Applied Science & Engineering Technology, 2018. **6** (6): p.1975-1978.
- Jasim, M. M., R.M. Al-Khaddar and A. Al-Rumaithi, *Prediction of bearing capacity, angle of internal friction, cohesion, and plasticity index using ANN (Case Study of Baghdad, Iraq)*. International Journal of Civil Engineering and Technology, 2019. **10** (1): p.2670-2679.
- Cantillo, V., V. Mercado and C. Pájaro, *Empirical correlations for the swelling pressure of expansive clays in the city of Barranquilla, Colombia*. Earth Sciences Research Journal, 2017. **21** (1): p. 45-49.
- Spagnoli, G. and M. Feinendegen, *Relationship between measured plastic limit and plastic limit estimated from undrained shear strength, water content ratio and liquidity index*. Cambridge University Press, 2017. **52** (4): p. 509-519.
- Shimobe, S., G. Spagnoli, *Relationships between undrained shear strength, liquidity index, and water content ratio of clays*. Bulletin of Engineering Geology and Environment, 2020.
- Barnes, G. E., *A multi-linear approach to strength and plasticity states between the Atterberg limits*. Proceedings of the Institution of Civil Engineers - Geotechnical Engineering, 2020.
- Golawska, K., Z. Lechowicz, W. Matusiewicz and M.J. Sulewska, *Determination of the Atterberg Limits of Eemian Gytja on samples with different composition*, Studia Geotechnica et Mechanica, 2020. **42**(2): p.168-178.
- Hussain, A. and C. Atalar, *Estimation of compaction characteristics of soils using Atterberg limits*, IOP Conference Series : Materials Science and Engineering, 2020. **800** (2020).
- Singh H. and A.K. Gupta, *Correlation between shear strength of soils and water content ratio as a substitute for liquidity index*. Advances in Computer Methods and Geomechanics, 2020. 56: p.299-306.
- Burmister, D. M., *Principles and techniques of soil identification*, Proceedings, Annual Highway Research Board Meeting. National Research Council, Washington, D.C., 1949. Vol. 29: p. 402-434.
- The districts of Istanbul [cited 2020 6 May]; Available from: <https://istanbulharitasi360.com/istanbul-ilce-haritasi>
- Seed, H. B., R.J. Woodward and R. Lundgren, *Fundamental aspects of the Atterberg Limits*, Journal of the Soil Mechanics and Foundations Division, 1964. **90** (6): p. 75-106.
- Nagaraj, T.S. and M.S. Jayadeva, *Critical reappraisal of plasticity index of soils*. J. Geotech. Eng. Div., ASCE, 1983. **109**(7): p.994-1000.
- Spagnoli, G., A. Sridharan, P. Oreste, D. Bellato and L.D. Matteo, *Statistical variability of the correlation plasticity index versus liquid limit for smectite and kaolinite*. Applied Clay Science, 2018. **156** (2018): p.152-159.